AFFDL-TR-78-78

LEVEL II

AD A072484

ANALYTICAL AND EXPERIMENTAL EVALUATION OF TWO DESIGNS FOR A GRAPHITE/EPOXY ANTENNA FEED TRUSS FOR A COMMUNICATIONS SATELLITE

OSCAR ORRINGER
JOHN F. MC CARTHY, JR.
MICHAEL WEINREICH
ALEXANDER HARRIS

CENTER FOR SPACE RESEARCH
MASSACHUSETTS INSTITUTE OF TECHNOLOGY
CAMBRIDGE, MASSACHUSETTS 02139

DDC
AUG 8 1979

JUNE 1978

TECHNICAL REPORT AFFDL-TR-78-78
Final Report June 1977 - March 1978

DDC FILE COPY

Approved for public release; distribution unlimited.

AIR FORCE FLIGHT DYNAMICS LABORATORY
AIR FORCE WRIGHT AERONAUTICAL LABORATORIES
AIR FORCE SYSTEMS COMMAND
WRIGHT-PATTERSON AIR FORCE BASE, OHIO 45433

79 08 07 030

NOTICE

When Government drawings, specifications, or other data are used for any purpose other than in connection with a definitely related Government procurement operation, the United States Government thereby incurs no responsibility nor any obligation whatsoever; and the fact that the government may have formulated, furnished, or in any way supplied the said drawings, specifications, or other data, is not to be regarded by implication or otherwise as in any manner licensing the holder or any other person or corporation, or conveying any rights or permission to manufacture, use, or sell any patented invention that may in any way be related thereto.

This report has been reviewed by the Information Office (OI) and is releasable to the National Technical Information Service (NTIS). At NTIS, it will be available to the general public, including foreign nations.

This technical report has been reviewed and is approved for publication.

Rodman D. Joblove

RODMAN D. JOBLOVE
Project Engineer

Larry G. Kelly

LARRY G. KELLY
Acting Chief, Structural Concepts Br
Structural Mechanics Division

FOR THE COMMANDER

Ralph L. Kuster Jr.

RALPH L. KUSTER, JR., Colonel, USAF
Chief, Structural Mechanics Division

"If your address has changed, if you wish to be removed from our mailing list, or if the addressee is no longer employed by your organization please notify AFFDL/FBS *,W-PAFB, OH 45433 to help us maintain a current mailing list".*

Copies of this report should not be returned unless return is required by security considerations, contractual obligations, or notice on a specific document.

AIR FORCE/56780/21 May 1979 — 150

UNCLASSIFIED

SECURITY CLASSIFICATION OF THIS PAGE (When Data Entered)

REPORT DOCUMENTATION PAGE	READ INSTRUCTIONS BEFORE COMPLETING FORM
1. REPORT NUMBER: AFFDL-TR-78-78	2. GOVT ACCESSION NO. / 3. RECIPIENT'S CATALOG NUMBER
4. TITLE (and Subtitle): ANALYTICAL AND EXPERIMENTAL EVALUATION OF TWO DESIGNS FOR A GRAPHITE/EPOXY ANTENNA FEED TRUSS FOR A COMMUNICATIONS SATELLITE.	5. TYPE OF REPORT & PERIOD COVERED: FINAL Rept. June 1977 - March 1978
	6. PERFORMING ORG. REPORT NUMBER: CSR-TR-78-1
7. AUTHOR(s): Oscar Orringer, John F. McCarthy, Jr., Michael Weinreich and Alexander Harris	8. CONTRACT OR GRANT NUMBER(s): F33615-77-C-3083
9. PERFORMING ORGANIZATION NAME AND ADDRESS: Center for Space Research, MIT, Cambridge, MA 02139	10. PROGRAM ELEMENT, PROJECT, TASK AREA & WORK UNIT NUMBERS: 69CW-01-35 01
11. CONTROLLING OFFICE NAME AND ADDRESS: Air Force Flight Dynamics Laboratory (FBS), Wright-Patterson Air Force Base, OH 45433	12. REPORT DATE: June 1978
	13. NUMBER OF PAGES: 320
14. MONITORING AGENCY NAME & ADDRESS (if different from Controlling Office): 331 p. PE 63211F	15. SECURITY CLASS. (of this report): Unclassified
	15a. DECLASSIFICATION/DOWNGRADING SCHEDULE

16. DISTRIBUTION STATEMENT (of this Report)

Approved for public release; distribution unlimited.

17. DISTRIBUTION STATEMENT (of the abstract entered in Block 20, if different from Report)

18. SUPPLEMENTARY NOTES

19. KEY WORDS (Continue on reverse side if necessary and identify by block number)

Composite Materials
Graphite/Epoxy Composites
Large Space Structures
Tubular Composite Structures

20. ABSTRACT (Continue on reverse side if necessary and identify by block number)

Two final candidate configurations for a communications satellite antenna feed truss are studied to determine which concept is better suited to the application. Both candidates are designed with graphite/epoxy tubing, and were screened from several other concepts in a preliminary study. The comparative assessment in the present study is based in part on cyclic thermal fatigue design development tests, and in part on dynamic response analyses and finite-element stress analyses.

DD FORM 1 JAN 73 1473 EDITION OF 1 NOV 65 IS OBSOLETE

UNCLASSIFIED

SECURITY CLASSIFICATION OF THIS PAGE (When Data Entered)

403 837

PREFACE

The developments documented in this report were carried out at the Center for Space Research and the Aeroelastic and Structures Research Laboratory, Massachusetts Institute of Technology, Cambridge, Massachusetts 02139, under Contract No. F33615-77-C-3083 (Project 69CW, Task 69CW01-35) from the U.S. Air Force Flight Dynamics Laboratory. Mr. Rod Joblove and Captain Richard A. Dirks (AFFDL/FBS) served as technical monitors.

The authors wish to express their appreciation to Dr. Bernard M. Halpin and Mr. Dana Granville, U.S. Army Materials and Mechanics Research Center, Watertown, MA, for making the AMMRC autoclave facility available for curing of the laminates which were fabricated for the experimental phase of the research.

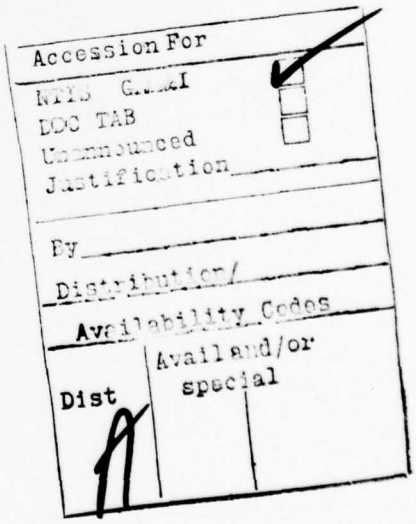


TABLE OF CONTENTS

SECTION		PAGE
I	INTRODUCTION	1
II	CANDIDATE DESIGNS AND STRUCTURAL REQUIREMENTS	3
	1. Background	3
	2. ATS/3-Ring Design	7
	3. Tripod-B Design	12
	4. Structural Requirements	15
III	MATERIAL PROPERTIES AND DESIGN DEVELOPMENT TESTS	19
	1. Test Objectives	19
	2. Static Tests for Material Properties	20
	3. Residual Strength Tests	22
VIII	ANALYSES OF CANDIDATE DESIGN CONCEPTS	24
	1. Analysis Objectives	24
	2. Dynamic Performance	24
	3. Joint Stress Analysis	28
	4. Assessment of Bursting Margin	33
	5. Assessment of Fatigue Damage Accumulation	35
V	COMPARATIVE ASSESSMENT OF CANDIDATE DESIGNS	37
VI	FABRICATION, INSPECTION AND QUALIFICATION	42
	1. Component Fabrication and Inspection	42
	2. Joint Fabrication	44
	3. Design Allowables	46
	4. Qualification of Flight Hardware	48
VII	OTHER SPACE APPLICATIONS	52
	1. Large Space Structures	52
	2. Design Requirements	54
	3. Impact on Design, Fabrication, and Testing	56
VIII	CONCLUSIONS AND RECOMMENDATIONS	61
	APPENDIX A - INVESTIGATION OF ANGLE-PLY DELAMINATION COUPON AS AN INTERLAMINAR STRENGTH TEST	67
	1. General	67
	2. The Delamination Coupon	69

TABLE OF CONTENTS (cont'd)

SECTION		PAGE
	3. Additional Engineering Analysis	72
	4. Test Specimen Fabrication	77
	5. Experimental Results	79
	6. Final Assessment of Specimen Quality	83
	7. Statistical Analysis of Delamination Failures	84
	8. Discussion and Conclusions	87
	APPENDIX B - TREND TESTS FOR INTERLAMINAR SHEAR STRENGTH	89
	1. General	89
	2. Test Specimen Fabrication	90
	3. Experimental Procedure and Test Matrix	92
	4. Experimental Results for Static Strength	95
	5. Experimental Results for Strength Degradation	104
	6. Discussion and Conclusions	116
	APPENDIX C - THERMAL FATIGUE TESTS OF JOINT DETAILS	117
	1. General	117
	2. Accelerated Testing	118
	3. Test Specimen Fabrication and Test Matrix	126
	4. Test Procedures	131
	5. Experimental Results	134
	6. Discussion of Results	140
	APPENDIX D - VIBRATION ANALYSIS APPROACH AND RESULTS	149
	1. General	149
	2. Vibration Analysis	149
	3. Modal Formulation for Response Analysis	152
	4. Calculation of Exceedance Rates	157
	5. Excitation Input Data	160
	6. Finite-Element Models	161
	7. Results of Eigenvalue Analysis	168
	8. Results of Response Analysis	175
	9. Static Margins	185
	10. Fatigue Damage Estimates	188
	APPENDIX E - TRUSSWORK FINITE-ELEMENT MODEL	199
	1. General	199
	2. Data Input Conventions	203
	3. Requirements for Permanent Storage Files	210
	4. Dimension Requirements	211
	5. Core Requirement and Execution Time	213

TABLE OF CONTENTS (cont'd)

SECTION		PAGE
	APPENDIX F - SPECTRAL ANALYSIS PROGRAM	215
	1. General	215
	2. Data Input Conventions	217
	3. Requirements for Storage Files	221
	4. Dimension Requirements	222
	5. Core Requirement and Execution Time	223
	APPENDIX G - THE TEE-JOINT ANALYSIS PROGRAM	225
	1. Introduction	225
	2. Coordinate Systems and Transformations	227
	3. Tube Intersections	231
	4. Applied Forces	232
	5. User's Guide	234
	6. Program Capacity	246
	APPENDIX H - THE AXISYMMETRIC JOINT ANALYSIS PROGRAM (PROGRAM "RADSYM")	249
	1. General	249
	2. Transformation of Elasticity Matrix	252
	3. User's Guide Part I: Mesh Generation	254
	4. User's Guide Part II: Input Data Format	257
	5. Program Capacity	265
	6. Example Joint Analysis	266
	APPENDIX I - EFFECT OF ADHEREND TAPER ON BONDED LAP JOINTS	275
	1. General	275
	2. Formulation	275
	3. Solution Procedure and Results	279
	APPENDIX J - DEPLOYMENT DYNAMICS	285
	1. Antenna Deployment Scenario	285
	2. Antenna Model	286
	3. Solution and Calibration of Antenna Model	289
	4. Dynamic Load Factors	293
	5. Discussion and Conclusions	296

TABLE OF CONTENTS (cont'd)

SECTION		PAGE
	APPENDIX K - FABRICATION OF TUBULAR GRAPHITE/EPOXY COMPONENTS	297
	1. Background	297
	2. Experience in Present Program	302
	3. Discussion and Conclusions	306
	APPENDIX L - COMPONENT PROOF TESTING	309
	1. Applicability	309
	2. Probabilistic Definition of Proof Load	310
	3. Relating Proof Load to Hydrostatic Test	314
	REFERENCES	315

LIST OF ILLUSTRATIONS

FIGURE		PAGE
1	Schematic of ATS-6 Communication Satellite	4
2	Schematic of Projected USAF Communication Satellite	5
3	ATS-6 Feed Truss	6
4	ATS/3-Ring Truss with Joint Details	9
5	Tripod-B Truss with Joint Details	13
6	Antenna Focus Errors Caused by Thermal Deformation of Standoff Truss	18
7	MJS77 Design Input Power Spectrum	27
8	Structure Modeled by Tee-Joint Program	30
9	Joint Dimensions for Stress Analysis	31
10	Laminate Parameter for Burst Model	35
11	Concept for Active Radar in Space	54
12	Comparison of Launch Spectra	56
13	Comparison of Load-Time Histories	58
14	Electromechanical Control System	60
A-1	Standard Tests for Interlaminar Shear Strength	68
A-2	Flatwise Tension Specimen	68
A-3	Delamination Coupon	69
A-4	Midplane Interlaminar Normal Stress in Edge Zone	71
A-5	Free-Body Diagram Illustrating Anticlastic Distribution of Interlaminar Normal Stress	73
A-6	Qualitative Distributions for Interlaminar Stresses	75
A-7	Comparison of Interlaminar Shear and Interlaminar Tension	76
A-8	Asymptotic Value of Interlaminar Tension at Free Edge as a Function of Delamination Coupon Design	77
A-9	Edge Views of Typical Delaminations	81/82
A-10	Typical Fiber Failure at Ultimate Load	82
B-1	Local Crippling Failure	90
B-2	Hand Tool Used to Perforate Mylar Inserts	91
B-3	Short-Beam Shear Test	92
B-4	Schematic Illustrations of Failure Modes	96

LIST OF ILLUSTRATIONS (cont'd)

FIGURE		PAGE
B-5	Typical $[0°_{12}/M1/0°/M1/0°/M1/0°_{12}]$ Laminate Failure	95
B-6	Comparison of Mean Static Strength Estimates	98
B-7	Plot of Mean Residual Strength Estimates	105
C-1	Comparison of Solutions for Symmetrical Heat Transfer Through Both Surfaces of a Wall	120
C-2	General Behavior of Temperature Gradient with Cooling Time	122
C-3	Comparison of Radiative Cooling with LN_2 Immersion of Insulated Test Specimens	123
C-4	Comparison of Radiative Cooling with LN_2 Immersion of Bare and Insulated Test Specimens	124
C-5	Temperature Distribution Assumed for Thermal-Shock Stress Analysis	125
C-6	Configuration of DDT Specimen	127
C-7	Photograph of Sleeve	128
C-8	Photograph of Completed DDT Article	128
C-9	Thermal Cycle Apparatus	132
C-10	Cycle Control Circuit	133
C-11	Schematic of Splitting Failure	136
C-12	Typical Bursting Failures	138
C-13	Typical End Failures	139
C-14	One-Dimensional Model of Joint	140
C-15	Free-Body Diagrams for Joint Model	141
C-16	Detail of Tube Cross Section	148
D-1	Input Spectra (from MJS77-3-240)	160
D-2	ATS/3-Ring Finite-Element Model	162
D-3	Tripod-B Finite-Element Model	163
D-4	Schematic Representation of Mode Shapes	171
D-5	Comparison of ATS/3-Ring Natural Frequencies with MJS77 Design Input Power Spectrum	173
D-6	Comparison of Tripod-B Natural Frequencies with MJS77 Design Input Power Spectrum	174

LIST OF ILLUSTRATIONS (cont'd)

FIGURE		PAGE
D-7	Level-Crossing Exceedance Curves Obtained from Spectral Analysis	190
D-8	Smith Diagram and Extrapolation	194
D-9	s_a - N Curve for 0° Graphite/Epoxy	195
E-1	Program SFRAME Architecture	200
E-2	Element STIF2M	201
F-1	Program Spectra Organization	216
F-2	Typical Record in File 16	222
G-1	Main Tube Coordinates and Orientation of Side Tubes	225
G-2	Side-Tube and Nodal Degree-of-Freedom Coordinate Systems	228
G-3	Details of Tube Intersection Geometry	232
G-4	Example of Tee-Joint Problem	244
G-5	Example of Specification Card Sequence	245
H-1	Two-Dimensional Representation of Three-Dimensional Axisymmetric Structure	250
H-2	Example Mesh	255
H-3	Finite-Element Mesh	266
H-4	Tube Axial Stresses Caused by 5,520-lb. Compressive Axial Load	268
H-5	Bond Stresses Caused by Axial Compression	270
H-6	Bond Stress Caused by 1.45 KIP-in. Torque	270
H-7	Bond Stresses Caused by Cold Soak	271
H-8	Assumed Temperature Distribution	272
H-9	Contour Plot of Radial Stress	273
H-10	Linear and Contour Plots of Hoop Stress	273
H-11	Linear and Contour Plots of Axial Stress	274
H-12	Contour Plot of Shear Stress	274
I-1	Lap-Joint Shear-Lag Model	277
I-2	Free-Body Diagrams	277
I-3	Hypothetical Improved Attachment Detail	284

LIST OF ILLUSTRATIONS (cont'd)

FIGURE		PAGE
J-1	Antenna Storage Scheme	285
J-2	Antenna Deployment Model	287
J-3	Torque as a Function of Deployment Angle	289
J-4	Deployment Weight Budget	291
J-5	Torque and Frequency Time-Histories	293
K-1	Tube Layup on Inner Mandrel	297
K-2	Layup on Inner Mandrel with Curing on Outer Mandrel	299
K-3	Cure Cycles (after Weed and Francis)	301
K-4	Cure Cycle for AS/3501-6	302
K-5	[90°/M1/$0°_{10}$/M1/90°] Tube with Elliptical Cross Section . .	303
K-6	Wall Thickness Variation in [90°/$0°_{10}$/90°] Tube	304
K-7	Nominal Wall Region	305
K-8	Thickened Wall Region	305

LIST OF TABLES

TABLE		PAGE
1	Graphite/Epoxy Ply Properties	7
2	ATS/3-Ring Key Design Parameters	11
3	Tripod-B Key Design Parameters	15
4	Comparison of Natural Frequencies	26
5	First-Passage Statistics for Compression Loads	29
6	Bondline Stress Survey	32
7	Graphite/Epoxy Tube Axial Stress Survey	33
8	Summary of Bursting Margins	36
9	Load Survey Summary	39
10	Assessment Summary	42
11	Relative Merits of Inner and Outer Mandrels	43
12	Typical Length Requirements for Bending Test	49
13	Comparison of General Characteristics	55
A-1	Summary of Measured Specimen Thicknesses	78
A-2	Summary of Loads Measured at Onset of Delamination	79
A-3	Summary of Measured Ultimate Loads	80
A-4	Summary of Calculated Strain (ε_x) at Delamination	85
B-1	Test Matrix	94
B-2	Short Beam Shear Test Data for $[0°_{26}]$ Laminate	99
B-3	Short Beam Shear Test Data for $[0°_{26}]$ Laminate	100
B-4	Short Beam Shear Test Data for $[0°_{12}/M1/0°/M1/0°/M1/0°_{12}]$ Laminate	101
B-5	Short Beam Shear Test Data for $[0°_{12}/M1/0°/M1/0°/M1/0°_{12}]$ Laminate	102
B-6	Short Beam Shear Test Data for $[0°_{12}/M1/0°/M1/0°/M1/0°_{12}]$ Laminate	103
B-7	Short Beam Shear Test Data for $[0°_{26}]$ Laminate	106
B-8	Short Beam Shear Test Data for $[0°_{26}]$ Laminate	107
B-9	Short Beam Shear Test Data for $[0°_{26}]$ Laminate	108
B-10	Short Beam Shear Test Data for $[0°_{26}]$ Laminate	109
B-11	Short Beam Shear Test Data for $[0°_{26}]$ Laminate	110

LIST OF TABLES (cont'd)

TABLE		PAGE
B-12	Short Beam Shear Test Data for $[0°_{12}/M1/0°/M1/0°/M1/0°_{12}]$ Laminate	111
B-13	Short Beam Shear Test Data for $[0°_{12}/M1/0°/M1/0°/M1/0°_{12}]$ Laminate	112
B-14	Short Beam Shear Test Data for $[0°_{12}/M1/0°/M1/0°/M1/0°_{12}]$ Laminate	113
B-15	Short Beam Shear Test Data for $[0°_{12}/M1/0°/M1/0°/M1/0°_{12}]$ Laminate	114
B-16	Short Beam Shear Test Data for $[0°_{12}/M1/0°/M1/0°/M1/0°_{12}]$ Laminate	115
C-1	Input Data Used in Heat Transfer Analysis	121
C-2	Survey of Bondline Stresses Caused by Temperature Gradient	125
C-3	Inventory of Graphite/Epoxy Tubes	126
C-4	Test Matrix	130
C-5	Synopsis of Joint-Assembly Processing and Experimental Observations	135
C-6	Pooled Data for Joint Strength	137
C-7	Dimensional Parameters	144
C-8	Approximate Material Properties	145
C-9	Load and Stress Comparisons	146
D-1	ATS/3-Ring Nodal Coordinates	164
D-2	Tripod-B Nodal Coordinates	165
D-3	ATS/3-Ring Element Properties	166
D-4	Tripod-B Element Properties	167
D-5	Analysis Parameters	168
D-6	Vibration Analysis of ATS/3-Ring	169
D-7	Vibration Analysis of Tripod-B	170
D-8	Comparison of Present Results with Approximate Estimate for First Bending Frequency	172
D-9	Rules for Assignment of Modal Damping	175
D-10	Standard Deviations (σ) and Zero-Crossing Rates ($\overline{\nu}_o$) of Displacements for ATS/3-Ring*	177

LIST OF TABLES (cont'd)

TABLE		PAGE
D-11	Standard Deviations (σ) and Zero-Crossing Rates ($\bar{\nu}_o$) of Displacements for Tripod-B*	178
D-12	Radial Clearance Required to Avoid First-Passage Collision	179
D-13	ATS/3-Ring Typical Internal Load Statistics for Longerons	181
D-14	Tripod-B Typical Internal Load Statistics for Longerons	182
D-15	ATS/3-Ring Typical Statistics for Axial Forces in Stabilizers	183
D-16	Tripod-B Typical Statistics for Axial Forces in Stabilizers and Antenna Supports	183
D-17	Summary of Load Statistics for Critical Locations	184
D-18	Expected Fraction of Critical Buckling Load Achieved at First Passage	185
D-19	Longeron Strength Check Based on First-Passage Loads	187
D-20	Spectrum Magnification Factors (μ)	191
D-21	Approximate Peak Distributions (μ=1)	191
D-22	Results of Laminate Fatigue Tests*	193
D-23	Summary of Fatigue Damage Estimates	196
E-1	DOF Convention	207
E-2	Required File Attributes	210
E-3	Typical Core and CPU Time Requirements	214
F-1	Consistent Units	216
F-2	Local DOF Key for Internal Load Spectra	221
F-3	Required Working File Attributes	222
F-4	CPU Time Requirements	224
H-1	Cases Studied	267
H-2	Stress Summary	272
I-1	Input Data for Tapered-Joint Analysis	280
I-2	Peak Shear at Free End of Fully Clamped Joint	282
I-3	Peak Shears in Partially Clamped Joint	283
J-1	Summary of Results	295
K-1	Comparison of Mandrel Materials	307
L-1	Summary of Example Analysis	313

SECTION I

INTRODUCTION

This report presents the results of the second phase of a design study of a graphite/epoxy antenna-feed truss for a hypothetical Air Force communications satellite in geosynchronous orbit.

In Phase I of the study, 15 design concepts were screened, based on structural weight, and eight of these concepts were sized by preliminary design based on thermal analysis, static stress analysis, and buckling calculations [1]. At the end of the first phase, the field of candidates had been narrowed to two concepts. In the second phase the two remaining concepts have been screened further based on dynamic analysis, stress analysis of some joint details, and fatigue calculations. Also, some preliminary experiments were conducted to obtain material allowables and to assess a design development test article simulating a bonded attachment-fitting joint.

As a result of these activities, a final concept selection has been made and qualification test requirements have been defined. Fabrication procedures have not been defined completely because of problems encountered in the manufacture of graphite/epoxy tubing. However, the results of the study should be found useful in exposing the engineering development required to achieve acceptable reliability in advanced-composite structural components for communications satellites and for possible future Air Force space applications involving Large Advanced Space Structures (LASS).

Using composite materials in space structures offers potential benefits of weight savings, thermal deformational stability, high stiffness, and low radar cross section. However, the value of a particular benefit depends heavily upon mission requirements. In this regard, a LASS concept for space-based radar (SBR) is discussed in Section VII to provide a contrast to the communications satellite application. The different mission requirements associated with these two applications will be seen to impact design trades and test requirements in different ways.

The body of the report summarizes briefly the major findings of each analytical and experimental task, and integrates the findings to present an overview. The detailed results have been relegated to appendices. Each appendix attempts to present a self-contained description of the motivation, procedures and results of one task. However, some cross-referencing between appendices has been unavoidable because of the interaction between tasks during the study.

SECTION II

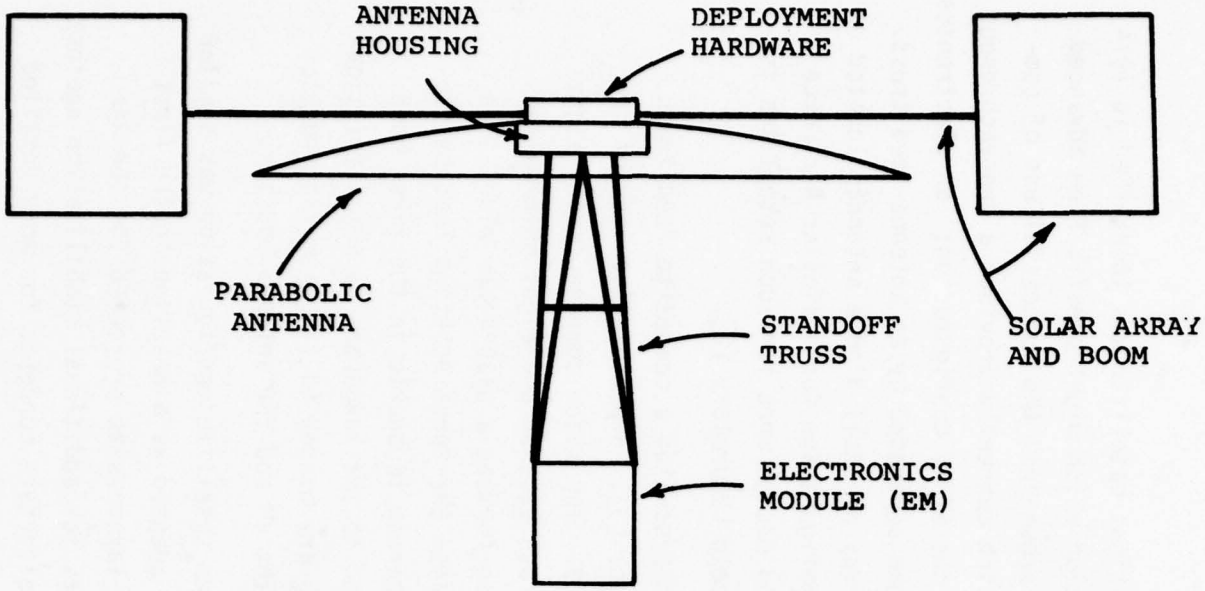
CANDIDATE DESIGNS AND STRUCTURAL REQUIREMENTS

1. BACKGROUND

The geosynchronous communications satellite was identified in 1974 as a potential Air Force space application which might benefit from advanced fiber composite materials. Motivation arose from the successful use of composites in the NASA ATS-6 satellite, which currently provides a geosynchronous television link. Figure 1 illustrates the ATS-6 configuration: an electronics module (EM) and a large parabolic antenna separated by an antenna-feed truss. The microwave feed is supplied by an array of small dipole antennas located on the top face of the EM. A projected configuration for a similar Air Force satellite is shown in Figure 2. Ongoing design work for such satellites is currently being pursued by the MIT Lincoln Laboratory [2].

The ATS-6 flight hardware incorporated a composite feed truss designed and fabricated by Hercules, Inc. [3]. A perspective view of the ATS-6 truss is reproduced in in Figure 3. The major components are eight graphite/epoxy longerons of circular cross section and eight thin-walled aluminum members of square cross section forming a stabilizer ring. The purpose of the stabilizer ring is to raise the truss buckling load by suppressing the ability of individual longerons to buckle in the first mode. The stabilizer ring members are attached to the longerons by metal friction-clamp bands. The ends of the longerons are bonded to titanium fittings to provide hard points for attachment to the EM and the antenna housing.

Since the projected Air Force satellite configuration was similar to the ATS-6, the ATS-6 feed truss was adapted as a baseline in the first phase of this study [1]. However, the larger size projected for the Air Force satellite resulted in requirements for additional stabilization against buckling, and led to selection of two alternate concepts for more detailed assessment. These candidate designs are described briefly in the following two sections (2 and 3).



LAUNCH WEIGHT = 3,050 LB

POWER AVAILABLE (5 YR) = 5 KW

SCALE (FEET)

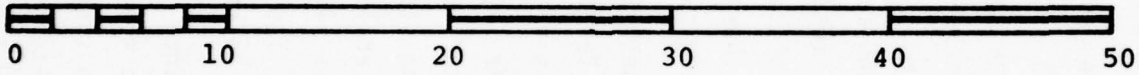


Figure 1. Schematic of ATS-6 Communication Satellite

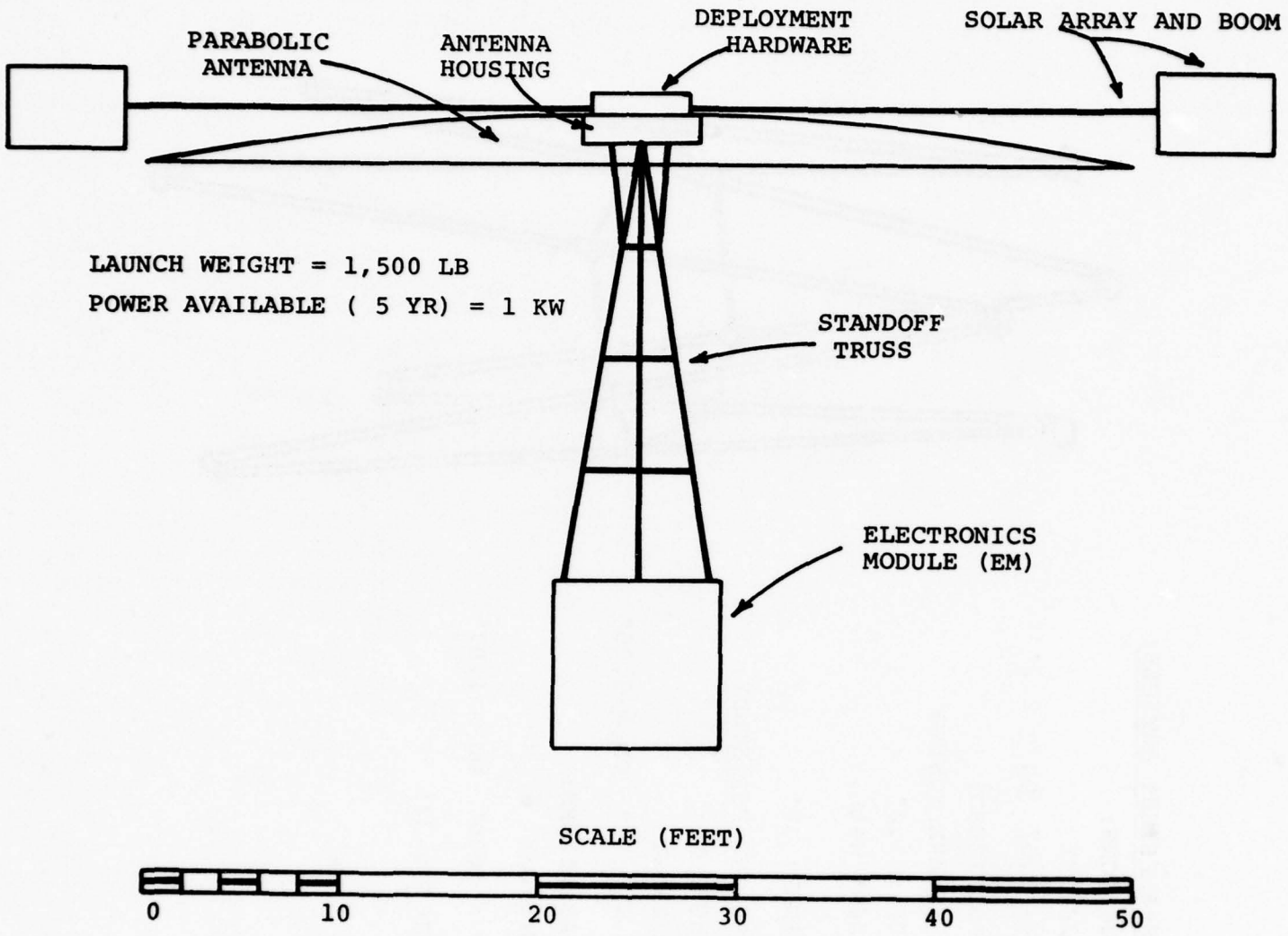


Figure 2. Schematic of Projected USAF Communication Satellite

ATS-6 FLIGHT ARTICLE:

LONGERONS:

GR/EPOXY

ID = 2.5" OD = 2.7"

STABILIZERS:

AL SQUARE TUBING

1.0" x 1.0"

0.049" WALL

HEIGHT: 14'

BASELINE FOR STUDY:

LONGERONS:

GR/EPOXY

ID = 3.56" OD = 3.75"

STABILIZERS:

GR/EPOXY

ID = 1.00" OD = 1.07"

HEIGHT: 22'

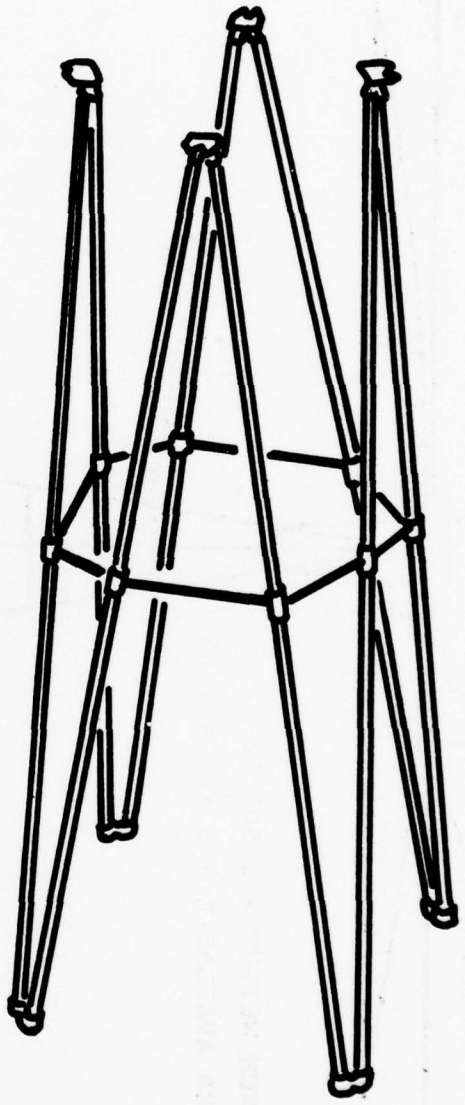


Figure 3. ATS-6 Feed Truss

2. ATS/3-RING DESIGN

The ATS/3-Ring concept (Figure 4) is a modification of the ATS-6 design. The number of stabilizer rings has been increased to three to suppress the second and third longeron buckling modes. The longerons and rings are designed as high-modulus graphite/epoxy cylindrical tubes. Metal fittings similar to the ATS-6 are planned for the end-attachments. However, the stabilizer ring joints are to be fabricated by secondary bonding of graphite/epoxy parts wrapped over by additional 90° graphite/epoxy or glass/epoxy plies (see detail B in Figure 4).

The material properties for high-modulus graphite/epoxy are summarized in Table 1. Generic values have been used for design purposes. In particular, the strength and modulus data were obtained from the Advanced Composites Design Guide [4]. Table 2 summarizes the approximate values of some of the key parameters established in the first phase of the study.

TABLE 1

GRAPHITE/EPOXY PLY PROPERTIES

Item	V A L U E S F O R	
	High-Modulus Gr/E	High-Strength Gr/E
Modulus parallel to fibers, E_L (psi)	25×10^6	21×10^6
Shear Modulus, G_{LT} (psi)	0.80×10^6	0.65×10^6
Tensile strength parallel to fibers, F (ksi)	100	180
Allowable tensile stress, F_{LA} (ksi)	60	108
Thermal expansion coefficients: parallel to fibers, α_L ($°C^{-1}$)	0.38×10^{-6}	0.38×10^{-6}
transverse to fibers, α_T ($°C^{-1}$)	28.8×10^{-6}	28.8×10^{-6}
Thermal conductivity, K(Wcm^{-2} $°C^{-1}$)	1.04	1.04
Infrared emissivity, ε	0.85	0.85
Heat capacity, C_p (Btu lb^{-1} $°F^{-1}$)	0.193	0.193
Weight density, ρ (lb in^{-3})	0.056	0.056

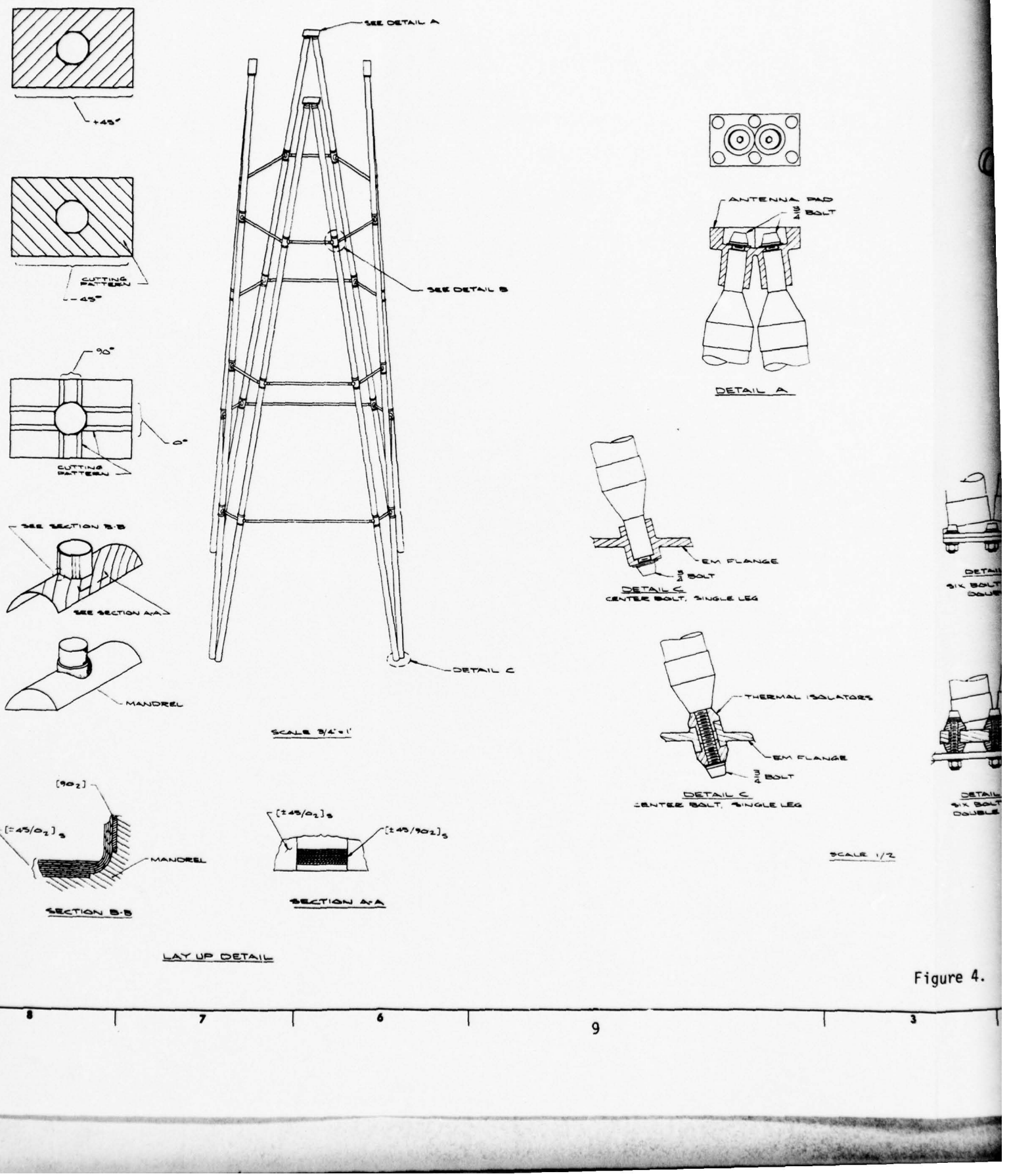

+45°
CUTTING PATTERN
-45°
90°
0°
CUTTING PATTERN
SEE SECTION B-B
SEE SECTION A-A
MANDREL
SEE DETAIL A
SEE DETAIL B
DETAIL C
SCALE 3/4" = 1'
[90₂]
[±45/0₂]s
MANDREL
SECTION B-B
[±45/0₂]s
[±45/90₂]s
SECTION A-A
LAY UP DETAIL
ANTENNA PAD
3/8 BOLT
DETAIL A
EM FLANGE
3/8 BOLT
DETAIL C
CENTER BOLT, SINGLE LEG
THERMAL ISOLATORS
EM FLANGE
3/8 BOLT
DETAIL C
CENTER BOLT, SINGLE LEG
SCALE 1/2

Figure 4.

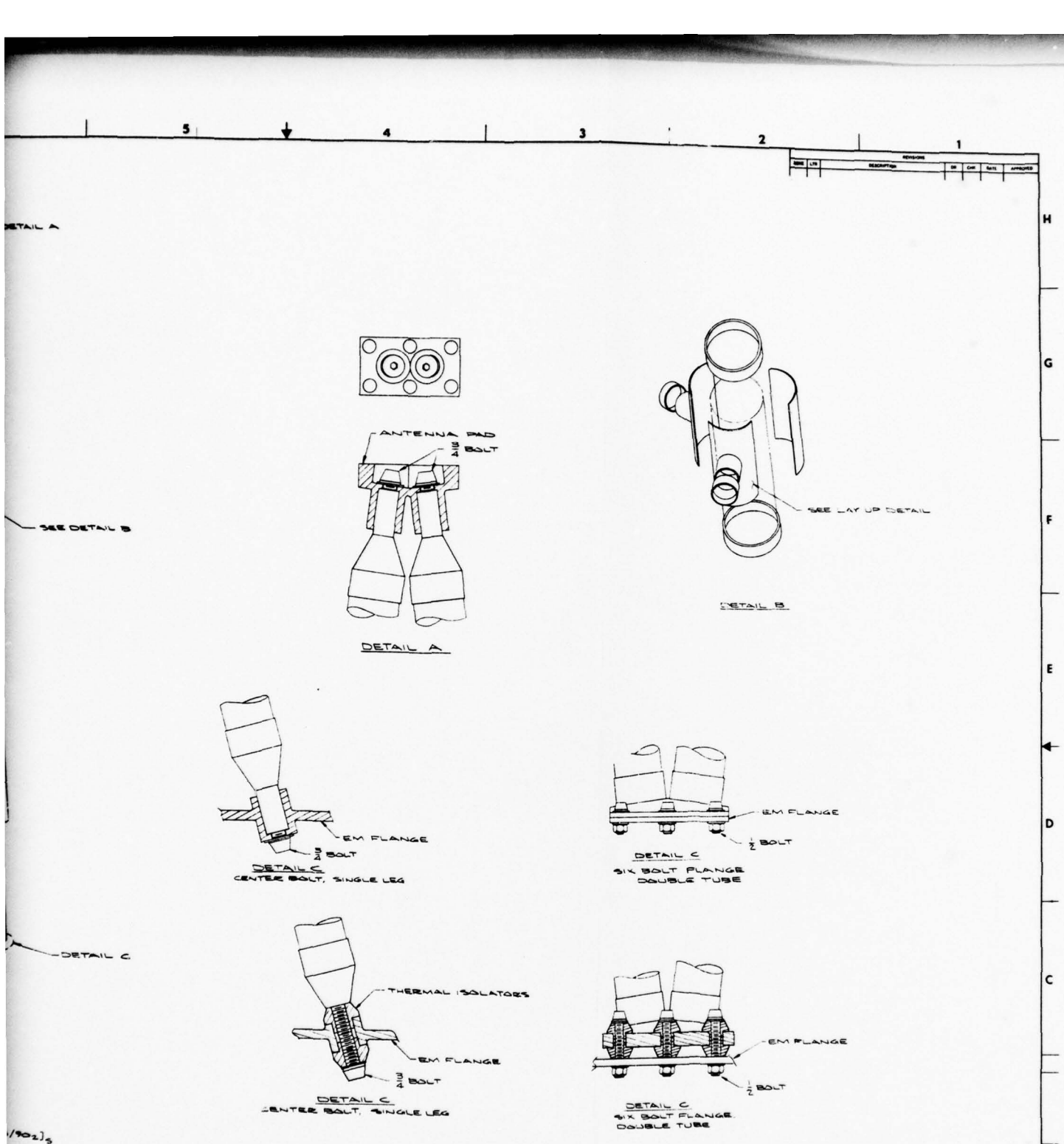


Figure 4. ATS/3-Ring Truss with Joint Details

THIS PAGE IS BEST QUALITY PRACTICABLE
FROM COPY FURNISHED TO DDC

TABLE 2

ATS/3-RING KEY DESIGN PARAMETERS

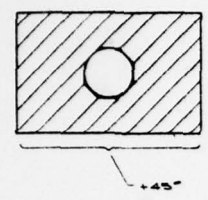
Item	Value
Longerons (8):	
Total length (in)	264
Unsupported length (in)	66
Approximate I.D. (in)	2.60
Approximate O.D. (in)	2.80
Layups considered in design:	
Primary	$[90^\circ_2/0^\circ_{16}/90^\circ_2]$
Alternate	$[90^\circ_2/0^\circ_{18}/90^\circ_2]$
Alternate*	$[\pm 73.25^\circ_{(50\%)}/0^\circ_{18}/\mp 74.45^\circ_{(50\%)}]$
Stabilizer Rings (3):	
Approximate I.D. (in)	0.88
Approximate O.D. (in)	1.00
Layups considered in design:	
Primary	$[90^\circ/0^\circ_{10}/90^\circ]$
Alternate*	$[\pm 64.8^\circ_{(75\%)}/0^\circ_{12}/\mp 68^\circ_{(75\%)}]$
Assembled Truss**	
Approximate weights (lb):	
Minimum	100
Maximum	159
Longeron buckling margin, P_{max}/P_{cr}	0.3
Estimated maximum stress (ksi)	60.9
Estimated first-bending frequency (Hz)	6.8

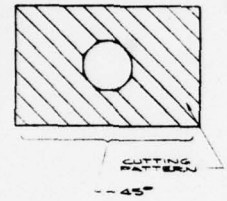
* Notation (%) represents percent overlap in angle-wrapping of prepreg plies.

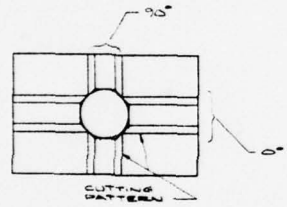
** Results based on static analysis and scaling of ATS-6 static test loads.

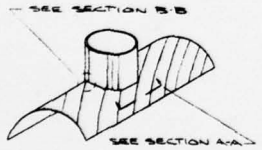
3. TRIPOD-B DESIGN

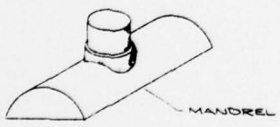
The Tripod-B concept (Figure 5) was selected as an alternate design with fewer components, and also because of the possibility of some weight savings. Three stabilizer rings are used, as in ATS/3-Ring, to suppress the first three longeron buckling modes. Tripod-B incorporates a third set of major components--the antenna supports, which are required to provide attachment points at the I.D. of the antenna housing. The material and joint details of ATS/3-Ring and Tripod-B are similar, except that the Tripod-B longerons are designed with high-strength graphite/epoxy (see Table 1), and that a complex joint fitting is required at the apex. Some key parameters established for Tripod-B in the first phase of the study are summarized in Table 3.

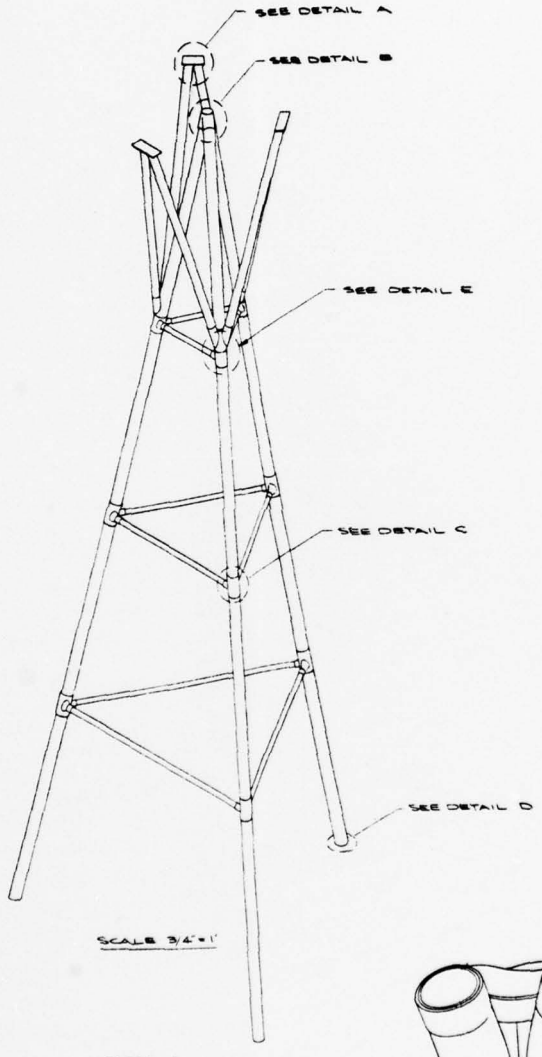




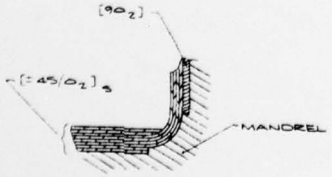




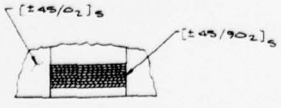




SCALE 3/4" = 1'



SECTION B-B

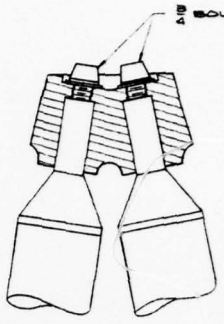


SECTION A-A

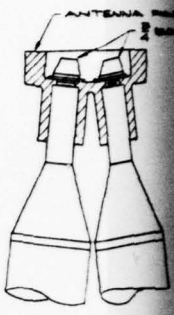
LAY UP DETAIL



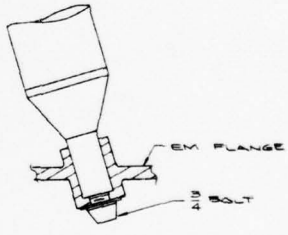
DETAIL E
NOT TO SCALE



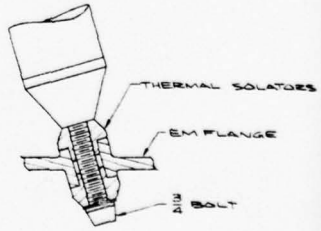
DETAIL B



DETAIL A



DETAIL D
CENTER BOLT, SINGLE LEG



DETAIL D
CENTER BOLT, SINGLE BOLT

SCALE 1/2

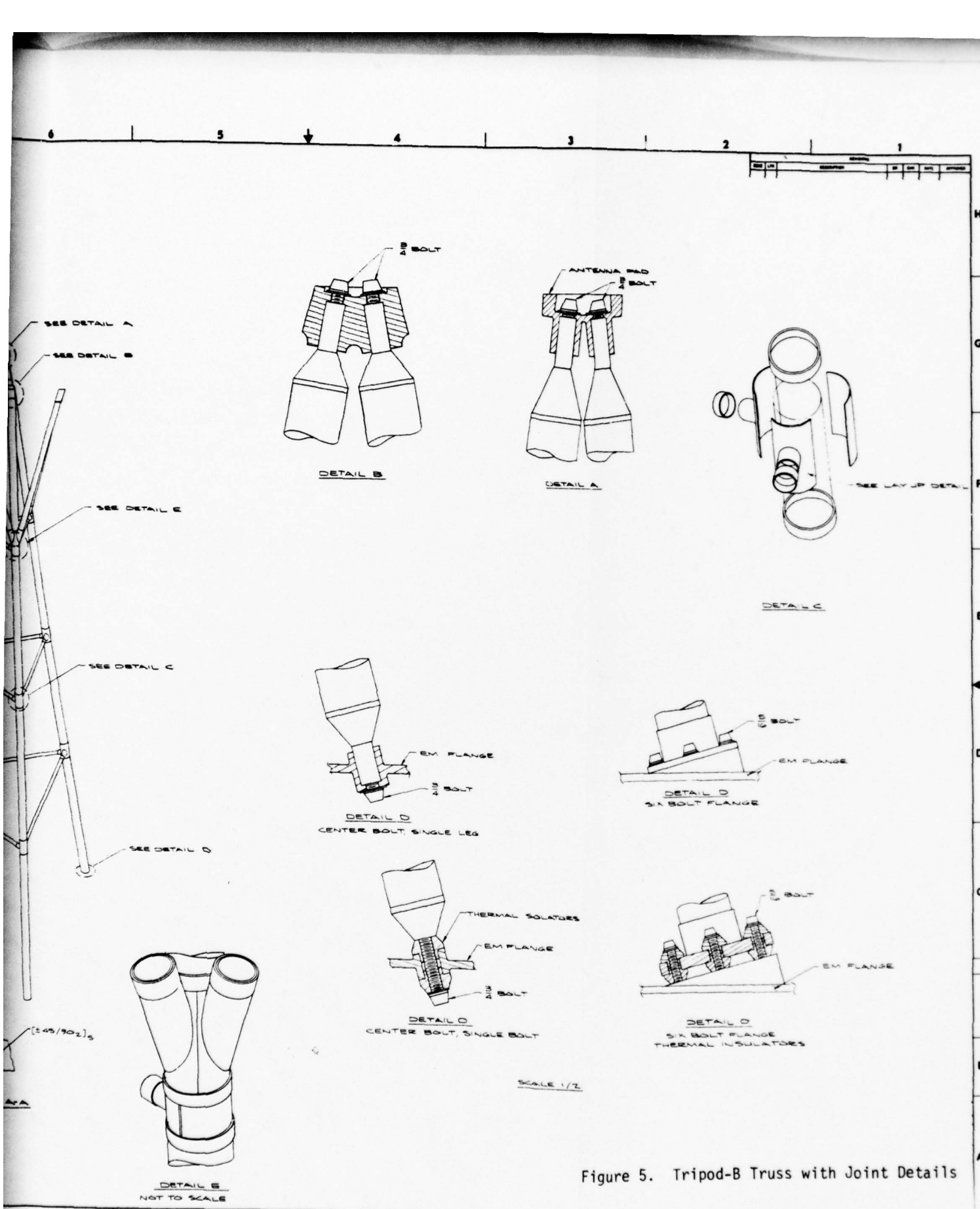


Figure 5. Tripod-B Truss with Joint Details

THIS PAGE IS BEST QUALITY PRACTICABLE
FROM COPY FURNISHED TO DDC

TABLE 3

TRIPOD-B KEY DESIGN PARAMETERS

Item	Value
Longerons (3):	
Total Length (in)	268
Unsupported length (in)	66
Approximate I.D. (in)	3.40
Approximate O.D. (in)	3.60
Layups considered in design:	
Primary	$[90^\circ_2/0^\circ_{16}/90^\circ_2]$
Alternate	$[90^\circ_2/0^\circ_{18}/90^\circ_2]$
Alternate*	$[\pm 77.25^\circ_{(50\%)}/0^\circ_{18}/\overline{+}78^\circ_{(50\%)}]$
Stabilizer Rings (3):	
Approximate I.D. (in)	1.33
Approximate O.D. (in)	1.40
Layups considered in design:	
Primary	$[90^\circ/0^\circ_{10}/90^\circ]$
Alternate*	$[\pm 55.6^\circ_{(50\%)}/0^\circ_7/\overline{+}57.5^\circ_{(50\%)}]$
Antenna Support Legs (6):	
Approximate length (in)	66
Approximate I.D. (in)	2.60
Approximate O.D. (in)	2.80
Layups considered in design:	
Primary	$[90^\circ_2/0^\circ_{16}/90^\circ_2]$
Alternate	$[90^\circ_2/0^\circ_{18}/90^\circ_2]$
Alternate*	$[\pm 73.25^\circ_{(50\%)}/0^\circ_{18}/\overline{+}74.45^\circ_{(50\%)}]$
Assembled Truss**	
Approximate weights (lb):	
Minimum	70
Maximum	108
Longeron buckling margin, P_{max}/P_{cr}	0.3
Estimated maximum stress (ksi)	77.3
Estimated first-bending frequency (Hz)	10.7

* Notation (%) represents percent overlap in angle-wrapping of prepreg plies.

** Results based on static analysis and scaling of ATS-6 static test loads

4. STRUCTURAL REQUIREMENTS

Survival of launch loads and thermal deformational stability are the two primary structural requirements which the antenna-feed truss must meet. A third and equally important requirement is that the truss must be able to withstand the effects of fatigue.

In the first phase of the study the effects of launch loading were considered only from a static analysis viewpoint. The ATS-6 antenna and supporting hardware weights were re-estimated for the projected Air Force satellite, and the resulting weight ratio was used to scale up the ATS-6 static qualification test loads [3] to provide design loads. Static stress and buckling calculations were then performed for the candidate designs. Each design was required to have component cross sections which would meet an arbitrarily chosen criterion for buckling margin:

$$P_{max}/P_{cr} \leq 0.3 \qquad (1)$$

where P_{max} is the maximum axial load caused in the component by application of the design loads and P_{cr} is the Euler buckling load corresponding to the unsupported length of the component.

In the present phase, launch loads are reconsidered from a dynamic analysis viewpoint. The launch environment is represented by three-axis uncorrelated random loading, assumed to be stationary and Gaussian with zero mean. A power spectrum for the loading was adopted from NASA specifications for a Titan-IIIC launch of the Mariner-Jupiter-Saturn spacecraft [5], a payload of weight similar to the 1,500 lb. weight projected for the Air Force communications satellite. Analyses of the responses of the feed-truss designs to the random loading are required to establish component loads/stress exceedance curves. Design static loads can then be established from first-passage statistics [6], and fatigue damage acucmulation can be estimated based on a generalization of Miner's

rule [7]. The general requirements which the candidate designs must meet are:

1) Adequate buckling margins with P_{max} in Eq. (1) replaced by the corresponding first-passage load.

2) Calculated damage summation $\Sigma(n/N) \ll 1$ at joint details, with stress concentration factors accounted for.

Thermal deformational stability is a critical design requirement because deflections of the feed truss due to temperature changes tend to defocus the parabolic reflector antenna with respect to the microwave dipoles on the electronics module. The allowable focus errors projected for the Air Force satellite are illustrated in Figure 6. These requirements were found to be met by the ATS/3-Ring and Tripod-B designs in the first phase of the study.

The potential fatigue effects of temperature changes must also be considered. Thermal fatigue tends to be concentrated at attachment-fitting joints, where temperature excursions may cause high stresses due to the mismatch of thermal expansion coefficients in composite tubes and metal fittings. Some thermal fatigue may also occur in the composite tubing per se due to the mismatch in expansion coefficients of the fibers and resin.

It is of interest in this regard to consider what the most severe temperature excursion might be. A satellite at geosynchronous altitude is normally in direct sunlight, and should establish equilibrium temperature in the range 280°K to 370°K. However, the satellite will pass through earth shadow once per day on about 90 days per year in the spring and fall, remaining in shadow for periods of up to 90 minutes. The temperature

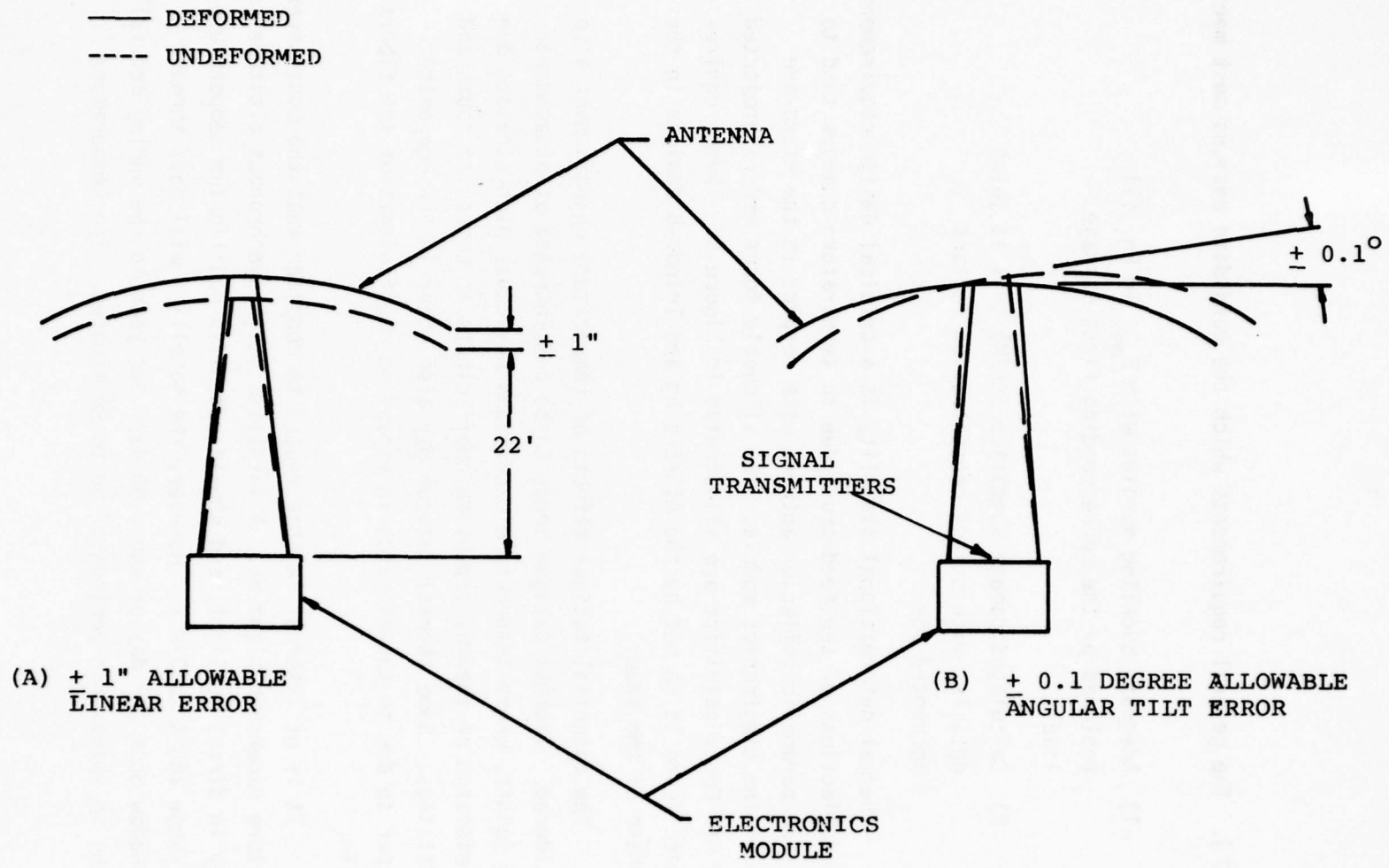


Figure 6. Antenna Focus Errors Caused by Thermal Deformation of Standoff Truss

excursion for earth-shadow passage can then be estimated by solving the radiative cooling equation for a point mass:

$$T_{COLD} \cong \left[\frac{C_P}{3\sigma\varepsilon A\Delta t} \right]^{1/3} \qquad (2)$$

where C_P is the heat capacity of the mass; A its surface area; ε its emissivity; σ is the Stefan-Boltzmann constant, and Δt is the period spent in shadow. If the properties of a graphite/epoxy longeron from either the ATS/3-Ring or the Tripod-B design are substituted in Eq. (2), a cold temperature of 167°K results. Hence, some 90 thermal cycles in the range $113 \leq -\Delta T \leq 203$°K can occur per year. In the present study, a more severe thermal cycle $-\Delta T = 218$°K between room temperature (295°K) and liquid nitrogen temperature(77°K) was adopted for experimental purposes.

It will be shown subsequently that, although the launch environment drives the design through static margin considerations, the possession of adequate static margins tends to imply that fatigue damage accumulation during launch will be insignificant. (The latter conclusion must, of course, be verified by calculations at joints.) However, the damage effects of thermal fatigue can be significant over the life of a geosynchronous satellite, which may be expected to remain operational for 10 to 20 years and may therefore experience 900 to 1,800 extreme temperature excursions.

SECTION III

MATERIAL PROPERTIES AND DESIGN DEVELOPMENT TESTS

1. TEST OBJECTIVES

The experimental objectives were to obtain some information about material properties and to make an initial assessment of the fatigue effects of thermal cycles. With regard to material properties, the primary concern is to establish design allowables for interlaminar stresses. Objectives for this purpose were investigation of the angle-ply delamination coupon as a means of measuring interlaminar tensile strength, trend assessment of different stacking sequences using short beam shear tests, and a preliminary assessment of resistance to thermal fatigue.

The stacking sequence investigation was aimed at assessing the potential degradation of interlaminar strength associated with placement of flexible inserts in a graphite/epoxy laminate. The insert concept has been proposed previously by Lackman and Pagano [8] for reducing interlaminar stresses at the edges of flat laminates by removing graphite/epoxy in a sawtooth pattern and backfilling with resin. For a cylindrical tube, such stress reduction might be wanted over several inches near the end to reduce concentrations of interlaminar stress associated with transfer of load to attachment fittings. Also, if the insert is continued through the entire tube, it may improve the local crippling strength (which increases with increasing separation between circumferential plies). The contemplated modification is to replace [90°/0°_N/90°] tubular laminates with [90°/Insert/0°_N/Insert/90°] laminates to achieve both goals. However, benefits in stress reduction and/or crippling strength improvement may be offset by degradation of interlaminar shear strength.

Two objectives were identified with regard to the effects of thermal fatigue: assessment of accelerated testing and assessment of bonded-joint strength degradation. It has already been mentioned that the radiative cooling process to which the antenna-feed truss is subjected in earth shadow is quite time-consuming, i.e., the entire 90-minute shadow period may be required to reach minimum temperature. Obviously, it would

be desirable to accelerate the cooling process in a ground test by immersing the test specimen in a cryogenic liquid. However, extremely rapid cooling of the surfaces of an immersed specimen will cause severe temperature gradients through the specimen thickness. The thermal-shock stresses associated with such gradients may be sufficiently large to cause fatigue damage which would not be expected in the operational structure. Although some analysis of the thermal-shock problem indicated that the fatigue effects would not be significant (see Section IV), it was decided to conduct some experiments to obtain additional verification.

The problem of joint strength degradation is associated with large excursions to uniform cold temperature. In such situations, large interlaminar stresses can be developed in the bond due to the difference between the thermal expansion coefficients of the metal attachment fitting and the composite tube. Since some 900 to 1,800 severe thermal cycles are expected over the 10 to 20 year operational life of a geosynchronous satellite, assessment of the residual strength degradation of such joints is important.

2. STATIC TESTS FOR MATERIAL PROPERTIES

Measurement of interlaminar strength in composite laminates is still an unsolved problem. The difficulty associated with such measurements arises from the lack of a test specimen configuration which provides a uniform interlaminar stress field and is also insensitive to tolerance variations. The ASTM D2733 notched tension coupon [9] and D2344 short beam shear test [10] are used frequently to obtain interlaminar shear strength data. However, the results obtained from the D2733 coupon tend to be highly sensitive to small variations in the notch depth. Statistically tighter observations can be obtained from the D2344 short beam shear test, but the data reduction method is based on a simplified engineering analysis and hence, does not give a true material property. Thus, while short beam shear tests are useful for establishing trends, the resulting strength data can not be used with confidence to predict, e.g., the onset of interlaminar failure at a point of stress concentration computed by finite-element analysis of a design detail.

Therefore, an investigation was made of the delamination coupon proposed by Pagano and Pipes [11] as a possible means of accurately measuring interlaminar tensile strength. The general configuration of the delamination coupon proposed by Pagano and Pipes is $[(\pm\theta)_M/90^\circ_N]_S$, where the ratio M/N is optimized to maximize the interlaminar tension field at the free edges. However, the stress-field analysis is based on an empirical model of an accurate finite-difference solution for $[0^\circ/90^\circ]_S$ and $[90^\circ/0^\circ]_S$ laminates.

In the present study, Hercules AS/3501-6 graphite/epoxy laminates were fabricated in the sequence $[(\pm 26^\circ)_2/90^\circ]_S$ and the atlernate sequence $[+26^\circ/-26^\circ_2/+26^\circ/90^\circ]_S$. The latter sequence was included in the investigation to assess the effect of reducing the anticlastic corner peaks which additional analysis had indicated should be present in the Pagano-Pipes coupon design. The delamination load measurements did indicate a reduction of these peaks by the alternate sequence. However, observations of the failure mode and comparison with failure predictions based on empirical stress-field models showed that the failures are caused by combined interlaminar shear and tension, and that a true material property could not be obtained without more accurate stress-field analysis. Hence, the problem of measuring true interlaminar strength by means of a simple test specimen remains unsolved. The details of these experiments and associated analyses are reported in Appendix A.

Trend data for interlaminar shear strength were measured by the ASTM D2344 short beam shear method. This series of experiments was used to assess strength degradation caused by flexible inserts, such as might be placed throughout a tubular component to reduce interlaminar stress concentration and to improve crippling strength. Laminates of $[0^\circ_{26}]$ and $[0^\circ_{12}/M1/0^\circ/M1/0^\circ/M1/0^\circ_{12}]$ were investigated, where M1 represents a 0.001-in. thick perforated Mylar insert. Mylar was chosen as the insert material to maintain control of the interply thickness during cure. (The alternate choice, insertion of extra B-staged resin, was rejected because bleeding during cure would prevent such control.) The perforations were made to allow proper bleeding from the plies which were sandwiched between the Mylar inserts.

Static strength tests of the $[0^\circ_{26}]$ laminate indicated interlaminar shear strengths of about 26 ksi at liquid nitrogen temperature (-321°F) and 17 ksi at 75° F. Extrapolation of these data indicate a static strength of about 14 ksi at 212° F. Tests of the laminate with inserts indicated interlaminar shear strengths of about 9 ksi at -321° F, 10 ksi at 75° F, and 11 ksi at 212° F. The reversal in trend with temperature could not be explained on physical grounds. The data quoted here refer to initial failures, which were observed to occur at the Mylar/resin interface near the specimen midplane, and which must be taken as the material allowable for design purposes. Based on these data, the conclusion is drawn that the strength penalties associated with Mylar inserts far outweigh the possible incremental benefits which might be obtained in stress-field reduction and/or crippling strength improvement. The details of these experiments are reported in Appendix B.

3. RESIDUAL STRENGTH TESTS

Additional series of $[0^\circ_{26}]$ and $[0^\circ_{12}/M1/0^\circ/M1/0^\circ/M1/0^\circ_{12}]$ short beam shear specimens were subjected to thermal cycles followed by residual strength tests at 75° F. An accelerated thermal cycle between 212° F and -321° F was applied 10, 50, 100, 500 and 1,000 times to different groups of specimens to assess the sensitivity of the material to thermal-shock fatigue. The test results indicated that the $[0^\circ_{26}]$ laminate experienced no strength degradation, while the laminate with inserts experienced about 20 percent degradation after 500 to 1,000 cycles. The latter effect is attributed tentatively to the effect of the thermal expansion coefficient differential between Mylar and graphite/epoxy at a uniform cold-soak temperature, rather than to thermal shock. The experimental data thus provide another reason against using Mylar inserts in composite components of space structures, but the data also establish confidence in the concept of accelerated testing for assessment of thermal fatigue. The details of these experiments are reported in Appendix B.

In another series of experiments, a limited number of design development test (DDT) specimens consisting of 5-inch lengths of 1.3-inch I.D. [90°/0°_{10}/90°] AS/3501-6 graphite/epoxy tubing bonded to interior steel sleeves simulating an end-attachment fitting were processed through up to 1,000 thermal cycles between 60° ±6° F and -321° F. Analysis with a simplified model indicated that the DDT specimens possess about the same ratio of cold-soak thermal stress to launch-vibration stress as the ATS/3-Ring and Tripod-B longeron attachment joints. After thermal cycling, the DDT joints were tested for residual strength, and in some cases a 2-inch length was cut from the free end of the composite tube and tested for crippling strength.

The small amount of joint strength data and the scatter in the results prevented the drawing of detailed conclusions. However, by pooling the data in two groups (zero to 100 cycles, and 500 or more cycles), it was possible to infer a strength degradation of at least 9 percent for long-term exposure to thermal cycles. Thus, although a measurable thermal fatigue effect was demonstrated, the experiments also showed that it is possible to design end attachments for maintenance of long-term reliability for structures, such as the antenna-feed truss, in which the orbital loads are quite low.

The tube strength data exhibited greater scatter, and the observed failure modes were not consistent with a crippling instability. Most of the test specimens failed by brooming at the end where the specimen had been cut free from the joint. These failures were attributed to poorly controlled processing (cutting with a hacksaw and finishing on an aluminum-oxide-grit sanding wheel). The remaining specimens failed by bursting at about 1/4 of the predicted crippling strength. These results were attributed to resin failures at butt seams in the 90° plies by correlating with a prediction made from a simplified stress-analysis model. In view of the deficiencies in fabrication and testing procedures, no conclusions could be drawn with regard to the effects of thermal fatigue on AS/3501-6 material in tubular configuration. Details of the design development tests and supporting analyses are reported in Appendix C.

SECTION IV

ANALYSES OF CANDIDATE DESIGN CONCEPTS

1. ANALYSIS OBJECTIVES

Assessment of the dynamic performance of the ATS/3-Ring and Tripod-B designs, and calculation of stress concentrations at typical joint details were the general analysis objectives for this phase of the study. With regard to dynamic performance, the specific objectives were to compute natural vibration frequencies up to at least 100 Hz and to compute structural response (displacements and component internal loads) to vibratory loading representing Titan-IIIC launch conditions.

Joint stress analysis was subdivided into two specific objectives: the effects of axisymmetric and torsional loads and of temperature changes on the stresses at end-attachment joints, and stress concentration due to general loading conditions at the joints between longerons and stabilizer rings. Also, a third objective was to combine the dynamic analysis and joint stress analysis to assess potential fatigue damage accumulation during launch.

2. DYNAMIC PERFORMANCE

Modal analyses of the ATS/3-Ring and Tripod-B designs were conducted using finite-element models consisting of assumed-displacement generalized bending-stretching-torsion elements, and using the subspace iteration method [12,13]. The ATS/3-Ring design was found to have 35 modes up to about 100 Hz, while Tripod-B was found to have 16 modes in the same range. Altogether, 60 modes up to 278 Hz for ATS/3-Ring and 40 modes up to 464 Hz for Tripod-B were computed. Results for the first few modes are summarized in Table 4. It is of interest to note that the static estimates for the first-bending frequency were reasonably accurate in both cases (compare with Tables 2 and 3). However, these estimates missed the lower-frequency first-torsion mode of Tripod-B.

TABLE 4

COMPARISON OF NATURAL FREQUENCIES*

Mode	D E S I G N			
	ATS/3-Ring		Tripod-B	
	f (Hz)	Mode Type	f (Hz)	Mode Type
1	6.99	First bending	2.67	First torsion
2	7.00	First bending	9,05	First bending
3	9.93	First torsion	9.05	First bending
4	14.62	First ovalizing	10.63	First top-rocking
5	15.44	Second ovalizing	10.67	First top-rocking
6	15.45	Second ovalizing	33.38	Second bending
7	16.45	Third ovalizing	33.68	Second torsion

*Converged to $\pm$10%.

For the purpose of calculating response to launch loads, the finite-element models were assumed to be subjected to base-acceleration inputs adapted from a NASA specification for the Titan-IIIC launch of the Mariner-Jupiter-Saturn spacecraft [5]. The specified power spectrum (Figure 7) was prepared for payloads in the range of 1,600 to 1,800 lb., i.e., close to the projected 1,500-lb. weight of the Air Force satellite. Only the low-frequency portion of the spectrum (up to 200 Hz) was used in the calculations, since it was assumed that inputs at higher frequencies would be attenuated by the electronics module.

The random process associated with the power spectrum shown in Figure 7 was assumed to be zero-mean Gaussian and to be applied as uncorrelated translational inputs along three orthogonal axes, as is the usual practice in spacecraft design verification analysis. In addition, although the power spectrum level is undoubtedly time-dependent, the random process was assumed for the purpose of analysis to be stationary over the Titan-IIIC first-stage boost phase, a total time of about 120 sec [14].

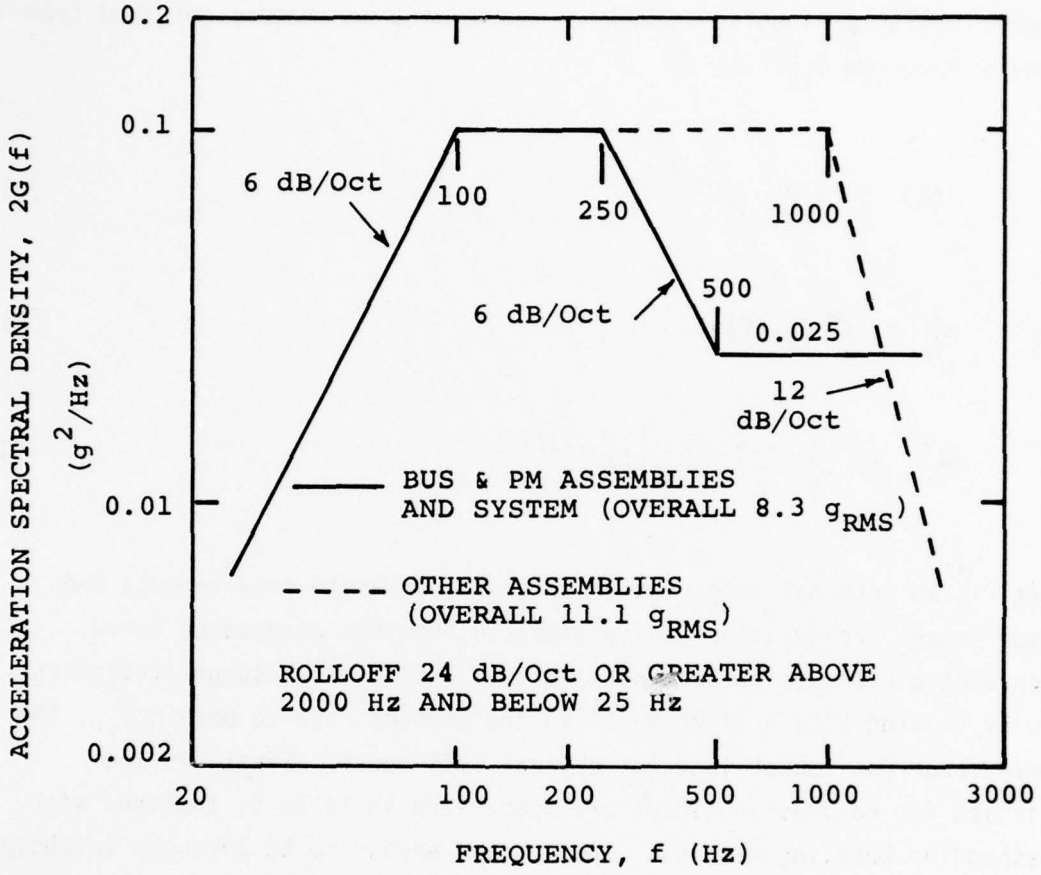


Figure 7. MJS77 Design Input Power Spectrum

Structural response calculations were performed by the modal superposition method, using assumed damping factors for each of the natural modes computed in the subspace iteration analysis. The assumed damping factors varied from 0.02 for frequencies below 10 Hz to 0.2 for frequencies above 110 Hz.

Under the foregoing assumptions the response of any quantity of interest $\xi(t)$, i.e., a displacement or an internal load, will be zero-mean stationary and Gaussian with finite parameters. The response can then be characterized by a Gaussian exceedance curve with parameters obtained from its power spectrum $G_{\xi\xi}(f)$ [15]:

$$E(\xi) = 1/2\ \bar{\nu}_{o\xi} e^{-\xi^2/2\sigma_\xi^2} \tag{3}$$

$$\sigma_\xi^2 = \int_o^\infty G_{\xi\xi}(f)df \tag{4}$$

$$\bar{\nu}_{o\xi} = \frac{2}{\sigma_\xi} \left[\int_o^\infty f^2 G_{\xi\xi}(f)df\right]^{1/2} \tag{5}$$

If $\xi(t)$ is an internal load, then both static strength requirements and fatigue damage accumulation can be assessed from the exceedance curve. Design static ultimate loads can be defined from first-passage statistics, e.g., by solving $E(\xi) = 1/120\ sec^{-1}$ in the present case to obtain $\bar{\xi}_{FP}$, the expected once-per-launch load for a Tital-IIIC boost. First-passage statistics for compression loads are summarized in Table 5, together with corresponding buckling margins. The margins appear to be adequate (although higher than the design goal $P/P_{CR} = 0.3$, margin = 0.7 used in the first phase of the study), except for the Tripod-B antenna-support legs. Redesign of the latter components to equalize the launch-survival reliabilities would add about 22 lbs. to the weight of Tripod-B.

Additional details of the formulation for the dynamic calculations and the results obtained are reported in Appendix D. The computer codes used for subspace iteration analysis and response calculation are documented in Appendices E and F, respectively.

TABLE 5

FIRST-PASSAGE STATISTICS FOR COMPRESSION LOADS

Location	First Passage Load, $\bar{P}_{FP}$ (KIPS)	Buckling Load P_{CR} (KIPS)	$\bar{P}_{FP}/P_{CR}$
ATS/3-Ring:			
Longeron	15.95	29.00	0.55
Third stabilizer	0.30	2.44	0.12
Tripod-B:			
Longeron	29.31	61.50	0.48
Third stabilizer	6.44	12.68	0.51
Antenna support	16.70	22.20	0.75

3. JOINT STRESS ANALYSIS

A mesh-generation scheme using multilayer bending-stretching plate finite elements [16] was developed to model in detail a short section of a longeron tube with short sections of adjacent stabilizer-ring tubes attached, as shown in Figure 8. The material properties and number of layers can be varied in the attachment region to simulate the presence of the secondarily bonded composite parts which make up the joint. This rather complicated code has been debugged, but there was no opportunity to run a convergence study on the calculations during the present phase of the investigation. Such a convergence study is mandatory to provide confidence in the stresses computed by this type of finite-element model, which represents cylindrical

shells approximately by a series of flat facets. Therefore, no attempt has been made to draw any conclusions about stress concentration in the longeron/stabilizer joints. These joints are not considered to be as critical as the end-attachment joints, which involve composite/metal bonds and are located in more highly loaded areas. However, since the stress-analysis code may be useful in future investigations, it is documented in Appendix G.

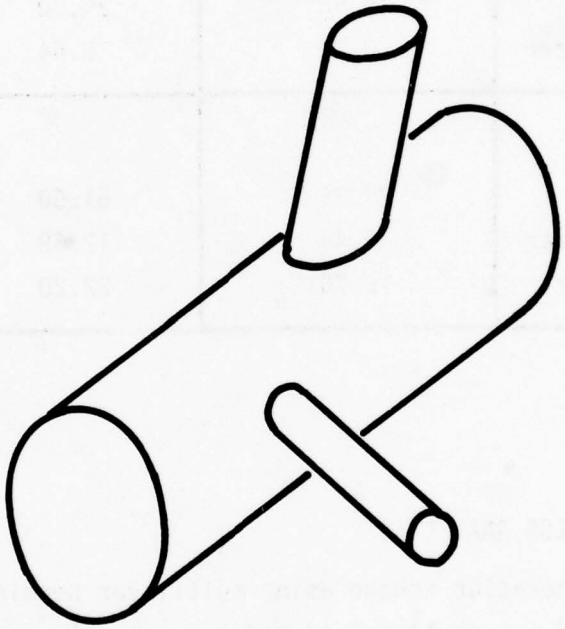


Figure 8. Structure Modeled by Tee-Joint Program

A second mesh-generating scheme using an axisymmetric solid finite-element modified for inclusion of torsional behavior was developed to model simple end-attachment joints consisting of untapered metal fittings bonded to multilayer composite tubes. A hypothetical case approximating the dimensions of the design development test article (Section 3.3) was analyzed under several loading conditions to assess the relative effects of mechanical loading and temperature changes on the stress fields. The dimensions of the analytical case are shown in Figure 9.

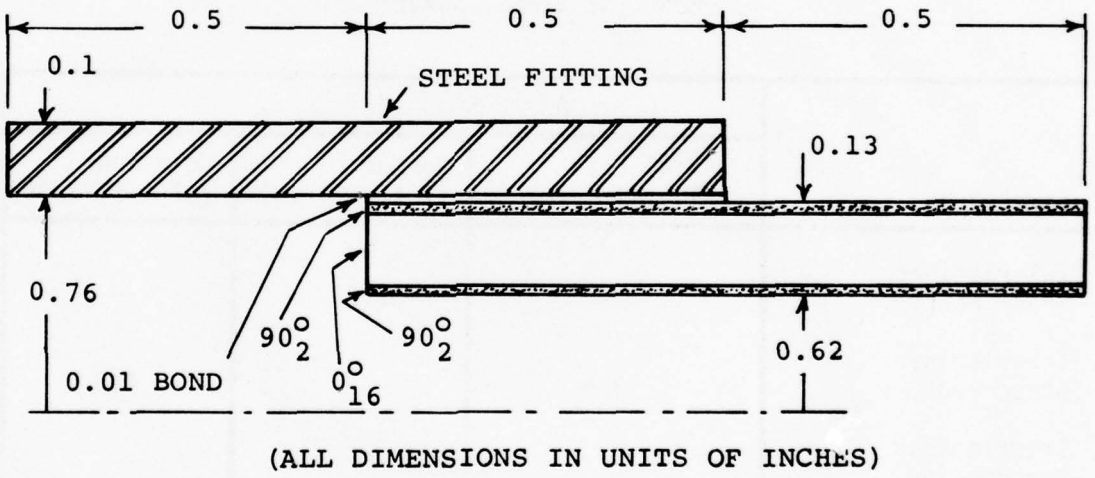


Figure 9. Joint Dimensions for Stress Analysis

A summary of results for various load cases is given in Table 6. The axial load of 10 ksi nominal stress in the tube remote from the attachment is roughly equivalent to first-passage load on the ATS/3-Ring and Tripod-B longerons. (The equivalence estimate was made by assuming that the DDT article would have been designed to a joint strength about twice its first-passage load. See Appendix C, Section C-6.) The remote torsional load of 1.45 KIP-in. is higher than actual computed longeron loadings obtained in static analyses in the first phase of the study [1]. The uniform temperature change $\Delta T = -217.6°C$ represents an earth-shadow-thermal excursion simulation (room temperature to liquid nitrogen temperature).

TABLE 6

BONDLINE STRESS SURVEY

	C A S E		
Stress*	Axial Load (10 ksi remote)	Torque (1.45 KIP-in)	Cold Soak ($\Delta T = -217.6°C$)
Interlaminar Shear Peak, $\tau_{r\theta}$	-	0.35	-
Interlaminar Shear Peak, τ_{rz}	3.8	-	4.3
Interlaminar Compression Peak, σ_r	4.0	-	1.4
*Stresses in units of ksi.			

These data indicate that the effects of thermal fatigue on joint strength are likely to be much more significant than the effects of launch loads. Such a conclusion is warranted by the fact that the stresses due to axial load are expected to occur once per launch (i.e., once per life), while 900 to 1,800 thermal cycles can be expected over the life of the satellite.

Table 7 summarizes some additional data from the axial load case. These data indicate that the stress concentration factors (SCF) associated with peak axial stresses in the composite tube at the joint entrance are reasonably low. Somewhat higher nominal SCF have been assumed for the purpose of making fatigue calculations due to launch loading.

TABLE 7

GRAPHITE/EPOXY TUBE AXIAL STRESS SURVEY

	PLY LOCATION		
Axial Location	Outermost 0° Ply	Outermost 90° Ply	Nominal
Remote stress (ksi)	12.25	1.00	10.0
Entrance Peak Stress (ksi)	18.0	3.20	15.0
SCF	1.47	3.20	1.50

One additional set of analysis cases was run to assess the effects of temperature gradients through the joint wall due to various rates of cooling representing radiation to free space, and immersion of insulated and bare test specimens in liquid nitrogen. These calculations indicated that thermal-shock stresses of the order of only 100 psi were to be expected for the worst case (bare immersion), and were used to justify the accelerated thermal-cycle design development tests discussion in Section 3.3. The details of this analysis, together with additional details of the analyses discussed above, and documentation of the computer code appear in Appendix H.

A brief analysis of the potential stress-reduction benefit which might be obtained by tapering the metal attachment fitting was made by series solution of the differential equations derived from a one-dimensional model of the shear-load-transfer process. Solutions for a variety of bondline thicknesses and small taper angles indicated that incremental thickening of the bond reduces the entrance peak much more rapidly than incremental steepening of the taper angle. Details of the analysis are reported in Appendix I. The regime of larger taper angles was addressed in the design development tests.

4. ASSESSMENT OF BURSTING MARGINS

A local failure model based on bursting at the butt seams of 90° plies in thin-walled $[90°_M/0°_{2N}/90°_M]$ tubes is presented in Appendix C:

$$P = 4\pi R t_1 S_\Theta f(\nu_{LT}, \nu_{TL}, t_1/t_2) \tag{6}$$

where P is the axial compression burst load; R is the tube's mean radius; S_Θ is a resin strength parameter; ν_{LT} and ν_{TL} are the ply major and minor Poisson ratios; and t_1, t_2 are respectively the thicknesses of M 90° plies and N 0° plies. The behavior of $f(\nu_{LT}, \nu_{TL}, t_1/t_2)$ in the range of interest for AS/3501-6 graphite/epoxy is illustrated in Figure 10.

The data in the appendix (Table C-5) indicate that taking $S_\Theta = F_{T2}$, the ply transverse tensile strength, does not predict the burst load with sufficient accuracy. A prediction of 35.6 KIPS for the test tubes is obtained, while the four accepted data points give a mean value of 24.5 KIPS with unbiased standard deviation of 3.2 KIPS.

However, it is reasonable to assume that the strength parameter, S_Θ, will be relatively insensitive to moderate changes in tube design. Hence, bursting loads for the ATS/3-Ring and Tripod-B longerons and antenna-support legs can be predicted by scaling the test data in accordance with:

$$\frac{P'}{P} = \left(\frac{R'}{R}\right)\left(\frac{t_1'}{t_1}\right)\frac{f(\nu_{LT}, \nu_{TL}, t_1'/t_2')}{f(\nu_{LT}, \nu_{TL}, t_1/t_2)} \tag{7}$$

where the unprimed and primed quantities refer to test and design dimensions, respectively. For the purpose of assessment, a 99-percent confidence lower bound estimate, P = 10 KIPS, is used in Eq. (7). The margins with respect to first-passage loads, $1 - \overline{P}_{FP}/P'$, are summarized in Table 8 for the primary and first alternate tube layup schemes assumed in preliminary design. The ATS/3-Ring longerons and Tripod-B antenna-support legs (2.6-in. I.D. tubes) have more margin against bursting than against buckling. However, the Tripod-B longerons (3.4-in. I.D. tubes) have greater margin against buckling. (Compare with Table 5; note that neither table accounts for the suggested modification of doubling the Tripod-B support-leg wall thickness.)

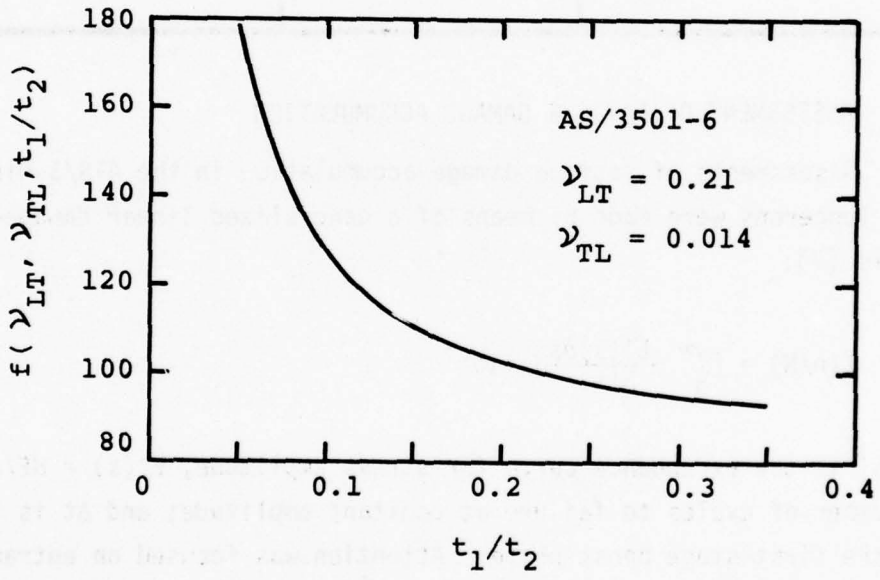


Figure 10. Laminate Parameter for Burst Model

TABLE 8

SUMMARY OF BURSTING MARGINS

Design and Component	L A M I N A T E	
	Primary $[90^\circ_2/0^\circ_{16}/90^\circ_2]$	First Alternate $[90^\circ_2/0^\circ_{18}/90^\circ_2]$
ATS/3-Ring Longerons	0.60	0.61
Tripod-B Longerons	0.43	0.44
Tripod-B Antenna-Support Legs	0.58	0.59

5. ASSESSMENT OF FATIGUE DAMAGE ACCUMULATION

Assessments of fatigue damage accumulation in the ATS/3-Ring and Tripod-B longerons were made by means of a generalized linear damage-summation hypothesis [7]:

$$\Sigma(n/N) = \left[\int_0^\infty \frac{-E'(s)ds}{N(s)}\right] \Delta t \qquad (8)$$

where E(s) is the exceedance curve for stress amplitude, E'(s) = dE/ds, N(s) is the number of cycles to failure at constant amplitude; and Δt is the duration of the first-stage boost phase. Attention was focused on entrance-peak axial stresses in the longerons (under combined axial and bending load).

Separate analysis were made assuming SCF of 1.5, 2.0 and 2.5 to represent a range of possible attachment designs. An N(s) curve for graphite/epoxy subjected to fully reversed loading was constructed by extrapolating available data [17,18].

The results of the analysis disclosed high damage accumulation for the ATS/3-Ring design, a situation caused by the use of high-modulus rather

than high-strength graphite/epoxy (see Section II.2, Table 1). To compare the candidate designs fairly, it was then assumed that the ATS/3-Ring would be redesigned with the high-strength graphite/epoxy used for Tripod-B. This change would require about 18 lb. additional weight in ATS/3-Ring to maintain the buckling margins. On this basis, the fatigue calculations for both concepts showed that some sophistication in the design of end attachments ($1.5 \leq SCF \leq 2.0$) leads to acceptably low estimate damage accumulation due to launch ($0.007 \leq \Sigma n/N \leq 0.16$). Details of the assumptions and calculations are reported in Appendix D, Sections D-9 and D-10.

SECTION V

COMPARATIVE ASSESSMENT OF CANDIDATE DESIGNS

Analyses of response to launch loads indicated requirements for minor redesign of both candidates. The material in ATS/3-Ring was changed from high-modulus to high-strength graphite/epoxy to assure low damage accumulation, and to provide a fair basis for comparison with Tripod-B. The wall thickness of the antenna-support legs in Tripod-B was increased to attain adequate buckling margins in these components, again to provide a fair basis for comparison. These design changes resulted in weight increments of about 18 lb. for ATS/3-Ring and 22 lb. for Tripod-B. Some slight improvement in the fatigue performance of the latter design might be expected to accompany the stiffening of the antenna-support legs. However, the probable effect at the longeron/electronics module attachment is small and will be neglected in the comparative assessment. Specific comparisons of the various performance characteristics will now be reviewed briefly.

With respect to buckling margins, the two designs are nearly equivalent. For ATS/3-Ring, $1-\overline{P}_{FP}/P_{CR} \geq 0.45$ in all components, while for Tripod-B, $1 - \overline{P}_{FP}/P_{CR} \geq 0.49$, where $\overline{P}_{FP}$ is the expected once-per-launch axial compression in a component. Similar results for bursting margin were also obtained: $1 - \overline{P}_{FP}/P' \geq 0.60$ in ATS/3-Ring and 0.43 in Tripod-B. The small difference in minimum margins does not favor either design.

Static strength checks at the longeron/electronics module attachments were made by assuming full correlation between the expected once-per-launch axial load and bending moment, and by including a conservative stress concentration factor to represent the effect of the joint entrance. Static margins of 0.1 for ATS/3-Ring and 0.29 for Tripod-B were obtained in this manner (see Appendix D). The component loads surveys (also in Appendix D) can be used to extend the strength check to other joints. Table 9 summarizes the survey of major loads, expressed as fractions of the loads at the longeron/EM attachments.

TABLE 9

LOAD SURVEY SUMMARY

(Fraction of Corresponding Load at Longeron/EM Attachments)

Location	D E S I G N			
	ATS/3-Ring		Tripod-B	
	Axial Load	Largest Moment	Axial Load	Largest Moment
EM Attachments	1.00	1.00	1.00	1.00
First Ring	1.00	0.21	1.00	0.13
Second Ring	1.00	0.41	1.00	0.43
Third Ring	1.00	0.89	1.00	0.57
Antenna Housing	1.00	1.21	1.05*	-
Apex Joint	-	-	0.05	0.09

*Expressed as fraction of ATS/3-Ring longeron/EM load because of similar dimensions of Tripod-B antenna-support legs.

The data in Table 9 suggest that static margins may be somewhat lower at the antenna attachments than at the EM attachments. For ATS/3-Ring, the factor of 1.21 on bending moment implies a negative margin at the antenna attachments, since bending contributes more stress to the longeron than does axial load. However, the apparent factor of 1.05 on axial load for Tripod-B will actually be about 0.5 when the wall-thickness increase in the antenna-support legs is accounted for.

With respect to the intermediate joints in both designs, it can be assumed that the longeron stress concentration factors will be low because the load survey indicates that the stabilizer-rings do not act as major load-transfer paths. In conjunction with the low load fractions at these joints, it can then be assumed that the end attachments possess the lowest static margins. Hence, the static margin survey favors Tripod-B. However, static margins in ATS/3-Ring could be recovered by addition of doublers to the ends of the longeron tubes.

Fatigue damage calculations were made at the longeron/EM joints, assuming stress concentration factors between 1.5 and 2.0, and using linear damage summation. The computed $\Sigma(n/N)$ values caused by launch loads were 0.007 to 0.113 for ATS/3-Ring and 0.010 to 0.162 for Tripod-B. These results would favor ATS/3-Ring. However, the reduced static margin at the ATS/3-Ring antenna attachments would also lead to increased $\Sigma(n/N)$ values at these locations. Therefore, the fatigue performances of the two designs are considered to be equivalent.

A low first-torsion frequency was discovered in the natural-modes analysis of Tripod-B (see Table 4 in Section IV). Although the effects of launch loads on this mode were accounted for in the subsequent dynamic analysis, the impact of torsional flexibility during antenna deployment must also be considered. Release of the parabolic reflector antenna from its housing is accompanied by a torque impulse with 4,000 lb. ft. estimated intensity; maximum stresses of 7.25 ksi in ATS/3-Ring and 77.3 ksi in Tripod-B were obtained from analyses of static response to the deployment torque [1].

Approximate analysis of deployment dynamics indicates that load factors of 1.13 and 1.48 must be applied to ATS/3-Ring and Tripod-B, respectively (see Appendix J). Thus, the dynamic deployment stress peaks will be about 8 ksi in ATS/3-Ring and 114 ksi in Tripod-B. These dynamic peaks will decay to about 5 percent of their initial values in approximately 24 cycles, assuming a modal damping factor $\zeta = 0.02$. Hence, antenna deployment is primarily a problem of static margin with regard to the feed truss. The results favor ATS/3-Ring, which will survive as designed. When stress concentration is accounted for, it appears that Tripod-B will require doublers at the ends of the longerons and/or the antenna-support legs to retain adequate static margin.

The foregoing comparisons are summarized in Table 10. Information developed previously about thermal stability and fabrication cost [1], is included in the table to provide a complete picture. Also, qualitative estimates of the risks associated with joint design are included. The "intermediate" risks listed for Tripod-B arise from the combination of high load transfer and complex geometry (apex fitting and fittings interconnecting longerons, antenna supports, and third stabilizer ring). Detail design of these joints for launch/deployment reliability may add about 10 lb. to the weight of Tripod-B. Overall, the assessment appears to favor the Tripod-B design.

TABLE 10

ASSESSMENT SUMMARY

Item	ATS/3-Ring	Tripod-B	Item Favors
Weight estimates (lb):			
Minimum	122	92	
Maximum	181	130	Tripod-B
Buckling and bursting margins	$\geq$ 0.45	$\geq$ 0.43	-
Lowest static margin (without doublers) for:			
Launch	$\leq$ 0	0.25	
Deployment	0.95	$\leq$ 0	-
Fatigue damage during launch, (n/N):			
SCF = 1.5	0.007[1]	0.010	
SCF = 2.0	0.113[1]	0.162	-
Thermal Defocussing[2] Due to:			
Uniform Cooling (ΔT=-300°C)			
Translation, ΔL (in)	-0.034	0.025	
Lateral solar incidence			
Translation, ΔL (in)	-0.015	0.0145	
Tilt, $\Delta\Theta$ (deg)	0.006	0.0032	Tripod-B
Cost[3]	$115,770	$79,615	Tripod-B
Risks in design of:			
End attachments	Low	Low	
Stabilizer-ring Joints	Low	Intermed.	
Apex Joint	-	Intermed.	ATS/3-Ring

[1] Larger values expected at antenna attachments.

[2] Data from Ref. 1, Table 7.

[3] Preliminary cost estimates from Ref. 1, Tables 12 and 13; labor and materials to fabricate flight and backup hardware.

SECTION VI

FABRICATION, INSPECTION AND QUALIFICATION

1. COMPONENT FABRICATION AND INSPECTION

Composite tubing designed for high axial stiffness and low axial thermal expansion can be assembled much more easily by using preimpregnated material for axial plies than by filament winding at very low helix angles. However, the problem of handling preimpregnated layups on cylindrical mandrels has not been solved. Improvements in processing have been demonstrated with two approaches: the Teflon inner mandrel [19] and the steel outer mandrel [20]. Both methods have been used successfully to fabricate laboratory test specimens with diameters from 0.5 to 3.0 in., but neither has been proved as a reliable manufacturing method. Relevant experience by other investigators and a review of problems encountered with the Teflon mandrel method in the present investigation are reported in Appendix K. A summary is presented in Table 11.

TABLE 11

RELATIVE MERITS OF INNER AND OUTER MANDRELS

Item	M E T H O D	
	Inner Teflon	Outer Steel
Axial Ply Wrinkling	No	No
Finish Tube Diameter Ref.	I.D. $\pm$0.002 in.	O.D. $\pm$0.002 in.
Unacceptable Wall Thickness Variation	Circumferential[1]	None reported
Unacceptable Void Content	In thick region[2]	No
Fiber Volume Fraction	Not assessed	Sensitive to mandrel tolerances
Initial Imperfection (Bowing) of Long Tubes	Possible[3]	Negligible

[1] [2]Apparently caused by use of squeegee rollers for layup.
[2]Apparently caused by substitution of heat-shrinkable outer sleeve for [3]vacuum bag.
[3]Caused by sagging of unsupported mandrel during cure.

Some suggestions for solving the wall thickness, void content, and fiber volume fraction problems are given in Appendix K. Sagging of long Teflon mandrels can be prevented either by vertical hanging or by insertion in a steel support tube of larger diameter. Vertical hanging may require a specially built autoclave, and may cause axial variation of resin bleed. Resting the mandrel in a support tube may create a resin-poor axial seam unless a flexible pad is placed between the mandrel and support tube.

Whichever method is ultimately chosen for production, it is apparent that the fabrication of laminated tubes for high-load applications should be accompanied by rigorous quality-assurance inspection at the component level. Dimensional measurements should include diameter, wall thickness, and bow at midspan. A tolerance for midspan bow can be established by reduction of design allowable buckling loads with initial imperfection sensitivity analysis. To supplement the dimensional measurements, a short ring should be cut from the end of each tube for photomicrography (determination of fiber volume fraction and void content), and perhaps for a hydrostatic burst test of the type proposed by Whitney, et al. [20]. However, the results of such ring tests should not be accepted uncritically as measures of quality along the entire length of long tubes.

Preimpregnated material may be used for 90° plies, as well as axial plies, to avoid potential complications in processing where filament-wound wet layups are made under and over B-staged axial plies. The presence of butt or lap seams in 90° plies can degrade local tube strength by reducing the axial load at which the tube will burst below the local crippling instability load. The present investigation has demonstrated that, in the case of straight butt seams, some combinations of stacking sequence and tube dimensions can result in static margins that are lower for bursting than for column buckling. Hence, inclusion of an equivalent hydrostatic proof test of the entire tube component should be considered.

A method for establishing the proof load level, based on launch load statistics and cost minimization, is given in detail in Appendix L. A numerical case representing the Tripod-B longerons was solved assuming

that the tubes would be designed to a mean strength equal to twice the first-passage load, and that manufactured tubes would exhibit about 10 percent coefficient of variation in strength. Under these assumptions, the optimum proof load is determined to be about 77 percent of design static strength, and a lower bound to launch reliability between 5 and 6 nines is obtained. These results demonstrate that reliable design of composite tubes containing butt seams is practical.

2. JOINT FABRICATION

Although a finite-element code was completed for stress analysis of the intermediate joints between longerons, antenna supports and stabilizer rings, the amount of analysis performed was not sufficient to predict the stress levels with confidence. Also, no DDT specimen development for these joints was undertaken in the present program. Therefore, no assessment can be made of potential fabrication problems for such joints. The intermediate joints are much less critical than the end-attachment joints, as far as a communications satellite antenna-feed truss is concerned. However, the concept of making tube/tube joints by secondary bonding of independently fabricated composite parts deserves attention for other applications where high load-transfer capability and thermal compatibility requirements exist.

Analyses and DDT specimen fabrication/test experience have shown that bonded composite/steel joints for attachments can be designed to have reduced entrance shear peaks in the bondline by tapering and slotting the steel fitting. Bonds approximately 0.001 in. thick using a commercial pot resin gave 95 percent confidence lower-bound strengths of about 7.4 KIPS initially and 4.1 KIPS after 500 to 1,000 thermal cycles (see Table C-6). These results can be scaled in accordance with:

$$\frac{P'}{P} = \frac{R'L'}{RL} \tag{9}$$

where R and L are the tube radius and bond length, respectively. Using the data assumed for the Tripod-B longerons (Table C-7) leads to estimates of

about 82 KIPS initially, and 45 KIPS after thermal exposure. Thus, the achievable initial strength in a Tripod-B longeron joint is about 2.8 times the estimated first-passage load.

The results of the investigation highlight several important factors. Strength degradation by thermal exposure is significant (about a factor of two reduction in tests which simulated five to ten years of life in orbit). However, the employment of taper and slots in the metal fitting keeps the long-term residual strength well above any mechanical loads which might be imposed by satellite attitude-control systems.

A cost reduction has been demonstrated by using steel fittings (as opposed to the titanium fittings used on ATS-6). The reduction is minor for the feed truss per se, but may be important in other applications (see Section VII).

Finally, fabrication experience indicates that bond thicknesses can be sensitive to I.D./O.D. tolerances between the composite tube and fitting. This sensitivity is suggested by the scatter in joint strength data (see Table C-6).

Some important issues were not resolved by this study. The I.D./O.D. tolerance problem implies not only axial strength variability, but also variation in joint strength and stiffness in bending. Even if a future program demonstrates adequate bending strength, joint stiffness must be quantified to permit better assessment of critical buckling loads and potential dimensional errors due to thermal/mechanical loads in orbit.

It is still not clear whether inside or outside metal fittings should be used in attachment joints. The designers of the ATS-6 truss chose outside fittings, but commented that inside fittings might reduce the stress concentrations [3]. Inside fittings were chosen in the present study primarily because the composite tubes were fabricated to better I.D. than O.D. tolerances. Future design trade studies should consider this question from the viewpoint of effects on butt seams in the composite tubes.

Finally, no experimentation with joint NDI methods was attempted in the present study. Ultrasonics and videothermography appear to be promising approaches [21]. Either method should be applicable when the composite tube is the outer structure, but NDI of outer metal fittings may be restricted to ultrasonics. In any case, experimental detection reliability studies will be required. The importance of validating such NDI methods is even greater when the presence of doublers is considered. Doublers will be required at the ends of the Tripod-B longerons and antenna support legs to counteract the high stress levels associated with antenna deployment (see Appendix J). The doublers may require secondary bonding to avoid potential difficulties in fabrication and quality assurance of a long tube with co-cured doublers.

3. DESIGN ALLOWABLES

The detail design/fabrication process should interact with a program for definition of design allowables. This program can be based primarily on DDT specimens. The correlation of axial compression and hydrostatic pressure tests of short-tube specimens to define a long-tube proof test (Appendix L) fits the category of design-allowable testing.

Long-tube DDT specimens should be subjected to environmental exposure to assess degradation effects. Dilatometer measurements should be made before and after exposure to quanitfy long-term dimensional stability. The dimensional stability of composites exposed to the space environment is of concern in current space programs [22], and will be crucial for larger microwave structures. After dimensional stability has been measured, the long tubes should be cut into short sections for compression or burst tests to assess strength degradation.

Environmental testing may be costly, and should be considered in terms of an integrated laboratory test program instead of a design-allowables task for a specific structure. Environmental effects which must be considered at geosynchronous altitude are micrometeroid damage, hard vacuum, ultraviolet radiation, the high-energy electromagnetic spectrum (X-rays, gamma rays), high-energy particles, and thermal cycles. Micrometeroid

damage is predictable to some extent, based on the work of Kerridge [23], Millman [24], and Cour-Palais [25]. A damage risk assessment method based on the data in Refs. 23, 24 and 25 was recently formulated by Orringer and Colombo, and is documented in Ref. 26. Vacuum and UV radiation can be simulated in the laboratory but their effects accumulate with calendar time, requiring long-term tests. These effects plus some of the high-energy spectrum will be experienced by test specimens planned for the NASA Long Duration Exposure Facility (LDEF). Data obtained from these tests should be incorporated in the integrated program. However, the LDEF experiment will not be subjected to deep thermal cycles. Therefore, long-term ground tests combining hard vacuum, UV radiation, and thermal cycles should be pursued independently to establish interaction effects. Assessment of accelerated test procedures should be a primary objective of the ground tests. For example, validation of the accelerated thermal cycle test for bonded joints would lead to cost savings in DDT programs for specific structures.

The design allowables test plan for a specific structure, such as the Tripod-B truss, should include static stiffness and strength tests (compression and bending) and residual compressive stiffness/strength measurements following environmental exposure (accelerated if thin-bond properties are shown to be insensitive to vacuum and radiation). Low-cycle mechanical fatigue, followed by residual stiffness/strength measurement, should also be included to establish empirical fatigue curves for estimation of launch damage. Constant-amplitude tests out to 10^4 to 10^5 cycles should be adequate for this purpose.

The test plan should be flexible. A few data points early in the detail design phase will permit rough definitions of mean values for a range of design variations. Toward the end of the detail design phase, when the joint details have been matured, enough data points should be taken to define a reasonable 95-percent confidence upper bound for the standard deviation of a given property, as well as a lower bound for the mean value. These data should be collected from manufacturing (as opposed to laboratory) specimens to quantify manufacturing quality for the reliability analyst.

Axial compression tests of DDT joints are straightforward, requiring only short sections of composite tubing outside the joint (length/diameter ratio equal to 3). However, proper simulation of bending effects in the DDT using only a lateral load may require much longer specimens. The ATS/3-Ring and Tripod-B longeron and attachments provide contrasting examples, as shown in Table 12.

TABLE 12

TYPICAL LENGTH REQUIREMENTS FOR BENDING TEST

Item	D E S I G N	
	ATS/3-Ring	Tripod-B
Moment, M (in. lb.)	4,643	3,783
Shear, V (lb.)	521	77
Required Length, L = M/V (in.)	8.9	49.1
Length/Diameter	3.3	14

4. QUALIFICATION OF FLIGHT HARDWARE

Flight hardware qualification should be planned as a series of tests, each of which increases the probability of success while allowing the options of design modifications and/or re-fabrication in case of test failures. Certain qualification tests can be conducted at the component level, e.g., the hydrostatic proof testing of longerons mentioned in Section VI.1. However, the general objective of most qualification tests is to verify global properties of the structure, a goal that cannot be achieved by component tests. The major milestones in the qualification

test program for a communications satellite antenna-feed truss are, in chronological order:

1) Microwave shadow and radar cross section.

2) Component proof tests.

3) Static test of assembled structure.

4) Dynamic test of assembled structure.

5) Dimensional stability.

6) Space-charging simulation.

Ideally, the microwave shadow test should be conducted in the preliminary design phase of a development program, while an option for changing the design concept completely is still available. The purpose of this test is to determine how the feed truss, intervening between the broadcasting dipoles and the reflector antenna, distorts the main and side lobe patterns of the reflector. Such tests are generally carried out with model structures at 1/5 to 1/20 scale, using an anechoic microwave chamber. The results of microwave shadow tests can also influence the definition of component proof loads by contributing to the penalty function a term that depends strongly on design conservatism (i.e., the effect of P/σ_L on component sizing, and hence on the shadow). A similar test for radar cross section can be conducted by mounting the model outdoors and measuring the return from a remote microwave source.

The remaining qualification tests are conducted toward the end of the detail design and fabrication cycle. Component proof testing should consist of a hydrostatic test for each production longeron and antenna-support leg. Production plans should include contingencies for extra articles to replace any components which fail the proof test. This approach increases the confidence in successful passage of the final structural tests, while paying a minimum price in terms of added cost and schedule delay.

Current practice in spacecraft manufacturing is to produce two assembled articles from the components that have passed proof testing. The flight hardware and backup structure are both subjected to final structural testing, but only one article need be tested for dimensional stability and space-charging.

The purpose of the static test is to verify that the most critical global modes of failure have been accounted for in design. Strength-dependent failure modes result from load transfer through joints (e.g., the apex joint and tee-joints in Tripod-B), and can be sensitive to inaccuracies in stress analysis. Global instability modes can arise from the fact that true joint stiffnesses are finite. The possibility of global instabilities in the ATS/3-Ring and Tripod-B designs was suggested previously [1], and should be addressed analytically in the detail design phase. Again, the predictions must be verified by testing because the analysis will be sensitive to variations in joint stiffness. Equivalent lateral and vertical loads to be applied at the top of the feed truss can be established by base-excitation analysis (Appendix D), using a simple bending-stretching beam model to represent the truss, and a concentrated mass to represent the reflector antenna and associated hardware. Load levels at the same multiple of the first-passage statistics as the component proof-test loads should be applied.

The purpose of the dynamic test is to simulate local internal overloads that may occur during launch, as a result of structural resonances. It is impossible to simulate such loading accurately in a static test without a large number of independently controlled load-application points. Hence, it is much simpler to mount the truss and antenna hardware on a shaker table for a sinusoidal sweep test. Appropriate RMS acceleration levels in the sweep test can be established from the design power spectrum (Figure 7) by energy-matching in frequency bands of width determined by estimated structural damping. Vertical and lateral excitation sweeps should be conducted separately to simulate the condition of uncorrelated inputs.

The purpose of the dimensional stability test is to verify the defocusing performance of the feed truss under thermal soak conditions. Two such tests should be conducted, with thermocouple instrumentation to verify temperature distributions over the structure. These tests should be carried out in a vacuum chamber to avoid heat conduction/convection through air. Heat can be supplied by IR lamps. One test should seek to establish a uniform soak temperature by combintion of lamps and reflecting foil around the structure. Linear defocusing due to cold soak in earth shadow can be estimated from the results of this test. In the second test, the structure should be heated from one angle, without reflecting foil, to represent a case of lateral solar incidence.

The space-charging phenomenon was encountered in some early high-altitude satellites, and is of great concern to designers because of its effects on electronics and attitude-control systems [27]. Electrical potentials can be accumulated on a satellite by impingement of ionized particles from the solar wind. Potential gradients between different points occur when the electrical conductivity of the intervening material is low, thus limiting the charge leak rate. The magnitudes of the gradients can be estimated during the detail design phase by an electrical conductivity model similar to the thermal model [1] which was used to estimate temperature gradients. Potential gradients may disturb electronics and/or damage the structure when they become sufficiently large to cause arc discharges. A simulation of the space-charging effect on the feed truss should be conducted in vacuum by using a DC supply to establish the estimated maximum potential difference between the antenna housing and the electronics module. Minor modifications to the truss, in the form of conductive strips or small "lightning rods", can be incorporated at this stage of the program, based on results of the discharge tests. Also, the probable effects on satellite electronics can be assessed by making measurements with Hertzian wave detectors at the base of the truss.

SECTION VII

OTHER SPACE APPLICATIONS

1. LARGE SPACE STRUCTURES

Much of the technology discussed in this study can be usefully applied to the Large Space Structures (LSS) currently being considered for various missions in low-earth orbit and at geosynchronous altitude. The most prominent LSS concept is a 5 x 12-km satellite, in equatorial geosynchronous orbit, for conversion of sunlight to microwave energy that is transmitted to the ground to provide baseload electrical power. The satellite solar power station has been studied in detail by NASA [28], and has been considered with respect to national energy policy by Congress [29].

High-energy laser platforms and active radars in space are LSS concepts with potential applications to Air Force missions. The active radar in space will be discussed here as a typical LSS example. Microwave antenna systems of the order of 100 meters in diameter are currently being studied [30], and could be applied to such radars. Large phased-array antennas with typical dimensions up to 1,000 meters have been suggested [31]. A concept for a phased-array LSS antenna is illustrated in Figure 11. The antenna surface is a 1,000 meter square singly curved panel supported by a rectangular truss framework, which is in turn stiffened by posts and tension cables.

Table 13 summarizes the contrast between the general characteristics of the communications satellite (Figure 2) and active radar structures. The weight estimate for the active radar was obtained by dimensionally scaling the weight estimate for Tripod-B. The cost estimates assume a Titan-IIIC launch for the communications satellite and 10 Space Shuttle flights at current cost for the active radar. It is important to recognize that, while the cost of the communications satellite per se dominates the total investment, transportation is a major cost for the active radar. Furthermore, the transportation cost for the active radar is sensitive to weight, while launch costs for the communications satellite are not affected by weight savings in the feed truss.

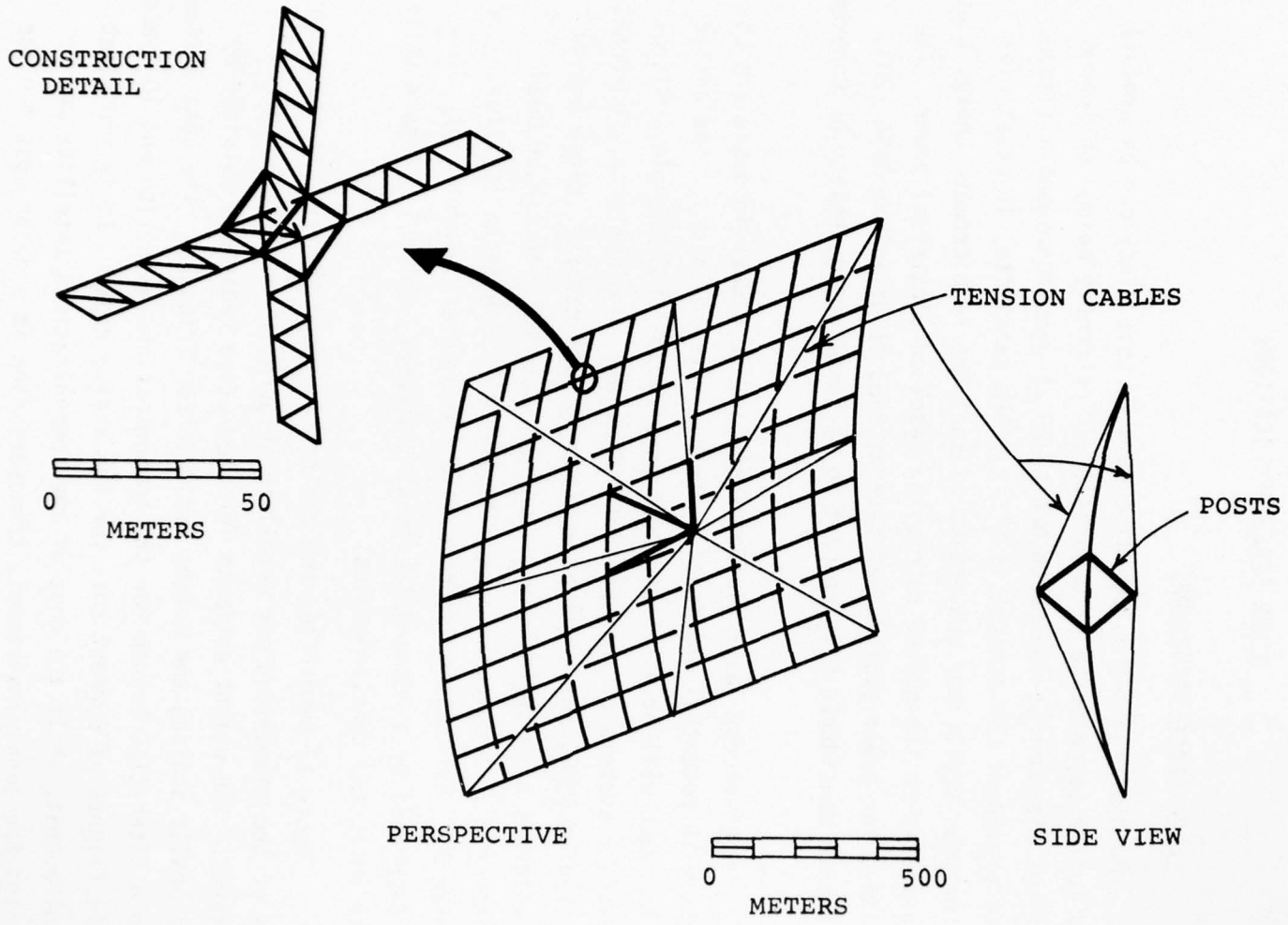


Figure 11. Concept for Active Radar in Space

TABLE 13

COMPARISON OF GENERAL CHARACTERISTICS

Item	S Y S T E M	
	Communications Satellite Feed Truss	Large Phased-Array Radar
Complexity		
Total major components	3	$\sim 5 \times 10^4$
Number of different components	3	6
Typical Dimensions		
Linear (m)	~ 7	$\sim 10^3$
Structural area* (m^2)	~ 3	$\sim 2 \times 10^4$
Weight (lbs)	~ 100	$\sim 3 \times 10^5$
Cost ($M)	~ 50	~ 450
Cost Breakdown (%)		
Fabrication	~ 80	~ 55
Transportation	~ 20	~ 45

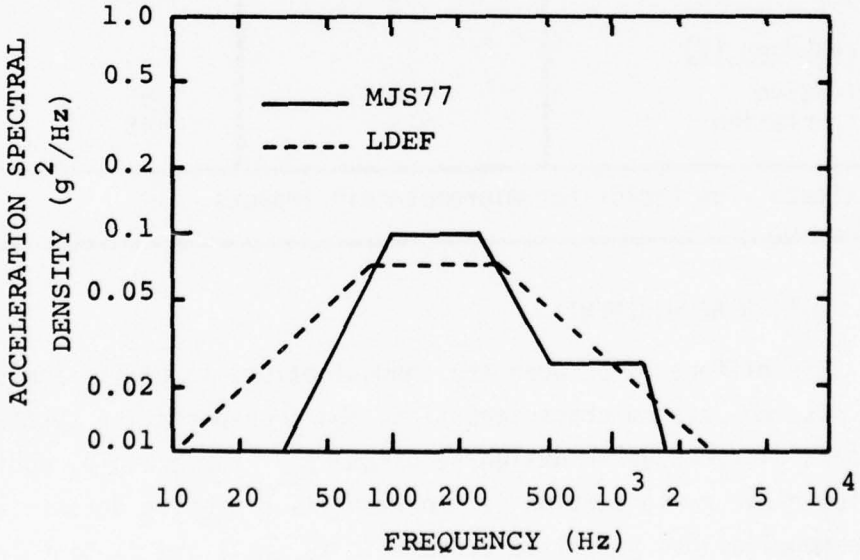
*Approximate view factor for micrometeroid impacts.

2. DESIGN REQUIREMENTS

The difference between the communications satellite and active radar in mission, system characteristics, and transportation system lead to important differences in design requirements. For example, achievement of low radar cross section is important as a passive defense measure for the communications satellite because it is small and distant from the earth, and because its active signal is a relatively low-power (1 KW) narrow beam directed toward friendly territory. On the other hand, the

active radar is large, may be in low-earth orbit, and will radiate a high-power (1 MW) beam toward the territory of a potential aggressor. Hence, there is no reason to design the active radar structure for low-radar cross section.

A superficial comparison of launch load spectra for the two systems (Figure 12) indicates that little difference in vibratory load levels is to be expected. However, the difference in launch configurations will have a significant effect. The communications satellite is a deployable system, with the feed truss erect and acting as a slender cantilever beam with concentrated tip mass during launch. As a consequence, high axial loads due to compression and bending are developed in the longerons and antenna-support legs (see Section IV and Appendix D). On the other hand, the active radar must be transported in the Space Shuttle as components, which will subsequently be assembled in orbit. It is reasonable to assume that the components will be stowed in isolation mountings, and hence will not experience any significant bending or axial loads during launch.



(LDEF spectrum from Ref. 32)

Figure 12. Comparison of Launch Spectra

The orbital load environments for the two systems will also be quite different. A large deployment transient is expected when the communications satellite antenna is released, and this event establishes some of the static margins in the Tripod-B truss (see Section IV and Appendix J). However, only small attitude-control loads are expected over the 10 to 20 year life of the satellite. On the other hand, attitude-control loads on the active radar will probably cause component stresses greater than the launch stresses. Also, the design life of the radar will probably exceed 20 years to amortize its cost at a reasonable rate. Hence, both static and fatigue margins will be influenced primarily by orbital loads.

Degradation due to micrometeroid impacts is relatively unimportant for the feed truss because of its small cross section (Table 13) and because the orbital loads are low. However, the situation is reversed for the active radar structure, and predictions of the type mentioned in Section VI.3 must be considered as a part of the design requirements.

Dimensional stability is crucial for both systems. In the case of the communications satellite, deformations caused by temperature variations defocus the reflector antenna and thereby increase sidelobe power at the expense of power in the main lobe, and/or misdirect the main lobe. In the case of active radar, out-of-surface (warping) thermal deformations across the antenna will tend to disperse the radiated wave and to degrade return detection capability.

3. IMPACT ON DESIGN, FABRICATION, AND TESTING

The foregoing differences in system characteristics and design requirements have several important consequences with regard to design, fabrication and testing of the structure for a large active radar in space. These consequences will be reviewed briefly in contrast with the feed-truss design study.

The principal benefit of fabricating the feed truss with composites was found to be dimensional stability for large excursions in temperature. For the active radar, potential weight savings are equally important because of the significance of launch costs. However, achievement of maximum weight savings will require design to reduced static loads.

Adequate static margins can still be attained for the active radar because of the different load-time history characteristics. Histories applicable to the feed truss and active radar are compared schematically in Figure 13. Design to large P/σ for launch and deployment determines static margins in the feed truss, while subsequent damage accumulation is dominated by thermal cycles. However, the combination of attitude control and thermal cycles in the active radar makes the long-term spectrum dominant. Hence, static margins for the active radar structure must be determined with fatigue damage accumulation in mind.

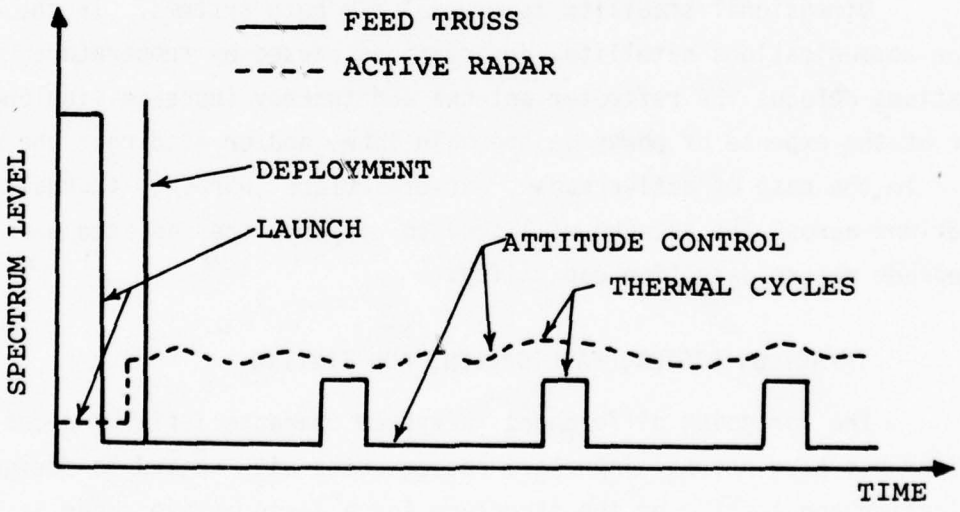


Figure 13. Comparison of Load-Time Histories

Also, the complexity of the radar structure suggests design for repairability and higher component reliability. Repairability implies the use of mechanically fastened joints to allow replacement of damaged components. Hence, bonded metal end-attachments may play a role in this type of structure. The Tripod-B longerons were designed to about 0.9_5 reliability, which implies a system launch reliability (considering only longeron failures) of about 0.9_4. To achieve the same system reliability in the active radar (considering only major component failures) would require design to about 0.9_9 component reliability, i.e., a higher proof-test load.

The foregoing considerations, in combination with the very strict dimensional stability requirements for phased-array radars, suggest that the structure must be actively controlled to meet the essential system design requirements. Active mechanical control without fuel consumption might be provided by solar-powered servo-actuators that vary the tensions in the cables shown in Figure 11. However, if mechanical actuation is relied upon as the sole control mechanism, the fatigue load levels may be unacceptably high. There will undoubtedly exist some ability in the radar electronics for control of the phasing of independently fed dipoles in different locations on the array. Very large phase-shift ability may be routinely designed into such a radar to permit operation in both forward-looking and squint modes. In such cases, the wave shape is determined by interaction of the phase state and the structural shape. The structural design of a phased-array radar in space should then be driven by somewhat relaxed dimensional stability requirements established from an interactive structural/electrodynamic system study. The conception of such a study is shown schematically in Figure 14.

Final structural qualification of the feed truss consists of several full-scale tests of the completed flight hardware (see Section VI). Obviously, this type of testing will be impossible for the large active radar, but there is still a need to assess the effects of static and dynamic loads, thermal cycles, and space-charging on the structure. These

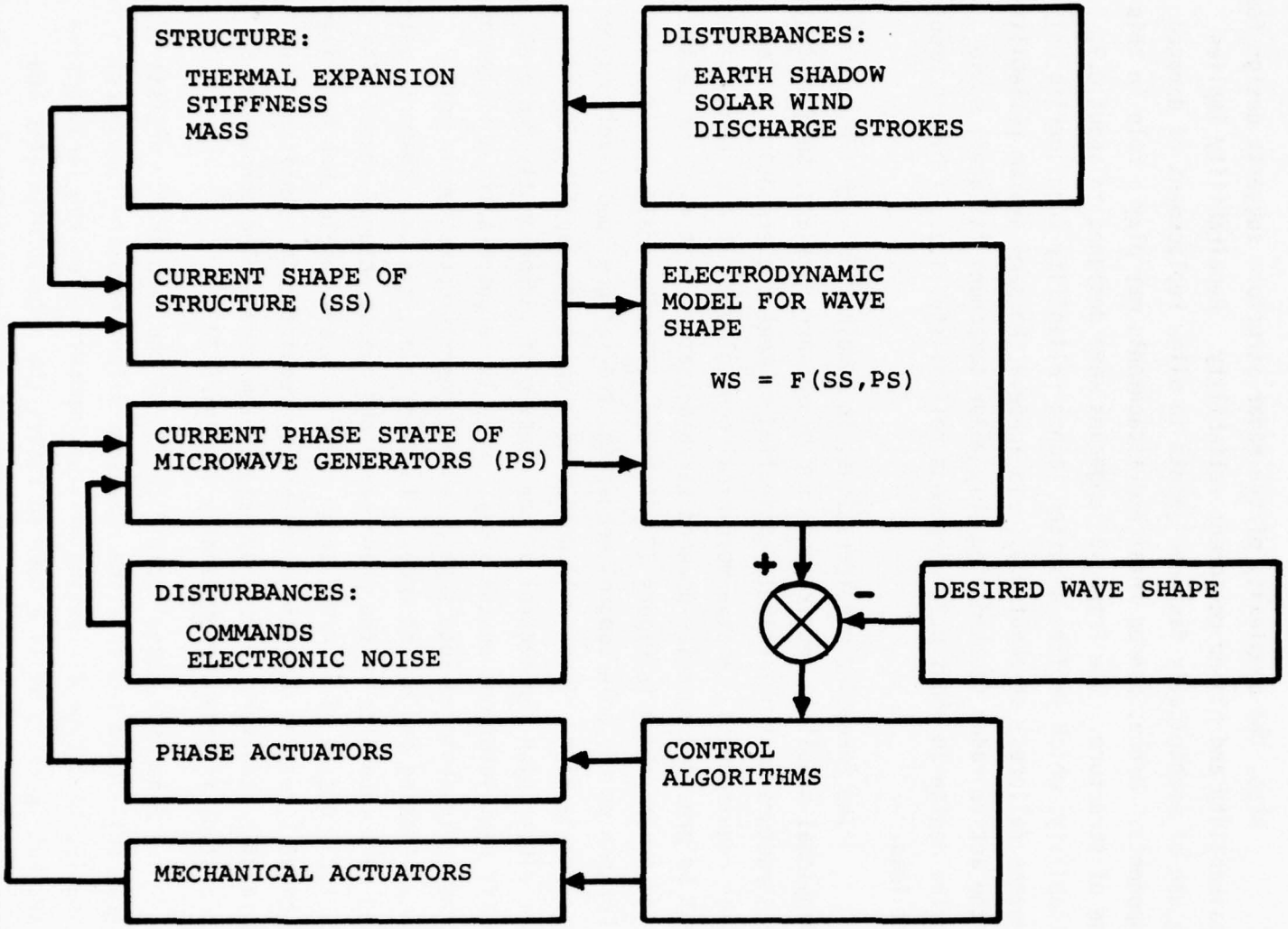


Figure 14. Electromechanical Control System

assessments can be made by design verification tests (DVT) of subassemblies. An extensive DVT program was conducted as a part of the B-1 design, the purpose in that case having been to increase confidence in successful passage of the full-scale fatigue and damage-tolerance tests [33]. In the case of the active radar in space, a DVT program must of necessity act as a substitute for full-scale testing.

SECTION VIII

CONCLUSIONS AND RECOMMENDATIONS

1. CONCLUSIONS

1) Laboratory experiments with delamination coupons failed to produce a test specimen configuration that could be used to determine true interlaminar strength properties. Additional experiments and better analyses are needed to achieve this goal (see Appendix A).

2) Short beam shear tests for interlaminar strength trends indicate that AS/3501-6 graphite/epoxy cured in accordance with the manufacturer's recommended procedure exhibits no strength degradation after accelerated thermal cycling equivalent to 10 years experience of earth-shadow cold soaks at geosynchronous altitude (see Appendix B). However:

   a) Only $[0^{\circ}_{26}]$ laminates were tested.

   b) Similar date for 0° laminates with Mylar inserts showed a slight degradation, suggesting that damage could accumulate from thermal stress cycles in laminates containing 90° and/or angle plies. Actual thermal cycle effects in these cases need to be assessed by experimentation before any definite conclusion can be drawn.

3) Detail fabrication costs for end-attachments bonded to composite tubes can be reduced by using steel instead of titanium fittings. Strength tests of such joints indicate that adequate initial strength for survival of launch loads and adequate resistance to the 10-year accelerated geosynchronous thermal fatigue simulation can be combined in the same joint design, provided that steep taper and/or slots are incorporated in the fitting (see Appendices C and I).

4) The scatter in joint strengths for production articles may be sensitive to variation in bond thickness, which in turn is sensitive to variation in I.D./O.D. tolerances between a composite tube and its end fittings. Quantification of this scatter early in the detail design phase is important for proper assessment of structural reliability (see Appendices C, D, K, and L).

5) The most critical local failure mode in $[90^\circ_M/0^\circ_{2N}/90^\circ_M]$ tubes with straight butt seams in the 90° plies under axial compression appears to be a bursting phenomenon at loads much lower than the crippling instability load; the bursting load appears to be controlled by ply Poisson ratios, a resin strength property, and M/N (for $M \ll N$), and can be correlated approximately with a simplified mechanics model (see Appendix C). For long tubes with butt seams, the static margin against bursting can be lower than the column buckling margin (see Section IV and Appendix D). Simplified mechanics models can be used to establish an equivalent hydrostatic proof test, in terms of design burst load, for tubes with butt seams (see Appendices C and L). However, the scatter in burst loads for production articles needs to be determined to make a final assessment of whether tubes with butt seams can be designed to acceptable levels of reliability.

6) For antenna feed-truss structures, the most critical static margins may be determined by antenna deployment if the deployment torque is sufficiently high and the truss first-torsion frequency is sufficiently low. In the present case, adequate margins were obtained by addition of doublers at joints. In other cases, nonlinear dynamic analysis may be required to obtain better estimates of dynamic load factors associated with deployment (see Appendices D and J).

7) Linear estimates of fatigue damage at critical joints indicate that damage accumulation during launch is insignificant in comparison with residual strength degradation due to thermal cycles in orbit (see Appendices C and D). However, combined mechanical and thermal fatigue must be considered for large space structures assembled in orbit and designed to attitude-control loads (see Section VII).

8) Component proof load levels can be optimized with respect to expected cost criteria. Optimal levels for a feed truss are consistent with launch reliability requirements, and are below levels at which the proof test might cause damage (see Section VI and Appendix L). However, optimum expected cost may have to be sacrified to obtain test benignity for large space structures.

9) Tube fabrication procedures require additional development and evaluation before reliable production can be achieved. Further investigation is warranted for both the inner Teflon and outer steel mandrel methods (see Appendix K).

10) The full-scale qualification tests recommended for hardware such as the antenna feed truss cannot be applied to large space structures, e.g., orbiting active phased-array radars. In such cases, the structure must be qualified by design verification tests (see Section VII).

11) The results of the communications satellite antenna feed-truss design study indicate that the Tripod-B design is superior to the ATS/3-Ring design in terms of structural performance, thermal deformational stability, weight, and cost.

2. RECOMMENDATIONS

1) An integrated laboratory test program is recommended for improvement of tube fabrication technology to support potential applications of composites to space structures. The laboratory program should address:

   a) Refinement of layup and curing procedures using both inner and outer mandrels.

   b) Preimpregnated material versus wet-layup filament-winding for 90° plies under and over dry-layup preimpregnated axial plies.

   c) Larger tube diameters and thicker walls.

   d) Correlation of axial burst load with hydrostatic burst load for tubes with butt seams in 90° plies.

   e) Improved test methods for interlaminar strength properties.

   f) Resistance to cyclic thermal fatigue and mechanical fatigue, in terms of residual strength degradation.

   g) Validity of accelerated cyclic thermal testing by comparison with NASA/LDEF experiments and long-term ground tests.

2) It is recommended that future design studies in support of composites applications to Air Force space programs be directed toward large space structures, where the potential payoff is sufficiently attractive to make the work worthwhile. Such design studies should be structured to:

   a) Develop design requirements based on integrated systems analysis, e.g., combining the disciplines of structural mechanics and electrodynamics to determine realistic control loads for structures such as an active radar in space.

   b) Investigate experimentally (by design development tests) and analytically the behavior of bonded composite/metal end-attachments.

2) (Continued)

c) Work toward fabrication and "qualification" of a design verification test article in which high load transfer between tubes joined at angles can be investigated analytically and experimentally, and which can be used as a vehicle to expose unidentified problems in design and qualification testing.

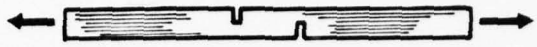
APPENDIX A

INVESTIGATION OF ANGLE-PLY DELAMINATION COUPON AS AN INTERLAMINAR STRENGTH TEST

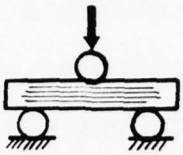
1. GENERAL

Interlaminar strength has long been recognized as an important property for composite laminates subjected to bending. Analyses and experiments have demonstrated the existence of interlaminar stresses in composites subjected to in-plane loading (e.g., the angle-ply analysis by Puppo and Evensen [34]; the edge-zone analysis by Pipes and Pagano [35]; and fatigue experiments reported by Grossman [36]). One can also show, by means of simplified engineering analyses, that interlaminar stresses must be considered in the design of large composite space structures (e.g., at the entrance of a composite tube into a metal fitting). Analysis of this last type has been reported by Burns and Toland [3]. Hence, interlaminar strength properties must be determined to provide design information, and although shear appears to be the dominant interlaminar stress component in most cases, there may be some design situations in which interlaminar tension must be accounted for.

Various inexpensive strength tests have been proposed for these interlaminar properties. The most frequently used tests for interlaminar shear strength are the notched tension coupon (ASTM D2733-70), and the short beam shear test (ASTM D2344-76), illustrated in Figure A-1. Both have been criticized for having stress fields too nonuniform to provide accurate strength measurements. The more expensive tube torsion test has also been used, but recent work indicates that data with equivalent accuracy can be obtained from tension tests of $[\pm 45°]_S$ flat coupons [37].



(A) NOTCHED TENSION COUPON (ASTM D2733)



(B) SHORT BEAM SHEAR TEST (ASTM D2344)

Figure A-1. Standard Tests for Interlaminar Shear Strength

In the case of interlaminar tensile strength, some organizations have relied upon the so-called "flatwise tension test" (Figure A-2, Part A), which to the present authors' knowledge is not documented by a specification standard. It is well known that the flatwise tension specimen has high interlaminar stress peaks along its edges and at its corners. Recent studies by Sandhu [38] indicate that these peaks can be reduced by chamfering the adherends and filling in the gaps with extra resin (Figure A-2, Part B). An alternate method for measuring interlaminar tensile strength might be available in the delimation coupon specimen, first proposed by Pagano and Pipes [11].

This appendix presents the results of an investigation of the delamination coupon for this purpose. The configuration of the specimen and related analyses are first reviewed briefly. The results of an experimental investigation are then presented and analyzed. Finally, some comments are offered regarding the applicability of delamination coupons to interlaminar strength testing.

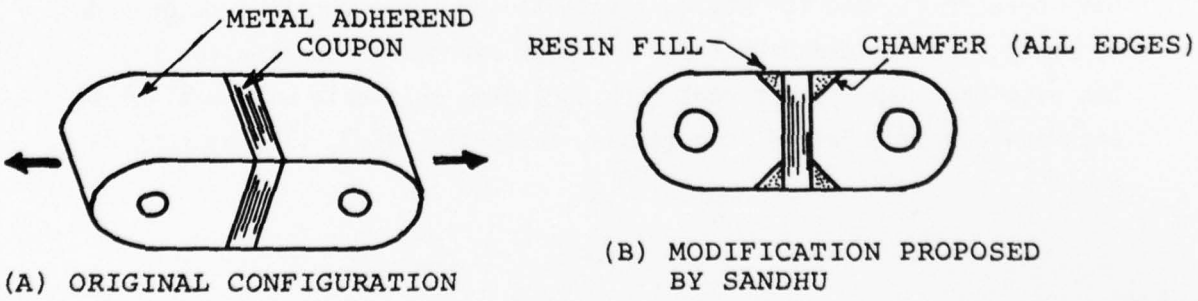


Figure A-2. Flatwise Tension Specimen

2. THE DELAMINATION COUPON

The configuration of the delamination coupon is illustrated in Figure A-3. Here and subsequently, the xy plane shall denote the laminate midplane, with the x-axis (0°) parallel to the applied in-plane tension loading, while the z-axis is perpendicular to the midplane. The laminate is symmetrical about the midplane, consisting of a total thickness, 2h, with thicknesses $2h_1$ of angle plies $\pm\theta$ on the outsides and $2h_2$ of 90° plies at the center of the specimen.

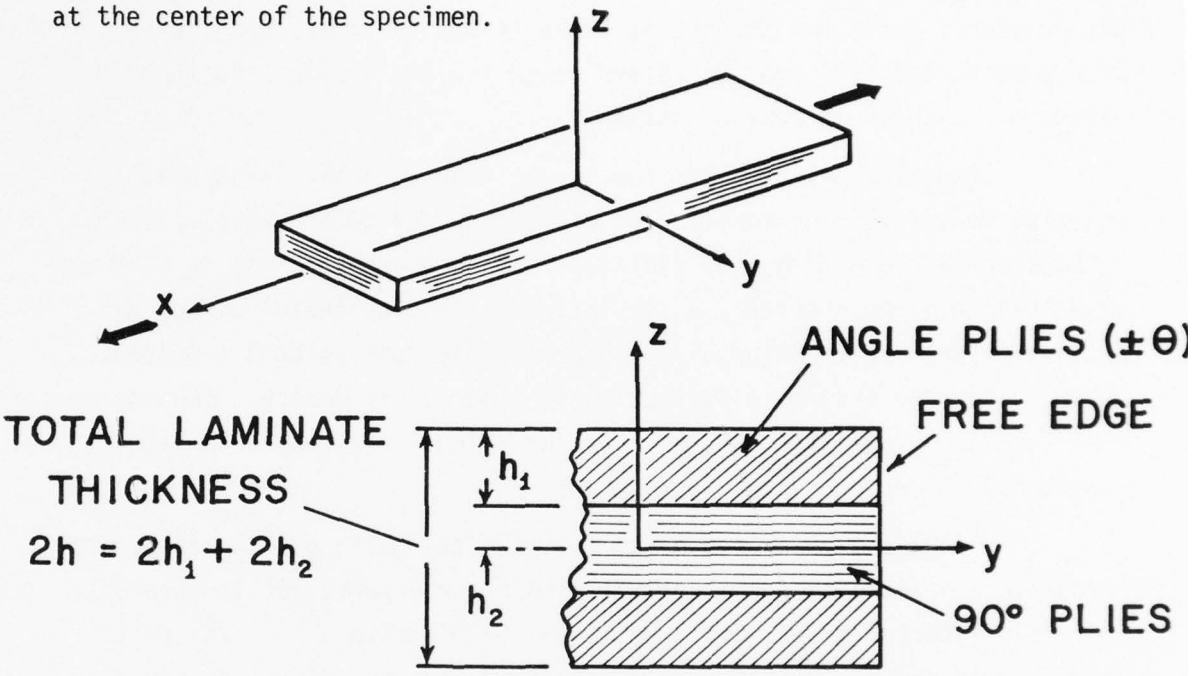


Figure A-3. Delamination Coupon

Analysis of a $[0°/90°]_S$ laminate subjected to uniform axial extension reported by Pipes [39] and Pagano [40] demonstrates the existence of interlaminar tension, σ_z, at the midplane, distributed as shown in Figure A-4, Part A. Heuristic arguments for a similar stress distribution in the delamination coupon can be made. Pagano and Pipes [11] approximate this distribution by assuming the general form shown in

Figure A-4, Part B; the distribution amplitude (peak interlaminar tension, σ_z^{max}) can then be determined from:

$$\sigma_z^{max}/\varepsilon_x = A \frac{(\nu_{xy}^{(1)} - \nu_{xy}^{(2)})\, Q_{yy}^{(1)}\, Q_{yy}^{(2)}\, \eta}{(1+\eta)\,(Q_{yy}^{(1)}\,\eta + Q_{yy}^{(2)})} \qquad \text{A-1}$$

where ε_x is the applied axial strain; ν_{xy} and Q_{yy} are, respectively, the ply Poisson's ratio and transverse plane-stress stiffness coefficient; with superscripts (1) and (2) referring to the angle plies and the 90° plies, $\eta = h_1/h_2$; and A is a constant.

Equation A-1 results from an engineering analysis in which an equation is written for equilibrium of moments due to the stress distributions acting on a free body isolated from the laminate. It is easy to show that only the constant, A, is influenced by the choice of approximation for the distribution of σ_z. For example, the value A = 45/28 is obtained for the assumed distribution in Figure A-4, Part B. The approximation shown in Figure A-4, Part C, for which A = 1, has also been considered in the present investigation.

Since the objective is to maximize the ratio $\sigma_z^{max}/\varepsilon_x$ in order to obtain a delamination failure prior to other effects, it is apparent that the interior plies should be at 90° to minimize $\nu_{xy}^{(2)}$. The test specimen may now be designed, according to Pagano and Pipes, by treating the thickness ratio, η, and ply angle, Θ, as free parameters. Note that $\nu_{xy}^{(1)}$ and $Q_{yy}^{(1)}$ are both functions of Θ. Pagano and Pipes consider the free parameters individually, first maximizing Eq. A-1 with respect to η. This leads to the expression:

$$\eta = [Q_{yy}^{(2)}/Q_{yy}^{(1)}]^{1/2} \qquad \text{A-2}$$

from which the relative number of angle plies and 90° plies can be determined after the value of Θ has been established. The specimen design is then completed by maximizing $\nu_{xy}^{(1)} - \nu_{xy}^{(2)}$ with respect to Θ.

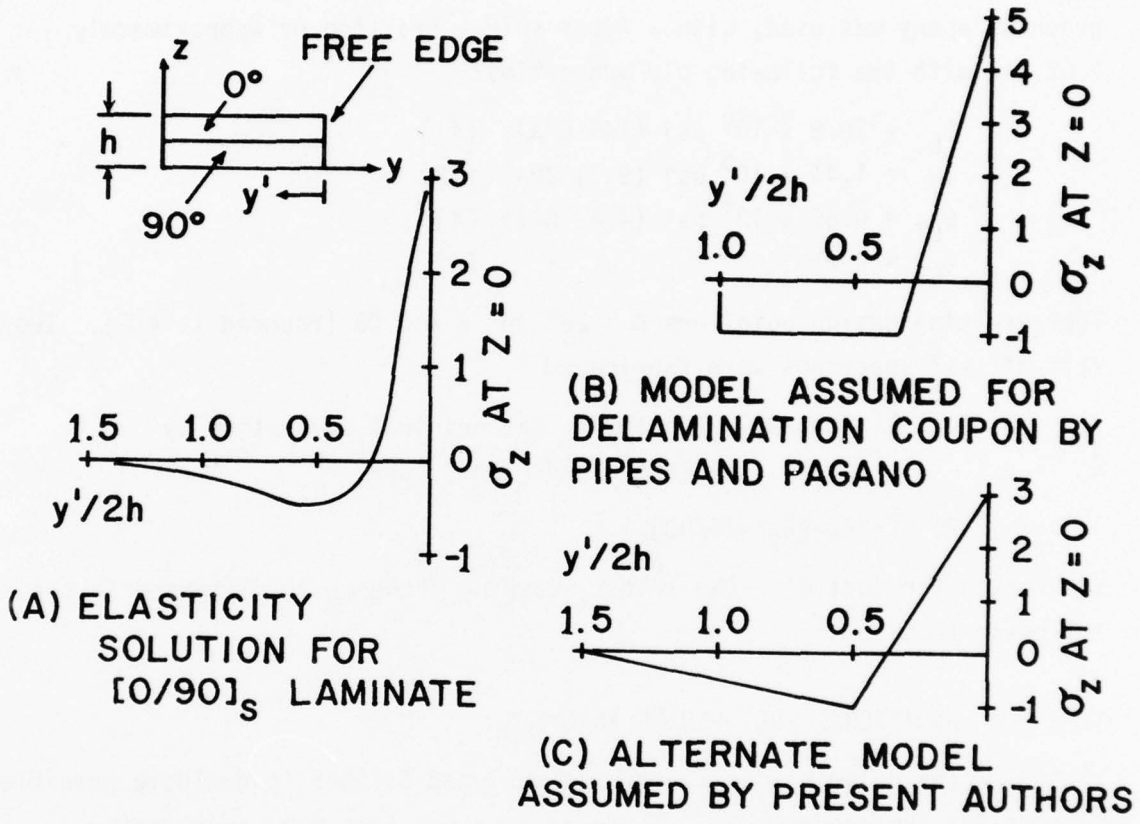


Figure A-4. Midplane Interlaminar Normal Stress in Edge Zone

In their original experiments [11], Pagano and Pipes fabricated specimens from HTS/ERLA 2256 graphite/epoxy with a fiber volume fraction of approximately 0.6, and with the following ply properties:

$E_L = 20 \times 10^6$ psi (138 GPa)
$E_T = 1.3 \times 10^6$ psi (8.95 GPa)
$G_{LT} = 0.8 \times 10^6$ psi (5.51 GPa)
$\nu_{LT} = 0.25$

The resulting design point was $\Theta = 25°$ and $\eta = 3.1$, the latter value being rounded to 4.0 for practical purposes. The test specimens were then fabricated as $[(\pm 25)_2/90]_S$.

In the present investigation, Hercules Magnamite AS/3501-6 graphite/epoxy was used, with a fiber volume fraction of approximately 0.62 and with the following ply properties:

$E_L = 20.9 \times 10^6$ psi (144 GPa) [41]
$E_T = 1.41 \times 10^6$ psi (9.71 GPa) [42]
$G_{LT} = 0.65 \times 10^6$ psi (4.48 GPa) [4]
$\nu_{LT} = 0.21$ [4]

The resulting design point was $\Theta = 26°$ and $\eta = 3.05$ (rounded to 4.0). Two sets of test specimens were fabricated:

1) $[(\pm 26)_2/90]_S$ (following the original suggestion by Pagano and Pipes), and

2) $[+26/-26_2/+26/90]_S$

The reason for including the letter stacking sequence is discussed in the following section.

3. ADDITIONAL ENGINEERING ANALYSIS

The delamination coupon was analyzed further to evaluate possible options for the experiments. Three-dimensional free-body equilibrium diagrams were constructed following the two dimensional procedure established by Pagano and Pipes [11, 43]. For a finite-length coupon, the dependence of σ_z on axial position, x, as well as location in the cross section plane, yz, must be considered. The diagram for a $[(\pm\Theta)_2/90]_S$ laminate (Figure A-5) suggests that the in-plane shear-stress couples on longitudinal section ABCD must be balanced by an anticlastic σ_z distribution, with peaks and minima at the specimen corners. The anticlastic part of the stress field should decay rapidly, leaving the Pagano-Pipes edge-zone distribution a few laminate thicknesses away from the coupon end-tabs. The presence of anticlastic σ_z peaks appears to

QUANTITY	EQUILIBRATING STRESS FIELDS	
	IN-PLANE	INTERLAMINAR
FORCE ALONG y	σ_y ON ABCD	τ_{yz} ON AEFB
MOMENT ABOUT EF	σ_y ON ABCD	SYMMETRIC PART OF σ_z ON AEFB
MOMENT ABOUT y	τ_{xy} COUPLES	ANTICLASTIC PART OF σ_z ON AEFB

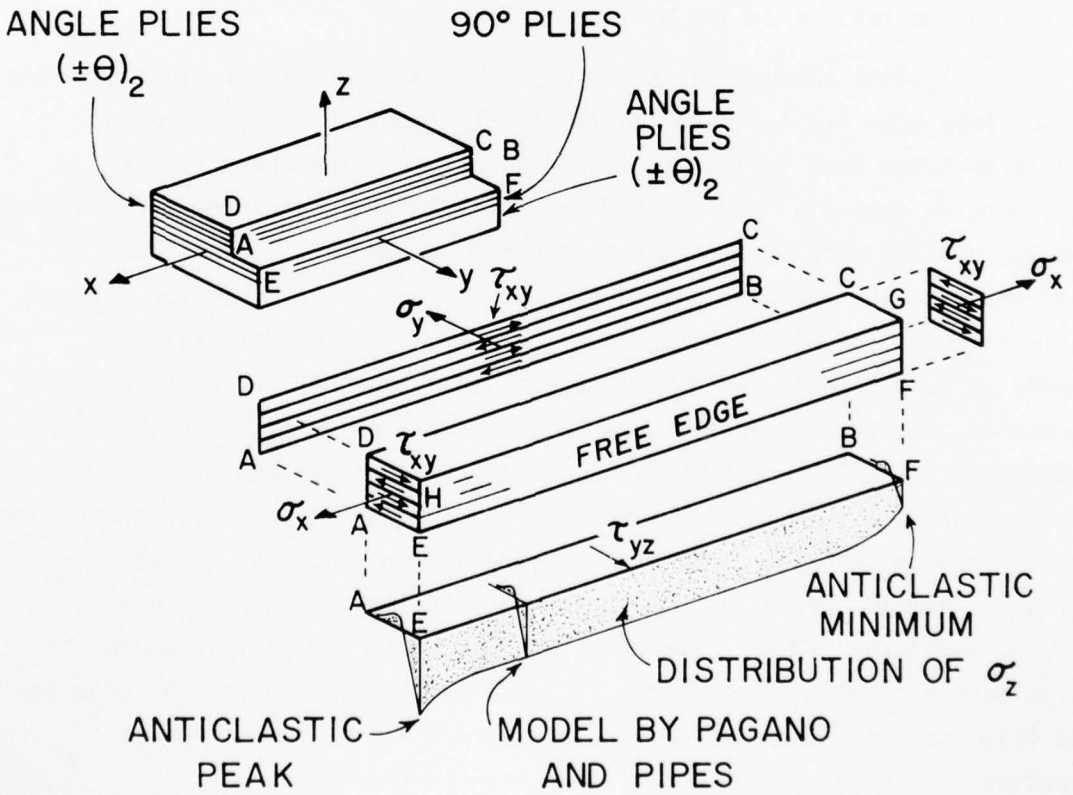


Figure A-5. Free-Body Diagram Illustrating Anticlastic Distribution of Interlaminar Normal Stress

have been confirmed in the numerical results reported by Rybicki [44]. The presence of anticlastic peaks in the coupon should have a significant influence on apparent interlaminar tensile strength.

The alternate stacking sequence $[+\theta/-\theta_2/+\theta/90]_S$ was considered as a means of reducing the anticlastic peaks. The three-dimensional free-body diagram for this sequence suggests that the difference between the peak σ_z value and the (asymptotic) *uniform* value along the free edge may be about one-half the difference expected in the $[(\pm\theta)_2/90]_S$ laminate. Also, the analysis suggests that the peaks might not be located on the specimen midplane in the $[+\theta/-\theta_2/+\theta/90]_S$ sequence. Hence, the alternate layup should exhibit higher values of applied load (or applied axial strain, ε_x) at initial delamination, provided that the initiation of failure is not by interlaminar shear.

Typical through-thickness distributions for interlaminar stresses at the free edge are indicated qualitatively in Figure A-6, based on estimates taken from various published solutions. The shear stress, τ_{xz}, attains maxima at $+\theta/-\theta$ interfaces [34,35] where the free-body diagrams result in unbalanced in-plane shear stress. These maxima can be of the same order as the midplane value of σ_z (see Figure A-7). However, τ_{xz} must vanish at the midplane, and its decay from the nearest maximum should be sufficiently rapid that its value at the $90/\theta$ interface will be small. The shear stress τ_{yz} is known to attain a maximum at the 90/0 interface in $[90/0]_S$ and $[0/90]_S$ laminates, and the maximum value is of the same order as the midplane value of σ_z [39,45]. A similar distribution for τ_{yz} should be expected in the delamination coupon. The normal stress σ_z attains its maximum value at the midplane for $[0/90]_S$ and $[90/0]_S$ laminates [39,45], and must follow a similar distribution in the delamination coupon. Furthermore, a two-dimensional free-body diagram for the delamination coupon can be constructed and a moment equilibrium equation involving σ_y and σ_z can be written to show that:

$$\frac{\sigma_z(z)}{\sigma_z^{max}} \approx 1 - \frac{(z/h_2)^2}{\eta + 1} \quad (0 \leq |z| \leq h_2) \qquad \text{A-3}$$

Hence, for $[(\pm\Theta)_2/90]_S$ and $[+\Theta/-\Theta_2/+\Theta/90]_S$ laminates, the value of σ_z at the 90/Θ interface should be approximately 80 percent of the midplane value. In a similar manner,

$$\frac{\sigma_z(z)}{\sigma_z^{max}} \approx \frac{[\eta + 1 - (z/h_2)]^2}{\eta(\eta + 1)} \quad (h_2 \leq |z| \leq h_1 + h_2) \qquad \text{A-4}$$

The foregoing considerations suggest that delamination failure might occur away from the midplane due to combined-stress effects, rather than at the midplane due to σ_z alone.

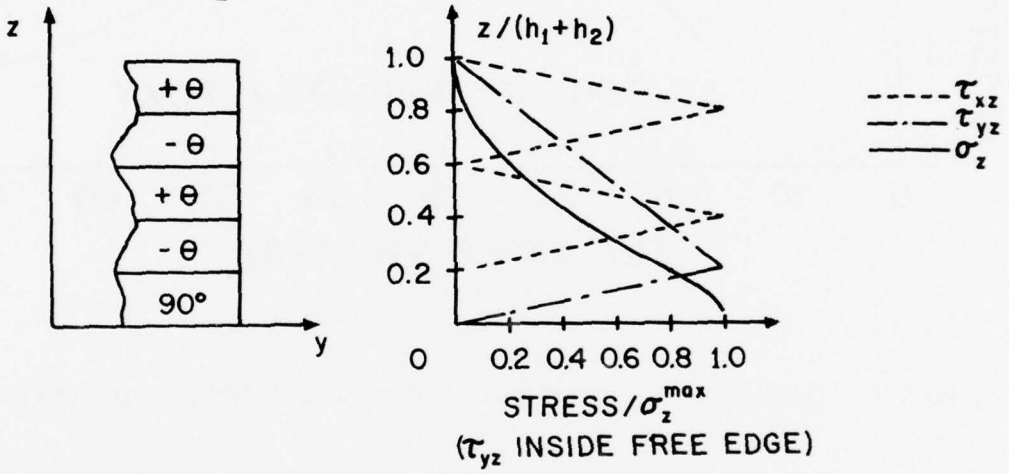


Figure A-6. Qualitative Distributions for Interlaminar Stresses

Some additional consideration was also given to the procedure for maximizing $\sigma_z^{max}/\varepsilon_x$ (Eq. A-1) to assure failure by interlaminar tension. Strictly speaking, this expression defines $\sigma_z^{max}/\varepsilon_x$ as a continuous function of the two independent variables Θ,η and maxima should therefore be sought from the behavior of the partial derivatives. However, because such an approach involves complicated trigonometric expressions in Θ and because only integral values of η are of practical interest, the simple expedient of calculating $\sigma_z^{max}/\varepsilon_x$ as a function of Θ and integral η was adopted.

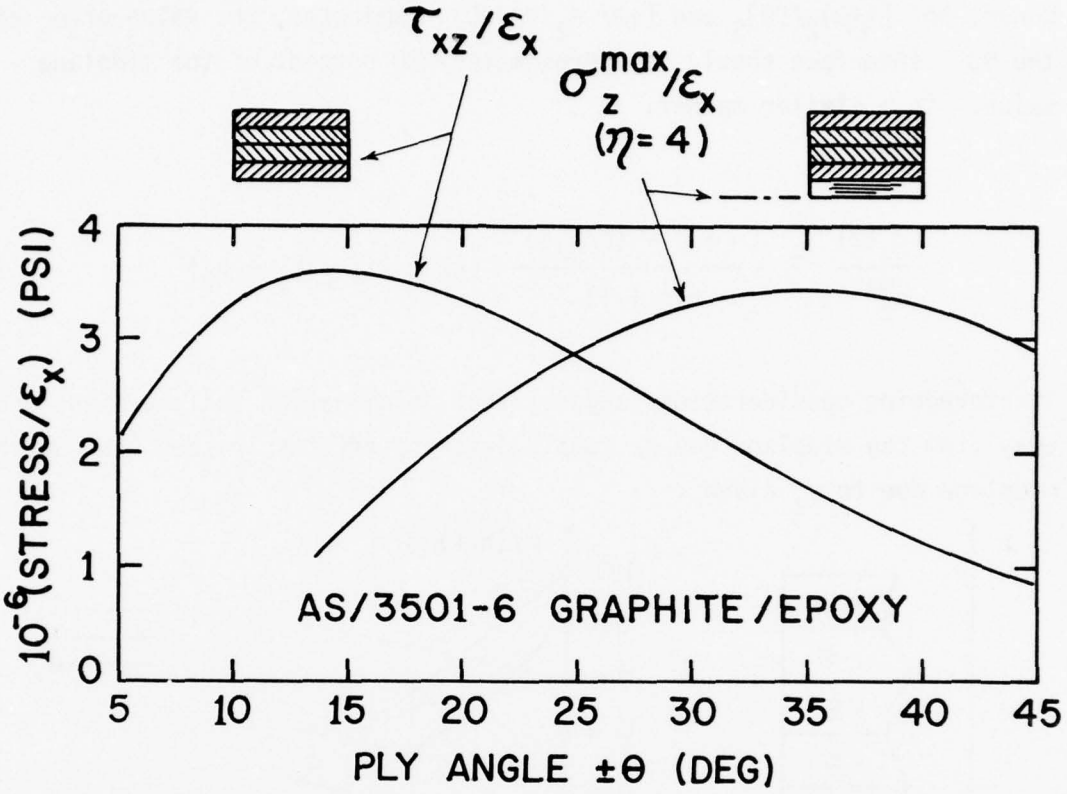


Figure A-7. Comparison of Interlaminar Shear and Interlaminar Tension

Plots of these results for several values of η, using the ply properties of AS/3501-6, are shown in Figure A-8. Surprisingly, the true maxima of $\sigma_z^{max}/\varepsilon_x$ tend to occur for angle plies $\pm\Theta$ from 30° to 40°, instead of near 25° as originally predicted. In spite of this discovery, it was decided to pursue the experimental program with the original specimen design, $\pm\Theta$ = 26°, to permit comparison with the previous investigation. (It should be noted that delamination failures were obtained previously [11], and that $\sigma_z^{max}/\varepsilon_x$ need not be an absolute maximum to obtain such failures in any case.)

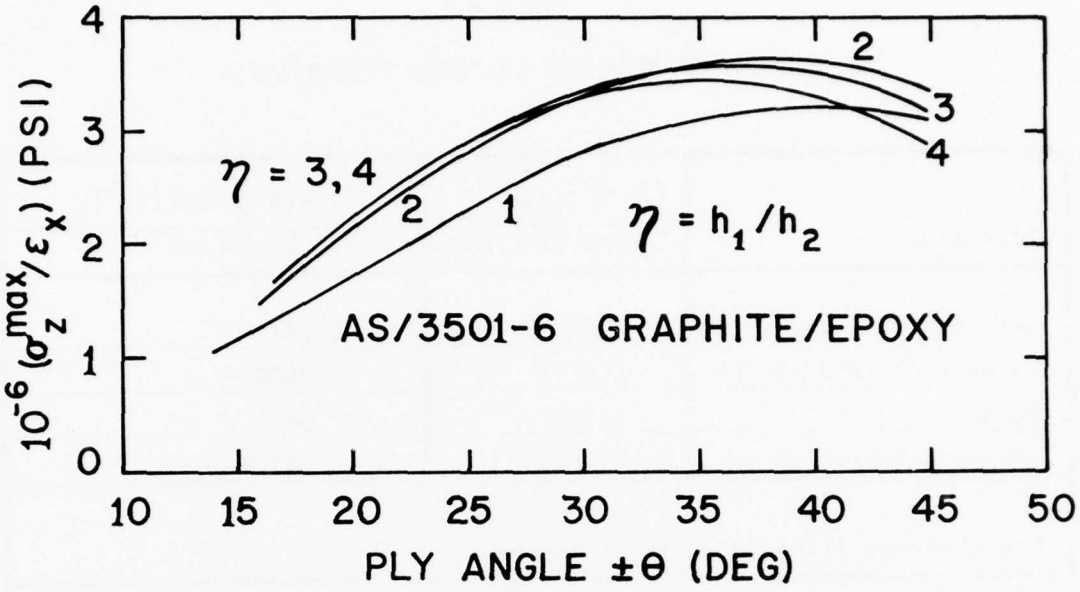


Figure A-8. Asymptotic Value of Interlaminar Tension at Free Edge as a Function of Delamination Coupon Design

4. TEST SPECIMEN FABRICATION

Two plates, approximately 5 x 17 inches (12.7 x 43.2 cm) were fabricated from AS/3501-6 material, following the supplier's recommendations for tooling, layup and cure cycle [42]. The plates were post-cured for one hour at 400°F (205°C). One plate was fabricated in the primary sequence $[(\pm 26°)_2/90°]_S$ and the second was fabricated in the alternate sequence $[+26°/-26°_2/+26°/90°]_S$. After removal from the tooling, discard of approximately 0.5 inch (1.27 cm) of material along each edge, and rejection of isolated areas damaged during removal, there remained sufficient material for eleven test coupons 1 x 5 inches (2.54 x 12.7 cm) from each plate. These coupons were cut to size using a Neuber type 1A1R (C = 50) resinoid-bond diamond wheel at approximately 2,000 RPM together with a water spray.

Thickness measurements were made on all specimens to assess fabrication quality. These measurements, summarized in Table A-1, indicate acceptable fabrication quality, since the nominal thickness for AS/3501-6 ten-ply laminates is 0.051 inch (0.13 cm).

TABLE A-1

SUMMARY OF MEASURED SPECIMEN THICKNESSES*

Statistic	$[(\pm 26°)_2/90°]_S$ Eleven Specimens	$[+26°/-26°_2/+26°/90°]_S$ Eleven Specimens
Smallest Observed Value	0.0490	0.0475
Largest Observed Value	0.0515	0.0500
Mean	0.0497	0.0486
Standard Deviation	0.00098	0.00073

*Measurements given in units of inches.

However, some concern about the quality of the specimens still remained because a slight bow in both plates was observed after edge discard but before cutting into coupons. The cause of the bow was determined to have been sticking of the rubber dams on the aluminum tool plate during the cooling portion of the cure cycle. Hence, although the individual coupons were not visibly bowed, it was decided to perform an additional quality control check by taking some of the specimens to ultimate load after measuring the delamination load. These results reconfirmed the quality of the test specimens. The details are presented and discussed subsequently.

Final preparation of the coupons consisted of bonding 1 x 1 inch grip tabs of 0.125 inch (0.318 cm) thick G11 glass/epoxy to both ends, leaving a 1 x 3 inch (2.54 x 7.62 cm) gage section. The coupons were tested individually by inserting them in self-aligning Templin grips in a BLH SR-4 mechanical-drive testing machine, which was run at a crosshead rate of approximately 0.005 inch/min. (0.0127 cm/min). The tests were conducted at room temperature and humidity, after the specimens had experienced approximately two weeks of shelf storage.

5. EXPERIMENTAL RESULTS

At first it was thought that some sophisticated means of signaling the onset of delamination might be needed to permit accurate measurement of the delamination load. However, experimentation with one test coupon demonstrated that delamination of the entire edge could be clearly observed visually, and that the entire event corresponded to about a 50-lb. (222 N) increment on the load-indicator dial of the testing machine.

Since the total loads at delamination were in the range of 1,000 to 2,000 lb. (4,448 to 8,896 N), all subsequent test measurements were made simply by observing both specimen edges visually and recording the measured load when a delamination appeared. The results, summarized in Table A-2, suggest distinct behavior for the two stacking sequences. This point is elaborated upon in Section A.7.

TABLE A-2

SUMMARY OF LOADS* MEASURED AT ONSET OF DELAMINATION

Statistic	$[(\pm 26°)_2/90°]_S$ Eleven Specimens	$[+26°/-26°_2/+26°/90°]_S$ Eleven Specimens
Smallest Observed Value	1,450	1,800
Largest Observed Value	1,825	2,175
Mean	1,583	1,979
Standard Deviation	121	109

*Measurements given in units of lb_f (1 lb_f = 4.448 N).

To obtain an additional assessment of specimen quality, five specimens from each stacking sequence were loaded to complete failure immediately after the delamination load was measured. The results of these measurements are summarized in Table A-3, and are compared with a simple strength prediction in Section A.6.

TABLE A-3

SUMMARY OF MEASURED ULTIMATE LOADS*

Statistic	$[(\pm 26°)_2/90°]_S$ Five Specimens	$[+26°/-26°_2/+26°/90°]_S$ Five Specimens
Smallest Observed Value	3,500	3,250
Largest Observed Value	4,180	4,110
Mean	3,916	3,832
Standard Deviation	256	392

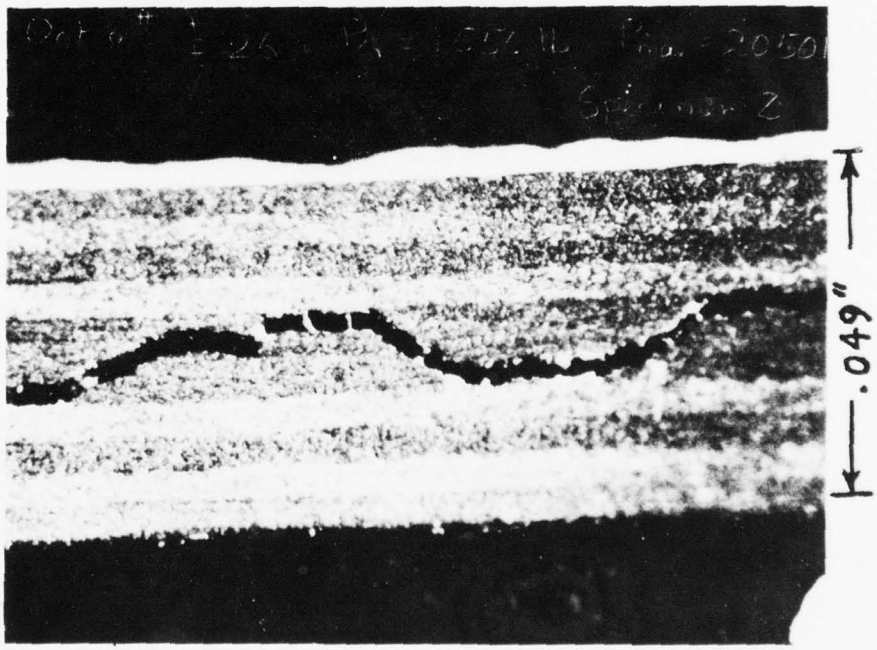
*Measurements given in units of lb_f (1 lb_f = 4.448 N)

Visual and auditory observations during the tests tended to support the idea of initial failure due to delamination, followed by resin failure in the 90° plies and fiber-dominated failure in those coupons which were taken to ultimate load. Little or no acoustic activity was observed prior to delamination, there being at most a few clicks at loads a few hundred pounds below the delamination load.

The ease with which the delamination could be observed has already been noted. Subsequent examination under a 30X optical microscope of those specimens which had been unloaded immediately after delamination showed that most of the delamination tends to occur at the interface between a 90° ply and the adjacent angle ply, rather than at the

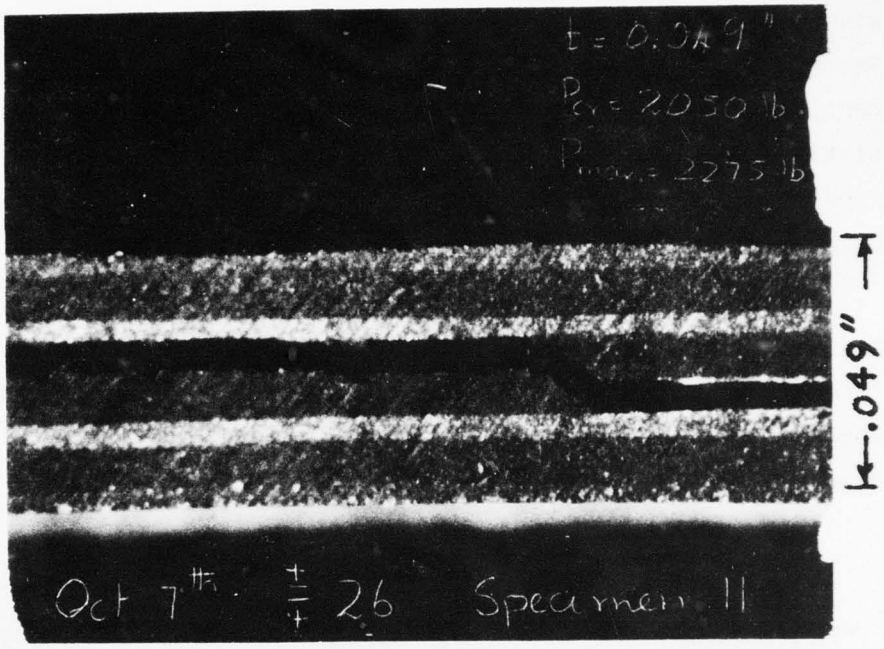
midplane interface. This observation appeared to be independent of stacking sequence. Typical delaminations in both layups are illustrated in Figure A-9, in which the 26°/90° and +26°/-26° interfaces can readily be identified by the different reflection properties of the various ply orientations under the side-lighting used. Similar results were apparently obtained recently by Rybicki, et al. [46] in experiments with $[(\pm 30)_2/90_2]_S$ boron/epoxy laminates.

For those specimens which were continued to ultimate load, increased acoustic activity was noted as final failure was approached. The final failures tended to be straight across (parallel to the y axis) at about mid-gage-section, with occasional evidence of local pullout near the edges. A typical example is shown in Figure A-10.



(A) Stacking sequence of $[(\pm 26)_2/90]_S$

Figure A-9. Edge Views of Typical Delaminations



(B) Stacking sequence of $[+26/-26_2/+26/90]_S$

Figure A-9. (concluded)

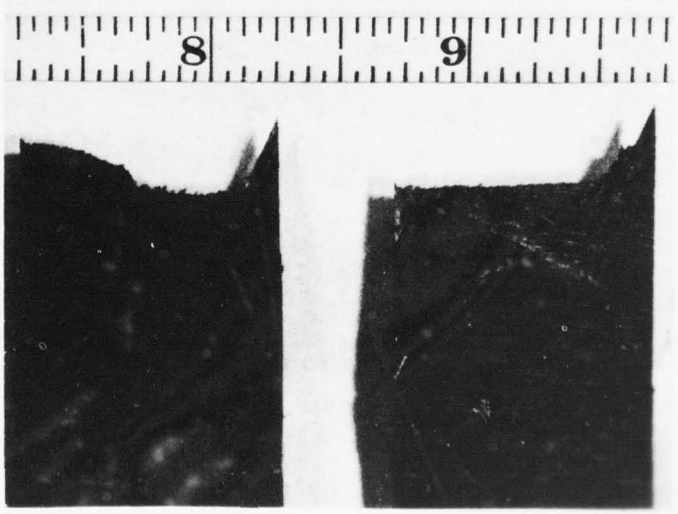


Figure A-10. Typical Fiber Failure at Ultimate Load

6. FINAL ASSESSMENT OF SPECIMEN QUALITY

A second assessment of specimen quality was made by comparing the measured ultimate loads with a nominal load predicted from the strength theory proposed by Hoffman [29]:

$$\frac{\sigma_1^2 - \sigma_1\sigma_2}{F_{C1}F_{T1}} + \frac{\sigma_2^2}{F_{C2}F_{T2}} + \frac{F_{C1} - F_{T1}}{F_{C1}F_{T1}}\sigma_1 + \frac{F_{C2} - F_{T2}}{F_{C2}F_{T2}}\sigma_2 + \frac{\tau_{12}^2}{F_{S12}^2} = 1 \qquad \text{A-5}$$

where axes 1, 2 are in a plane parallel to the xy plane, with axis 1 parallel to and axis 2 perpendicular to the fibers, and where the quantities denoted by F represent the tensile, compressive and shear strengths of a ply. The appropriate values for AS/3501-6 are [41,42]:

$F_{C1} = F_{T1}$ = 280 ksi (1,930 MPa)

F_{C2} = 25 ksi (172 MPa)

F_{T2} = 8.5 ksi (58.5 MPa)

F_{S12} = 20.2 ksi (139 MPa)

Equation A-5 was applied in the present case by neglecting the 90° plies, which were assumed to have failed by resin cracking and to have unloaded prior to ultimate load. Stress components σ_1, σ_2, σ_{12} for a typical angle ply were then obtained by assuming compatibility between angle plies to still be in effect, and by using lamination theory and the conditions:

$$\sigma_x \neq 0 \qquad \sigma_y = 0 \qquad \varepsilon_{xy} = 0 \qquad \text{A-6}$$

The last of Eq. A-6 was used to determine the in-plane shear stress, τ_{xy}, for the typical ply. Substitution of these results (after applying a Mohr circle transformation) into Eq. A-5 then leads to a solution for the predicted axial stress, σ_x, and the predicted failure load is obtained by multiplying this value by the nominal cross section area of the eight $\pm$26° plies. The result of these calculations was 5,016 lb. (22.3 kN). Comparison with Table A-3 shows that the measured mean ultimate loads are about 23 percent below the predicted load. This is considered to be a confirmation of specimen quality, in view of the fact that the test specimens were fully delaminated (and hence both damaged and unbalanced) prior to final failure, while the theoretical prediction assumes a balanced, undamaged specimen.

7. STATISTICAL ANALYSIS OF DELAMINATION FAILURES

Although the visual observations tend to support the hypothesis that failure in both layups is initiated by delamination, the tendency of the delamination to jog through the 90° plies (Figure A-9), suggests that first-ply failure might be the actual initiator. Therefore, strains at delamination were calculated for comparison with the AS/3501-6 first-ply failure strain, the latter property being taken as 0.63×10^{-2} [42]. The "observed" strains were calculated from the measured delamination loads (Table A-2), average measured laminate thickness and the following plane stress stiffness coefficients obtained by applying lamination theory to the material properties previously given for AS/3501-6:

$$Q_{xx} = 11.74 \times 10^6 \text{ psi } (81.0 \text{ GPa})$$

$$Q_{yy} = 6.00 \times 10^6 \text{ psi } (41.3 \text{ GPa})$$

$$G_{xy} = 2.74 \times 10^6 \text{ psi } (18.9 \text{ GPa})$$

The results, summarized in Table A-4, suggest that delaminations actually did occur prior to first-ply failure.

TABLE A-4

SUMMARY OF CALCULATED STRAIN (ε_x)
AT DELAMINATION

Statistic	$[(\pm 26°)_2/90°]_S$ Eleven Specimens	$[+26°/-26°_2/+26°/90°]_S$ Eleven Specimens
Mean	0.304×10^{-2}	0.388×10^{-2}
Standard Deviation	0.0232×10^{-2}	0.0214×10^{-2}

Some approximate physical arguments were made previously to explain why the delamination load for the $[+26°/-26°_2/+26°/90°]_S$ laminate might be higher or lower than for the $[(\pm 26°)_2/90°]_S$ laminate. In fact, the former layup appears to have a consistently higher delamination load than the latter (Table A-2), but it remains to be seen whether this observation has a physical basis or is merely a fortuitous result of expected random fluctuations of the observations.

Statistical decision theory can be brought to bear upon this question by recognizing that the observed mean and standard deviation can be combined to form a t-variate. Specifically, a one-sided tolerance interval of the form [48]

$$\Pr\left[\mu_p < \bar{P} - \frac{s_p t_{N-1;\alpha}}{\sqrt{N}}\right] = \alpha \qquad \text{A-7}$$

can be placed on the location of the underlying mean delamination load, μ_p, in terms of one set of N samples giving rise to observed values $\bar{P}$ and

s_P for the mean and standard deviation, respectively, where $t_{N-1;\alpha}$ is the α percentile of Student's t-distribution with N-1 degrees of freedom. For example, choosing $\alpha = 0.01$ and with N = 11 in the present case, $t_{10;0.01} = 2.764$ is obtained from standard distribution tables. Substituting this value, together with $\bar{P}$ = 1,979 lb. and s_P = 109 lb. from Table A-2 then places the following tolerance on the underlying mean delamination load for $[+26°/-26°_2/+26°/90°]_S$ laminates:

$$\Pr [\mu_P < 1{,}888 \text{ lb.}] = 0.01 \qquad \text{A-8}$$

In the light of Eq. A-8 and the physical arguments previously given, the observation $\bar{P}$ = 1,583 lb. for $[(\pm 26°)_2/90°]_S$ laminates may be interpreted as 99-percent confident support for the hypothesis of some difference in the failure modes, such as the postulated difference between the anticlastic σ_z peaks in the two layups.

It is also interesting to assess the accuracy of the approximate stress distribution models (Figure A-4, Parts B and C) as estimators of the interlaminar tensile strength property. For example, since observed data are available for delamination strain, ε_x, an assessment can be made by predicting ε_x from Eq. A-1 based on the assumption that $\sigma_z^{max} = F_{T2}$ at failure initiation. Acceptable accuracy would be demonstrated if the predictions of both models were consistently biased with respect to the observations. Unfortunately, the results indicate that predictions are extremely sensitive to the details of models of the type shown in Figure A-4. The observed strains of 0.304×10^{-2} and 0.388×10^{-2} (Table A-4) are bracketed by the predictions 0.285×10^{-2} for the distribution shown in Figure A-4 (Part B) and 0.485×10^{-2} for the distribution shown in Figure A-4 (Part C). Furthermore, it is apparent that both predictions lie well outside the 99-percent confidence intervals which can be established for either layup.

8. DISCUSSION AND CONCLUSIONS

The stacking sequence $[(\pm\Theta)_2/90°]_S$ has a lower delamination load than the sequence $[+\Theta/-\Theta_2/+\Theta/90°]_S$. It appears that this effect occurs because the latter configuration is less subject to anticlastic corner peaks in the distribution of interlaminar tension. It then follows that the $[+\Theta/-\Theta_2/+\Theta/90°]_S$ stacking sequence is more desirable for investigating delamination phenomena.

However, it is apparent that the currently accepted procedure for designing a delamination coupon, in terms of ply angle and relative number of 90° and angle plies, results in delamination at the 90°/angle interface instead of the desired 90°/90° midplane interface. Furthermore, the failure appears to be caused by combined interlaminar tension and interlaminar shear, rather than by interlaminar tension alone. The combined-stress failure mode is not desirable for determining material properties.

Finally, it is apparent that the current approximate models for the distribution of interlaminar tension across the specimen width (Figure A-4, Parts B and C) are inadequate for the purpose of determining interlaminar tensile strength with acceptable confidence, even if a delamination coupon could be designed to fail in a nearly pure interlaminar tension mode. Therefore, it will be worthwhile to pursue a more accurate formulation for the interlaminar stress fields in angle-ply delamination coupons, similar to the elasticity solutions for $[0/90]_S$ and $[90/0]_S$ laminates.

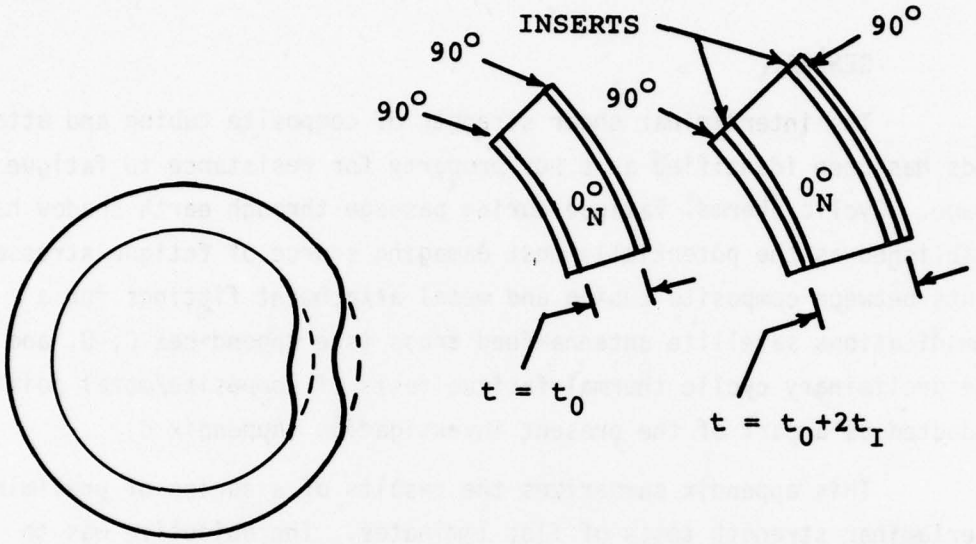
APPENDIX B

TREND TESTS FOR INTERLAMINAR SHEAR STRENGTH

1. GENERAL

The interlaminar shear strength of composite tubing and attachment bonds has been identified as a key property for resistance to fatigue damage. Cyclic thermal fatigue during passage through earth shadow has been established as the potentially most damaging source of fatigue stresses at joints between composite tubing and metal attachment fittings for a communications satellite antenna-feed truss (see Appendices C, D, and H). Some preliminary cyclic thermal fatigue tests of composite/metal joints were conducted as a part of the present investigation (Appendix C).

This appendix summarizes the results of a series of preliminary interlaminar strength tests of flat laminates. The objective was to establish strength trends as a function of soft-insert thickness, test temperature, and cyclic thermal fatigue. The rationale for inserting soft layers of material between graphite/epoxy plies in a composite tube is to increase the resistance of the tube to local crippling due to compression and/or torsion. In a $[90°/0°_N/90°]$ tube, the local crippling strength is determined primarily by the separation between the 90° plies. As shown schematically in Figure B-1, increasing the separation by inserting soft layers should increase the crippling strength by effectively increasing the circumferential bending rigidity of the wall. However, if inserts are to be considered as a design option, their effects on interlaminar shear strength must be assessed to determine the potential penalty to fatigue resistance.



(A) TYPICAL CRIPPLING FAILURE BY LOCAL CIRCUMFERENTIAL BENDING

(B) CIRCUMFERENTIAL BENDING RIGIDITY IS PROPORTIONAL TO t^2

Figure B-1. Local Crippling Failure

2. TEST SPECIMEN FABRICATION

Laminates of Hercules AS/3501-6 graphite/epoxy with and without inserts were fabricated by hand layup on 0.5-inch thick aluminum tooling plates, following procedures recommended by the material supplier for damming, bagging, and curing cycle [42]. Mylar and extra resin were considered as insert candidates after initial screening of several materials. The latter option was discarded after preliminary experiments indicated that insert thickness would be difficult to control because of resin bleeding during cure.

The insert choices finally adopted were a smooth-surface, 0.001-inch thick Mylar (M1) and a rough-surface, 0.003-inch thick Mylar (M3). In both cases, the insert material was perforated with a hand tool (Figure B-2) to permit proper resin bleeding from the interior graphite/epoxy plies. Laminates of $[0°_{26}]$, $[0°_{12}/M1/0°/M1/0°/M1/0°_{12}]$ and $[0°_{12}/M3/0°/M3/0°/M3/0°_{12}]$ construction were fabricated as 5 x 17-inch plates, from which approximately 0.5 inch of material along each edge was discarded to avoid areas of excess resin buildup near the tooling dams.

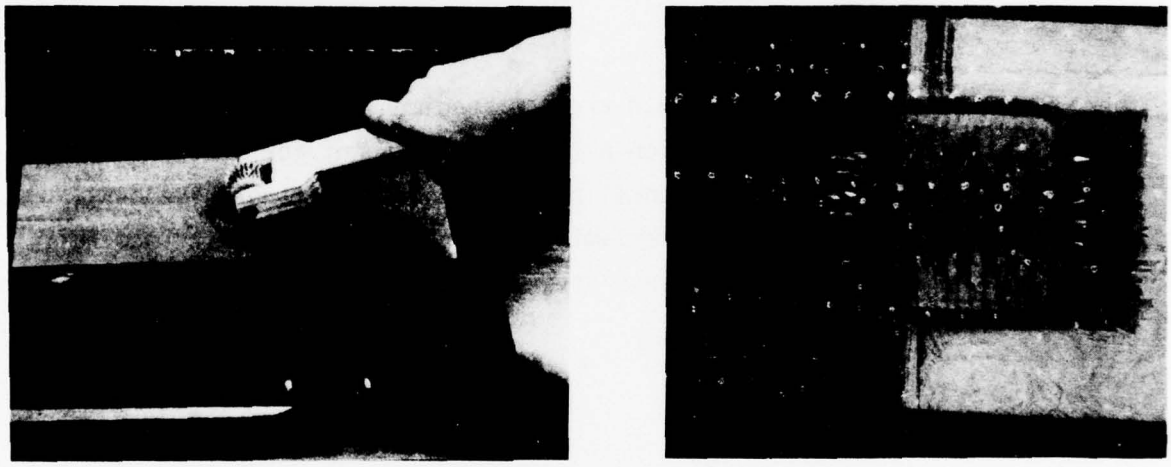


Figure B-2. Hand Tool used to Perforate Mylar Inserts

Test specimens approximately 0.8 inch long and of varying widths were cut from the laminates using a Neuber type 1A1R (C = 50) resinoid-bond diamond wheel at approximately 2,000 RPM, together with a water spray. Most of the specimens with M3 inserts were observed to have debonded at the insert after cutting. Hence, the strength test program was restricted to the $[0°_{26}]$ nominal specimens and the specimens with M1 inserts. (Since no initial debonding was observed in the latter two laminates, the M3 insert debonds were attributed to an undetermined fault in either the layup procedure or the curing cycle.)

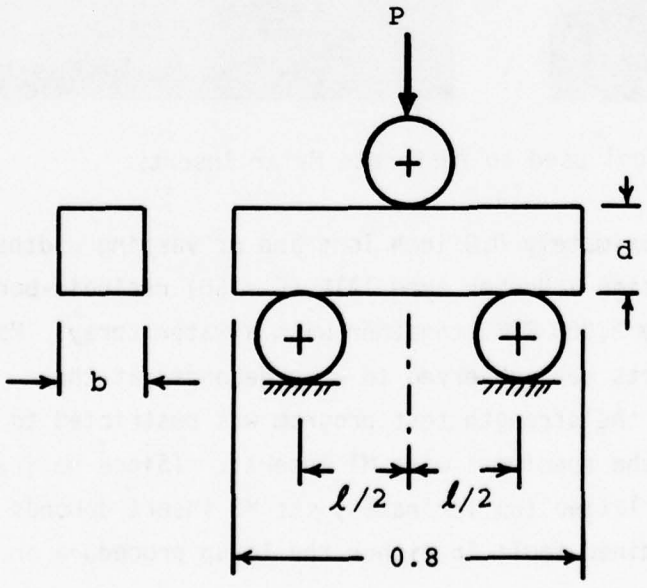
3. EXPERIMENTAL PROCEDURE AND TEST MATRIX

Interlaminar shear strength data were obtained using ASTM procedure D-2344 for short beam shear tests [10]. The short beam shear test specimen rests on two tool-steel dowel pins, and a mid-span load is applied through a third pin (Figure B-3) at a crosshead rate of 0.05 in/min. The dimensions given in the figure refer to actual test conditions.

The interlaminar shear strength of a test specimen is evaluated from:

$$s = \frac{0.75P}{bd} \qquad \text{B-1}$$

where P is the failure load and b,d are the specimen width and thickness, as defined in Figure B-3. Equation B-1 does not account for stress concentration effects near the dowel pins, and hence does not give an accurate estimate of the true interlaminar strength. However, the nominal strength value can be used to assess strength trends for test specimens of similar construction.



DIM	MIN	MAX
b	0.107	0.201
d	0.117	0.136

$\ell = 0.5$

ALL DIMENSIONS IN UNITS OF INCHES

Figure B-3. Short-Beam Shear Test

Static strength tests were conducted at room temperature, 75°F (20°C), liquid nitrogen temperature, -321°F (-196°C), and boiling water temperature, 212°F (100°C). The latter two conditions were obtained by immersing the test fixture and specimen in LN_2 or boiling water and soaking for a few minutes to reach thermal equilibrium. In addition, some specimens were subjected to cyclic thermal fatigue between LN_2 temperature and 212±10°F, and then subjected to residual static strength tests at room temperature. The low-temperature soak was performed by immersion in LN_2. The high-temperature soak was performed either by immersion in boiling water, or by infrared (IR) radiative heating of the specimens to 212±10°F, using the automated apparatus described in Appendix C. The liquid soak time was established at approximately 40 sec by immersing a bag of test specimens in LN_2 and noting the time required for rapid boiling to cease. The IR radiation soak time was established by monitoring an iron-constantan thermocouple placed in the test specimen bag, with the bag positioned mechanically in the IR chamber. Table B-1 summarizes the test matrix.

TABLE B-1

TEST MATRIX

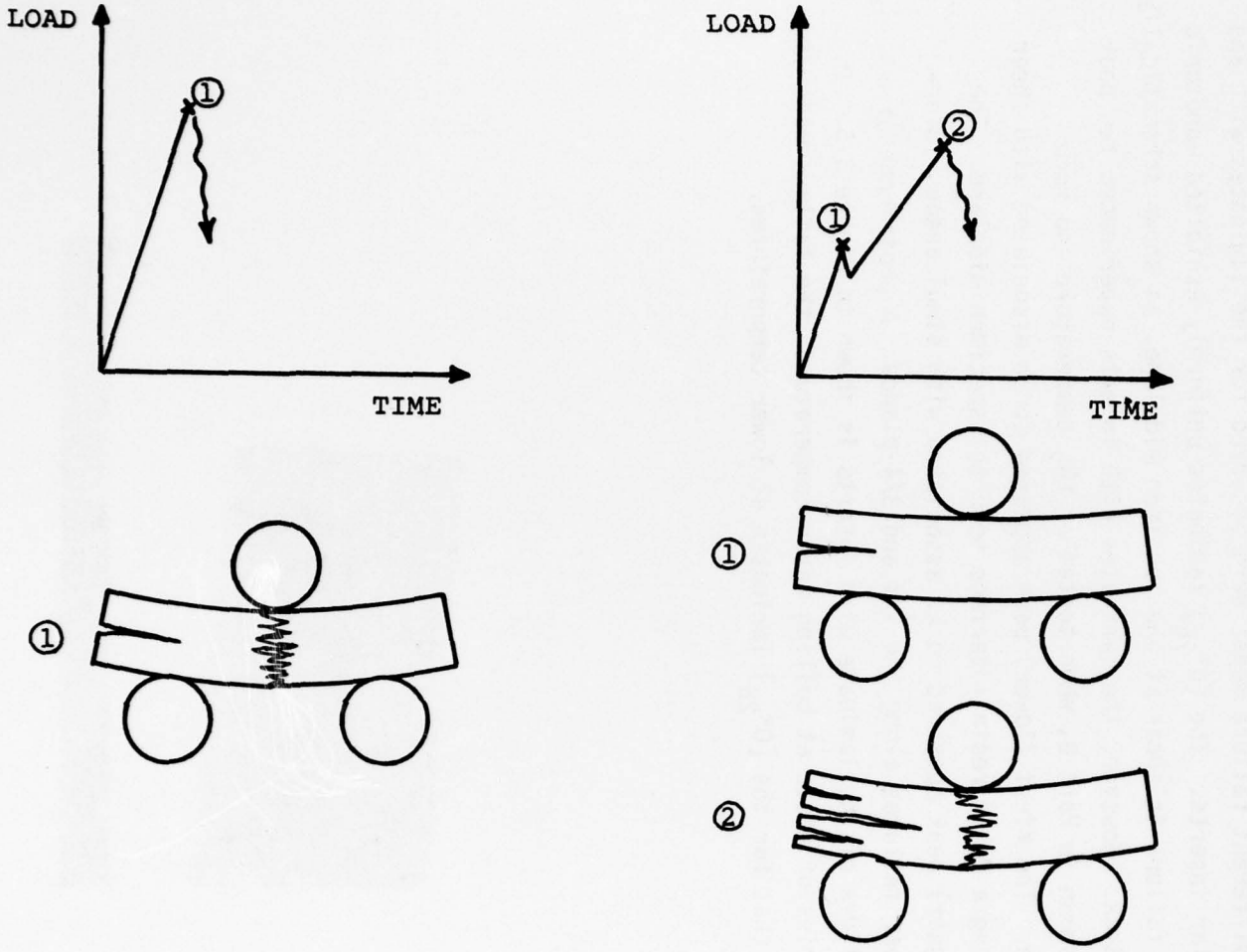
Test Conditions \ Stacking Sequence	Number of Specimens Tested	
	$[0°_{26}]$	$[0°_{12}/M1/0°/M1/0°/M1/0°_{12}]$
Static at -321°F	10	10
75°F	10	9
212°F	--	8
Residual static at 75°F after number of cycles between -321°F and 212±10°F indicated:		
10	7	10
50	6	10
100	9	10
500	4	10
1000	7	10

4. EXPERIMENTAL RESULTS FOR STATIC STRENGTH

Different failure modes were observed for the laminates with and without Mylar inserts. The $[0°_{26}]$ laminates uniformly exhibited monotonic loading to failure in shear at the specimen midplane, as shown schematically in Figure B-4A. However, the laminates with inserts experienced two peak loads, as shown in Part B, when tested at LN_2 temperature and room temperature. The first (lower) peak appeared to be associated with shear failure along a Mylar/resin interface near the specimen midplane. The second (higher) peak appeared to be associated with simultaneous interlaminar shear failures along the 1/4 and 3/4-planes. A photograph of a typical failure of the laminate with inserts is shown in Figure B-5. In a third series of tests at boiling water temperature, the failure mode was similar to that for the $[0°_{26}]$ laminates at lower temperatures.



Figure B-5. Typical $[0°_{12}/M1/0°/M1/0°/M1/0°_{12}]$ Laminate Failure



(A) $[0°_{26}]$ Laminate

(B) $[0°_{12}/M1/0°/M1/0°/M1/0°_{12}]$ Laminate

Figure B-4. Schematic Illustrations of Failure Modes

The mean static strength estimates are compared in Figure B-6. For each test condition, 95-percent confidence limits on the mean shear strength were obtained by treating $(\bar{s} - \hat{\sigma}_s)/\hat{\sigma}_s$ as a t-variate [48]:

$$\bar{s} - \frac{\hat{\sigma}_s t_{N-1;\,0.025}}{\sqrt{N}} \leq \mu_s \leq \bar{s} + \frac{\hat{\sigma}_s t_{N-1;\,0.025}}{\sqrt{N}} \; ; \; C = 0.95 \qquad \text{B-2}$$

where $\bar{s}$, $\hat{\sigma}_s$, are the observed mean and standard deviation; μ_s is the underlying mean; and N is the sample size. It is apparent from these results that the presence of a Mylar spacing layer in the laminate degrades the initial interlaminar shear strength by more than 50 percent at LN_2 temperature, and by about 40 percent at room temperature.

Although not of interest as design allowables, the second-peak shear strength values have been computed in accordance with Eq. B-1. The rationale for using Eq. B-1 in this case is to treat the specimen as two separate beams resting one upon the other, after initial failure at the midplane. Hence, each beam is assumed to have a depth d/2 and to bear a load P/2 at the second peak. Details of the experimental data are presented in Tables B-2 through B-6.

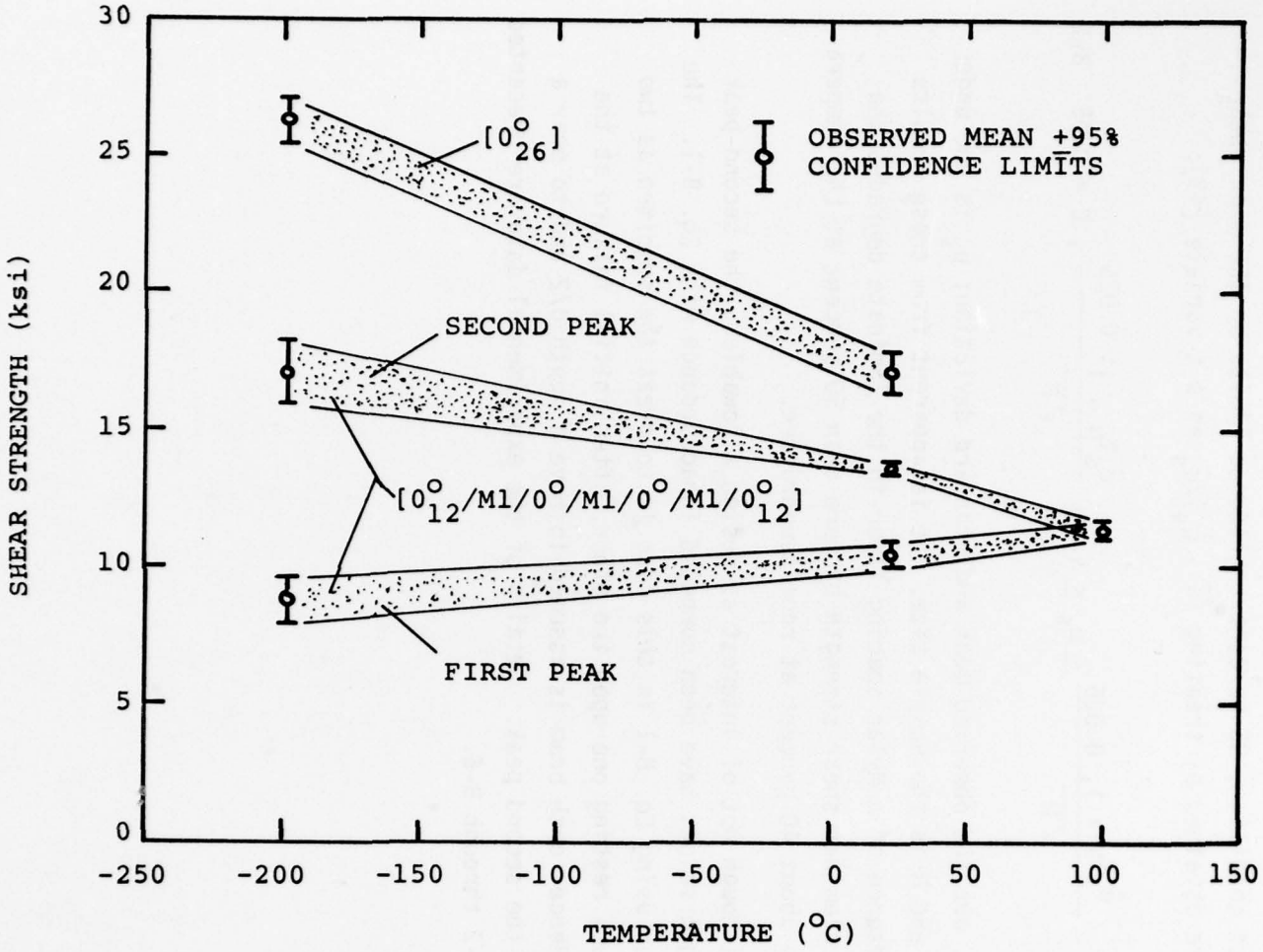


Figure B-6. Comparison of Mean Static Strength Estimates

TABLE B-2

SHORT BEAM SHEAR TEST DATA FOR $[0°_{26}]$ LAMINATE

TEST CONDITIONS: Virgin static strength at -321°F				
Specimen Number	Width, b (in)	Depth, d (in)	Failure Load, P (lb)	Computed Shear Stress, s (ksi)
1	0.1820	0.1320	858	26.8
2	0.1890	0.1230	821	26.5
3	0.1750	0.1240	776	26.8
4	0.1660	0.1280	690	24.4
5	0.1700	0.1310	740	24.9
6	0.1740	0.1270	761	25.8
7	0.1850	0.1320	896	27.5
8	0.1630	0.1300	712	25.2
9	0.1680	0.1250	788	28.1
10	0.1680	0.1320	788	26.6
Observed Mean				26.3
Observed Standard Deviation				1.18
95% Confidence Limits on Mean				0.85

TABLE B-3

SHORT BEAM SHEAR TEST DATA FOR $[0°_{26}]$ LAMINATE

TEST CONDITIONS: Virgin static strength at 75°F				
Specimen Number	Width, b (in)	Depth, d (in)	Failure Load, P (lb)	Computed Shear Stress, s (ksi)
1	0.1770	0.1310	576	18.6
2	0.1790	0.1300	550	17.7
3	0.1740	0.1300	519	17.2
4	0.1890	0.1310	559	16.9
5	0.1710	0.1290	484	16.5
6	0.1720	0.1290	476	16.1
7	0.1660	0.1300	452	15.7
8	0.1770	0.1310	494	16.0
9	0.1810	0.1290	540	17.4
10	0.1820	0.1300	590	18.7
Observed Mean				17.1
Observed Standard Deviation				1.06
95% Confidence Limits on Mean				0.76

TABLE B-4

SHORT BEAM SHEAR TEST DATA FOR
$[0°_{12}/M1/0°/M1/0°/M1/0°_{12}]$ LAMINATE

TEST CONDITIONS: Virgin static strength at -321°F						
			First Peak		Second Peak	
Specimen Number	Width, b (in)	Depth, d (in)	Failure Load, P (lb)	Computed Shear Stress, s (ksi)	Failure Load, P (lb)	Computed Shear Stress, s (ksi)
1	0.1470	0.1280	180	7.2	470	18.7
2	0.1630	0.1340	328	11.3	540	18.5
3	0.1500	0.1290	182	7.1	405	15.7
4	0.1560	0.1340	261	9.4	426	15.3
5	0.1530	0.1340	241	8.8	534	19.5
6	0.1690	0.1350	258	8.5	574	18.9
7	0.1580	0.1340	212	7.5	508	18.0
8	0.1570	0.1330	248	8.9	391	14.0
9	0.1520	0.1280	224	8.6	395	15.2
10	0.1630	0.1360	310	10.5	500	16.9
Observed Mean				8.8		17.1
Observed Standard Deviation				1.20		1.60
95% Confidence Limits on Mean				0.86		1.15

TABLE B-5

SHORT BEAM SHEAR TEST DATA FOR
$[0°_{12}/M1/0°/M1/0°/M1/0°_{12}]$ LAMINATE

TEST CONDITIONS: Virgin static strength at 75°F						
			First Peak		Second Peak	
Specimen Number	Width, b (in)	Depth, d (in)	Failure Load, P (lb)	Computed Shear Stress, s (ksi)	Failure Load, P (lb)	Computed Shear Stress, s (ksi)
1	0.1475	0.1340	280	10.6	410	15.5
2	0.1475	0.1325	250	9.6	365	14.0
3	0.1400	0.1330	282	11.4	330	13.3
4	0.1760	0.1325	302	9.7	435	14.0
5	0.1850	0.1330	346	10.6	425	13.0
6	0.1490	0.1340	290	10.9	325	12.2
7	0.1540	0.1340	292	10.6	395	14.4
8	0.1720	0.1315	300	10.0	367	12.2
9	0.2010	0.1340	407	11.3	484	13.5
Observed Mean				10.5		13.6
Observed Standard Deviation				0.65		0.31
95% Confidence Limits on Mean				0.50		0.24

TABLE B-6

SHORT BEAM SHEAR TEST DATA FOR
$[0°_{12}/M1/0°/M1/0°/M1/0°_{12}]$ LAMINATE

TEST CONDITIONS: Virgin static strength at 212°F (immersed in boiling water)						
			First Peak		Second Peak	
Specimen Number	Width, b (in)	Depth, d (in)	Failure Load, P (lb)	Computed Shear Stress, s (ksi)	Failure Load, P (lb)	Computed Shear Stress, s (ksi)
1	0.1565	0.1350	327	11.6	SECOND PEAK NOT OBSERVED	
2	0.1550	0.1300	302	11.2		
3	0.1680	0.1340	344	11.5		
4	0.1670	0.1350	345	11.5		
5	0.1610	0.1355	309	10.6		
6	0.1460	0.1340	312	12.0		
7	0.1605	0.1350	325	11.3		
8	0.1630	0.1305	322	11.4		
Observed Mean				11.4		
Observed Standard Deviation				0.40		
95% Confidence Limits on Mean				0.35		

5. EXPERIMENTAL RESULTS FOR STRENGTH DEGRADATION

Details of the experimental results for residual strength after thermal cycling are presented in Tables B-7 through B-16. Equation B-2 has been used again to establish 95-percent confidence limits on the mean shear strength for each test condition.

The mean residual strength estimates are plotted in Figure B-7, to which the static strengths have been added for comparison. Statistically acceptable interpretations of these data are that the $[0°_{26}]$ laminate appears to experience no strength degradation after 1,000 thermal cycles (to 95-percent confidence), but that the Mylar/resin interface shear strength in the $[0°_{12}/M1/0°/M1/0°/M1/0°_{12}]$ laminate does appear to degrade slowly. However, no clear interpretation of the second-peak strength behavior in the latter laminate can be made from the data in the figure.

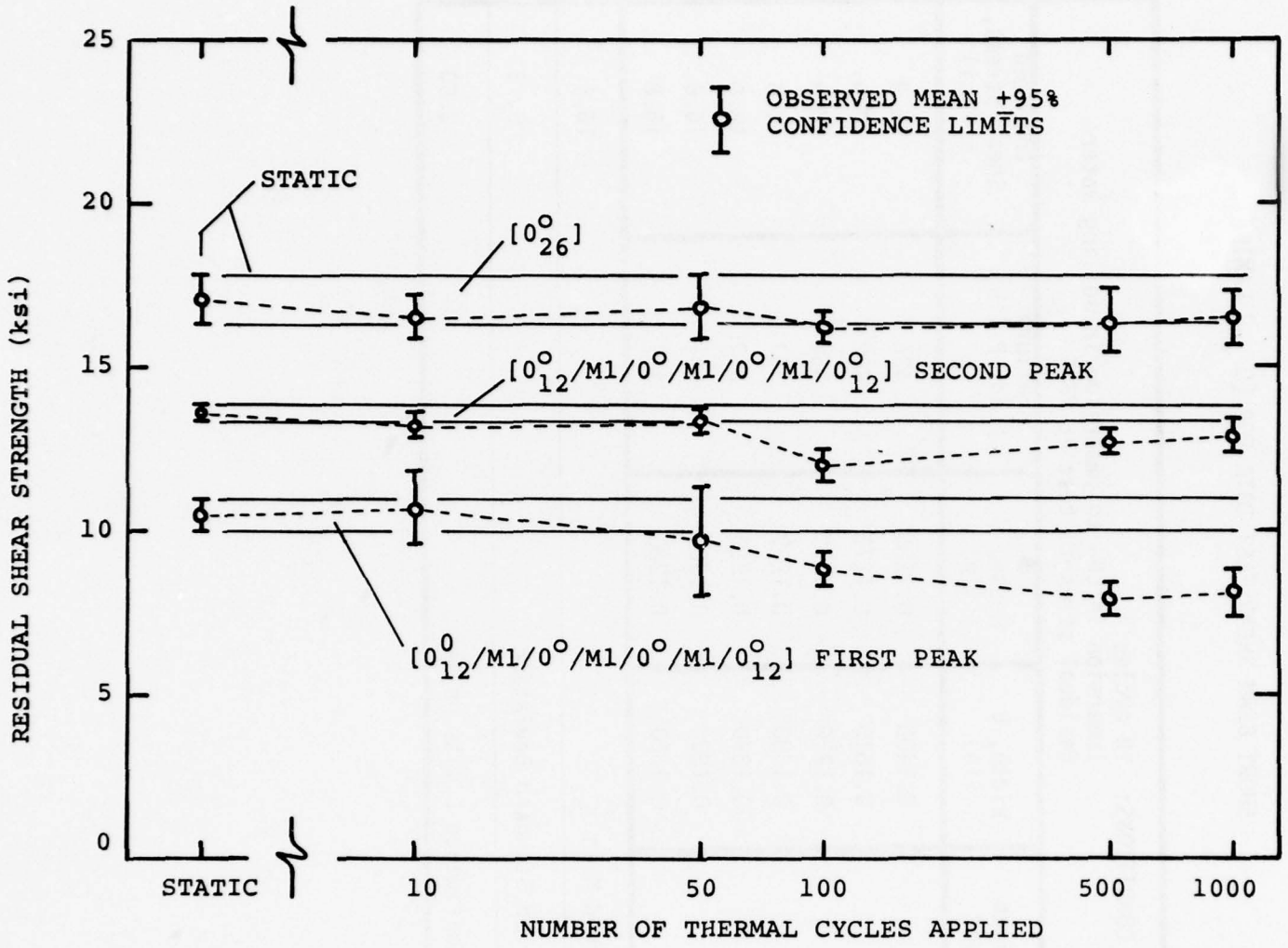


Figure B-7. Plot of Mean Residual Strength Estimates

TABLE B-7

SHORT BEAM SHEAR TEST DATA FOR $[0^{\circ}_{26}]$ LAMINATE

TEST CONDITIONS: 10 cycles Immersion in LN_2 to immersion in boiling water Residual strength test at 75°F				
Specimen Number	Width, b (in)	Depth, d (in)	Failure Load, P (lb)	Computed Shear Stress, s (ksi)
1	0.1405	0.1285	406	16.9
2	0.1615	0.1275	492	17.9
3	0.1270	0.1275	352	16.3
4	0.1380	0.1290	380	16.0
5	0.1390	0.1285	380	16.0
6	0.1800	0.1305	521	16.6
7	0.1260	0.1280	339	15.8
Observed Mean				16.5
Observed Standard Deviation				0.73
95% Confidence Limits on Mean				0.68

TABLE B-8

SHORT BEAM SHEAR TEST DATA FOR $[0°_{26}]$ LAMINATE

TEST CONDITIONS: 50 cycles Immersion in LN_2 to immersion in boiling water Residual strength test at 75°F				
Specimen Number	Width, b (in)	Depth, d (in)	Failure Load, P (lb)	Computed Shear Stress, s (ksi)
1	0.1250	0.1280	375	17.6
2	0.1410	0.1280	378	15.7
3	0.1370	0.1280	408	17.5
4	0.1420	0.1290	382	15.6
5	0.1275	0.1260	357	16.7
6	0.1295	0.1275	387	17.6
Observed Mean				16.8
Observed Standard Deviation				0.94
95% Confidence Limits on Mean				0.99

TABLE B-9

SHORT BEAM SHEAR TEST DATA FOR $[0^\circ_{26}]$ LAMINATE

TEST CONDITIONS:	100 cycles Immersions in LN_2 to IR Heating (212 $\pm$10°F) Residual Strength Test at 75°F			
Specimen Number	Width b (in)	Depth d (in)	Failure Load P (lb)	Computed Shear Stress s (ksi)
1	0.1275	0.1290	366	16.7
2	0.1420	0.1295	384	15.7
3	0.1645	0.1285	493	17.5
4	0.1350	0.1205	361	16.6
5	0.1375	0.1235	357	15.8
6	0.1345	0.1260	346	15.3
7	0.1285	0.1205	340	16.5
8	0.1310	0.1270	359	16.2
9	0.1310	0.1290	349	15.5
Observed Mean				16.2
Observed Standard Deviation				0.70
95% Confidence Limits on Mean				0.54

TABLE B-10

SHORT BEAM SHEAR TEST DATA FOR $[0°_{26}]$ LAMINATE

TEST CONDITIONS: 500 cycles Immersion in LN_2 to IR heating (212±10°F) Residual strength test at 75°F				
Specimen Number	Width, b (in)	Depth, d (in)	Failure Load, P (lb)	Computed Shear Stress, s (ksi)
1	0.1360	0.1295	391	16.7
2	0.1340	0.1220	363	16.7
3	0.1410	0.1240	391	16.8
4	0.1360	0.1175	330	15.5
Observed Mean				16.4
Observed Standard Deviation				0.62
95% Confidence Limits on Mean				0.98

TABLE B-11

SHORT BEAM SHEAR TEST DATA FOR $[0°_{26}]$ LAMINATE

TEST CONDITIONS: 1,000 cycles Immersion in LN_2 to IR heating (212±10°F) Residual strength test at 75°F				
Specimen Number	Width, b (in)	Depth, d (in)	Failure Load, P (lb)	Computed Shear Stress, s (ksi)
1	0.1695	0.1295	466	15.9
2	0.1875	0.1300	481	14.8
3	0.1365	0.1290	400	17.0
4	0.1840	0.1300	557	17.5
5	0.1635	0.1310	469	16.4
6	0.1335	0.1275	376	16.6
7	0.1345	0.1285	402	17.5
Observed Mean				16.5
Observed Standard Deviation				0.96
95% Confidence Limits on Mean				0.89

TABLE B-12

SHORT BEAM SHEAR TEST DATA FOR
$[0°_{12}/M1/0°/M1/0°/M1/0°_{12}]$ LAMINATE

TEST CONDITIONS: 10 cycles Immersion in LN_2 to immersion in boiling water Residual static strength test at 75°F						
			First Peak		Second Peak	
Specimen Number	Width, b (in)	Depth, d (in)	Failure Load, P (lb)	Computed Shear Stress, s (ksi)	Failure Load, P (lb)	Computed Shear Stress, s (ksi)
1	0.1520	0.1310	341	12.8	355	13.4
2	0.1490	0.1300	289	11.2	350	13.6
3	0.1335	0.1330	259	10.9	302	12.8
4	0.1320	0.1320	216	9.3	291	12.5
5	0.1335	0.1330	283	12.0	297	12.6
6	0.1310	0.1335	185	7.9	324	13.9
7	0.1540	0.1340	285	10.4	365	13.3
8	0.1700	0.1350	269	8.8	390	12.8
9	0.1255	0.1340	271	12.1	313	14.0
10	0.1320	0.1350	283	11.9	313	13.2
Observed Mean				10.7		13.2
Observed Standard Deviation				1.61		0.53
95% Confidence Limits on Mean				1.15		0.38

TABLE B-13

SHORT BEAM SHEAR TEST DATA FOR

$[0°_{12}/M1/0°/M1/0°/M1/0°_{12}]$ LAMINATE

TEST CONDITIONS: 50 cycles Immersion in LN_2 to immersion in boiling water Residual static strength test at 75°F						
			First Peak		Second Peak	
Specimen Number	Width, b (in)	Depth, d (in)	Failure Load, P (lb)	Computed Shear Stress, s (ksi)	Failure Load, P (lb)	Computed Shear Stress, s (ksi)
1	0.1285	0.1285	204	9.3	294	13.4
2	0.1320	0.1325			339	14.5
3	0.1300	0.1290	240	10.7	282	12.6
4	0.1310	0.1345	177	7.5	313	13.3
5	0.1285	0.1330			304	13.3
6	0.1305	0.1330			301	13.0
7	0.1570	0.1335	303	10.8	387	13.9
8	0.1580	0.1275	272	10.1	340	12.7
9	0.1520	0.1350			360	13.2
10	0.1315	0.1330			313	13.4
Observed Mean				9.7		13.3
Observed Standard Deviation				1.36		0.55
95% Confidence Limits on Mean				1.69		0.39

TABLE B-14

SHORT BEAM SHEAR TEST DATA FOR $[0^\circ_{12}/M1/0^\circ/M1/0^\circ/M1/0^\circ_{12}]$ LAMINATE

TEST CONDITIONS: 100 cycles
Immersion in LN_2 to IR Heating (212 +10°F)
Residual Static Strength Test at 75°F

Specimen Number	Width b (in)	Depth d (in)	First Peak		Second Peak	
			Failure Load P (lb)	Computed Shear Stress s (ksi)	Failure Load P (lb)	Computed Shear Stress s (ksi)
1	0.1130	0.1325	176	8.8	231	11.6
2	0.1155	0.1340	171	8.3	241	11.7
3	0.1165	0.1325	194	9.4	258	12.5
4	0.1155	0.1335	183	8.9	251	12.2
5	0.1070	0.1320	157	8.3	211	11.2
6	0.1160	0.1325	212	10.3	250	12.2
7	0.1125	0.1325	144	7.3	223	11.2
8	0.1160	0.1325	183	8.9	267	13.0
9	0.1150	0.1310	190	9.5	262	13.0
10	0.1145	0.1320	175	8.7	225	11.2
Observed Mean				8.8		12.0
Observed Standard Deviation				0.80		0.70
95% Confidence Limits on Mean				0.57		0.50

TABLE B-15

SHORT BEAM SHEAR TEST DATA FOR

$[0°_{12}/M1/0°/M1/0°/M1/0°_{12}]$ LAMINATE

TEST CONDITIONS: 500 cycles Immersion in LN_2 to IR heating (212±10°F) Residual static strength test at 75°F						
			First Peak		Second Peak	
Specimen Number	Width, b (in)	Depth, d (in)	Failure Load, P (lb)	Computed Shear Stress, s (ksi)	Failure Load, P (lb)	Computed Shear Stress, s (ksi)
1	0.1340	0.1345	215	9.0	310	12.9
2	0.1345	0.1345	192	8.0	302	12.5
3	0.1330	0.1250	153	6.9	273	12.3
4	0.1315	0.1350	185	7.8	297	12.5
5	0.1355	0.1325	188	7.9	317	13.2
6	0.1315	0.1340	173	7.4	296	12.6
7	0.1335	0.1345	167	7.0	283	11.8
8	0.1625	0.1345	237	8.1	392	13.5
9	0.1295	0.1330	204	8.9	294	12.8
10	0.1675	0.1345	237	7.9	400	13.3
Observed Mean				7.9		12.7
Observed Standard Deviation				0.69		0.49
95% Confidence Limits on Mean				0.50		0.35

TABLE B-16

SHORT BEAM SHEAR TEST DATA FOR

$[0°_{12}/M1/0°/M1/0°/M1/0°_{12}]$ LAMINATE

TEST CONDITIONS: 1,000 cycles Immersion in LN_2 to IR heating (212±10°F) Residual static strength test at 75°F						
			First Peak		Second Peak	
Specimen Number	Width, b (in)	Depth, d (in)	Failure Load, P (lb)	Computed Shear Stress, s (ksi)	Failure Load, P (lb)	Computed Shear Stress, s (ksi)
1	0.1345	0.1280	173	7.5	307	13.4
2	0.1320	0.1345	233	9.8	311	13.1
3	0.1170	0.1340	178	8.5	282	13.5
4	0.1320	0.1275	152	6.8	255	11.4
5	0.1300	0.1340	183	7.8	303	13.0
6	0.1645	0.1350	225	7.6	410	13.8
7	0.1325	0.1235	162	7.4	260	11.9
8	0.1310	0.1355	209	8.8	302	12.8
9	0.1300	0.1355	226	9.6	311	13.2
10	0.1320	0.1315	175	7.6	299	12.9
Observed Mean				8.1		12.9
Observed Standard Deviation				0.99		0.69
95% Confidence Limits on Mean				0.71		0.50

6. DISCUSSION AND CONCLUSIONS

With regard to static strength, the temperature dependence of interlaminar shear strength in laminates without inserts follows a trend expected on physical grounds, namely that apparent resin strength at constant strain rate should increase as the environment temperature falls below the glass-transition temperature of the resin. The reverse trend exhibited by Mylar/resin interfaces is a surprising result. Although this trend cannot be explained by the usual physical models for polymers, the data in Figure B-6 do appear to indicate something more than random sampling error.

With regard to cyclic thermal strength degradation, the results obtained for laminates without inserts are encouraging. The absence of any apparent degradation after 1,000 cycles between -321°F (-196°C) and +212°F (+100°C) performed by immersing the bare specimens in liquids indicates that there are no significant thermal shock effects associated with the accelerated test procedure and the thermal conductivity properties of graphite/epoxy, at least up to thicknesses of the order of 0.06 inch from the specimen surfaces to the centerline. The slight degradation observed at the Mylar/resin interface in the laminates with inserts is tentatively attributed to thermal stresses set up at the soak temperatures by different material expansion coefficients.

Finally, comparison of the performances of the $[0°_{12}/M1/0°/M1/0°/M1/0°_{12}]$ and $[0°_{26}]$ laminates indicates that the latter laminate maintains significantly higher interlaminar shear strength both statically and after thermal cycling. Hence, it is doubtful whether any potential improvement of crippling strength which might be obtained by placing Mylar inserts in graphite/epoxy $[90°/0°_N/90°]$ tubes would outweigh the associated fatigue strength penalty.

APPENDIX C

THERMAL FATIGUE TESTS OF JOINT DETAILS

1. GENERAL

Vibratory launch loads and thermal cycles in orbit are two possible sources of fatigue damage accumulation in a communications satellite antenna-feed truss. The first of these sources is treated in detail for the ATS/3-Ring and Tripod-B truss designs in Appendix D, where it is shown that nominal axial stresses (due to axial load) of 22 and 31.2 ksi, respectively, are expected once per launch, while nominal axial stresses due to combined axial load and bending of 64.8 and 51.2 ksi, respectively, might be expected once per launch if the axial and bending loads are correlated. Stress concentration factors between 1.5 and 2 applied to these stresses (simulating a well designed attachment fitting) result in small values of calculated damage accumulation for the graphite/epoxy longeron tube.

Another potential source of fatigue is the stress field which may be developed in the bond between the composite tube and its attachment fitting due to temperature changes in orbit. Of most concern in this regard for a satellite at geosynchronous altitude are the approximate 90 days per year on which the satellite passes through earth shadow. Over a 10 to 20 year operational life, the satellite may experience 900 to 1,800 deep thermal excursions due to radiation cooling during the 60 to 90 minutes spent in earth shadow. A preliminary finite-element analysis of a hypothetical joint detail has shown that such thermal cycles can develop significant interlaminar stresses in the bond (see Appendix H). Hence, although the mechanical loads on the antenna-feed truss will be quite low after deployment, it is still important to assess the potential for residual strength degradation caused by thermal cycles over the life of the spacecraft.

For this purpose, graphic/epoxy tubes were obtained from a supplier and were bonded to steel fittings to simulate an end-attachment joint. These

joint details were subjected to varying numbers of accelerated temperature cycles between 60 ±6°F (15.5 ±3.3°C) and -321°F (-196°C) to assess the effect of cyclic thermal fatigue on residual strength. This appendix presents a justification for the accelerated test procedure, summarizes the test specimen fabrication and quality, describes the test apparatus and procedures used, and presents the experimental results.

2. ACCELERATED TESTING

The assessment of residual strength degradation of composites intended for space applications should ideally involve a real-time test procedure which incorporates vacuum, the orbital radiation and micrometeoroid environments, and thermal excursions. However, time and cost preclude the use of such extensive tests in the early stages of design development. Furthermore, the bond between a longeron tube and its metal end-attachment fitting will be protected from micrometeroids and ultraviolet radiation by the surrounding structure, and will be able to lose volatiles to the vacuum only through its edges. Hence, the potential effects of cyclic thermal stresses will be relatively more important for bondline fatigue.

Since cyclic thermal testing is to be conducted in the absence of environmental components whose effects depend upon calendar-time exposure, the possibility of accelerated testing can be considered. The importance of accelerated testing is apparent when one recognizes that the radiative cooling process in orbit may occupy the entire 60 to 90 minutes per earth-shadow entry without reaching an equilibrium temperature. A much more rapid cycle can be obtained by immersing the test specimen in a cryogenic liquid to take advantage of convective and/or conductive heat transfer. However, acceleration of the test in this manner also increases the severity of transient temperature gradients across the specimen wall thickness, a situation which may create more damage than would be expected in orbit.

Consequently, a one-dimensional heat-transfer analysis was conducted to assess the wall-temperature gradients expected for radiative cooling

and cooling by immersion in liquid nitrogen (LN_2) at -321°F. The analysis solves the one-dimensional heat-conduction equation,

$$K \frac{\partial^2 T}{\partial x^2} = \rho C_p \frac{\partial T}{\partial t} \qquad \text{C-1}$$

subject to boundary conditions of the form:

$$K \left.\frac{\partial T}{\partial x}\right|_{surface} = \varepsilon\sigma T^4_{surface} \qquad \text{(Radiative Cooling)} \qquad \text{C-2A}$$

$$K \left.\frac{\partial T}{\partial x}\right|_{surface} = H(T_{surface} - T_{liquid}) \qquad \text{(Conductive and/or Convective Cooling)} \qquad \text{C-2B}$$

where K, ρ, c_p, are respectively the material thermal conductivity, weight density, and specific heat at constant pressure; σ is the Stefan-Boltzmann constant; ε is the surface emmissivity; and H is the surface heat-transfer coefficient. A finite-difference solution scheme was used, and is compared for accuracy with two independent solution methods [49,50] in Figure C-1. The analysis procedure was then applied to a combined composite/steel tube wall with the properties given in Table C-1.

Cases studied include radiative cooling and LN_2 immersion assuming the tube surface to be protected by asbestos insulation layers of various thicknesses. For the latter cases, it was assumed that a liquid interface at -321°F would be maintained at the outer surface of the insulation. Also, immersion of a bare tube was analyzed under the assumption of convective heat transfer through a thin vapor film between the tube and the LN_2. This assumption is based on the occurrence of film boiling in the LN_2 when $T_{surface} - T_{LN_2} \geq 28°F$ [51].

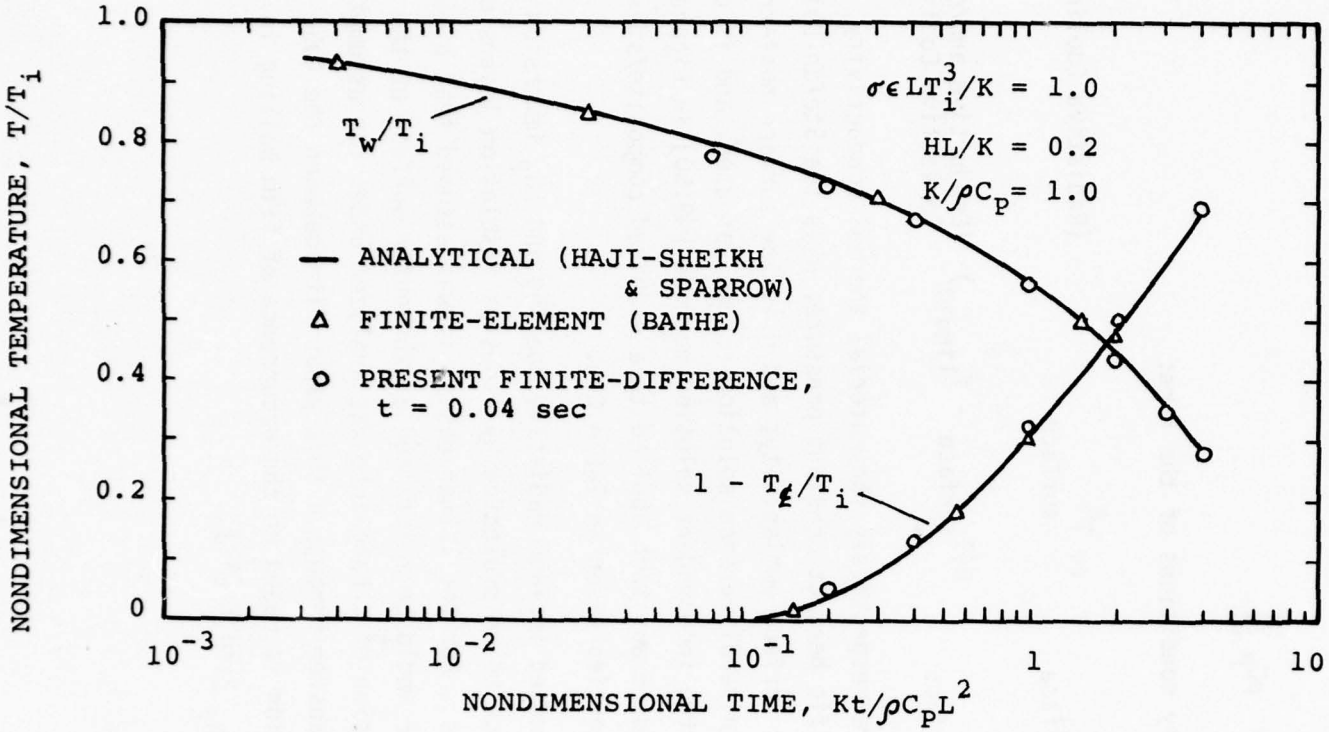


Figure C-1. Comparison of Solutions for Symmetrical Heat Transfer Through Both Surfaces of a Wall

TABLE C-1

INPUT DATA USED IN HEAT TRANSFER ANALYSIS

Item \ Portion of Tube	Composite	Steel	Insulation
K (Btu/in sec °F)	0.579×10^{-5}	0.741×10^{-3}	0.532×10^{-6}
ρ (lb/in^3)	0.056	0.283	0.521×10^{-2}
C_p (Btu/lb °F)	0.193	0.113	0.450
Wall Thickness (in)	0.05	0.05	0.1 to 0.3
Surface Parameters and Physical Constants: $H = 0.108 \times 10^{-3}$ Btu/in^2 sec °F; $\varepsilon = 0.9$; $\sigma = 3.37 \times 10^{-15}$ Btu/in^2 sec °R^4			

Results of the analysis are presented in terms of the total temperature gradient across the wall, $\Delta T(t)$, assuming that only the outer surface is exposed to LN_2. The general behavior of the temperature gradient is shown schematically in Figure C-2. Initially there is no gradient, but ΔT rises to a maximum value ΔT_{max} in a finite time. The magnitude of ΔT_{max} increases and the time required to reach ΔT_{max} decreases as the efficiency of the heat-transfer process between the tube and its surroundings increases. After ΔT_{max} is attained, ΔT decays asymptotically to zero (thermal equilibrium) as $t \to \infty$. Thus, the gradient ΔT_{max} can be used to make a comparative assessment of thermal shock effects on stresses in the bondline and tube walls. Results of the cases actually studied are shown in Figures C-3 and C-4.

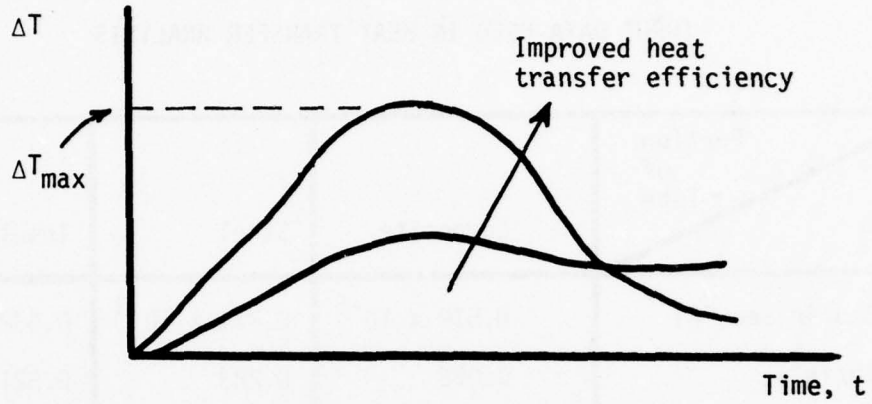


Figure C-2. General Behavior of Temperature Gradient with Cooling Time

Program RADSYM (Appendix H) was used to compute joint stresses due to the maximum thermal gradient for four representative cases. In each case, temeprature distributions between T = 0 at the exposed surface and T = ΔT_{max} at the inner surface were assumed to vary linearly through the wall thickness, and along the length of the tube, as shown in Figure C-5. A survey of the resulting bondline stresses (Table C-2) indicates that even the bare-tube accelerated test causes thermal-gradient stresses which are insignificant compared with the thermal stresses due to soaking at uniform temperature[1]. In view of these analytical results and the fact that accelerated thermal tests of flat laminate specimens appeared to cause no thermal-shock degradation (Appendix B), the accelerated testing procedure was adopted to assess the joint details.

---

[1]The latter values were found to be approximately -2,000 psi (radial) and 6,000 psi (shear) for cooling from room temperature LN_2 temperature. Additional results for stresses in the tube walls are reported in Appendix H.

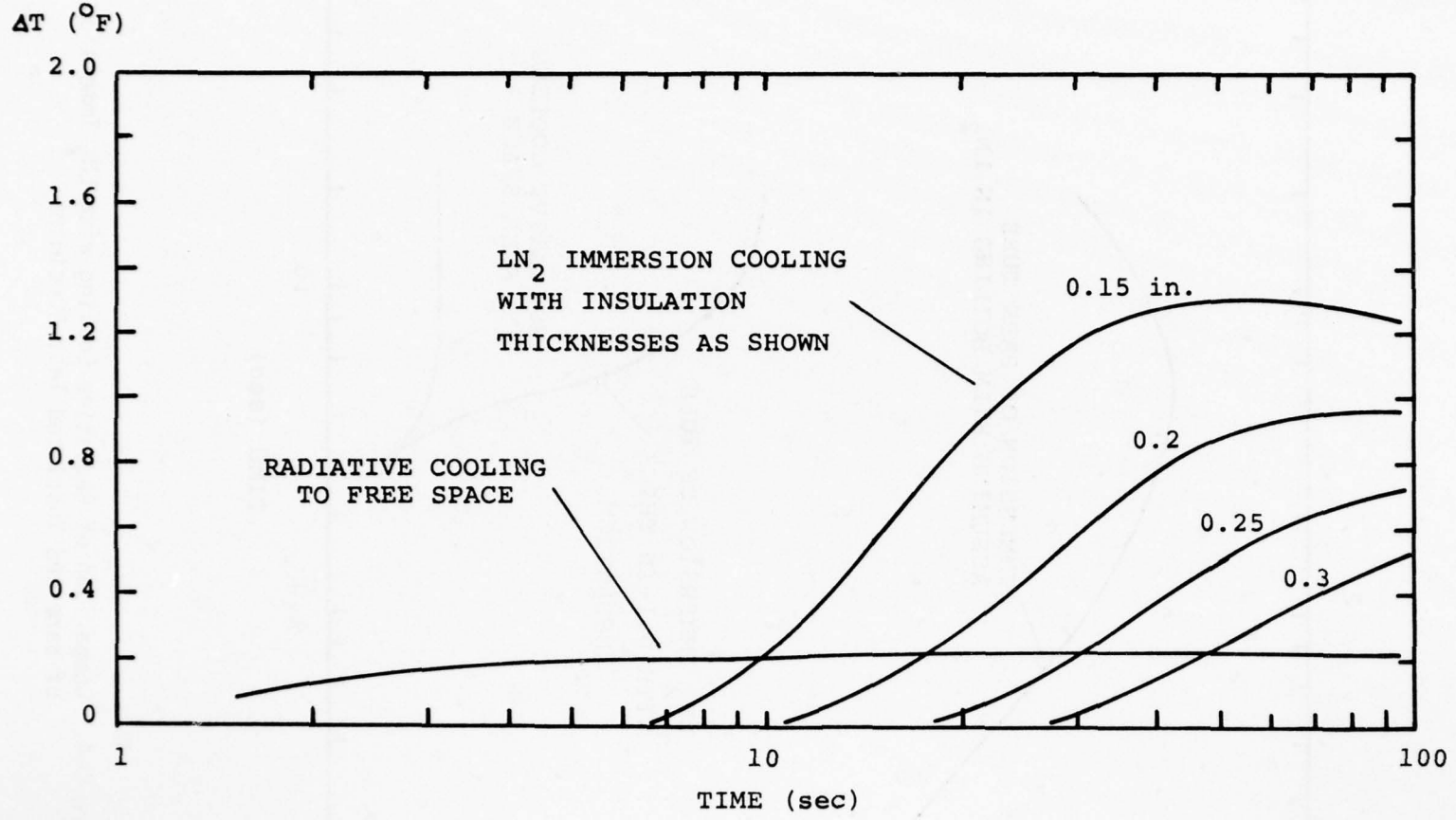


Figure C-3. Comparison of Radiative Cooling with LN_2 Immersion of Insulated Test Specimens

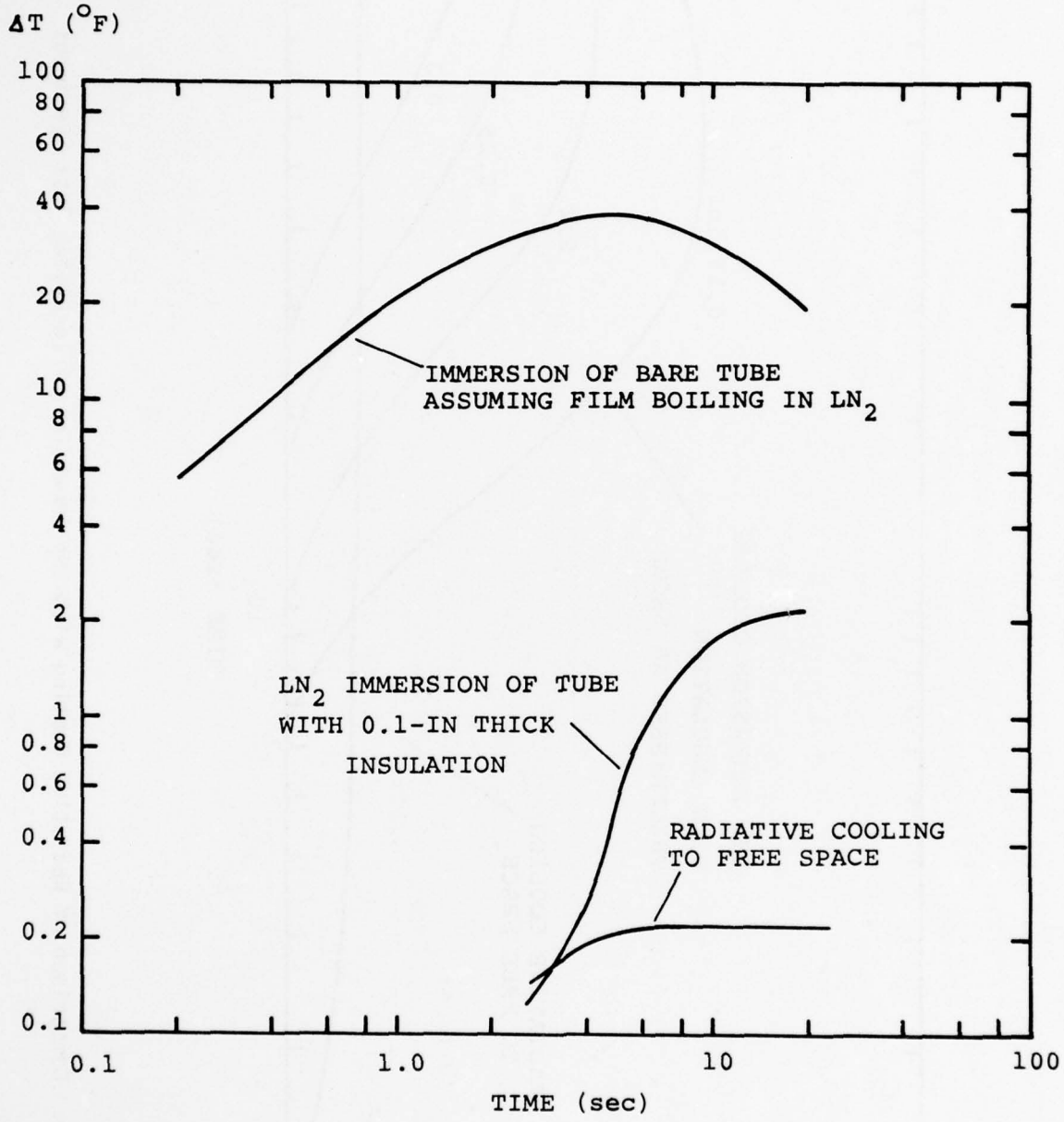
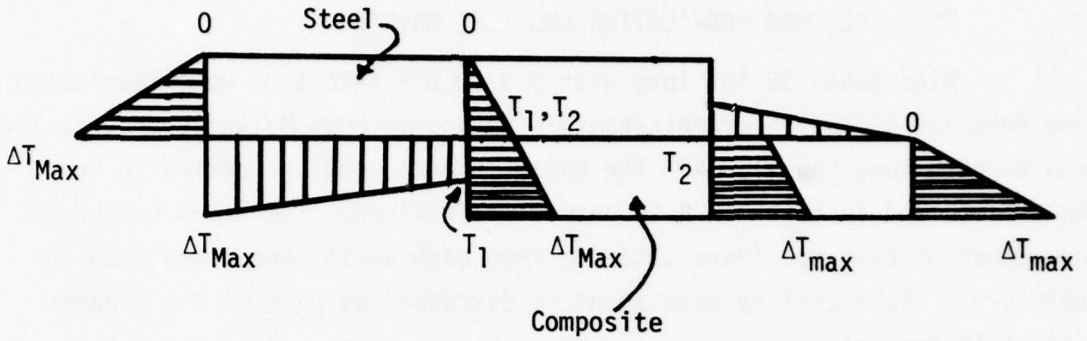


Figure C-4. Comparison of Radiative Cooling with LN_2 Immersion of Bare and Insulated Test Specimens



T_1 = Temperature at steel/bond interface.

T_2 = Temperature at composite/bond interface.

T_1, T_2 obtained from ΔT_{Max} by linear interpolation.

Figure C-5. Temperature Distribution Assumed for Thermal-Shock Stress Analysis

TABLE C-2

SURVEY OF BONDLINE STRESSES CAUSED BY TEMPERATURE GRADIENT

ΔT_{Max}		Radial Stress (psi)		Shear Stress (psi)	
°C	°F	Max.	Min.	Max	Min.
0.139	0.25	+0.73	-0.70	+1.06	-0.63
1.111	2.0	-3.4	-43.0	+9.25	-2.58
11.11	20	+116	-112	+92.5	-25.8
22.22	40	+116	-112	+169	-100

3. TEST SPECIMEN FABRICATION AND TEST MATRIX

Nine tubes 36 in. long with 1.3 $\pm$0.005 inch I.D. were fabricated from Hercules AS/3501-6 graphic/epoxy with and without Mylar inserts by the Avco Corporation, Lowell, MA. The Mylar inserts were perforated in the manner outlined in Appendix B to permit resin bleed. The layup sequences and number of test specimens obtained from each series are summarized in Table C-3. Tube quality assessment is discussed as part of the broader context in Appendix K.

TABLE C-3

INVENTORY OF GRAPHITE/EPOXY TUBES

Layup Sequence*	No. of 36-in. Tubes Fabricated	No. of 5-in. Test Specimens Obtained
$[90°/0°_{10}/90°]$	3	21
$[90°/M1/0°_{10}/M1/90°]$	3	21
$[90°/M2/0°_{10}/M2/90°]$	3	21
*M1 = 0.001-in. Mylar insert, M2 = 0.002-in. Mylar insert.		

Each tube was cut into 5-in. lengths for design development test (DDT) specimens, using a Neuber type 1A1R (C=50) resinoid-bond diamond wheel at approximately 2,000 RPM, together with a water spray. An end-attachment fitting was simulated by bonding a steel sleeve to the inside of each test specimen. Dimensional details are shown in Figure C-6. Photographs of a sleeve and a completed DDT article are shown in Figures C-7 and C-8.

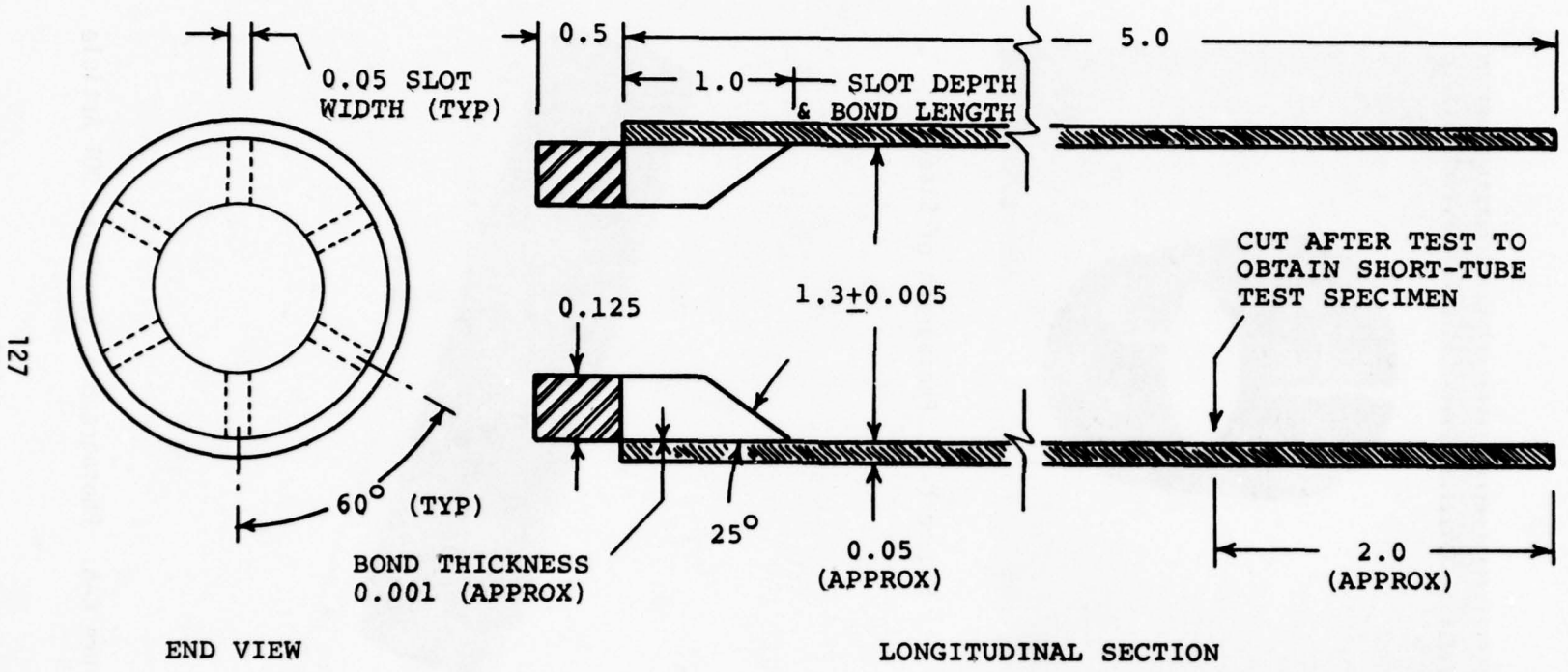


Figure C-6. Configuration of DDT Specimen

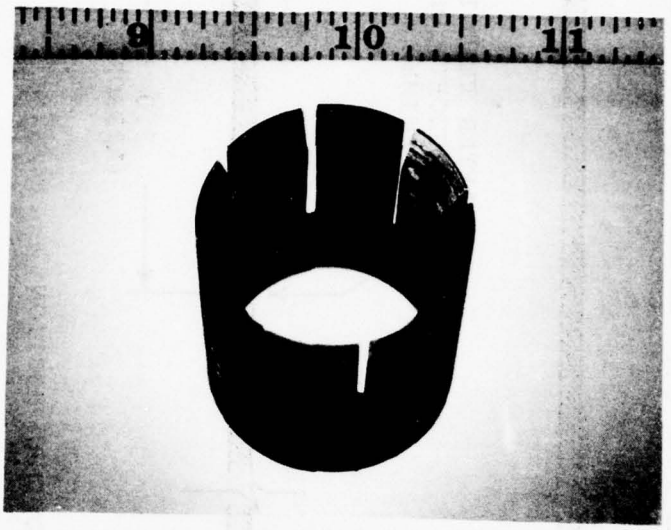


Figure C-7. Photograph of Sleeve



Figure C-8. Photograph of Completed DDT Article

The steel fitting was slotted and given a 25° taper to permit experimental study of a configuration closer to a realistic joint than the geometries which were treated by the analysis procedures outlined in Appendices H and I. An inside fitting was chosen primarily to maintain uniformity of the bond thickness, since the O.D. of the composite tubes was found to be much more variable than the I.D.

After the fitting and tube surfaces were cleaned, the fittings were bonded with B.F. Goodrich A-1333-B epoxy resin [52] and oven-cured at 160°F for 2 hours. A post-cure period of 3 to 8 days was then allowed before beginning testing. Some variations occurred in the bond processing, and were apparently responsible for anomalies in the experiental results. The variations involved different cleaning agents, waiting time between assembly and curing, and resin temperature during mixing. The details are presented together with the test results in Section C.5.

After the strength test of a joint was completed, approximately 2-in. of the composite tube was retrieved from the free end by cutting with a hacksaw to obtain a second specimen for a residual-strength test of the tube itself (see Figure C-6). The newly cut end of the second specimen was then refinished on a sanding wheel with No. 60 aluminum oxide grit.

Due to late receipt of the composite tubes and the time-consuming nature of the cyclic thermal testing, only a part of the intended test matrix could be completed within the program schedule. Planned and completed tests are summarized in Table C-4.

TABLE C-4

TEST MATRIX

Test Conditions	LAYUP SEQUENCE		
	$[90°/0°_{10}/90°]$	$[90°/M1/0°_{10}/M1/90°]$	$[90°/M2/0°_{10}/M2/90°]$
Residual strength test at 75°F after number of thermal cycles indicated:			
0	3/2*	4/1 (1/1)**	(5/5)
10	-	(3/3)	(3/3)
50	3/2	(3/3)	(3/3)
100	6/3	(3/3)	(3/3)
500	3/2	(3/3)	(3/3)
1000	3/0 (2/2)	(3/3)	(3/3)

*3/2: 3 = joint strength test; 2 = tube strength test.

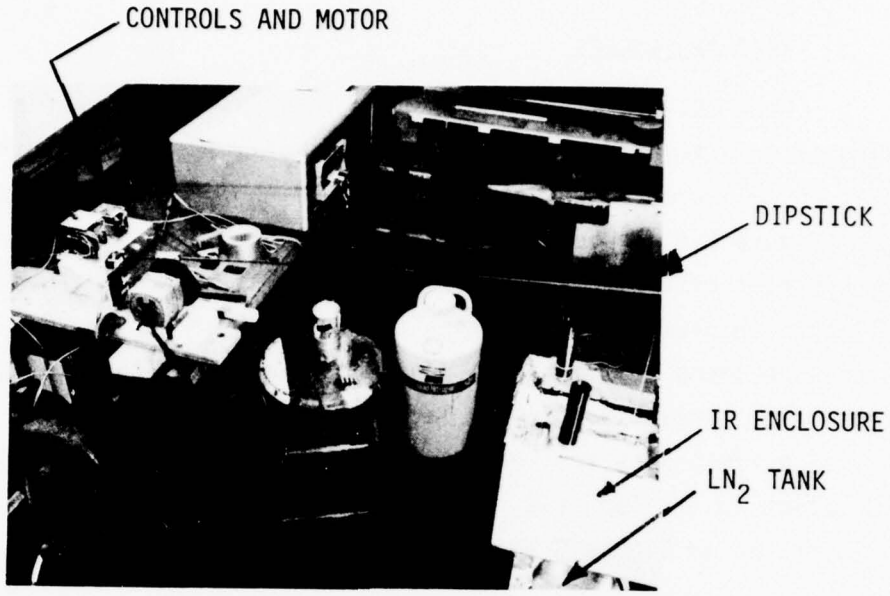
**( ) Tests planned but not completed.

4. TEST PROCEDURES

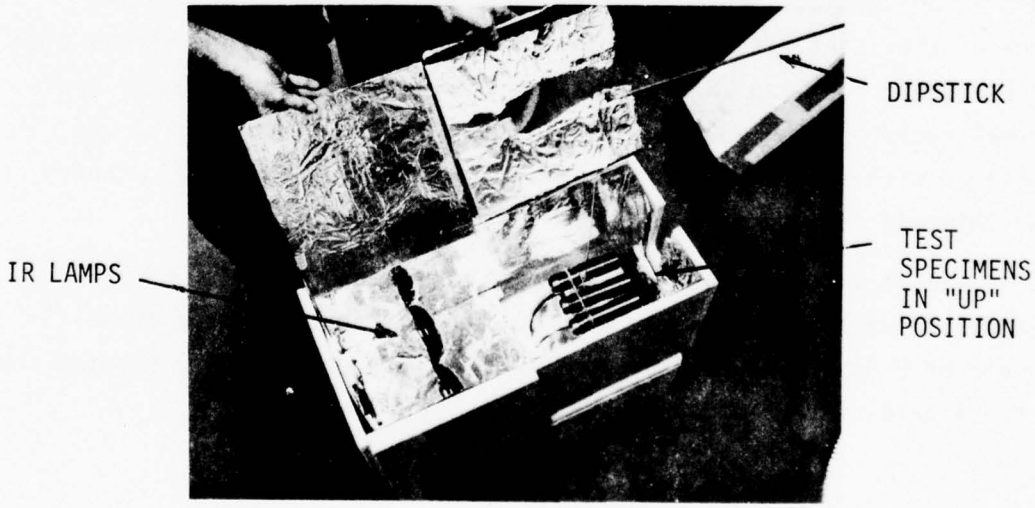
Bare DDT specimens were ganged in groups of three for thermal cycling in an automated test rig consisting of a 12-in lb, variable-RPM AC motor turning a wheel with an eccentric bearing to control a dipstick and hanger (Figure C-9). When the dipstick is in the "up" position, the test specimens rest in a partial enclosure containing two 250-W infrared lamps and lined with aluminum foil. When the dipstick is in the "down" position, the test specimens rest in an insulated open-top tank containing LN_2 (periodically replenished from a large Dewar flask). Operation of the motor is controlled by two set/reset timers and limit switches engaged by the dipstick in the "up" and "down" positions. The control circuit schematic is illustrated in Figure C-10.

The soak time at LN_2 temperature was established by immersing a DDT specimen fabricated from scrap tubing and observing the time required for the LN_2 to cease boiling. To establish the soak time in the infrared enclosure, an iron-constanstan thermocouple was applied to the inside surface of the steel fitting, and the thermocouple temperature versus time after emergence from the LN_2 bath was monitored. By repeated experiments, a thermal cycle between -321°F (-196°C) and +60 $\pm$6°F (15.5 $\pm$3.3°C) was established with soak times of approximately 50 sec in LN_2 and 7 minutes in the infrared enclosure.

Joint strength and tube strength were measured on a BLH SR-4 mechanical-drive testing machine with 50,000-lb. capacity, at a cross-head rate of 0.05 in/min. Both types of test were conducted by placing the test specimen directly between the platens.



(A) OVERALL VIEW



(B) VIEW INTO IR ENCLOSURE

Figure C-9. Thermal Cycle Apparatus

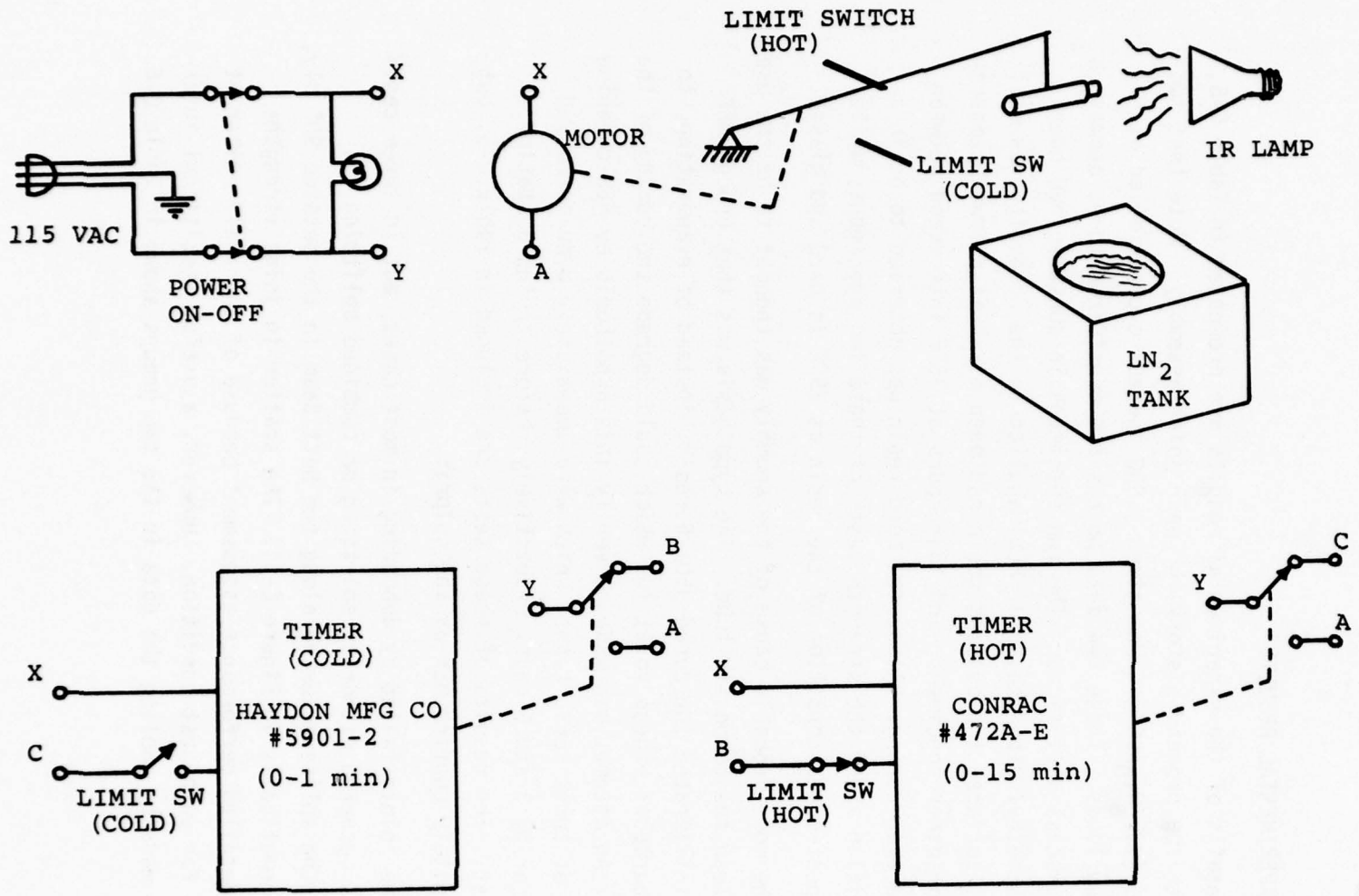


Figure C-10. Cycle Control Circuit

5. EXPERIMENTAL RESULTS

Details of the experimental results are presented in Table C-5, together with the process history for each joint assembly. Note that two of the three $[90°/0°_{10}/90°]$ tubes given 1,000 thermal cycles failed at extremely low loads. These two data points are considered to be anomalous results of process variations. The two specimens in question had been cleaned with methyl ethyl keytone (MEK) applied to the composite, as well as the steel surface, the bonding resin had been mixed at a lower temperature than for other specimens, and four hours at 75°F intervened between assembly and oven curing. Also, the bond resin was observed to be in a sticky condition after the strength tests of these two specimens, while the normal post-cured condition of the resin at 75°F is hard and glassy.

The most probable cause of the anomaly was thought to be the use of MEK to clean the composite tube. The hypothesis was that enough MEK might have infiltrated the cured 3501-6 resin, instead of evaporating, to provide a source of excess volatiles which could degrade the curing of the bond resin. An attempt was made to verify this hypothesis by MEK-cleaning and bonding of three scrap tubes, which were immediately oven-cured and post-cured for 0, 3 and 5 days, respectively, before trying a static strength test. The results of these tests are included in Table C-5, but do not definitely confirm MEK as the culprit.

The joints failed by debonding in most cases, but in three tests the failures occurred either by splitting or combined splitting and debonding. The splits occurred along the butt seam in the outside 90° ply, as shown schematically in Figure C-11. The scatter in joint strengths precludes a detailed performance assessment because of the small number of data points for each test condition. However, a useful statistical inference can be made by pooling the data in the two groups shown in Table C-6.

TABLE C-5

SYNOPSIS OF JOINT-ASSEMBLY PROCESSING AND EXPERIMENTAL OBSERVATIONS

Test Specimen / Item	Nominal Scrap Tubes			Nominal Tubes [90°/0°$_{10}$/90°]																		[90°/M1/0°$_{10}$/M1/90°]			
	1	2	3	1	2	3	4	5	6	7	8	9	10	11	12	13	14	15	16	17	18	1	2	3	4
Metal fitting cleaned with (a)	MEK	MEK	MEK	MC	MC	MC	MC	MC	MC	MC	MC	MC	MC	MC	MC	MEK + AC	MC	MC	MEK + AC	MEK	MEK	MC	MC	MC	MC
Composite tube cleaned with (a)	MEK	MEK	MEK	AIR	AIR	AIR	AIR	AIR	AIR	AIR	AIR	AIR	AIR	AIR	AIR	AC	AIR	AIR	AC	MEK	MEK	AIR	AIR	AIR	AIR
A-1333-B resin mix temperature (°F)	75	75	75	75	75	75	75	75	75	75	75	75	75	75	75	75	60	60	75	60	60	75	75	75	75
Delay time before oven cure (hr)	-	-	-	-	-	-	-	-	-	-	-	-	-	-	-	-	-	-	-	4	4	-	-	-	-
Post-cure time at 75°F (days)	0	3	5	3	6	6	3	3	3	3	3	3	3	3	3	3	4	4	8	5	5	4	4	4	6
Number of thermal cycles	-	-	-	-	-	-	50	50	50	100	100	100	100	100	100	500	500	500	1000	1000	1000	-	-	-	-
Joint strength (KIPS)	3.75	5.10	3.30	10.05	9.80	5.90	7.00	7.60	8.70	8.55	10.00	9.50	13.00	15.80	15.25	5.15	7.10	4.50	4.95	0.20	0.20	6.20	7.15	8.10	5.10
Joint failure mode (b)	DB	DB	DB	SPLIT	DB	DB	DB	DB	DB	DB	DB	DB	SPLIT + DB	BROOM	SPLIT + DB	DB	DB	DB	DB	DB	DB	DB at MY	DB at MY	DB at MY	DB at MY
A-1333-B resin appearance (c)	N	N	DISC	N	N	N	N	N	N	N	N	N	N	N	N	N	N	N	N	ST	ST	N	N	N	N
Tube (KIPS) strength	-	-	-	-	17.35	15.40	28.30	25.95	13.15	19.20	13.40	15.56	8.80	-	16.90	22.10	-	21.70	-	-	-	-	-	-	19.60
Tube failure mode (c)	NOT MEAS	NOT MEAS	NOT MEAS		BROOM	BROOM	B	B	BROOM	BROOM	BROOM	BROOM	SPLIT	-	SPLIT	B	BROOM	B	NOT MEAS	NOT MEAS	NOT MEAS	NOT MEAS	NOT MEAS	NOT MEAS	B

(a) Cleaning agents: AC = acetone; AIR = compressed air; MC = methyl chloride; MEK = methyl ethyl keytone.

(b) Failure modes: DB = normal debond; SPLIT = splitting failure in composite tube; BROOM = brooming of composite tube; B = bursting of composite tube; MY = mylar.

(c) Resin appearance: N = normal; DISC = discolored; ST = sticky.

The one-sided confidence limits shown in Table C-6 can be interpreted as follows:

$$\mu_p \geq 8.38 - 0.97 = 7.41 \text{ KIPS (Zero to 100 thermal cycles)} \quad C\text{-}3$$

$$\mu_p \leq 5.42 + 1.35 = 6.77 \text{ KIPS (500 to 1,000 thermal cycles)} \quad C\text{-}4$$

where μ_p is the underlying mean value. Hence, one may conclude that at least 9 percent degradation of joint strength occurs after long-term thermal cycling, with 90 percent confidence.

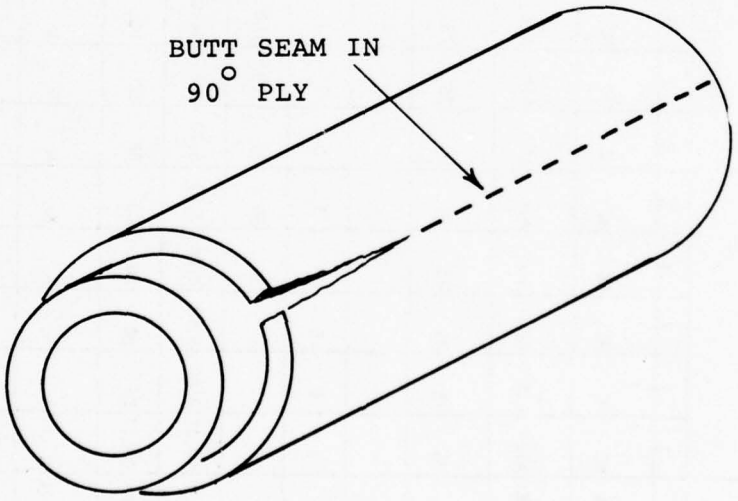


Figure C-11. Schematic of Splitting Failure

TABLE C-6

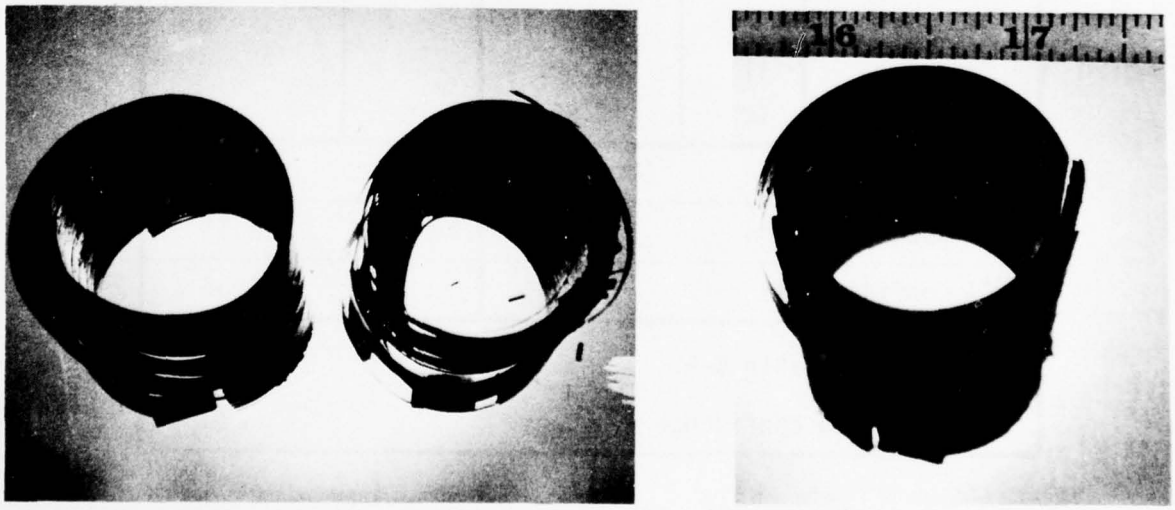
POOLED DATA FOR JOINT STRENGTH

(Layup Sequence of [90°/0°_{10}/90°] only;
Splitting, Brooming, and Anomalous Failures Excluded)

Item	G R O U P			
	Data for 0, 50 and 100 Thermal Cycles		Data for 500 and 1,000 Thermal Cycles	
	No.*	Strength**	No.*	Strength**
Observations	2	9.80	13	5.15
	3	5.90	14	7.10
	4	7.00	15	4.50
	5	7.60	16	4.95
	6	8.70		
	7	8.55		
	8	10.00		
	9	9.50		
	11	15.80		
	12	15.25		
Mean		9.81		5.42
Standard Deviation		3.10		1.15
95% Confidence***		1.80		1.35

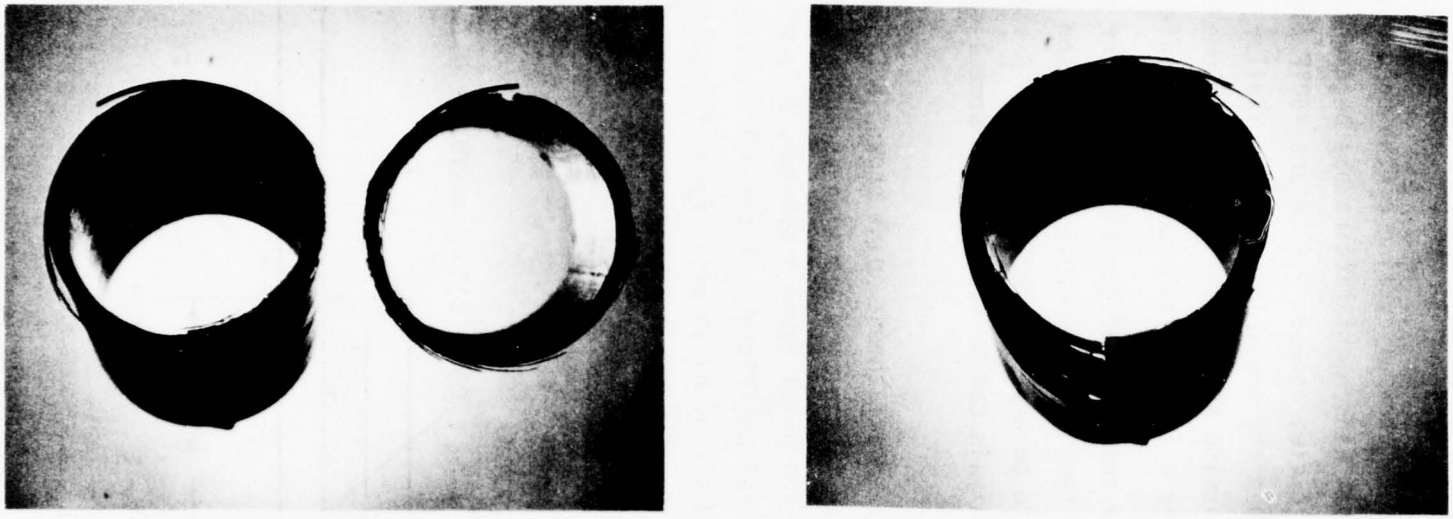
*Keyed to Table C-5.
**(KIPS)
***One-sided confidence limit.

Three tube failure modes are noted in Table C-5, but none appeared to be associated with local crippling. Several tubes (including one with Mylar inserts) failed at the loads between 20 and 29 KIPS in an apparent bursting mode. Examples are shown in Figure C-12. However, most of the remaining tubes failed at much lower loads by brooming at one end, and sometimes accompanied by splitting along the 90°-ply butt seam (see Figure C-11 for splitting schematic). The brooming failures tended to occur at the tube end which had been cut with a hacksaw. Typical examples are shown in Figure C-13. Because of the scatter in the strength data and lack of consistency in the failure modes, no conclusions can be drawn with regard to the effect of thermal cycles on the basic tube material. However, some critique of fabrication and test procedures is warranted, and is presented following the discussion of joint strength.



(a) $[90°/0°_{10}/90°]$ (b) $[90°/M1/0°_{10}/M1/90°]$

Figure C-12. Typical Bursting Failures



(a) Plain Brooming

(b) Brooming and Splitting

Figure C-13. Typical End Failures

6. DISCUSSION OF RESULTS

Fatigue degradation by thermal cycling of the bond between a graphite/epoxy tube and a steel attachment fitting has been demonstrated experimentally. The thermal cycle, between -321°F and +60°F, is considered to be somewhat more severe than the probable cycle for similar joints in a geosynchronous satellite passing through earth shadow. Some 900 to 1,800 such cycles could occur during a 10 to 20 year operational life.

There remains to be answered the question of whether the thermal stress levels induced in the test are reasonable in comparison with the mechanical fatigue stresses to be expected during launch. A simplified one-dimensional shear-lag analysis can be used to shed some light on this question.

Consider the idealized attachment joint shown in Figure C-14, where subscripts 1 and 2 refer to the metal fitting and composite tube, respectively, and where E is the axial Young's modulus, A is the cross section area, and α is the axial coefficient of thermal expansion. The joint is assumed to be loaded either by an axial force P (neglecting the associated flaring couple) or by a uniform temperature change ΔT. Since hoop effects are neglected, the model does not distinguish between inside and outside fittings.

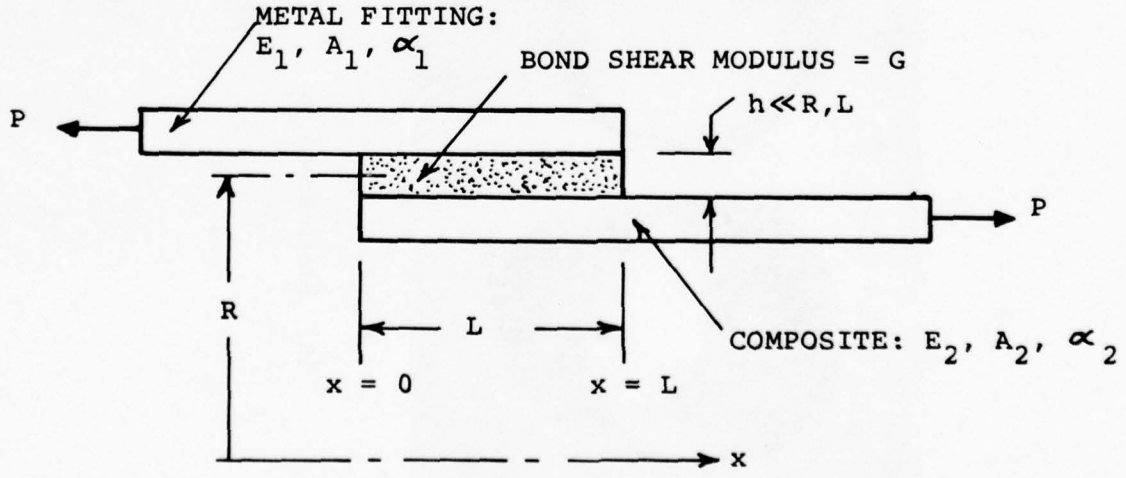


Figure C-14. One-Dimensional Model of Joint

Let s_i, u_i and v_i ($i = 1,2$) represent the component axial stresses, elastic displacements and total displacements, respectively, and let s_B be the shear stress in the bond. It then follows from the free-body diagrams shown in Figure C-15 that the equations of equilibrium for the model are given by:

$$A_1 s_1' - 2\pi R s_B = 0 \quad A_2 s_2' + 2\pi R s_B = 0 \qquad \text{C-5}$$

where $(\,)' = d(\,)/dx$. Also, the stress-strain relations are given by:

$$s_1 = E_1 u_1' \quad s_2 = E_2 u_2' \quad s_B = \frac{G}{h}(v_1 - v_2) \qquad \text{C-6}$$

and the following expressions relate elastic and total strains:

$$v_1' = u_1' + \alpha_1 \Delta T \quad v_2' = u_2' + \alpha_2 \Delta T \qquad \text{C-7}$$

(Note that from the third of Eqs. C-6, the shear strain in the bond is assumed to be uniform, and is determined by the relative difference in the <u>total</u> displacements of the fitting and tube.)

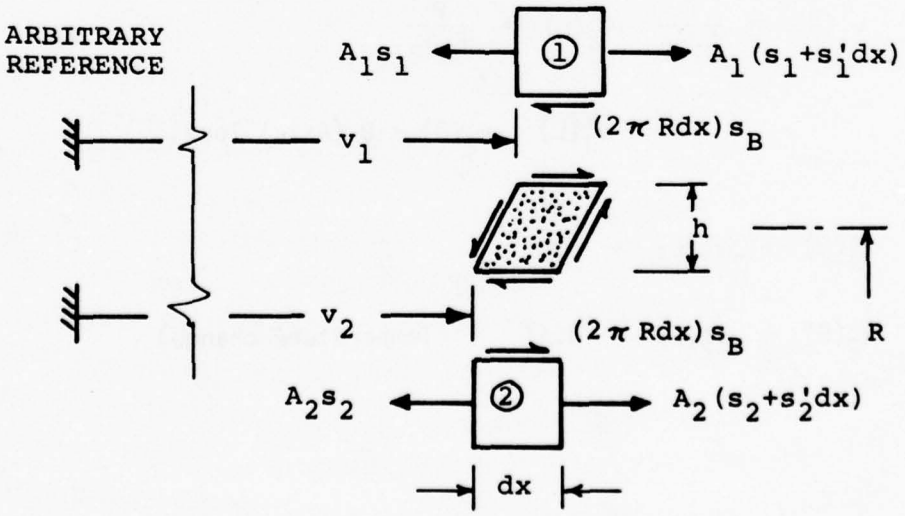


Figure C-15. Free-Body Diagrams for Joint Model

Equations C-5 through C-7 can be combined to eliminate s_i, u_i, ($i = 1,2$) and s_B, with the result that the following field equations are obtained in terms of v_i:

$$E_1A_1v_1'' - \frac{2\pi RG}{h}(v_1 - v_2) = 0 \qquad \text{C-8A}$$

$$E_2A_2v_2'' + \frac{2\pi RG}{h}(v_1 - v_2) = 0 \qquad \text{C-8B}$$

The general solution of Equations C-8A and B is:

$$v_1 = A\sinh(\lambda x) + B\cosh(\lambda x) \qquad \text{C-9A}$$

$$v_2 = C\sinh(\lambda x) + D\cosh(\lambda x) \qquad \text{C-9B}$$

where:

$$\lambda = \left[\frac{2\pi RG(E_1A_1 + E_2A_2)}{hE_1A_1E_2A_2}\right]^{1/2} \qquad \text{C-10}$$

The constants A,B,C,D are determined by the following boundary conditions for the two cases of interest:

$$v_1'(0) = \frac{P}{E_1A_1} \quad v_2'(L) = \frac{P}{E_2A_2}$$

$$v_1'(L) = v_2'(0) = 0 \text{ (Axial load)} \qquad \text{C-11}$$

$$v_1'(0) = v_1'(L) = \alpha_1\Delta T$$

$$v_2'(0) = v_2'(L) = \alpha_1\Delta T \quad \text{(Temperature change)} \qquad \text{C-12}$$

After satisfaction of the boundary conditions and back-substitution, the following expressions are obtained for the magnitudes of the peak shear stresses in the bond:

$$s_B^P(0) = \frac{GP}{\lambda h \sinh(\lambda L)} \left[\frac{\cosh(\lambda L)}{E_1 A_1} + \frac{1}{E_2 A_2} \right] \qquad \text{C-13A}$$

$$s_B^P(L) = \frac{GP}{\lambda h \sinh(\lambda L)} \left[\frac{1}{E_1 A_1} + \frac{\cosh(\lambda L)}{E_2 A_2} \right] \qquad \text{C-13B}$$

$$s_B^{\Delta T}(0) = s_B^{\Delta T}(L) = \frac{G|\alpha_1 - \alpha_2|\Delta T}{\lambda h \sinh(\lambda L)} [\cosh(\lambda L) - 1] \qquad \text{C-14}$$

Approximations to Equations C-13 and C-14 for large values of λL are given by:

$$\max(s_B^P) \simeq \frac{GP}{\lambda h[\min(E_1 A_1, E_2 A_2)]} \qquad \text{C-15}$$

$$s_B^{\Delta T} \simeq |\alpha_1 - \alpha_2| \frac{G\Delta T}{\lambda h} \qquad \text{C-16}$$

Consider now the following three cases: the DDT article, the ATS/3-Ring longeron and the Tripod-B longeron. Approximate dimensional parameters for each case are summarized in Table C-7 for two possible conditions: bond assumed to be restricted to secondary-curing resin, and bond assumed to include the neighboring 90° graphite/epoxy plies (0.005 in per ply). In all cases, λL is sufficiently large to warrant using the approximate peak-stress expressions (Equations C-15 and C-16). Approximate material properties used in the calculations are summarized in Table C-8.

TABLE C-7

DIMENSIONAL PARAMETERS

Item \ Design	DDT Article $[90°/0°_{10}/90°]$	ATS/3-Ring $[90°_2/0°_{16}/90°_2]$	Tripod-B $[90°_2/0°_{16}/90°_2]$
R (in.)	0.65	1.40	1.80
L (in.)	1.00	2.72 (est.)	4.00 (est.)
Wall thickness of graphite/epoxy tube (in.)	0.05	0.10	0.10
Wall thickness of steel fitting (in.)	0.125	0.10 (est.)	0.10 (est.)
Assuming only secondary bond in shear:			
h (in.)	0.004	0.005	0.005
$\lambda(in.^{-1})$	17.35	13.4	13.4
λL	17.35	36.5	53.6
Assuming inclusion of neighboring 90° plies in shear:			
h (in.)	0.009	0.015	0.015
λ $(in.^{-1})$	11.56	7.75	7.75
λL	11.56	21.10	31.00

The thermal shear peak for each case corresponds to the representative orbital excursion $\Delta T \cong 390°F$ (216°C). For comparison, axial loads P = 15,950 lb. for ATS/3-Ring and 29,313 lb. for Tripod-B are expected to occur once per launch (see Appendix D). To compare the DDT article on a similar basis, it is reasonable to assume that as a primary member it would

TABLE C-8

APPROXIMATE MATERIAL PROPERTIES

Material	Property Values
Steel Fittings	$E_1 = 30 \times 10^6$ psi $\alpha_1 = 11.2 \times 10^{-6}$ °C^{-1}
Graphite/Epoxy	$E_2 = E_L \cong 21 \times 10^6$ psi $\alpha_2 = \alpha_L \cong 0.3 \times 10^{-6}$ °C^{-1}
Bond	$G \cong 10^6$ psi

be designed to experience about one-half the demonstrated 10,000-lb. static joint strength as a once-per-launch expected load. The loads and stress calculations are summarized in Table C-9. The comparisons also include average shear stress due to axial load.

The data in Table C-9 demonstrate a common aspect of the DDT article and the longeron designs: the similar ratios of thermal stress to once-per-launch stress. Hence, it is reasonable to conclude that the relative amounts of damage accumulation caused by thermal cycling and launch will be similar. Fatigue calculations for the longeron tubes indicate that the expected launch-loading damage accumulation is small in the tubes, per se; a similar result can be assumed for the bondline. On the other hand, the DDT experiments demonstrate some degradation of residual strength after the 500 to 1,000 thermal cycles, and similar degradations can be expected in the ATS/3-Ring and Tripod-B longerons.

TABLE C-9

LOAD AND STRESS COMPARISONS

Item \ Design	DDT Article	ATS/3-Ring	Tripod-B
Once per launch load (lb)	5,000	15,950	29,313
Earth shadow thermal cycle, ΔT (°C)	216	216	216
Stresses assuming only secondary bond in shear:			
s_B^P (ksi)	16.0	15.7	22.4
$s_B^{\Delta T}$ (ksi)	33.6	34.8	34.8
s_B^P (Avg) = $\frac{P}{2\pi RL}$ (ksi)	1.22	0.675	0.648
$s_B^{\Delta T}/s_B^P$ (Peak/Peak)	2.10	2.22	1.56
$s_B^{\Delta T}/s_B^P$ (Peak/Avg)	27.5	51.5	53.8
Stresses assuming inclusion of 90° plies in shear:			
s_B^P (ksi)	10.7	9.06	12.9
$s_B^{\Delta T}$ (ksi)	22.4	20.1	20.1
s_B^P (Avg) = $\frac{P}{2\pi RL}$ (ksi)	1.22	0.675	0.648
$s_B^{\Delta T}/s_B^P$ (Peak/Peak)	2.10	2.22	1.56
$s_B^{\Delta T}/s_B^P$ (Peak/Avg)	18.3	29.8	31.0

As far as the communications satellite is concerned, cyclic thermal strength degradation is not a critical factor because the residual strength at the end of operational life will still be one to two orders of magnitude larger than the orbital mechanical laods. However, cyclic thermal fatigue may be more critical for large space structures. Large space structures may be designed to reduced static requirements, assuming assembly in orbit, may be subjected to larger orbital loads, and may have longer operational life requirements.

Theoretical prediction of tube strength from crippling stability analysis [4] leads to an expected failure load of 80 KIPS. It is apparent that crippling was not achieved in the tube tests, in view of the observed failure modes and the low strength data (8 to 29 KIPS). The strengths of those tubes which did not experience brooming (20 to 29 KIPS) can be correlated approximately with a simple failure model.

Consider a tube with the cross-section dimensions shown in Figure C-16 and suppose that a uniform axial strain e_z is imposed by the testing machine. If the tube is treated as a thin-walled cylinder ($t_1, t_2 \ll R$, radial stress $s_r \ll s_\theta, s_z$), the following approximate relationship between the total compression load, P, the tensile hoop stress in the 90° plies, s_θ, and the properties of a single ply can be derived:

$$P = 4\pi R t_1 \left[\frac{\nu_{LT} - \nu_{TL}}{} + \frac{(1 - \nu_{LT}\nu_{TL})\left(\frac{\nu_{TL}}{\nu_{LT}} + \frac{t_1}{t_2}\right)\left(1 + \frac{\nu_{LT} t_2}{\nu_{TL} t_1}\right)}{\nu_{LT} - \nu_{TL}} \right] s_\theta \qquad \text{C-17}$$

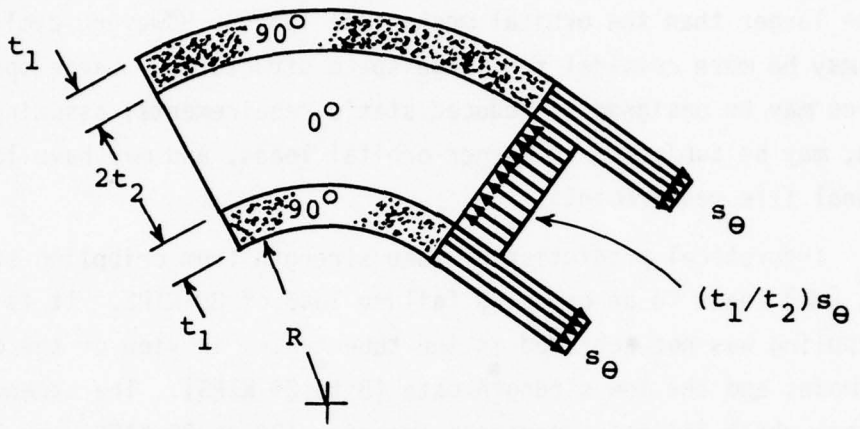


Figure C-16. Detail of Tube Cross Section

In the present case, $t_1/t_2 = 0.2$, $t_1 \cong 0.005$ inch, and R = 0.65 in. Substituting this value and the ply properties of AS/3501-6 graphite/epoxy (see Appendix A) in Eq. C-17 leads to:

$$P \cong 4.19\, s_\theta \qquad \text{C-18}$$

If $F_{T2} = 8.5$ ksi is substituted in Eq. C-18 for s_θ, a failure load $P \cong 35.6$ KIPS is predicted, a value not far from the data for the four bursting failures. This suggests that the tube strength is bounded by resin strength in the 90°-ply butt seam region.

The data for the brooming failures cannot be correlated with the bursting model presented above. Poor maintenance of end conditions in the test (placing the specimen directly between the platens) may have contributed in part to these results. However, the major cause is thought to be damage introduced in the specimens by cutting with a hacksaw and finishing the new end on a sanding wheel.

APPENDIX D

VIBRATION ANALYSIS APPROACH AND RESULTS

1. GENERAL

The ATS/3-Ring and Tripod-B antenna-feed truss design concepts were subjected to identical vibration analyses to provide data for estimating maximum loads and potential fatigue damage accumulation during launch. The analyses were executed by two tandem computer codes: program SFRAME and program SPECTRA.

Program SFRAME is used to assemble a finite-element model of the truss and to solve the undamped natural-vibration eigenvalue problem. Program SFRAME was also used previously to perform static analyses of both designs [1]. Program SFRAME is documented in Appendix E.

The natural frequencies and mode shapes computed by program SFRAME are used by program SPECTRA to perform a response analysis. Program SPECTRA assumes that the truss is subjected to base excitation consisting of three uncorrelated zero-mean stationary Gaussian processes with identical power spectra. Modal analysis is employed to compute the corresponding response power spectra for each degree of freedom and each member internal load in the structure, and appropriate integrals of the power spectra are computed to obtain exceedance rates. Program SPECTRA is documented in Appendix F.

This appendix reviews briefly the theoretical foundations of the dynamic analysis tasks. Following the review, the excitation input data are presented and discussed, and the results of the analyses of the ATS/3-Ring and Tripod-B designs are given.

2. VIBRATION ANALYSIS

The undamped natural-vibration eigenvalue problem is solved by the subspace iteration method [12,13]. The problem is formulated as:

$$[K]\,[U] = [M]\,[U]\,[\lambda] \qquad \text{D-1}$$

where [K], [M] are assembled stiffness and mass matrices of order N, $[\lambda]$ is a diagonal eigenvalue matrix of order N' < N, and [U] is an N x N' rectangular eigenmatrix. Each column of [U] represents one eigenvector, and the corresponding coefficient of $[\lambda]$ represents the square of the associated natural frequency.

The algorithm for computing [U] and $[\lambda]$ is based on updating the current estimate for [U] by means of an eigensolution obtained from condensed stiffness and mass matrices. Assume that an arbitrary initial guess $[U^{(0)}]$ is made, and let $[U^{(i)}]$ represent the estimate after completion of the i^{th} iteration step. The $(i + 1)^{th}$ iteration step is then carried out as follows. First, the current eigenmatrix estimate is used to compute condensed stiffness and masses:

$$[k] = [U]^T [K] [U] \qquad \text{D-2A}$$

$$[m] = [U]^T [M] [U] \qquad \text{D-2B}$$

Note that [k], [m] are of order N'. The auxiliary eigenvalue problem with N' degrees of freedom:

$$[k] [u] = [m] [u] [\lambda^{(i + 1)}] \qquad \text{D-3}$$

is now solved. In the present case, this is accomplished by first determining the canonical form of [m] alone, and then using the canonical form to transform Eq. D-3 to [53]:

$$([m]^{-1/2} [k] [m]^{-1/2}) [v] = [v] [\lambda^{(i + 1)}] \qquad \text{D-4}$$

where

$$[u] = [m]^{-1/2} [v] \qquad \text{D-5}$$

The numerical solutions for the canonical forms of [m] and $[m]^{-1/2}$ [k] $[m]^{-1/2}$ are executed by the Jacobi method of iteration with plane rotation

transformations [54,55]. The von Neumann convergence criterion for Jacobi iteration [56] is used to maintain solution accuracy. After [u] and $[\lambda^{(i+1)}]$ have been obtained, the uncondensed eigenmatrix is updated as follows:

$$[U^{(i+1)}] = [K]^{-1}\,[M]\,[U^{(i)}]\,[u] \qquad \text{D-6}$$

Equation D-6 combines a projection operation $[U^{(i)}]\,[u]$ (i.e., realignment of the uncondensed eigenvectors toward the condensed eigenvectors) with static processing $[K]^{-1}\,[M]$ analogous to the matrix iteration method. In practice, the inverse $[K]^{-1}$ is not computed directly; rather $[U^{(i+1)}]$ is computed by means of a static equation-solving algorithm.

It has been shown that the procedure outlined by Eqs. D-2 through D-6 is convergent, i.e., $[U^{(i)}] \rightarrow [U]$, $[\lambda^{(i)}] \rightarrow [\lambda]$, and the N' lowest modes are obtained. In practice, the procedure is bounded by a convergence test of the form:

$$\left| \frac{\lambda^{(i+1)} - \lambda^{(i)}}{\lambda^{(i)}} \right| < \varepsilon \qquad \text{D-7}$$

where $\varepsilon << 1$ is a prescribed tolerance. Thus, convergence assures that the error in each computed eigenvalue is bounded by ε, and in each frequency by $\sqrt{\varepsilon}$. The procedure is also bounded by a prescribed maximum number of subspace iteration steps.

Finally, it is noted that a previous investigation [57] has determined that optimum rapidity of convergence is usually obtained by including more modes in the subspace than the number for which convergence is desired. For example, let N' represent the order of the subspace and N" < N', the number of modes to be converged. Then optimum results are generally obtained when:

$$N'' + 3 \leq N' \leq 2N'' \qquad \text{D-8}$$

3. MODAL FORMULATION FOR RESPONSE ANALYSIS

An important property of the eigenmatrix is its ability to decouple the undamped equations of motion:

$$[M]\{\ddot{q}\} + [K]\{q\} = \{Q(t)\} \qquad \text{D-9}$$

where $\{q\}$ is a vector of the degrees of freedom (nodal displacements and rotations) in the assembled finite-element model and $\{Q(t)\}$ is a corresponding vector of applied loads. Let $\{q\}$ be represented as a linear combination of the natural mode shapes $[U]$, each multiplied by a time-dependent scale factor $\beta(t)$:

$$\{q(t)\} = [U]\{\beta(t)\} \qquad \text{D-10}$$

Then premultiplication of Eq. D-9 by $[U]^T$, and substitution of Eq. D-10 lead to:

$$[\bar{M}]\{\ddot{\beta}\} + [\bar{K}]\{\beta\} = \{\bar{Q}(t)\} \qquad \text{D-11}$$

where

$$[\bar{M}] = [U]^T [M] [U] \qquad \text{D-12A}$$

$$[\bar{K}] = [U]^T [K] [U] \qquad \text{D-12B}$$

$$\{\bar{Q}(t)\} = [U]^T \{Q(t)\} \qquad \text{D-12C}$$

The decoupled equations of motion can be extended to the case of lightly damped structures, e.g., by assuming directly a set of nondimensional modal damping factors, ζ, based on engineering judgement. Premultiplication of Eq. D-11 by $[\bar{M}]^{-1}$, and introduction of the damping terms then leads to:

$$\{\ddot{\beta}\} = [2\zeta_n\omega_n]\{\dot{\beta}\} + [\omega_n^2]\{\beta\} = \{\alpha(t)\} \qquad \text{D-13}$$

where $\omega_n^2 = \bar{K}_n/\bar{M}_n$ (n = 1, 2, ..., N') and

$$\{\alpha(t)\} = [\bar{M}]^{-1} \{\bar{Q}(t)\} \qquad \text{D-14}$$

Assume now that the finite-element model is to be subjected to dynamic excitation by applying time-dependent displacements at the constrained nodes, instead of forces at the free nodes. In the present case, this represents a physical model which assumes that excitation is input to the antenna-feed truss through motions of a rigid truss/spacecraft.interface. Assume that the input motions are described by three translational components aligned with the finite-element model global reference axes XYZ:

$$\{r(t)\} = \begin{Bmatrix} x(t) \\ y(t) \\ z(t) \end{Bmatrix} \qquad \text{D-15}$$

A kinematic description of the effects of these motions of the truss is given by:

$$\{q_R(t)\} = [U_R] \{r(t)\} \qquad \text{D-16}$$

where $[U_R]$ is an Nx3 "modal" matrix analogous to the N x N' matrix of natural modes [U], and where {r} is analogous to {β}. In other words, each column of $[U_R]$ specifies the nodal displacements corresponding to a unit rigid-body translation of the structure along one global axis.

Since rigid-body motions can neither store strain energy nor induce damping in the structure by means of relative displacements or velocities across components, only the d'Alembert inertial forces need be included in the equations of motion, which now become:

$$[M] (\{\ddot{q}\} + \{\ddot{q}_R\}) + [C] \{\dot{q}\} + [K] \{q\} = \{0\} \qquad \text{D-17}$$

Premultiplication of Eq. D-17 by $[U]^T$, and substitution of Eqs. D-10 and D-16 then lead to decoupled equations similar to Eq. D-13:

$$\{\ddot{\beta}\} + [2\zeta_n\omega_n]\{\dot{\beta}\} + [\omega_n^2]\{\dot{\beta}\} = -[\bar{M}]^{-1}[A_R]\{\ddot{r}\} \qquad \text{D-18}$$

where

$$[A_R] = [U]^T[M][U_R] \qquad \text{D-19}$$

Structural responses can be calculated by solving the uncoupled equations of motion (Eq. D-13 or D-18) and then using modal superposition (Eq. D-10) to obtain $\{q\}$. For example, a straightforward algorithm has been developed for transient response analysis, in which $\{q(t_{i-1})\}$, $\{\dot{q}(t_{i-1})\}$ and the values of the excitations at times t_{i-1} and t_i are used to compute $\{q(t_i)\}$ and $\{\dot{q}(t_i)\}$, assuming linear interpolation between t_{i-1} and t_i for the excitation [58]. In the present case, the objective is to formulate a solution for response to excitation by stationary random processes. For this purpose, it is permissible to treat the time-dependent quantities formally as if their Fourier transforms exist, e.g.:

$$\{B(i\omega)\} = \int_{-\infty}^{\infty} e^{-i\omega t}\{\beta(t)\}\,dt \qquad \text{D-20}$$

It is then easy to show that:

$$\begin{aligned} \int_{-\infty}^{\infty} e^{-i\omega t}\{\dot{\beta}(t)\}\,dt &= i\omega\{B(i\omega)\} \\ \int_{-\infty}^{\infty} e^{-i\omega t}\{\ddot{\beta}(t)\}\,dt &= -\omega^2\{B(i\omega)\} \end{aligned} \qquad \text{D-21}$$

and, as a result, Eq. D-18 can be solved for $\{B(i\omega)\}$ to yield:

$$\{B(i\omega)\} = -\left[\phi_n(i\omega)\right] [A_R] \{\ddot{R}(i\omega)\} \qquad \text{D-22}$$

where

$$\phi_n(i\omega) = \frac{1/\bar{M}_n}{\omega_n^2 - \omega^2 + 2i\zeta_n\omega_n\omega} = \frac{1/\bar{K}_n}{1 - \frac{\omega^2}{\omega_n^2} + 2i\zeta_n \frac{\omega}{\omega_n}} \qquad \text{D-23}$$

$(n = 1, 2, \ldots, N')$

$$\{\ddot{R}(i\omega)\} = \int_{-\infty}^{\infty} e^{-i\omega t} \{\ddot{r}(t)\}\, dt \qquad \text{D-24}$$

Power spectra and cross-spectra for the response quantities can now be obtained by working with finite Fourier transforms, applying Parseval's theorem, and going through a limit operation [15], e.g., for any two quantities $\xi(t)$ and $\eta(t)$:

$$\Xi(i\omega,T) = \int_{-T}^{T} e^{-i\omega t}\, \xi(t)\, dt \qquad \text{D-25}$$

$$H(i\omega,T) = \int_{-T}^{T} e^{-i\omega t}\, \eta(t)\, dt$$

$$G_{\xi\eta}(i\omega) = \lim_{T\to\infty} \left[\frac{\Xi^*(i\omega,T)\, H(i\omega,T)}{4\pi T} \right] \qquad \text{D-26}$$

Applying a similar procedure to Eq. D-22 then leads to the following relation between the input spectra and the modal response spectral density matrix:

$$\left[G_{\beta\beta}(i\omega)\right] = \left[\phi_n^*(i\omega)\right] [A_R] \left[G_{\ddot{r}\ddot{r}}(i\omega)\right] [A_R]^T \left[\phi_n(i\omega)\right] \qquad \text{D-27}$$

Assume now that the input base motions are uncorrelated between reference axes, and that the power spectra are identical for each axis. In this case, the input spectral density matrix reduces to a special form,

$$\left[G_{\ddot{r}\ddot{r}}(i\omega)\right] = G(\omega) \begin{bmatrix} 1 & 0 & 0 \\ 0 & 1 & 0 \\ 0 & 0 & 1 \end{bmatrix} \qquad \text{D-28}$$

and Eq. D-27 can be simplified to:

$$\left[G_{\beta\beta}(i\omega)\right] = G(\omega) \left[\phi_n^*\right] [A_R] [A_R]^T \left[\phi_n\right] \qquad \text{D-29}$$

The typical coefficient in Eq. D-29 is a cross-spectral density between $\beta_m(t)$ and $\beta_n(t)$, given by:

$$G_{\beta_m\beta_n}(i\omega) = \left[\begin{array}{l}\text{mn coefficient of} \\ \text{the matrix product} \\ [A_R]\,[A_R]^T\end{array}\right] \times \qquad \text{D-30}$$

$$\times \left[\frac{G(\omega)/\bar{K}_m\bar{K}_n}{\left[1 - \frac{\omega^2}{\omega_m^2} - 2i\zeta_m\frac{\omega}{\omega_m}\right]\left[1 - \frac{\omega^2}{\omega_n^2} + 2i\zeta_n\frac{\omega}{\omega_n}\right]}\right]$$

Hence, numerical computation of the modal spectral density matrix is straightforward, after an eigenvalue analysis has been executed to determine [U], $[\diagdown\overline{K}\diagup]$, $[\diagdown\omega_n^2\diagup]$ and when the rigid-body modes $[U_R]$ have been defined. It is then an easy step to obtain response spectra for physical quantities of interest. For example, the transformation between displacements {q} and modal responses {β} is real-valued and static (Eq. D-10). Hence:

$$[G_{qq}(i\omega)] = [U]\,[G_{\beta\beta}(i\omega)]\,[U]^T \qquad \text{D-31}$$

In a similar manner, let [J] be a logical matrix which selects a nodal-displacement subset, [J] {q}, which are the degrees of freedom to which a given element is coupled. The internal loads acting on the element are then obtained from another real-valued static transformation,

$$\{f\} = [k]\,[J]\,\{q\} = [k]\,[J]\,[U]\,\{\beta\} = [A]\,\{\beta\} \qquad \text{D-32}$$

where [k] is the element stiffness matrix, and the corresponding response spectra are:

$$[G_{ff}(i\omega)] = [A]\,[G_{\beta\beta}(i\omega)]\,[A]^T \qquad \text{D-33}$$

4. CALCULATION OF EXCEEDANCE RATES

If a zero-mean stationary random process is assumed to be Gaussian, then its statistics are uniquely determined by weighted integrals of its power spectral density [15]. Specifically, let x(t) be a Gaussian random process with power spectral density $G_{xx}(\omega)$. Then the level exceedance curve for x(t) is given by:

$$E(x) = 1/2\ \overline{\nu}_{ox}\ e^{-x^2/2\sigma_x^2} \qquad \text{D-34}$$

where E(x) is the number of upcrossings of the level, x, per unit time (or number of downcrossings of -x), and where:

$$\sigma_x^2 = \int_{-\infty}^{\infty} G_{xx}(\omega)\, d\omega \qquad \text{D-35}$$

$$\bar{\nu}_{ox} = \frac{1}{\pi\sigma_x}\left[\int_{-\infty}^{\infty} \omega^2 G_{xx}(\omega)\, d\omega\right]^{1/2} \qquad \text{D-36}$$

A more complicated expression involving $\int_{-\infty}^{\infty} \omega^4 G_{xx}(\omega)d\omega$ has been derived for peak exceedances [15]. However, the level and peak exceedance curves are asymptotic for large values of x/σ_x, where the number of peaks per unit time in an infinitesimal band at level, x, can be approximated by -dE(x)/dx.

The foregoing concepts can be applied efficiently to finite-element models by recognizing that the spectral density integrations can be carried out at the modal level. Also, since

$$[G_{\beta\beta}(i\omega)] = \text{Re}\,[G_{\beta\beta}(\omega)] + i\,\text{Im}\,[G_{\beta\beta}(\omega)] \qquad \text{D-37}$$

where the real and imaginary parts are symmetric and skew-symmetric, respectively, the numerical procedure can be reduced to integration of $\text{Re}[G_{\beta\beta}]$ over $\omega \geq 0$. Define:

$$[S_{\beta\beta}^{(0)}] = \int_0^{\infty} 2\text{Re}\,[G_{\beta\beta}(\omega)]\, d\omega \qquad [S_{\beta\beta}^{(2)}] = \int_0^{\infty} 2\omega^2\, \text{Re}\,[G_{\beta\beta}(\omega)]\, d\omega \qquad \text{D-38}$$

$$[S_{qq}^{(0)}] = [U]\,[S_{\beta\beta}^{(0)}]\,[U]^T \qquad [S_{qq}^{(2)}] = [U]\,[S_{\beta\beta}^{(2)}]\,[U]^T \qquad \text{D-39}$$

$$[S_{ff}^{(0)}] = [A]\,[S_{\beta\beta}^{(0)}]\,[A]^T \qquad [S_{ff}^{(2)}] = [A]\,[S_{\beta\beta}^{(2)}]\,[A]^T \qquad \text{D-40}$$

Then, for example, $[S_{qq}^{(0)}]$ can be recognized as the correlation matrix for the nodal displacements $q_1, q_2, \ldots, q_N$:

$$[S_{qq}^{(0)}] = \begin{bmatrix} \sigma_1^2 & & & & \text{(Symmetric)} \\ \rho_{12}\sigma_1\sigma_2 & \sigma_2^2 & & & \\ \rho_{13}\sigma_1\sigma_3 & \rho_{23}\sigma_2\sigma_3 & \sigma_3^2 & & \\ \vdots & \vdots & \vdots & \ddots & \\ \rho_{1N}\sigma_1\sigma_N & \rho_{2N}\sigma_2\sigma_N & \rho_{3N}\sigma_3\sigma_N & \cdots & \sigma_N^2 \end{bmatrix} \qquad \text{D-41}$$

Also, the information required to calculate the zero-crossing rate, $\bar{\nu}_{oj}$ for q_j appears in the j^{th} diagonal of $[S_{qq}^{(2)}]$:

$$[S_{qq}^{(2)}] = \pi^2 \begin{bmatrix} (\sigma_1\bar{\nu}_{o1})^2 & & & \text{(Symmetric)} \\ & (\sigma_2\bar{\nu}_{o2})^2 & & \\ & & \ddots & \\ \text{(Plus off-diagonal terms)} & & & (\sigma_N\bar{\nu}_{oN})^2 \end{bmatrix} \qquad \text{D-42}$$

The matrices $[S_{ff}^{(0)}]$ and $[S_{ff}^{(2)}]$ can be used in a similar manner for the internal-load exceedance rates. In the present case, cross-correlations are of no interest. Hence, only the diagonal terms in $[S_{qq}^{(0)}],\ldots,[S_{ff}^{(2)}]$ need be computed.

5. EXCITATION INPUT DATA

Specification MJS77-3-240 [5] for the Mariner-Jupiter-Saturn mission was used as a guideline for the present investigation. The specification included random-vibration input spectra based on a 1600 to 1800 lb. spacecraft atop a Titan-IIIC booster, a configuration similar to the hypothetical communications satellite launch which acts as a baseline for this study. The input spectra are illustrated in Figure D-1. The two spectra shown refer to different locations in the MJS spacecraft. The specification calls for exposure of the structure to the same spectrum on three orthogonal axes, but makes no statement about cross-correlation between axes.

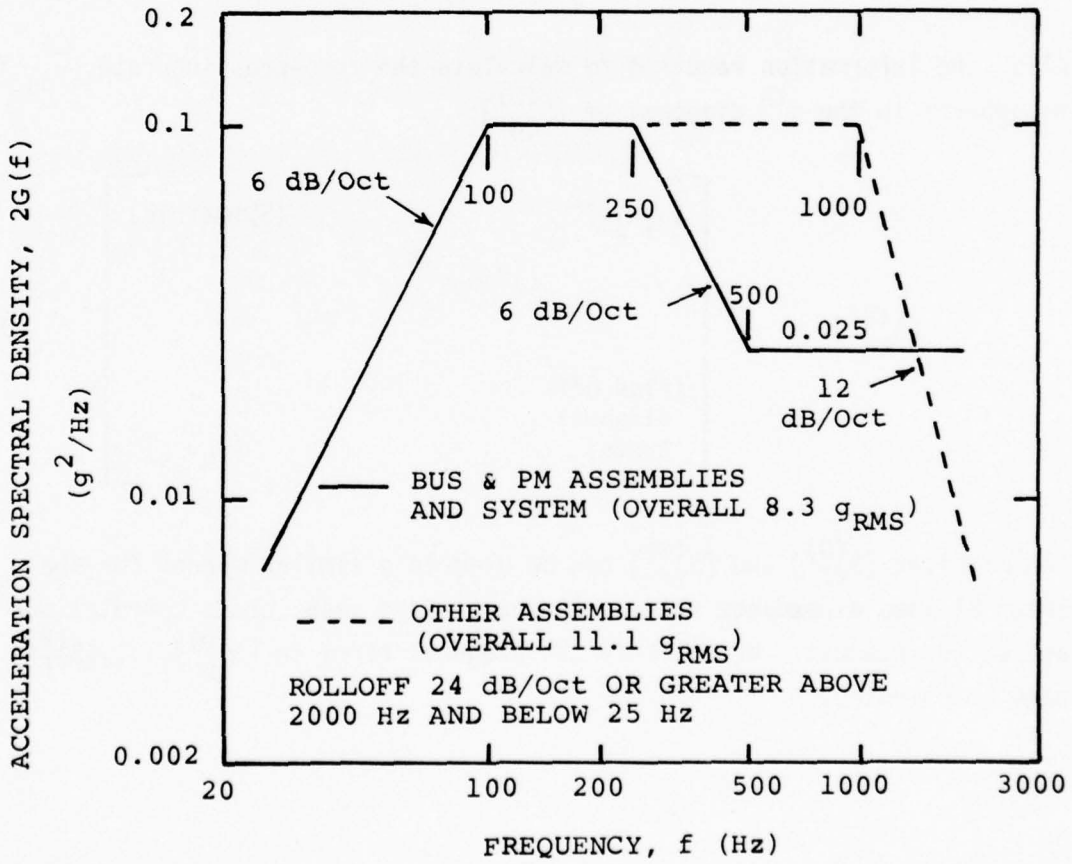


Figure D-1. Input Spectra (from MJS77-3-240)

In the present case, two somewhat optimistic assumptions have been combined with the MJS guidelines. First, it has been assumed that there is no correlation between the inputs (condition of minimum phase reinforcement) because of the lack of correlation data and because the analysis procedure is simplified. Second, it has been assumed arbitrarily that inputs above 200 Hz will be attenuated by the spacecraft structure between the booster and feed-truss interfaces. Hence, the spectral analysis was carried out only in the frequency range $2 \leq \omega/2\pi \leq 200$ Hz. Both assumptions should be re-examined when more experimental data become available.

6. FINITE-ELEMENT MODELS

The finite-element models of the ATS/3-Ring and Tripod-B designs are illustrated schematically in Figures D-2 and D-3, respectively. The ATS/3-Ring model consists of 64 elements and 40 nodes (240 degrees of freedom) with the first 8 nodes (48 degrees of freedom) constrained. The Tripod-B model consists of 30 elements and 16 nodes (96 degrees of freedom) with the first three nodes (18 degrees of freedom) constrained. The constraints represent the antenna/spacecraft interface, at which the base excitation is input.

Coordinates of the nodes with respect to the axes shown in the figures are presented in Tables D-1 and D-2. The section properties assumed for the elements are summarized in Tables D-3 and D-4. Note that because all element cross-sections are assumed to be circular, the section torsion constant is simply $J = 2I$.

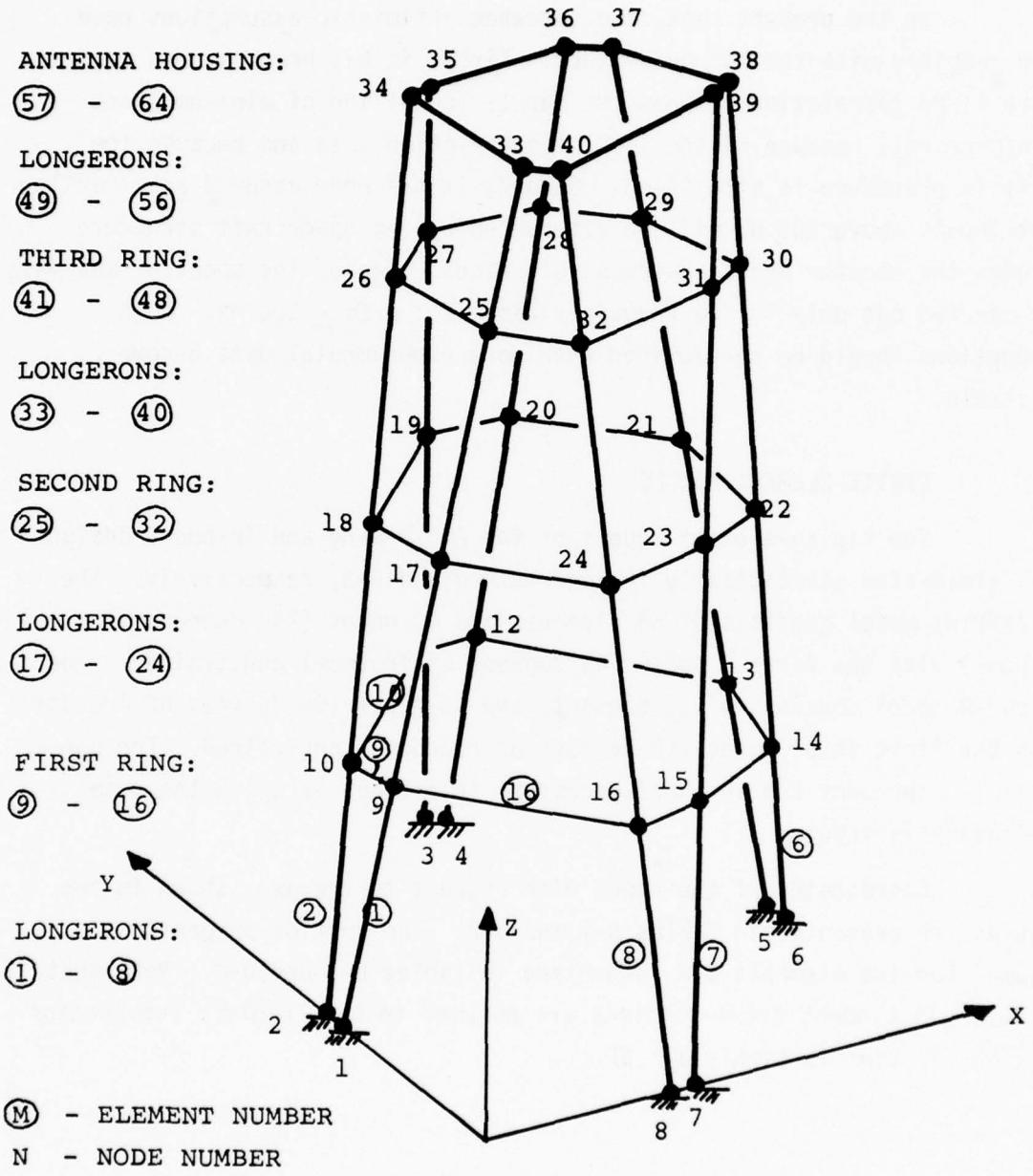


Figure D-2. ATS/3-Ring Finite-Element Model

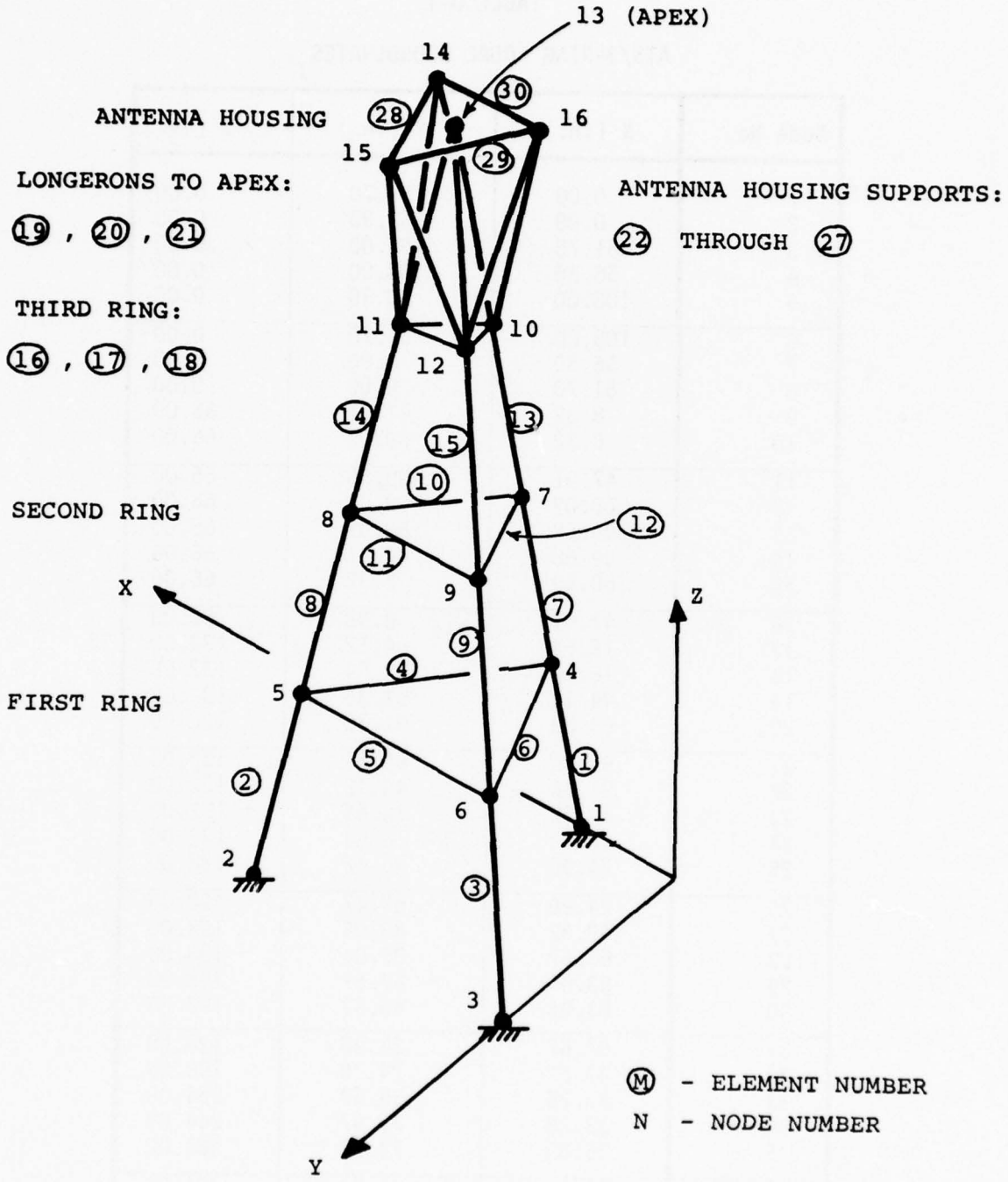


Figure D-3. Tripod-B Finite-Element Model

TABLE D-1

ATS/3-RING NODAL COORDINATES

Node No.	X (in.)	Y (in.)	Z (in.)
1	0.00	51.70	0.00
2	0.00	56.30	0.00
3	51.70	108.00	0.00
4	56.30	108.00	0.00
5	108.00	56.30	0.00
6	108.00	51.70	0.00
7	56.30	0.00	0.00
8	51.70	0.00	0.00
9	8.32	47.91	66.00
10	8.32	60.09	66.00
11	47.91	99.68	66.00
12	60.09	99.68	66.00
13	99.68	60.09	66.00
14	99.68	47.91	66.00
15	60.09	8.32	66.00
16	47.91	8.32	66.00
17	16.64	44.12	132.00
18	16.64	63.89	132.00
19	44.12	91.36	132.00
20	63.89	91.36	132.00
21	91.36	63.89	132.00
22	91.36	44.12	132.00
23	63.89	16.64	132.00
24	44.12	16.64	132.00
25	24.96	40.32	198.00
26	24.96	67.67	198.00
27	40.32	83.04	198.00
28	67.67	83.04	198.00
29	83.04	67.67	198.00
30	83.04	40.32	198.00
31	67.67	24.96	198.00
32	40.32	24.96	198.00
33	33.28	36.53	264.00
34	33.28	71.47	264.00
35	36.53	74.72	264.00
36	71.47	74.72	264.00
37	74.72	71.47	264.00
38	74.72	36.53	264.00
39	71.47	33.28	264.00
40	36.53	33.28	264.00

TABLE D-2

TRIPOD-B NODAL COORDINATES

Node No.	X (in.)	Y (in.)	Z (in.)
1	0.000	45.033	0.000
2	78.000	90.067	0.000
3	78.000	0.000	0.000
4	13.000	45.033	66.000
5	71.500	78.809	66.000
6	71.500	11.258	66.000
7	26.000	45.033	132.000
8	65.000	67.550	132.000
9	65.000	22.517	132.000
10	39.000	45.033	198.000
11	58.500	56.292	198.000
12	58.500	33.775	198.000
13	52.000	45.033	264.000
14	38.500	68.416	264.000
15	79.000	45.033	264.000
16	38.500	21.651	264.000

TABLE D-3

ATS/3-RING ELEMENT PROPERTIES

Location & Element Number	Element Type	Young's Modulus E (psi)	Shear Modulus G (psi)	Section Area A (in^2)	Bending Area Inertia I, (in^4)	Mass/Unit Length ρ ($lb\ sec^2/in^2$)	Thermal Exp. Coefficient α ($°C^{-1}$)
Longerons 1-8, 17-24, 33-40, 49-56	Beam	25×10^6	0.8×10^6	0.725	0.669	1.13×10^{-4}	0.3×10^{-6}
Stabilizer Rings 9-16, 25-32, 41-48	Pin-Joint Bar	25×10^6	0.8×10^6	0.177	0.0196	2.74×10^{-5}	0.3×10^{-6}
Antenna Housing 57-64	Beam	20×10^6	0.8×10^6	0.880	0.959	7.87×10^{-3}	20.0×10^{-6}

TABLE D-4

TRIPOD-B ELEMENT PROPERTIES

Location & Element Number	Element Type	Young's Modulus E (psi)	Shear Modulus G (psi)	Section Area A (in^2)	Bending Area Inertia I, (in^4)	Mass/Unit Length ρ ($lb\ sec^2/in^2$)	Thermal Exp. Coefficient α ($°C^{-1}$)
Longerons 1-3, 7-9, 13-15, 19-21	Beam	21×10^6	0.65×10^6	0.933	1.43	1.45×10^{-4}	0.3×10^{-6}
Stabilizer Rings 4-6, 10-12, 16-18	Pin-Joint Bar	25×10^6	0.65×10^6	0.150	0.034	2.33×10^{-5}	0.3×10^{-6}
Antenna Housing Supports 22-27	Pin-Joint Bar	25×10^6	0.65×10^6	0.848	0.774	1.32×10^{-4}	0.3×10^{-6}
Antenna Housing 28-30	Beam	25×10^6	0.65×10^6	0.733	0.782	8.87×10^{-3}	20.0×10^{-6}

7. RESULTS OF EIGENVALUE ANALYSIS

Eigenvalue analyses of the ATS/3-Ring and Tripod-B designs were conducted with the parameters shown in Table D-5, using program SFRAME (Appendix E). A tolerance parameter $\varepsilon = 10^{-2}$ was specified. Hence, the errors in the computed frequencies which have converged are bounded by $\pm$10 percent. The results obtained for the two designs are given in Tables D-6 and D-7. Note that the bending and rocking modes occur in pairs corresponding to motions in two separate vertical-lateral planes. The mode-shape descriptions are interpreted schematically in Figure D-4.

TABLE D-5

ANALYSIS PARAMETERS

Parameter \ Design	ATS/3-Ring	Tripod-B
Total DOF in finite-element model	240	96
No. DOF Constrained	48	18
No. free DOF	192	78
No. modes in Subspace, N'	60	40
No. modes asked to converge, N"	40	25
No. modes actually converged	41	40
No. Iterations completed	7	14

TABLE D-6

VIBRATION ANALYSIS OF ATS/3-RING

Mode	Frequency (Hz)	Remarks*	Mode	Frequency (Hz)	Remarks
1	6.99	First	31	94.66	
2	7.00	Bending	32	94.68	
3	9.93	1-T	33	97.86	
4	14.62	1-OV	34	109.8	
5	15.44	2-OV	35	109.8	
6	15.45	2-OV	36	143.3	
7	16.45	3-OV	37	159.6	
8	16.81		38	159.7	
9	17.82		39	171.2	
10	17.83		40	172.2	
11	19.49		41	173.3	
12	28.54		42	175	Not Fully
13	42.98		43	180	Converged
14	44.07		44	182	
15	44.08		45	182	
16	44.65		46	182	
17	47.92		47	182	
18	48.38		48	184	
19	48.48		49	186	
20	48.48		50	187	
21	50.46		51	191	
22	75.99		52	194	
23	75.99		53	212	
24	75.99		54	217	
25	76.14		55	242	
26	90.05		56	251	
27	90.08		57	271	
28	90.52		58	272	
29	90.80		59	273	
30	94.15		60	278	

*T = Torsion; OV = ovalizing.

TABLE D-7

VIBRATION ANALYSIS OF TRIPOD-B

Mode	Frequency (Hz)	Remarks
1	2.67	First Torsion
2	9.05	First
3	9.05	Bending
4	10.63	First Top
5	10.67	Rocking
6	33.38	Second Bending
7	33.68	Second Torsion
8	34.69	
9	34.91	
10	45.50	
11	46.08	
12	65.68	
13	65.69	
14	91.65	
15	91.65	
16	94.32	
17	145.6	
18	145.6	
19	157.4	
20	174.7	
21	190.8	
22	191.0	
23	199.3	
24	208.9	
25	210.8	
26	210.8	
27	212	Convergence Still OK
28	245	
29	245	
30	261	
31	314	
32	316	
33	321	
34	341	
35	343	
36	372	
37	372	
38	386	
39	463	
40	464	



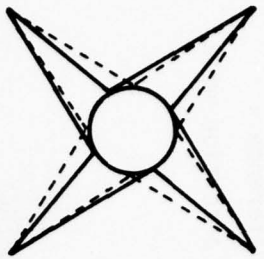
FIRST BENDING
ATS/3-RING #1,2
TRIPOD-B #2,3



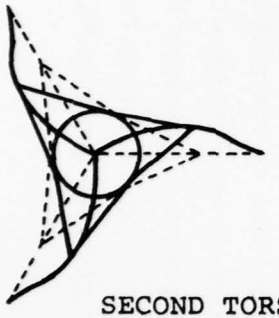
SECOND BENDING
TRIPOD-B #6



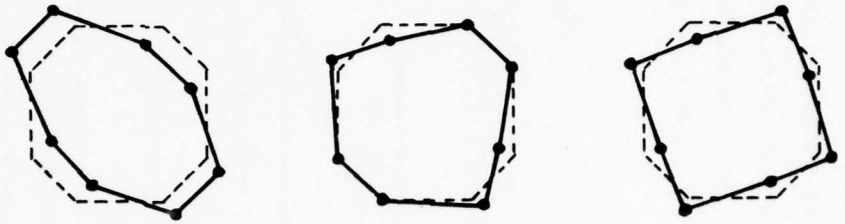
FIRST TOP-ROCKING
TRIPOD-B #4,5



FIRST TORSION
(PLAN VIEW)
ATS/3-RING #3
TRIPOD-B #1



SECOND TORSION
(PLAN VIEW)
TRIPOD-B #7



FIRST (#4) SECOND (#5,6) THIRD (#7)

ATS/3-RING OVALIZING MODES (CROSS SECTION SHOWN AT TYPICAL STABILIZER RING)

Figure D-4. Schematic of Mode Shapes

The results for the first bending modes agree well with previous estimates obtained by computing an effective stiffness for the truss from static deflection due to lateral load [1]. The comparison is summarized in Table D-8. Note that the approximate method used in Reference 1 failed to identify the lowest natural mode for Tripod-B, a torsion mode (see Table D-7).

TABLE D-8

COMPARISON OF PRESENT RESULTS WITH
APPROXIMATE ESTIMATE FOR FIRST BENDING FREQUENCY

Method \ Design	ATS/3-Ring	Tripod-B
Present eigenvalue analysis	6.99 7.00	9.05 9.05
Approximate static Estimate	6.80	10.7
(Frequencies in Hz)		

Figures D-5 and D-6 illustrate the relationship between the natural frequencies of the two designs and the MJS input power spectra. One conclusion which can be drawn immediately from these plots is that the first few modes in each design will be well isolated from the inputs. Hence, the presence of the very low-frequency torsional mode in Tripod-B is not of great concern during launch. Nevertheless, all modes obtained for both designs were included in the subsequent response analyses.

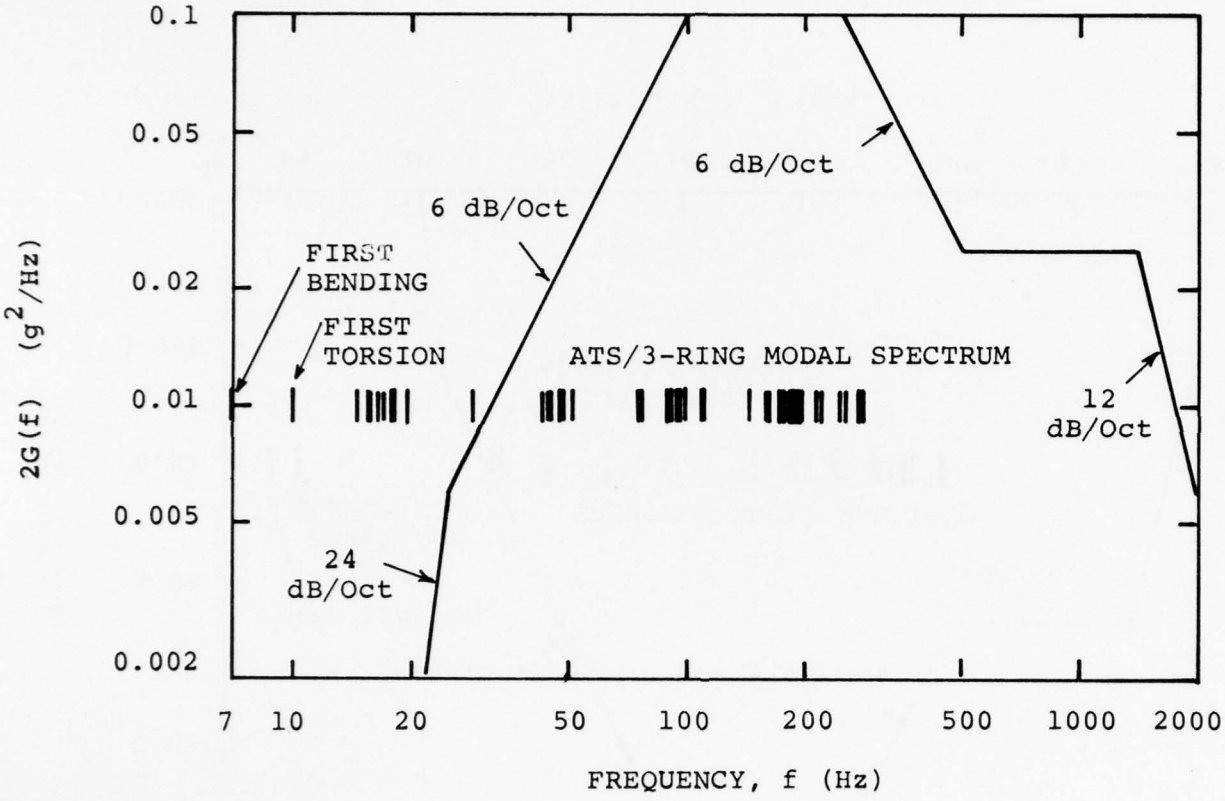


Figure D-5. Comparison of ATS/3-Ring Natural Frequencies with MJS77 Design Input Power Spectrum

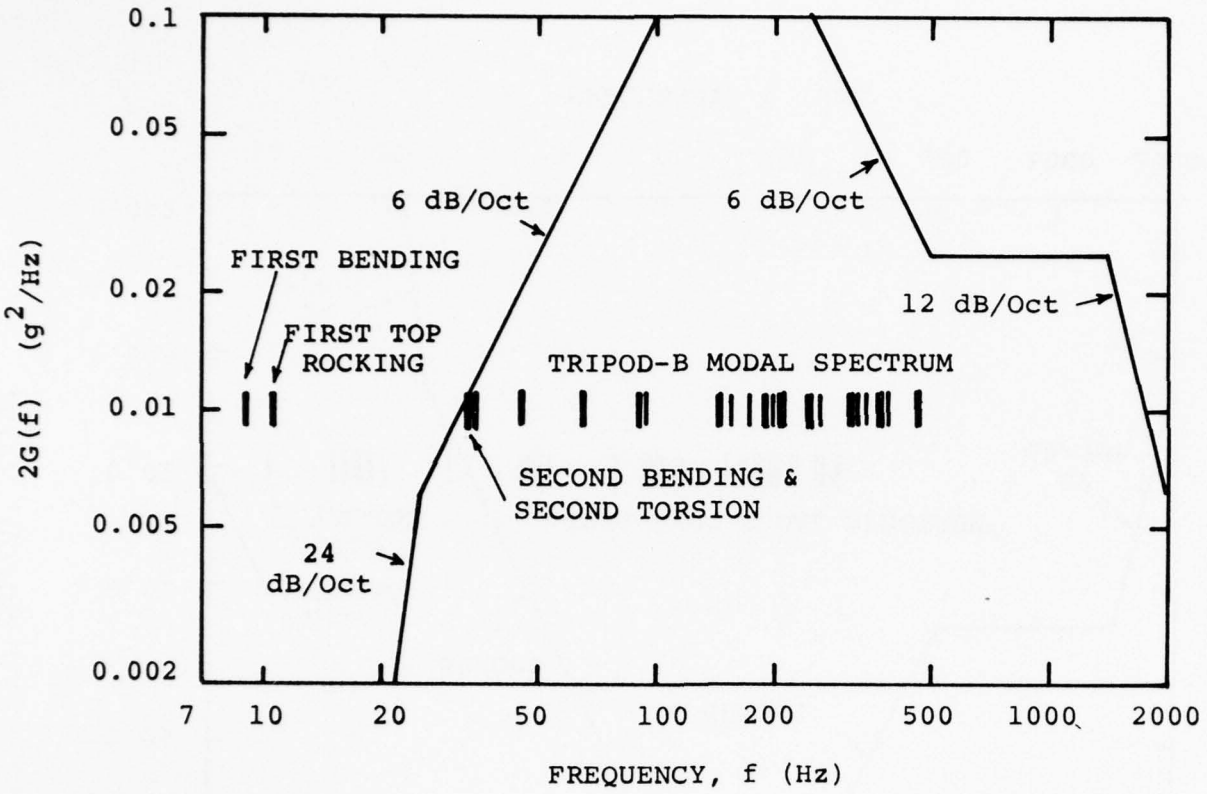


Figure D-6. Comparison of Tripod-B Natural Frequencies with MJS77 Design Input Power Spectrum

8. RESULTS OF RESPONSE ANALYSIS

Response analyses of both designs were conducted in the manner outlined by Eqs. D-17 through D-42, but with modal integration restricted to $2 \leq f = \omega/2\pi \leq 200$ Hz:

$$[S^{(0)}_{\beta\beta}] \cong \int_2^{200} 2\mathrm{Re}\,[G_{\beta\beta}(f)]\,df \qquad \text{D-43}$$

$$[S^{(2)}_{\beta\beta}] \cong \int_2^{200} 2f^2\,\mathrm{Re}\,[G_{\beta\beta}(f)]\,df$$

Note that, with the frequency domain in units of Hz, Eq. D-36 for the zero-crossing rate must be replaced by:

$$\text{(D-44)} \qquad \bar{\nu}_o = \frac{2}{\sigma}\left[\int f^2 G(f)\,df\right]^{1/2} \qquad \text{D-44}$$

These analyses were conducted with program SPECTRA (Appendix F). The same rules for assigning damping factors to natural modes were applied to both designs, as indicated in Table D-9.

TABLE D-9

RULES FOR ASSIGNMENT OF MODAL DAMPING

Natural Frequency $f = \frac{\omega}{2\pi}$ (Hz)	Damping Factor, ζ
$0 < f \leq 10$	0.02
$10 < f \leq 35$	0.05
$35 < f \leq 110$	0.10
$110 < f$	0.20

Tables D-10 and D-11 summarize the results obtained for displacement responses. The most significant data pertain to lateral deflections (XY plane) of the nodes at the antenna housing support points. These deflections can also be assumed to represent the deflections at the outer rim of the antenna housing, where clearance inside the payload fairing must be assured. The two designs can be comparatively assessed by means of first-passage statistics for antenna lateral deflection. Assuming that the larger deflections occur independently of one another, exceedances of a given amount will be Poisson-distributed in time. The expected time to first passage of a given value of deflection, x, parallel to the X-axis is then given by:

$$\bar{t}_{FP} = 1/E(x) = \frac{2e^{x^2/2\sigma_x^2}}{\bar{\nu}_{ox}} \text{ sec} \qquad \text{D-45}$$

Since the Titan-IIIC first-stage boost phase consumes 120 sec [14], the required clearance may be estimated, e.g., by designing to first passage in one stage time. Substituting $\bar{t}_{FP}$ = 120 sec, and $\bar{\nu}_o$ = 274 sec^{-1} in Eq. D-45 then leads to $x/\sigma_x = 4.4$.

However, the clearance problem is not as simple as indicated by Eq. D-45 because the simultaneous effects of lateral displacements x and y must be considered. Bounds on the first-passage value of radial deflection,

$$r = \sqrt{x^2 + y^2} \qquad \text{D-46}$$

can be considered by examining two extreme cases. If x and y are perfectly correlated, then $r = x\sqrt{2}$ is Gaussian and the first-passage value is given by:

$$r_{120}^{max} = 4.4\,\sigma_x\sqrt{2} \qquad \text{D-47}$$

TABLE D-10

STANDARD DEVIATIONS (σ) AND ZERO-CROSSING RATES ($\bar{\nu}_o$) OF DISPLACEMENTS FOR ATS/3-RING*

Location	DISPLACEMENT ALONG AXIS					
	X		Y		Z	
	σ	$\bar{\nu}_o$	σ	$\bar{\nu}_o$	σ	$\bar{\nu}_o$
Plane of first stabilizer ring	.402	274	.201	274	.0433	274
	.398	274	.201	274	.0429	274
	.193	275	.402	274	.0433	274
	.193	275	.402	274	.0429	274
	.398	274	.198	274	.0425	274
	.398	274	.198	274	.0433	274
	.197	275	.402	274	.0433	274
	.197	275	.406	274	.0437	274
Plane of second stabilizer ring	1.063	274	.510	275	.122	274
	1.051	274	.510	275	.121	274
	.506	274	1.055	274	.121	274
	.506	274	1.055	274	.122	274
	1.055	274	.510	275	.121	274
	1.055	274	.510	275	.121	274
	.510	274	1.055	274	.121	274
	.510	274	1.063	274	.122	274
Plane of third stabilizer ring	1.302	275	.684	275	.144	275
	1.291	275	.684	275	.143	275
	.692	275	1.291	275	.142	275
	.692	275	1.291	275	.143	275
	1.294	275	.684	275	.144	275
	1.294	275	.684	275	.143	275
	.692	275	1.291	275	.143	275
	.692	275	1.298	275	.144	275
Attachments to antenna housing	.696	275	.696	275	.0518	274
	.696	275	.696	275	.0518	274
	.696	275	.696	275	.0518	274
	.696	275	.696	275	.0518	274
	.696	275	.696	275	.0518	274
	.696	275	.696	275	.0518	274
	.696	275	.696	275	.0518	274
	.696	275	.696	275	.0518	274

*Standard deviations in inches.
Zero-crossing rates per second.

TABLE D-11

STANDARD DEVIATIONS (σ) AND ZERO-CROSSING RATES ($\bar{\nu}_0$)
OF DISPLACEMENTS FOR TRIPOD-B*

Location	DISPLACEMENT ALONG AXIS					
	X		Y		Z	
	σ	$\bar{\nu}_0$	σ	$\bar{\nu}_0$	σ	$\bar{\nu}_0$
Plane of first stabilizer ring	.150	274	.150	273	.0071	267
	.150	274	.150	273	.0069	267
	.150	274	.150	273	.0074	270
Plane of second stabilizer ring	.375	273	.376	273	.0282	273
	.375	273	.377	273	.0287	274
	.376	273	.377	273	.0284	273
Plane of third stabilizer ring	.452	273	.464	274	.0213	272
	.460	274	.460	273	.0214	273
	.460	273	.460	273	.0216	273
Apex joint	.358	273	.356	272	.0076	254
Attachments to antenna housing	.440	273	.440	272	.0196	270
	.444	273	.440	272	.0185	266
	.440	273	.440	272	.0192	268

*Standard deviations in units of inches.
Zero-crossing rates per second.

On the other hand, if $\sigma_x = \sigma_y$, but x and y are uncorrelated, then

$$r = \sqrt{x^2 + y^2}$$

follows a Rayleigh distribution:

$$F(r) = 1 - e^{-r^2/2\sigma_x^2} \qquad \text{D-48}$$

In this case, a first-passage value can be estimated by equating cumulative distribution values:

$$1 - F\left(r_{120}^{min}\right) = 1 - \Phi\left(\frac{x_{120}}{\sigma_x}\right) = 1 - \Phi\,(4.4) = 5.41 \times 10^{-6} \qquad \text{D-49}$$

where Φ is the cumulative Gaussian distribution. The results of these calculations, summarized in Table D-12, indicate that the Tripod-B design requires somewhat less clearance than the ATS/3-Ring design.

TABLE D-12

RADIAL CLEARANCE REQUIRED TO AVOID FIRST-PASSAGE COLLISION

Bound \ Design	C L E A R A N C E (Inches)	
	ATS/3-Ring	Tripod-B
Uncorrelated, r_{120}^{Min}	3.43	2.18
Correlated, r_{120}^{Max}	4.33	2.76

Tables D-13 through D-17 present a survey of typical statistics obtained for the internal loads. Longeron locations near the end attachments, stabilizer rings, and (for Tripod-B) the apex joint are shown in Tables D-13 and D-14. Note that the forces and moments in these tables are given in the global reference-axis system (see Figures D-2 and D-3). Tables D-15 and D-16 cover the pin-joint elements used to model the stabilizers and (for Tripod-B) the antenna supports. Table D-17 brings together the most highly stressed locations in each design for the purpose of comparative assessment of static margin and fatigue damage accumulation. The longeron locations in Table D-17 are described in terms of components resolved in the element local-axis system.

TABLE D-13

ATS/3-RING TYPICAL INTERNAL LOAD STATISTICS FOR LONGERONS

Reference Axis	X		Y		Z	
Force Parallel to Axis	σ (lb)	$\bar{\nu}_o$ (sec^{-1})	σ (lb)	$\bar{\nu}_o$ (sec^{-1})	σ (lb)	$\bar{\nu}_o$ (sec^{-1})
Spacecraft Attachments	502	274	228	274	3621	274
First Ring	495	274	221	274	3621	274
Second Ring	487	274	203	274	3621	274
Third Ring	479	274	230	274	3621	274
Antenna Attachments	479	274	230	274	3621	274
Moment About Axis	σ (in lbs)	$\bar{\nu}_o$ (sec^{-1})	σ (in lbs)	$\bar{\nu}_o$ (sec^{-1})	σ (in lbs)	$\bar{\nu}_o$ (sec^{-1})
Spacecraft Attachments	2117	274	4134	274	284	273
First Ring	298	254	858	272	36	235
Second Ring	692	273	1704	272	74	269
Third Ring	711	271	3686	275	226	273
Antenna Attachments	1982	265	4985	274	188	246

TABLE D-14

TRIPOD-B TYPICAL INTERNAL LOAD STATISTICS FOR LONGERONS

Reference Axis	X		Y		Z	
Force Parallel to Axis	σ (lb)	$\bar{\nu}_0$ (sec^{-1})	σ (lb)	$\bar{\nu}_0$ (sec^{-1})	σ (lb)	$\bar{\nu}_0$ (sec^{-1})
Spacecraft Attachments	1321	273	36	272	6530	273
First Ring	1310	273	18	260	6530	273
Second Ring	1287	273	11	279	6530	273
Third Ring	41	276	18	286	291	276
Apex Joint	41	276	18	286	291	276
Moment About Axis	σ (in lbs)	$\bar{\nu}_0$ (sec^{-1})	σ (in lbs)	$\bar{\nu}_0$ (sec^{-1})	σ (in lbs)	$\bar{\nu}_0$ (sec^{-1})
Spacecraft Attachments	2736	273	2767	274	541	273
First Ring	241	221	491	265	51	226
Second Ring	981	267	1302	271	190	266
Third Ring	1789	282	1356	276	349	282
Apex Joint	210	314	284	279	45	312

TABLE D-15

ATS/3-RING TYPICAL STATISTICS FOR AXIAL FORCES IN STABILIZERS

Location	σ (lb)	$\bar{\nu}_0$ (sec^{-1})
First Ring	8	282
Second Ring	23	267
Third Ring	68	259

TABLE D-16

TRIPOD-B TYPICAL STATISTICS FOR AXIAL FORCES IN STABILIZERS AND ANTENNA SUPPORTS

Location	σ (lb)	$\bar{\nu}_0$ (sec^{-1})
First Ring	10	325
Second Ring	27	353
Third Ring	1461	273
Antenna Supports	3791	272

TABLE D-17

SUMMARY OF LOAD STATISTICS FOR CRITICAL LOCATIONS

Location	Axial Force, P		Shear Force, V		Bending Moment, M		Torque, T	
	σ_P (lb)	$\bar{\nu}_{oP}(sec^{-1})$	σ_V (lb)	$\bar{\nu}_{oV}(sec^{-1})$	σ_M (in lb)	$\bar{\nu}_{oM}(sec^{-1})$	σ_T(in lb)	$\bar{\nu}_{oT}(sec^{-1})$
ATS/3-RING:								
Longeron at spacecraft attachment	3625	274	521	274	4643	274	311	274
Third Stabilizer	68	259	-	-	-	-	-	-
TRIPOD-B:								
Longeron at spacecraft attachment	6662	273	77	273	3783	273	1060	273
Third Stabilizer	1461	273	-	-	-	-	-	-
Antenna Support	3791	272	-	-	-	-	-	-

9. STATIC MARGINS

Static margins for preliminary design were previously based on approximate scaling of the NASA ATS-6 antenna-feed truss qualification test loads [1]. However, better estimates for the maximum applied loads can now be made in terms of first-passage statistics. Axial compression is the critical load component for buckling, and the combination of axial load plus bending must be considered for a strength check on the longerons.

Table D-18 summarizes the comparisons between first-passage axial loads for a 120-sec boost, 4.4 σ_P, and Euler buckling loads P_{CR}. The latter were obtained by scaling the value P_{CR} = 29 KIPS obtained previously for the ATS/3-Ring longerons [1] in accordance with:

$$P'_{CR} = P_{CR} \left(\frac{L}{L'}\right)^2 \left(\frac{I'}{I}\right) \qquad \text{D-50}$$

for other members, where L is the unsupported length and I is the section inertia for bending. The results indicate that all components except the Tripod-B antenna housing supports possess adequate margins, although the $\overline{P}_{FP}/P_{CR}$ ratios are higher in most cases than was allowed in preliminary design. However, the value $\overline{P}_{FP}/P_{CR} \cong .75$ for the Tripod-B antenna housing supports is unacceptable. An acceptable value $\overline{P}_{FP}/P_{CR} \cong .375$ could be obtained by doubling the wall thickness of these components, a design change which would add about 22 lb. to the weight of the structure.

TABLE D-18

EXPECTED FRACTION OF CRITICAL BUCKLING LOAD ACHIEVED AT FIRST PASSAGE

Location	First Passage $\overline{P}_{FP} = 4.40\ \sigma_P$ (KIPS)	Buckling Load P_{CR} (KIPS)	$\overline{P}_{FP}/P_{CR}$
ATS/3-Ring:			
Longeron	15.95	29.00	0.55
Third Stabilizer	0.30	2.44	0.12
Tripod-B:			
Longeron	29.31	61.50	0.48
Third Stabilizer	6.44	12.68	0.51
Antenna Support	16.70	22.20	0.75

Strength-check calculations for the longerons were made by combining first-passage loads with engineering beam theory:

$$\overline{S}_P^{FP} = 4.4\ \sigma_P/A \qquad \text{D-51A}$$

$$\overline{S}_B^{FP} = 4.4\ \sigma_M\ R_{max}/I \qquad \text{D-51B}$$

$$\overline{S}_T^{FP} = 4.4\ \sigma_T\ R_{max}/J \qquad \text{D-51C}$$

where $\overline{S}_P^{FP}$, $\overline{S}_B^{FP}$, and $\overline{S}_T^{FP}$ are, respectively, axial tension or compression stress, maximum tension or compression stress due to bending, and maximum shear stress due to torsion, and where A is the section area, I and J the bending and torsion inertias, and R_{max} the outside radius of the tube. In addition, stress concentration factors (SCF) between 1.5 and 2.5 for axial and bending stress were assumed to account for possible effects of the metal joint which attaches the longeron to the spacecraft. The results are summarized in Table D-19.

It is apparent that the applied torque makes only a small contribution to the stress state. Also, the axial stresses alone would be well within the allowables for both designs. However, an in-phase combination of axial and bending stresses exceeds the design allowables for both ATS/3-Ring and Tripod-B, and exceeds static ultimate strength for ATS/3-Ring as well. To remedy the latter situation while maintaining $\overline{P}_{FP}/P_{CR}$ ratios constant would require a 19 percent increase in the longeron wall thickness, or about 18 lb. weight added to the ATS/3-Ring structure.

Finally, it should be noted that the steady-state contribution to axial loading in the longerons has been neglected. This is reasonable in view of the relative orders of magnitude involved. For example, assuming that the steady acceleration is 10g along the truss Z-axis, and recognizing that the total hardware weights above the spacecraft (antenna hardware plus feed truss) are approximately 640 and 589 lb., respectively, for ATS/3-Ring

TABLE D-19

LONGERON STRENGTH CHECK BASED ON FIRST-PASSAGE LOADS

Item	D E S I G N	
	ATS/3-Ring	Tripod-B
Material	High-modulus Gr/E	High Strength Gr/E
Static Strength, s_s (ksi)	100	180
Design Allowable, 0.6 s_s (ksi)	60	108
First-Passage (120-sec) stresses:		
Axial, $\overline{S}_P^{FP}$ (ksi)	22.0	31.2
Bending, $\overline{S}_B^{FP}$ (ksi)	42.8	21.0
Shear, $\overline{S}_T^{FP}$ (ksi)	1.4	2.8
$\overline{S}_P^{FP} + \overline{S}_B^{FP}$ (ksi)	64.8	52.2
$(\overline{S}_P^{FP} + \overline{S}_B^{FP})$ (SCF=1.5) (ksi)	97.2	78.3
$(\overline{S}_P^{FP} + \overline{S}_B^{FP})$ (SCF=2.0) (ksi)	129.6	104.4
$(\overline{S}_P^{FP} + \overline{S}_B^{FB})$ (SCF=2.5) (ksi)	162.0	128.0

and Tripod-B, the steady axial load per longeron is given by:

$$P_{ST} \cong \frac{6400}{8 \times 0.9905} = 808 \text{ lb.} \quad \text{(ATS/3-Ring)} \qquad \text{D-52A}$$

$$P_{ST} \cong \frac{5890}{3 \times 0.9811} = 2{,}001 \text{ lb.} \quad \text{(Tripod-B)} \qquad \text{D-52B}$$

where the factors 0.9905 and 0.9811 are the direction cosines between the Z-axis and the longeron axes in the two designs. Thus, it can be seen that the steady contribution is small compared to the first-passage load:

$$P_{ST}/\overline{P}_{FP} \cong 0.051 \quad \text{(ATS/3-Ring)} \qquad \text{D-53A}$$

$$P_{ST}/\overline{P}_{FP} \cong 0.068 \quad \text{(Tripod-B)} \qquad \text{D-53B}$$

10. FATIGUE DAMAGE ESTIMATES

The Palmgren-Miner linear damage-summation hypothesis [59,60] is still widely used in the aerospace industry as a design screening tool. If a material is subjected to stationary random loading, the Palmgren-Miner rule can be adapted to formulate an expected damage accumulation rate:

$$dD/dt = \int_0^\infty \frac{p(s_a)\, ds_a}{N(s_a, s_m)} \qquad \text{D-54}$$

where $p(s_a)$ is the expected rate of occurrence of peaks in an infinitesimal band adjacent to the stress amplitude s_a, and where $N(s_a, s_m)$ is the number of constant-amplitude cycles to failure at amplitude s_a in the presence of a given mean stress, s_m. Strictly speaking, Eq. D-54 should be applied only to narrow-band processes, where there exists a reasonably clear relationship between peak occurrences and the occurrence of stress cycles which will actually cause damage. However, since design screening is often limited to

order-of-magnitude estimates, and since the designs are generally such that only the seldom-occurring peaks will contribute significant damage, it is reasonable to use Eq. D-54 for broadband processes, and at the same time to invoke the asymptotic approximation for the peak distribution (see Section D.4):

$$dD/dt \cong \int_0^\infty \frac{-dE(s_a)/ds_a}{N(s_a, s_m)} ds_a \qquad \text{D-55}$$

where

$$E(s_a) = 1/2\ \bar{\nu}_{oa}\ e^{-s_a^2/2\sigma_a^2} \qquad \text{D-56}$$

for a Gaussian stationary process. If it is also assumed that during a finite operating time (e.g., the 120-sec Titan-IIIC boost) enough cycles occur to justify neglecting transients, then Eq. D-55 can be interpreted as a total damage accumulation when $\bar{\nu}_{oa}$ is expressed in units of (total time)$^{-1}$ in Eq. D-56.

The foregoing approximations have been adopted here as a convenient means of making a comparative assessment of the ATS/3-Ring and Tripod-B designs. The approach taken below is to begin with exceedance curves for the axial load, P, or stress S_P, to adjust those curves to reflect bending stress S_B (assumed to be perfectly correlated with S_P) and to account for stress concentration where a longeron enters a metal attachment fitting. Typical axial-load exceedance curves for a 120-sec boost are illustrated in Figure D-7. The spectrum magnification factors are obtained from Table D-19 as:

$$\mu = \left[\frac{\bar{S}_P^{FP} + \bar{S}_B^{FP}}{\bar{S}_P^{FP}} \right] (SCF) \qquad \text{D-57}$$

with the results given in Table D-20. The peak distributions in terms of unmagnified occurrences are summarized as staircase approximations in Table D-21.

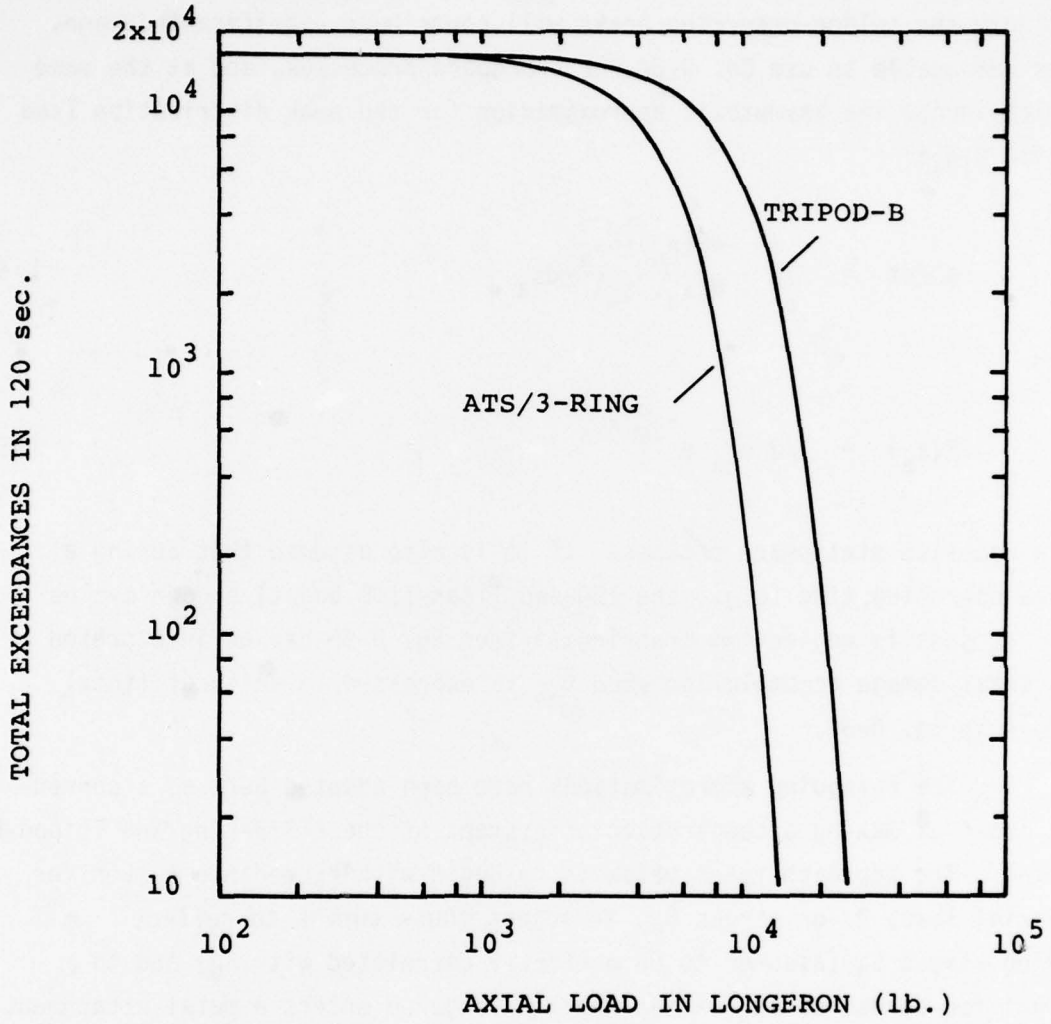


Figure D-7. Level-Crossing Exceedance Curves Obtained from Spectral Analysis

TABLE D-20

SPECTRUM MAGNIFICATION FACTORS (μ)

SCF	D E S I G N	
	ATS/3-Ring	Tripod-B
1.5	4.42	2.51
2.0	5.89	3.35
2.5	7.36	4.10

TABLE D-21

APPROXIMATE PEAK DISTRIBUTIONS (μ=1)

Step	Occurrences*, n	P E A K L O A D (lb)	
		ATS/3-Ring	Tripod-B
1	360	725	1,332
2	905	1,450	2,665
3	1,442	2,175	3,997
4	1,798	2,900	5,330
5	1,957	3,625	6,662
6	1,972	4,350	7,994
7	1,825	5,075	9,327
8	1,610	5,800	10,659
9	1,315	6,525	11,992
10	1,029	7,250	13,324
11	764	7,975	14,656
12	541	8,700	15,989
13	363	9,425	17,321
14	232	10,150	18,654
15	144	10,875	19,986
16	84	11,600	21,318
17	48	12,325	22,651
18	26	13,050	23,983
19	13	13,775	25,316
20	6	14,500	26,648
21	4	15,225	27,980
22	1	15,950	29,313

*Total occurrences expected for 120-sec boost.

Existing data on the fatigue behavior of graphite/epoxy laminates [17,18] had to be extrapolated in the present investigation, in order to define the denominator of Eq. D-55. The referenced data were obtained in a series of carefully controlled experiments with T300/Fiberite-934, with two stacking sequences tested at two different fixed values of minimum stress. Some pertinent details are reproduced in Table D-22, together with the 50-percentile fatigue stresses at 10^6 cycles.

The equivalent data for mean and alternating stresses are plotted on a nondimensional Smith diagram in Figure D-8. Also shown for comparison are the truss exposures, including a small mean component due to an assumed 10g steady acceleration along the Z-axis. It is apparent that the exposure spectrum can be treated for practical purposes as fully reversed ($s_m = 0$). Linear extrapolations have been made from the T300/Fiberite-934 test data to obtain intercepts for fully reversed loading, and these intercepts have in turn been linearly extrapolated to obtain a point at 10^6 cycles on the s_a - N curve for fully reversed loading of unidirectional material. Finally, it has been assumed that a linear relationship exists between log (s_a) and log (N) to construct the s_a - N curve shown in Figure D-9. It must be strongly emphasized that there is no physical justification for the foregoing extrapolation procedure, and that the result in Figure D-9 should not be taken seriously beyond its role of providing a comparative evaluation in a design study.

The data in Tables D-17, D-19, D-20, and D-21 as well as Figure D-9, have been combined to produce the expected fatigue damage summations presented in Table D-23. Of the five cases considered, the ATS/3-Ring design with high-modulus material in the longerons stands out as an obvious failure. This result merely reconfirms the assessment based on static margins (see Section D.9).

TABLE D-22

RESULTS OF LAMINATE FATIGUE TESTS*

Property	STACKING SEQUENCE	
	$[0/45/90/-45_2/90/45/0]_S$	$[0/45/0_2/-45/0]_{2S}$
Percent 0° Plies	25	67
Static Strength, s_s (ksi) (ksi)	69	140
Zero-tension test to 10^6 cycles:		
s_{max} (ksi)	42	80
Equivalent Stresses:		
s_a (ksi)	21	40
s_m (ksi)	21	40
Tension-Compression test to 10^6 cycles:		
s_{max} (ksi)	42	70
s_{min} (ksi)	-16	-30
Equivalent Stresses:		
s_a (ksi)	29	50
s_m (ksi)	13	20

*From references 17,18.

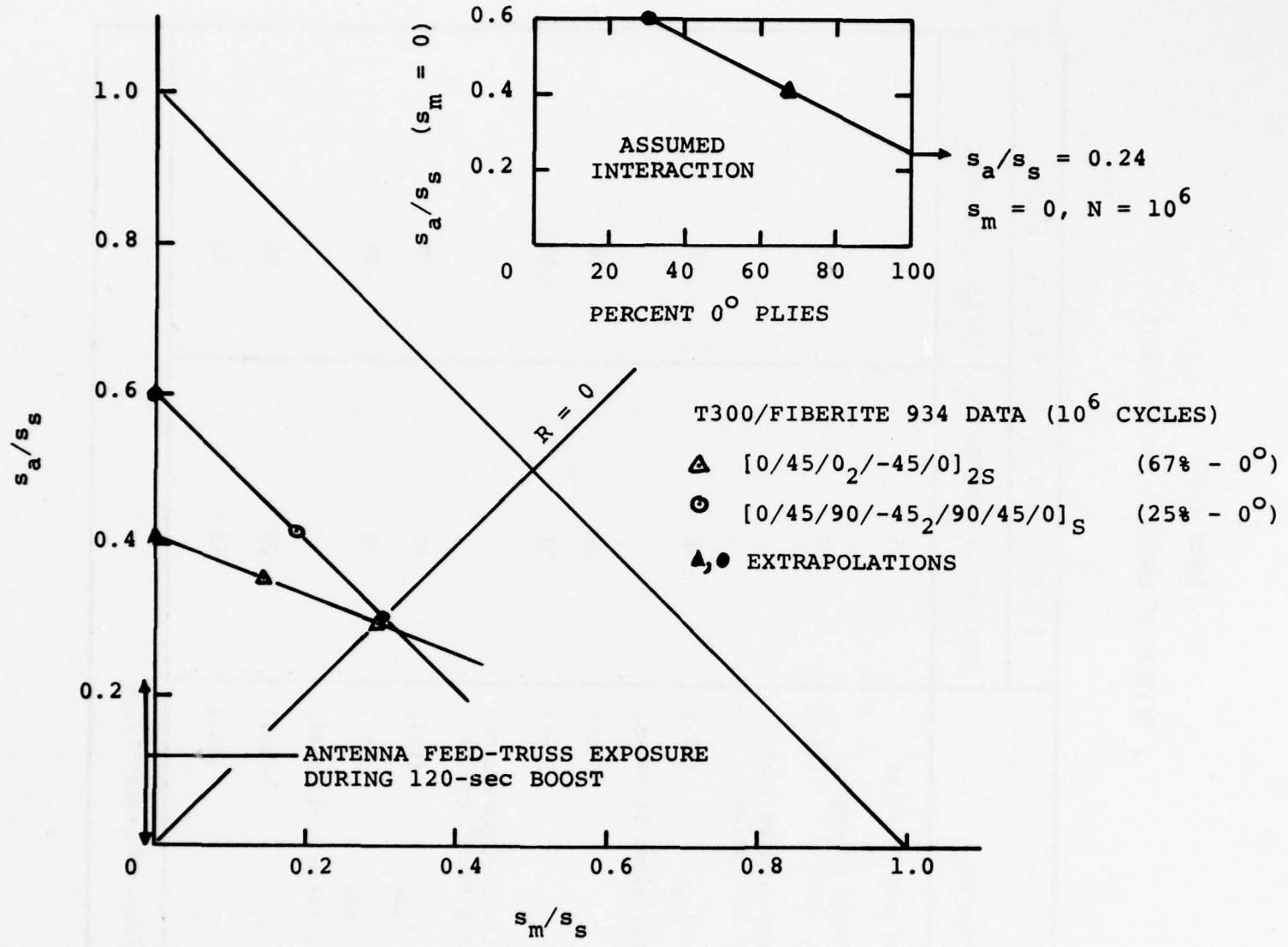


Figure D-8. Smith Diagram and Extrapolation

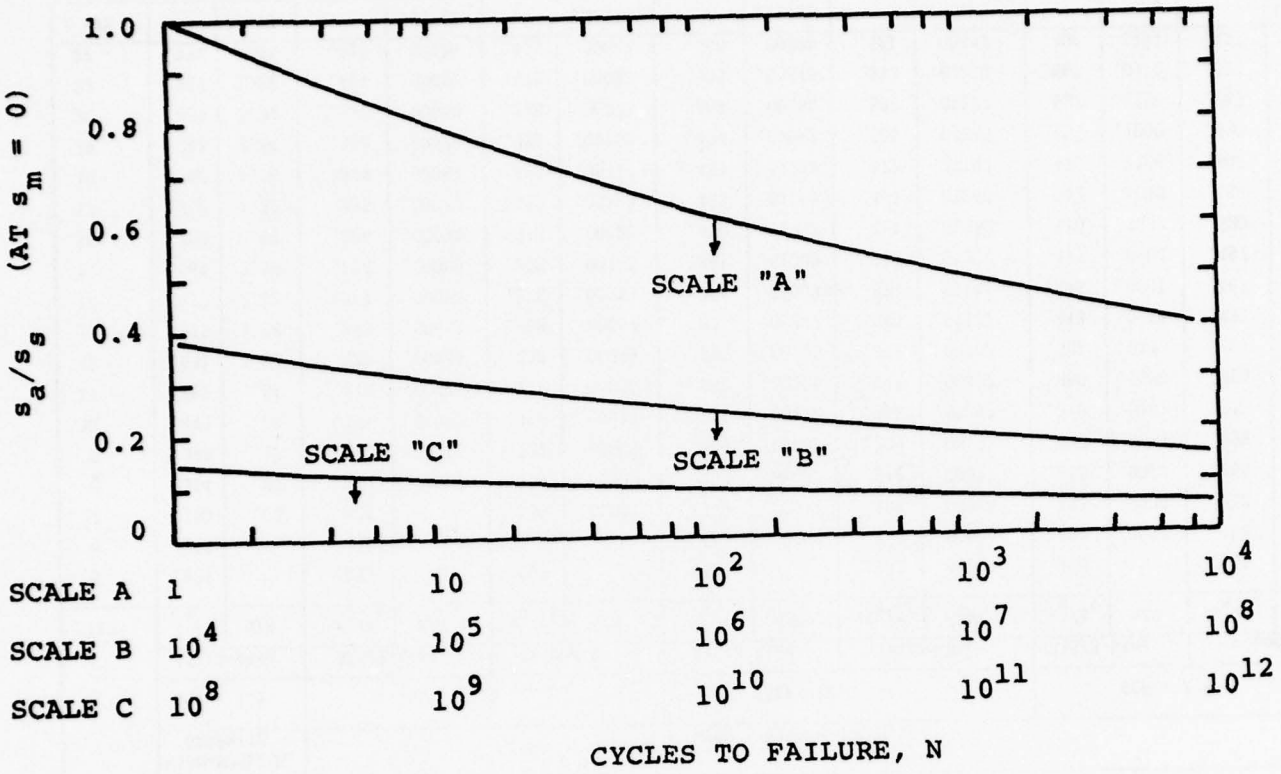


Figure D-9. s_a - N Curve for 0^o Graphite/Epoxy

TABLE D-23

SUMMARY OF FATIGUE DAMAGE ESTIMATES

	HIGH-MODULUS GRAPHITE		HIGH-STRENGTH GRAPHITE											
	SCF = 1.5		SCF = 1.5				SCF = 2.0				SCF = 2.5			
	ATS/3-Ring		ATS/3-Ring		Tripod-B		ATS/3-Ring		Tripod-B		ATS/3-Ring		Tripod-B	
STEP*	s_a/s_s	n/N	s_a/s_s	n/N	s_a/s_s	n/N	s_a/s_s	n/N	s_a/s_s	n/N	s_a/s_s	n/N	s_a/s_s	n/N
5	.221		.095		.099		.127		.132	.00001	.158		.165	.0001
6	.266		.115		.119		.153	.00002	.159	.00004	.192	.0002	.198	.0003
7	.310	.03	.134		.139	.00001	.179	.00011	.185	.00016	.223	.0009	.232	.0013
8	.354	.07	.153	.00002	.159	.00003	.204	.00032	.212	.00077	.255	.0027	.265	.0040
9	.398	.17	.172	.00005	.179	.00008	.229	.00082	.239	.00132	.287	.0051	.298	.0105
10	.442	.34	.191	.00012	.199	.00017	.255	.00172	.265	.00257	.318	.0147	.332	.0228
11	.487	.64	.210	.00021	.218	.00030	.280	.00325	.291	.00477	.350	.0283	.363	.0436
12	.531	1.00	.229	.00036	.238	.00049	.305	.00565	.317	.00752	.382	.0492	.397	.0694
13	.575	1.58	.248	.00052	.258	.00067	.331	.00807	.344	.01171	.413	.0649	.430	.0908
14	.620	2.32	.267	.00058	.278	.00089	.356	.01009	.371	.01546	.445	.0801	.463	.1220
15	.664	2.66	.286	.00080	.298	.00120	.381	.01309	.397	.01800	.477	.0984	.497	.1500
16	.708	2.80	.306	.00094	.318	.00120	.408	.01312	.424	.01868	.510	.1077	.530	.1616
17	.752	2.82	.325	.00089	.338	.00123	.433	.01280	.451	.01848	.542	.1090	.563	.1713
18	.796	2.76	.344	.00084	.358	.00118	.459	.01239	.477	.01792	.573	.1106	.597	.1731
19	.841	2.24	.363	.00072	.378	.00108	.484	.01082	.504	.01548	.605	.1000	.630	.1510
20	.885	1.71	.382	.00060	.398	.00075	.509	.00760	.531	.01177	.637	.0750	.663	.1071
21	.929	1.82	.401	.00057	.418	.00077	.535	.00816	.557	.01230	.668	.0770	.697	.1142
22	.974	.74	.420	.00020	.436	.00029	.560	.00328	.581	.00497	.700	.0294	.727	.0416
Σ n/N		23.70		.00742		.01034		.11131		.16193		.9532		1.4347

*Step keyed to Table D-21.

The remaining cases compare the two designs with the same (high-strength) graphite/epoxy in the longerons, i.e., 18 lb. weight added to ATS/3-Ring but Tripod-B unmodified. The following conclusions can be drawn from these results:

1) Fatigue damage accumulation during launch can be rendered insignificant by careful design of the end-attachment fittings, i.e., to achieve the low SCF of 1.5. In this case, it is immaterial if the fatigue calculations are unconservative by an order of magnitude.

2) However, adhievement of SCF = 1.5 may be difficult or may create other design problems. Achievement of SCF = 2 may be a much more reasonable goal, and in this case the accuracy of the fatigue-damage estimates and small differences between the two designs become important.

3) The "design to cost" philosophy should not be applied uncritically to the longeron/end-fitting detail. An inexpensive design might result in SCF > 2, with attendant launch-survival reliability problems for the structure.

4) The modified ATS/3-Ring design appears to possess better fatigue resistance than the unmodified Tripod-B. It is likely, but not certain, that this trend would be preserved if Tripod-B were also modified, as suggested in Section D.9, to improve its static buckling margins.

5) The fatigue resistance of the Tripod-B apex joint has not been addressed because of the relatively low load levels at that location. However, the apex joint must remain a matter of concern until the associated SCF can be properly evaluated.

APPENDIX E

TRUSSWORK FINITE-ELEMENT MODEL

1. GENERAL

Displacements and internal loads in the antenna-feed truss structure are computed using a finite-element model consisting of generalized bending-stretching-torsion beam elements for the longerons and pin-jointed bar elements for the lateral rings. Static and dynamic analyses of the model are conducted by the Matrix Displacement Method, using subspace iteration for modal vibration analysis. This appendix documents program SFRAME, which drives the MIT Aeroelastic and Structures Research Laboratory FEABL-5/EGL software [58] to carry out these calculations. The program makes no assumptions about the truss configuration. Hence, it can be used to analyze large space structures other than communications satellite antenna-feed trusses.

Program architecture is illustrated in Figure E-1. A dummy MAIN program provides the required DIMENSION and EQUIVALENCE declarations. Reading of input data, model assembly and solution, and output to printer and FORTRAN files are accomplished in subroutine SFRAME.

EGL element STIF2M (Figure E-2) is used to model the longerons. Although STIF2M can accommodate asymmetric sections, its use in the present investigation has been limited to circular sections ($I_{yy} = I_{zz}$, $I_{yz} = 0$). Stiffness and mass matrices for the pin-joint elements representing the lateral rings are computed directly in subroutine SFRAME. If the coordinates of the element nodes are defined as shown in Figure E-2, direction cosines C_X, C_Y, C_Z between the element axis and the global reference axes can be calculated from:

$$C_X = \frac{X_2 - X_1}{L} \qquad C_Y = \frac{Y_2 - Y_1}{L} \qquad C_Z = \frac{Z_2 - Z_1}{L} \qquad \text{E-1}$$

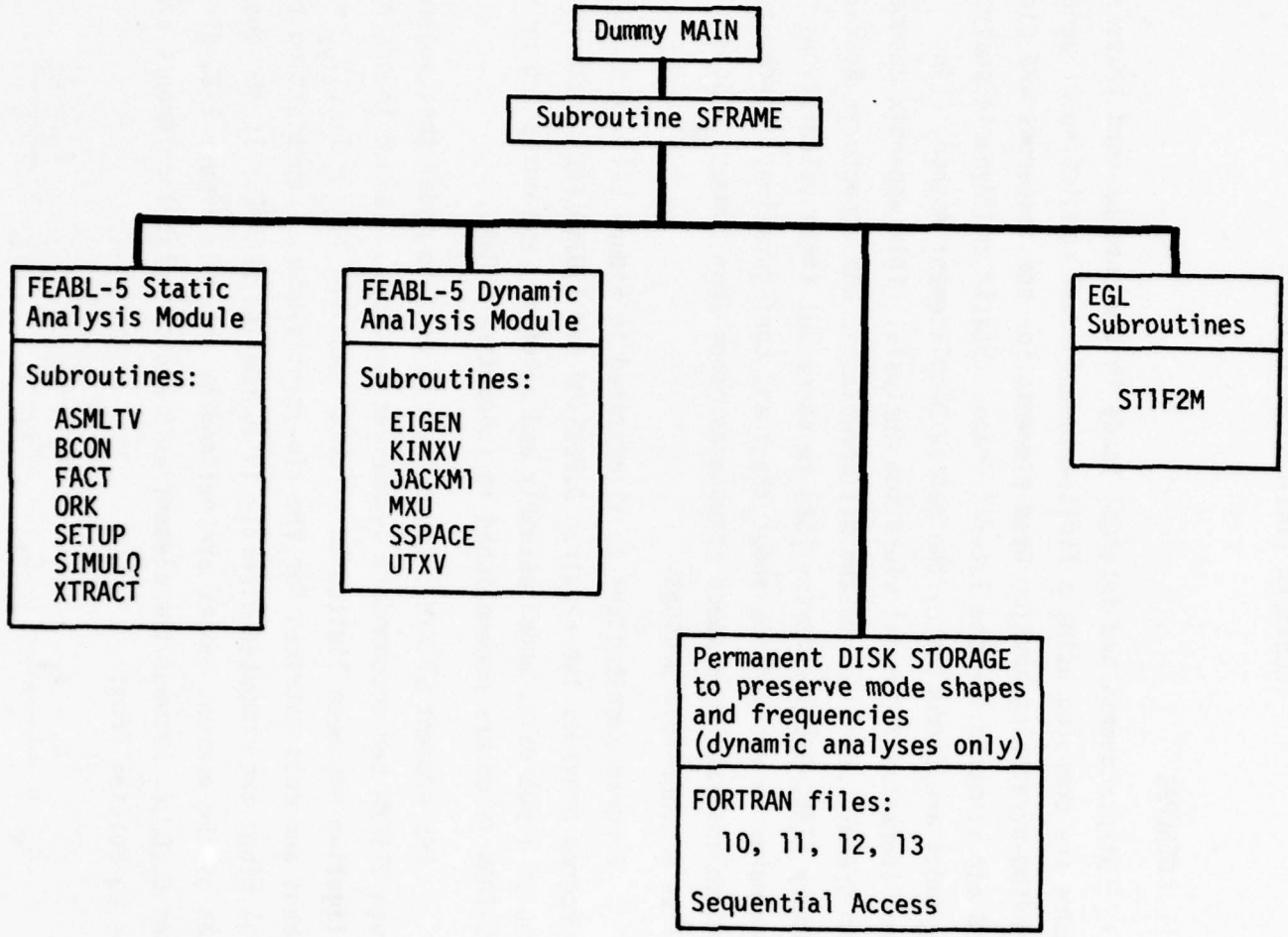
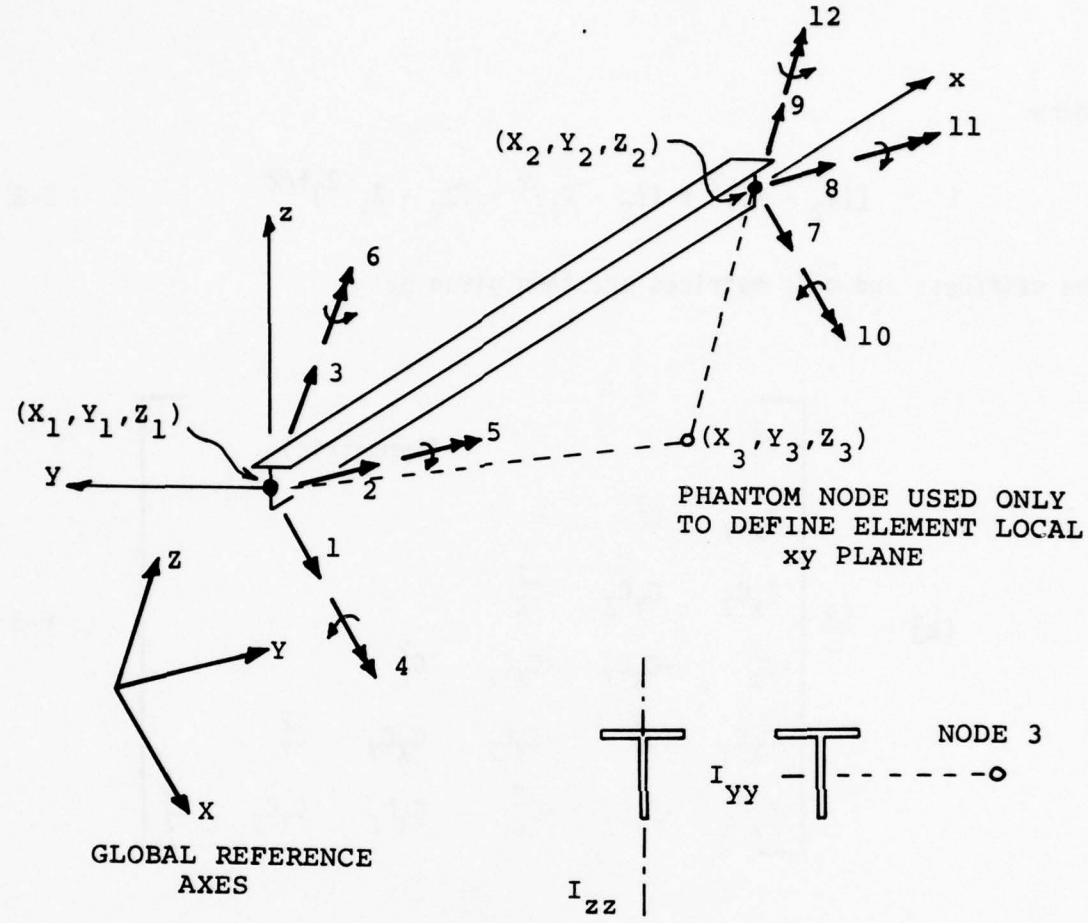


Figure E-1. Program SFRAME Architecture



Calculations executed by subroutine STIF2M produce the following quantities in the global reference coordinate system XYZ:

[k] = Element stiffness matrix

[m] = Consistent mass matrix

{Q} = Consistent nodal forces corresponding to given weight per unit length, acting in -Z direction

{R} = Rotation transformation matrix from local to global reference frame:

$\{Q\} = [R] \{q\}$ $\{Q\}, \{q\}$ = forces or displacements

Figure E-2. Element STIF2M

where

$$L = [(X_2 - X_1)^2 + (Y_2 - Y_1)^2 + (Z_2 - Z_1)^2]^{1/2} \qquad \text{E-2}$$

The stiffness and mass matrices are then given by:

$$[k] = \frac{EA}{L} \begin{bmatrix} C_X^2 & & & & & \\ C_X C_Y & C_Y^2 & & & \text{(Symmetric)} & \\ C_X C_Z & C_Y C_Z & C_Z^2 & & & \\ -C_X^2 & -C_X C_Y & -C_X C_Z & C_X^2 & & \\ -C_X C_Y & -C_Y^2 & -C_Y C_Z & C_X C_Y & C_v^2 & \\ -C_X C_Z & -C_Y C_Z & -C_Z^2 & C_X C_Z & C_Y C_Z & C_Z^2 \end{bmatrix} \qquad \text{E-3}$$

$$[m] = \frac{\rho L}{6} \begin{bmatrix} 2 & & & & & \\ 0 & 2 & & & \text{(Symmetric)} & \\ 0 & 0 & 2 & & & \\ 1 & 0 & 0 & 2 & & \\ 0 & 1 & 0 & 0 & 2 & \\ 0 & 0 & 1 & 0 & 0 & 2 \end{bmatrix} \qquad \text{E-4}$$

where E is Young's modulus, A is the element cross section area, and ρ is the mass per unit length.

2. DATA INPUT CONVENTIONS

Program data input permits analysis of any number of consecutive cases (all static or all dynamic) in a single run. If consecutive structures are similar, the input data can be updated rather than completely repeated, subject only to one restriction noted below. The input data are subdivided into nine groups, each of which is identified by a heading card in the following format:

KEYW, N_1, N_2, F, TITLE	(A4,6X,2I5,E10.3,10X,10A4)

KEYW - Alphanumeric keyword to identify the group.

N_1 - Integer, right-justified to card column 15

N_2 - Integer, right-justified to card column 20

F - Floating-point number in columns 21-30

TITLE - Any alphanumeric information, by which the user may wish to identify the group, in columns 41-80.

The interpretation of N_1, N_2 and F varies. Details of the data input for each group are as follows.

Group 1 (Internal Option, Dynamic or Static)

KEYW = IØDY

N_1 = 0 or 1 (static analysis)
or 2 (dynamic analysis)

N_2,F - Not used.

There are no other cards in Group 1. Do not repeat this group for subsequent cases in the same run.

Group 2 (Nodal Information)

KEYW = NØDE

N_1 = Total number of real nodes in the model

N_2 = Total number of phantom nodes

F - Not used

Phantom nodes are permitted for convenience in defining the orientation of beam elements with respect to the global axes XYZ (Figure E-2), i.e., they provide coordinate reference points but are not assembled into the finite-element model. Program dimensions permit $N_1 + N_2 \leq 150$. The Group 2 heading card must be followed by $N_1 + N_2$ coordinate cards identifying the nodes in ascending order:

M, X, Y, Z, T	(I5, 4E15.7)

M = Node number

X,Y,Z = Global coordinates of the node

T = Temperature at the node

Node numbers may not be skipped, i.e., node numbers $1,2,\ldots,N_1$ must be used for the real nodes, followed by $N_1 + 1$, $N_1 + 2,\ldots N_1 + N_2$ for the phantom nodes.

Group 3 (Element Information)

KEYW = ELEM

N_1 = Total number of elements

N_2,F - Not used

Program dimensions permit $N_1 \leq 150$. The heading card for Group 3 must be followed by N_1 cards identifying elements $1,2,\ldots,N_1$ in ascending order:

M, LPR, ND1, ND2, ND3	(5I5)

M = Element number

LPR = Reference number for element properties table

ND1,ND2 = Real node numbers to which element is connected

ND3 = Element orientation node number (Figure E-2)

The element orientation node may be either a real node or a phantom node. ND3 need not be defined for pin-joint elements.

Group 4 (Element Property Types)

KEYW = TYPE

N_1 = Total number of different property types

N_2,F - Not used

Program dimensions permit $N_1 \leq 50$. The heading card for Group 4 must be followed by N_1 sets of three cards identifying property types LPR = $1,2,\ldots,N_1$ in ascending order:

M, L, EL, ALFA	(2I5, 50X, 2E10.3)

M = Property type number

L = 1 (pin-joint element)
or 2 (beam element)

EL = Effective length of element

ALFA = Coefficient of linear thermal expansion

E, G, A, J, I_{yy}, I_{zz}, I_{yz}, W	(8E10.3)

E = Young's modulus

G = Shear modulus

A = Cross section area

J = Section torsion constant

I_{yy}, I_{zz}, I_{yz} = Section area inertias for bending (Figure E-2)

W = Section weight per unit length

D (E10.3) = Section mass per unit length

Properties $G, J, I_{yy}, I_{zz}, I_{yz}$ are used only by beam elements (L = 2). Values of W are used to produce nodal forces in the -Z direction for static analysis. Values of D are used to produce the element mass matrix.

Group 5 (Constraints Information)

KEYW = CØNS

N_1 = Number of nodes at which one or more degrees of freedom will be constrained

N_2, F = Not used

The heading card for Group 5 must be followed by N_1 cards to identify the specific degrees of freedom to be constrained:

M, ID(1), ID(2), ID(3), ID(4), ID(5), ID(6) (7I5)

M = Node number

ID(I) = 0 (degree of freedom not constrained) or 1 (degree of freedom constrained)

The convention for degrees of freedom at each node is shown in Table E-1. The program permits up to 50 degrees of freedom to be constrained. In addition to the physical constraints on the structure, DOF 4,5,6 should be constrained at any node to which only pin-joint elements are connected.

TABLE E-1

DOF CONVENTION

DOF No., I=	Interpretation
1	Displacement parallel to X
2	Displacement parallel to Y
3	Displacement parallel to Z
4	Rotation about X
5	Rotation about Y
6	Rotation about Z
XYZ = Global Reference Axes	

Group 6 (Static Loads)

KEYW = Load

N_1 = Number of nodes at which loads will be placed

N_2,F - Not used

The heading card for Group 6 must be followed by N_1 cards to identify the loads associated with the degrees of freedom at each loaded node:

M, Q(1), Q(2), Q(3), Q(4), Q(5), Q(6)	(I5, 5X, 6E10.3)

M = Node number

Q(I) = Value of load corresponding to Ith degree of freedom

Loads corresponding to displacements are interpreted as concentrated forces. Loads corresponding to rotations are interpreted as concentrated moments. (See Table E-1 for interpretations of DOF.) Group 6 may be omitted entirely for dynamic analysis (Option 2 in Group 1), and for static analyses of thermal-stress effects only. The program permits up to 50 individually prescribed loads.

Group 7 (Temperature Update Information)

KEYW = TEMP

N_1, N_2, F - Not used

Group 7 is optional. It allows the user to change the temperature field on the structure for parametric study of loads induced by thermal deformations. The heading card for Group 7 must be followed by one card for each real node, in ascending order:

M, T	(I5, 45X, E15.7)

M = Node number (same as in Group 3)

T = Revised temperature at the node

Group 7 can be used, e.g., for parametric studies of an orbiting space structure. The element connections, node locations, properties, etc. remain fixed, but several different temperature fields must usually be studied to assess the effects of different orientations of the structure with respect to the sun. Thus, the user may run a sequence of cases in which the finite-element model is defined in the first case, while only revised temperature data are input for subsequent cases. When Group 7 is input, the nodal temperature data in Group 2 will be overwritten, and the first 20 characters of the Group 2 heading card title will be overwritten by the first 20 characters of the Group 7 heading card title.

Group 8 (Eigenvalue Analysis Parameters)

KEYW = EIGN

N_1 = Number of eigenvalues (natural frequencies) for which convergence is desired

N_2 = Maximum number of iterations allowed

F = Convergence tolerance

There are no other cards in Group 8. Program dimensions permit $N_1 \leq$ Minimum of (60, total number of unconstrained degrees of freedom). The N_1 lowest modes will be converged. The N_1 lowest frequencies and mode shapes will be printed; for the higher modes frequencies only will be printed for modes $N_1 + 1$, $N_1 + 2$,...,60. Values of $10 \leq N_2 \leq 20$ iterations and $10^{-4} \leq F \leq 10^{-2}$ tolerance are recommended. For converged modes, the numerical error in the estimate for natural frequency will be $\sqrt{F}$. Group 8 may be omitted entirely in static analysis runs.

Group 9 (Run Command)

KEYW = RUN

N_1,N_2 - Not used

F = Reference temperature, T_R

There are no other cards in Group 9. Group 9 must be included in the input for every case, and must be physically the last data group for the case. For static analyses, T_R is assumed to be the (uniform) temperature at which the structure is stress-free. Thermal deformations and loads will be calculated based on internally computed temperature changes $\Delta T = T - T_R$ at each real node.

3. REQUIREMENTS FOR PERMANENT STORAGE FILES

Program SFRAME will store the results of an eigenvalue analysis on four permanent sequential-access files, which must be properly defined by job control language instructions compatible with the procedures in effect at the user's computing facility. The FORTRAN unit numbers and file attributes are summarized in Table E-2. If a sequence of cases is being run, only the results of the last case will be permanently filed. These data can be accessed subsequently by program SPECTRA (Appendix F) to compute response power spectra and exceedance rates.

TABLE E-2

REQUIRED FILE ATTRIBUTES

FORTRAN Unit No.	Data Format	No. Words/ Record	No. of Records*
10	Unformatted	20	108
11	Unformatted	60	202
12	Unformatted	100	201
13	Unformatted	210	100

*Number of records required for models with up to 100 elements and 200 unconstrained degrees of freedom; up to 60 natural modes allowed.

The data files are not used for static analysis and need not be created to run static cases. If the user does not intend to execute a response analysis following the eigenvalue solution, the data files are not required and need not be created. However, subroutine SFRAME must be modified to prevent the program from attempting to write the files when executing a dynamic analysis. The necessary modifications are as follows:

1) Place a "C" in column 1 of the card identified by the word "FILES" in columns 73-80.

2) Delete the "C" from column 1 of the card identified by the word "STOPFILE" in columns 73-80.

4. DIMENSION REQUIREMENTS

The dimension requirements for program SFRAME are given here to permit redimensioning for larger or smaller finite-element models. The auxiliary vectors and arrays in the dummy MAIN program should be dimensioned as follows:

```
STIF(M), EMASS(M), DSTIF(M), DEMASS(M), INCØNV(MØDES),
EV(MØDES*MØDES), T(MØDES,MØDES), AM(MØDES,MØDES),
ASQ(MØDES)
```

where:

MØDES = Total number of modes included in the eigenvalue analysis

M = MØDES*(MØDES+1)/2

As a general rule, more modes should be included in the analysis than the number for which convergence is desired:

$$N + 3 \leq MODES \leq 2N$$

where convergence is desired for the N lowest modes.

The dimension of vectors RE and IN may need to be increased, depending upon the number of nodes in the model and the nature of its element interconnections. Also, a larger dimension will be required for dynamic than for static analysis of the same model. If redimensioning is necessary, the correct dimension will be indicated in an error message printed automatically by the program when execution is attempted.

If dimensions are changed in the MAIN program, the accompanying DATA statement must also be changed to agree with the current dimensions:

```
DATA LENGTH, NSPACE/IDIM,MØDES/
```

where IDIM is the dimension assigned to vectors RE and IN. The value IDIM will be used by the program to check dimensional adequacy.

Subroutine SFRAME contains a number of internal vectors and arrays which must be redimensioned if the user wishes to exceed the restrictions stated in Section E.2. If N > 150 total (real plus phantom) nodes are wanted, modify the dimensions of the following variables:

```
X(N), Y(N), Z(N), TMP(N)
```

If models containing M > 150 elements are wanted, modify the dimensions of the following variables:

```
NDPE(M), NDPR(M)    MCPL(M,4), LPARM(M)
```

If K1 > 50 different sets of element properties are wanted, modify the dimensions of the following variables:

```
LTYP(K1), PR(K1,9), ALFA(K1), ELENGT(K1)
```

If K2 > 50 degrees of freedom are to be constrained, modify the dimension of:

NCD(K2)

If K3 > 50 nodal loads are to be applied to the structure, modify the dimensions of:

NLD(K3), FQ(K3)

5. CORE REQUIREMENT AND EXECUTION TIME

Core memory requirements and execution time will vary, depending upon the analysis option (static or dynamic), the model size (total nodes and interconnection pattern), the efficiency of the FORTRAN complier program at the user's computing facility, and the input/output buffer requirements for permanent files. The statistics summarized in Table E-3 reflect experience with an IBM S-370/168 under a VM operating system.

TABLE E-3

TYPICAL CORE AND CPU TIME REQUIREMENTS

Item \ Model	TRIPOD-B		ATS/3-RING	
	78 Unconstrained Degrees of Freedom		192 Unconstrained Degrees of Freedom	
	Static	Dynamic[1]	Static	Dynamic[2]
No of Cases in Run	2	1	2	1
No. of Iterations[3]	-	14	-	7
CPU Time (min.)	0.1	6.7	0.2	15.5
Core (KBYTES)[4]	134	298	134	514

[1] 40 of 40 modes converged.

[2] 41 of 60 modes converged.

[3] To converge to 10^{-2} tolerance (10^{-1} error bound on frequencies).

[4] One KBYTE = 250_{10} = 372_{8} single-precision words.

APPENDIX F

SPECTRAL ANALYSIS PROGRAM

1. GENERAL

Program SPECTRA executes response analyses of antenna-feed truss structures subjected to three-axis stationary random base excitation assumed to possess the following properties:

1) Identical power spectrum for each axis;

2) No correlation between axes; and

3) Gaussian processes.

It is further assumed that the input spectrum refers to accelerations. Typical sets of consistent physical units for the truss finite-element model and the input spectrum are shown in Table F-1.

Program organization is indicated in Figure F-1. Retrieval of modal data from the permanent files created by program SFRAME, establishment of the input power spectrum 2G(f) at several points, and the matrix operations and integrations are carried out in MAIN program SPECTRA. Function subprogram PSD is called during the integration to evaluate 2G(f) by linear interpolation in logarithmic coordinates:

$$\log_{10}[2g(f)] = \log_{10}(2G_{i-1}) + \log_{10}\left(\frac{G_i}{G_{i-1}}\right) \frac{\log_{10}(f/f_{i-1})}{\log_{10}(f_i/f_{i-1})} \qquad \text{F-1}$$

where $G_{i-1} = G(f_{i-1})$; $G_i = G(f_i)$; and $f_{i-1} \leq f \leq f_i$. Seven pairs of values ($\log_{10}f_i$, $\log_{10}G_i$) are defined by program SPECTRA in common block SPCTRM. These points describe the MJS "other assemblies" spectrum (Figure D-1, in Appendix D) between 1.05 Hz and 1750 Hz in nondimensional units of g^2/Hz. To maintain consistency of physical units, the G_i values should be scaled by the following before using the program:

$$g^2 = (386.4)^2 \text{ in}^2/\text{sec}^4 \qquad \text{(English)} \qquad \text{F-2A}$$

$$g^2 = (9.807)^2 \text{ m}^2/\text{sec}^4 \qquad \text{(Metric)} \qquad \text{F-2B}$$

TABLE F-1

CONSISTENT UNITS

Quantity	English	Metric
Nodal coordinates; element lengths	inches	meters
Young's modulus; shear modulus	psi	Pa
Section area	in^2	m^2
Torsion and bending area inertias	in^4	m^4
Weight per unit length	lb in^{-1}	Nm^{-1}
Mass per unit length	lb sec^2/in^2	Kg
Applied forces; output standard deviations	lb	N
Applied moments; output standard deviations	lb in	Nm
Displacements; output standard deviations	inches	meters
Input spectrum	in^2 sec^{-4} Hz^{-1}	m^2 sec^{-4} Hz^{-1}

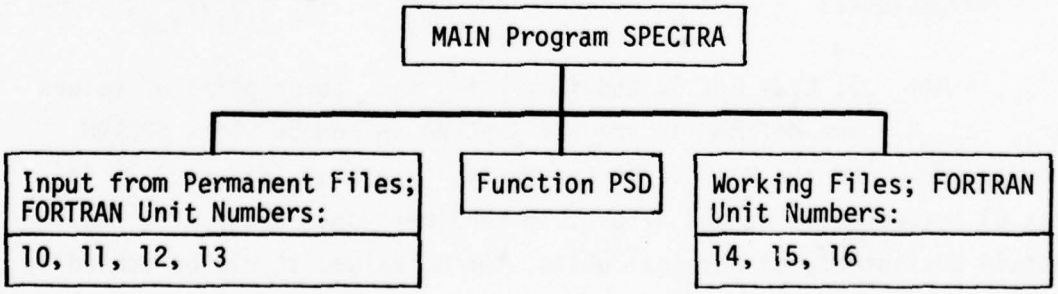


Figure F-1. Program Spectra Organization

Program SPECTRA also uses three working files, which may be either temporary or permanent. Intermediate data are stored in Files 14 and 15, while response power spectra for selected internal loads are recorded on File 16. If the latter file is declared to be permanent, these spectra can be accessed later for printing or plotting.

Program SPECTRA assumes that all degrees of freedom associated with a subset of lowest-numbered nodes in the finite-element model are constrained. For example, the Tripod-B model is considered to be fixed to the spacecraft at the bottom ends of its three legs, i.e., at nodes 1, 2, 3 with degrees of freedom 1 through 18 constrained. Similarly, the ATS/3-Ring model is fixed at the first eight nodes (one for each leg) with degrees of freedom 1 through 48 constrained. This restriction has been made to facilitate the input of data from which the rigid-body mode shapes can be determined (see Eq. D-16, Section D.3 in Appendix D).

2. DATA INPUT CONVENTIONS

Program SPECTRA is able to execute only one analysis case per run. The following input data cards are required to describe the case.

Group 1 (Title Card)

Any alphanumeric information in card columns 1 through 80 to identify the case.

Group 2 (Model Size Information)

NCON, NDT, NET, MODES	(4I5)

NCON = Total number of constrained degrees of freedom.

NDT = Total number of constrained plus unconstrained degrees of freedom.

NET = Total number of elements.

MODES = Number of modes to be included in the spectral analysis.

The values of NDT and NET must agree with the data input to program SFRAME (Appendix E, Section E.2, heading cards for Groups 2 and 3, respectively). Note that NDT = 6x (number of real nodes). The value of NCON must agree with the total number of constraints displayed in the program SFRAME output. The MODES lowest modes will be used in the spectral analysis, with any value in the range $1 \leq \text{MODES} \leq N'$ permitted (N' = total modes included in the subspace).

Group 3 (Description of Rigid-Body Modes)

ID(1), ID(2), ... , ID(16)	(16I5)

.
.
.

. . . . . , ID(NF)	(16I5)

The purpose of this group of cards is to identify at each unconstrained node the degrees of freedom associated with each rigid-body mode. A total of NF = NDT - NCON degree-of-freedom numbers are expected. Begin with the mode of translation parallel to the global X-axis. The appropriate DOF at the n^{th} node is 6n-5. Pack these data on the input cards with sufficient blank fields following the last DOF number to make a total of NF inputs. Repeat for the Y and Z axes using DOF numbers 6n-4 and 6n-3, respectively.

Group 4 (Modal Damping Factors)

$\zeta_1, \zeta_2, \cdots, \zeta_8$	(8F10.3)

.
.
.

$\cdots, \zeta_{MODES}$	(8F10.3)

ζ_j = Damping factor for j^{th} natural mode.

The program expects one damping factor for each mode included in the spectral analysis.

Group 5 (Integration Control)

FMIN(1)	(F10.3)
NRG	(I5)
FMAX(1), FMAX(2), ..., FMAX(8)	(8F10.3)
FMAX(9), ..., FMAX(NRG)	(8F10.3)
NSTEP(1), NSTEP(2), ... NSTEP (NRG)	(16I5)

FMIN(1) = Lower-bound frequency (Hz).

NRG = Total number of frequency ranges.

FMAX(I) = Upper-bound frequency for i^{th} range (Hz).

NSTEP(I) = Number of integration steps for i^{th} range.

From 1 to 16 frequency ranges are permitted to allow variation of the integration step size in regions of varying modal content. The modal spectral density matrix will be integrated from FMIN(1) to FMAX(NRG). Within each range, trapezoidal integration will be performed in NSTEP steps of size:

$$\Delta f = \frac{FMAX - FMIN}{NSTEP} \qquad F\text{-}3$$

Group 6 (Spectra Output Selection)

NSEL	(I5)
LNUM(1), IDOF(1)	(2I5)
.	
.	
.	
LNUM(NSEL), IDOF(NSEL)	(2I5)

NSEL = Number of elements selected for power spectral output.

LNUM(I) = Element number for i^{th} selection.

IDOF(I) = Local DOF number of i^{th} selection.

Up to 10 different elements may be selected for recording of power spectral densities on File 16. At each selected element, only one local DOF number can be chosen. The internal load spectrum corresponding to the chosen DOF number is interpreted in Table F-2.

TABLE F-2

LOCAL DOF KEY FOR INTERNAL LOAD SPECTRA

Load	Axis[2]	Element Type and Connections[1]			
		Pin-Joint Element		Beam Element	
		Node ND1	Node ND2	Node ND1	Node ND2
Load Force Parallel to	X	1	4	1	7
	Y	2	5	2	8
	Z	3	6	3	9
Moment about	X			4	10
	Y			5	11
	Z			6	12

[1] See data group 3, Subsection E.2 and Fig. E-2, Appendix E for definitions of ND1 and ND2.
[2] Global reference axes used to identify nodal coordinates of the finite element model.

3. REQUIREMENTS FOR STORAGE FILES

Program SPECTRA is designed to access the data stored by program SFRAME on permanent FORTRAN Files 10 through 13. Refer to Section E.3 in Appendix E for the attributes required for these files.

In addition, program SPECTRA requires three working storage files with the attributes indicated in Table F-3. The selected internal loads spectra are stored in File 16.

If File 16 is declared permanent, the selected internal loads spectra can be accessed later for printing or plotting. Each record of File 16 contains the spectral density values for the NSEL chosen elements/DOF and the value of the corresponding frequency. The storage format for a typical record is indicated in Figure F-2. One record will be

TABLE F-3

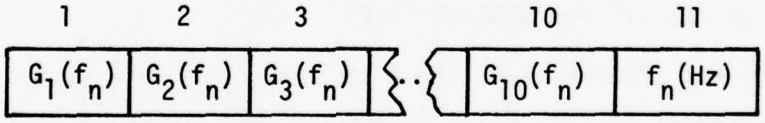
REQUIRED WORKING FILE ATTRIBUTES

FORTRAN Unit No.	Data Format	No. Words/ Record	No. of Records*
14	Unformatted	1200	100
15	Unformatted	201	400
16	Unformatted	11	400

*Number of records required for models containing up to 100 elements and analyses with up to 400 frequency points.

written for each frequency point in each range of the modal spectral density matrix integration.

WORD:



G_m = Power spectral density for m^{th} choice at n^{th} frequency point.

Figure F-2. Typical Record in File 16

4. DIMENSION REQUIREMENTS

Program SPECTRA is dimensioned to accommodate models with up to 100 elements, 200 unconstrained degrees of freedom, and 60 natural modes. The number of constrained degrees of freedom has no effect on program dimensions. The number of frequency integration points is limited only by the number of records assigned to Files 15 and 16.

If the user wishes to analyze larger models with L > 100 elements, N > 200 unconstrained degrees of freedom, and M > 60 natural modes, program SPECTRA must be redimensioned as follows:

```
ICON(M), LIST(L,20), NDPE(L)
EA(20,M), EU(20,M), ESIG2(L,20), EZ2(L,20)
U(N,M), UR(N,3), AM(K), AMRN(3,M), AM2(M,M)
IDOF(N,3)
SM(M), SF(M), SZETA(M), HR(M), HI(M)
QSIG2(N), QZ2(N)
SR(M,M), SI(M,M)
```

where K = N(N + 1)/2. Also, the accompanying DATA statements must be modified to properly initialize ESIG2, EZ2, AMRN, IDOF, QSIG2, QZ2, and SI, unless initialized storage is provided by the operating system.

5. CORE REQUIREMENT AND EXECUTION TIME

Core memory requirements and execution time will vary, depending on the problem size, input/output buffer requirements for the files, and the number of frequency integration points. On an IBM S-370/168 under a VM operating system, program SPECTRA requires 280 KBYTES ($70K_{10}$ or $210{,}560_8$ words) of core memory. Execution-time experience is summarized in Table F-4.

TABLE F-4

CPU TIME REQUIREMENTS

Model	Tripod-B	ATS/3-Ring
No. of Unconstrained degrees of freedom	78	192
No. of elements	30	64
No. of modes used	40	60
No. of frequency integration points	182	182
CPU time (min.)	14.9	68.8

APPENDIX G

THE TEE-JOINT ANALYSIS PROGRAM

1. INTRODUCTION

The Tee-Joint Analysis Program was developed in order to investigate the details of the stress distributions at the junctures of composite tubes, such as is shown in Figure G-1. This program was designed to treat the case of a main tube with one or two side tubes. The program design limits the geometry by requiring that the side tubes do not themselves intersect, and that the axes of the side tubes, when extended into the interior of the main tube, intersect with the axis of the main tube. Apart from these restrictions, the side tube geometry may be specified as desired.

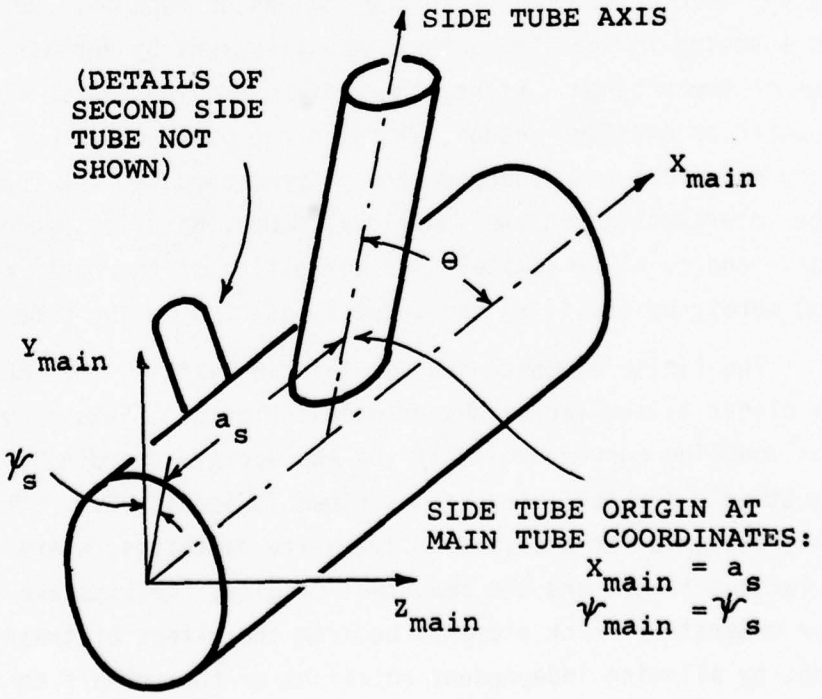


Figure G-1. Main Tube Coordinates and Orientation of Side Tube

One end of the main tube is constrained, while the other end of the main tube and the ends of the side tubes have applied forces specified. The user specifies tension or compression, shears, torsion, and bending moments, and these generalized forces are automatically decomposed into axial and circumferential forces at the nodes located at the tube ends.

The tubes may be multilayer orthotropic materials with principal material axes oriented in any prescribed directions. Different tubes, and different portions of each tube, may have different material properties. Stresses are calculated by the program at the lower, middle, and upper surface of each layer in each element, providing the desired information concerning stress concentrations in the regions of the tube intersections.

The Tee-Joint Analysis Program provides substantial, but not fully automatic, mesh generation capabilities. The program automatically generates a basic rectangular mesh for each tube. The user must then specify the necessary modifications to the nodal locations and element definitions, forming the appropriate meshes in the regions of tube intersections. The user is assisted in specifying these modifications by various helpful features of the program. First, the program provides, upon request, plots of the basic or modified meshes, allowing the user to picture and check the necessary modifications. Second, the program computes the coordinates of the tube intersections on the individual tubes, both for presentation on the plots, and to allow simpler user definition of the nodes on the intersections merely by providing the angular position on the side tube.

The finite element used for this analysis is the "MLP3K" element [16], a planar triangular or quadrilateral element. This element can be used for modeling curved shells if the appropriate coordinate transformations and adjustments are performed as described in Section G.2. This element is specially designed for analysis of composite laminates, where the stresses in the various layers are the important results. Results are quite good even for moderately thick elements because the effect of transverse shear is included, by allowing independent rotations of the normals to the midsurface so that they need not remain normal to the midsurface after deformation.

The element routines allow computation of the stresses at the lower surface, middle, and upper surface of each layer, at the element centroid (or at the other locations, if requested). The existing MLP3K element stiffness routine has been used without change, while an existing routine for stress calculation, "MLP3S", has been modified and renamed "MLP3B" in order to provide an element stress-displacement-relation (B) matrix.

Finite element analysis of this problem requires an extremely large number of nodes in order to provide sufficient accuracy. This makes it impossible to accomplish the required assembly and solution of the global stiffness matrix "in-core". Therefore, the Tee-Joint Analysis Program uses the Frontal Analysis Program (FRAP) [61], which was developed for the numerical solution of such problems. The FRAP subroutines, ECON and WAFR, were utilized with only minor revisions concerning the format of the output. The FRAP solution procedure requires that an "element file" be prepared on a random-access device, with stiffness and stress-displacement-relation information for each element. In-core information specifying the element nodal connectivities must also be provided. The FRAP procedure avoids complete assembly of the global stiffness matrix by dynamically assembling and solving the equations simultaneously. The in-core storage requirement is dictated by the maximum front width of the problem, i.e., the maximum number of degrees of freedom that have been introduced by previous elements, but also will appear in later elements so they may not yet be eliminated from the in-core storage. The user's control of the maximum front width is accomplished by specification of the order of the elements on the element file. The Tee-Joint Analysis Program has, therefore, been designed to provide a convenient facility for specifying that order.

2. COORDINATE SYSTEMS AND TRANSFORMATIONS

The use of plate elements to form a curved shell structure and the variable orientation of the side tubes with respect to the main tube require the use of a number of distinct coordinate systems for the analysis. Various transformations between these coordinate systems are also required.

The Global Coordinate System is the same as the main tube's Tubular Cartesian Coordinate System (TCCS). This system, shown in Figure G-1, has its origin on the main tube axis at the beginning of the main tube. The TCCS x axis runs along the tube axis. The corresponding main tube's Tubular Polar Coordinate System (TPCS), the corresponding cylindrical system, is also shown in Figure G-1.

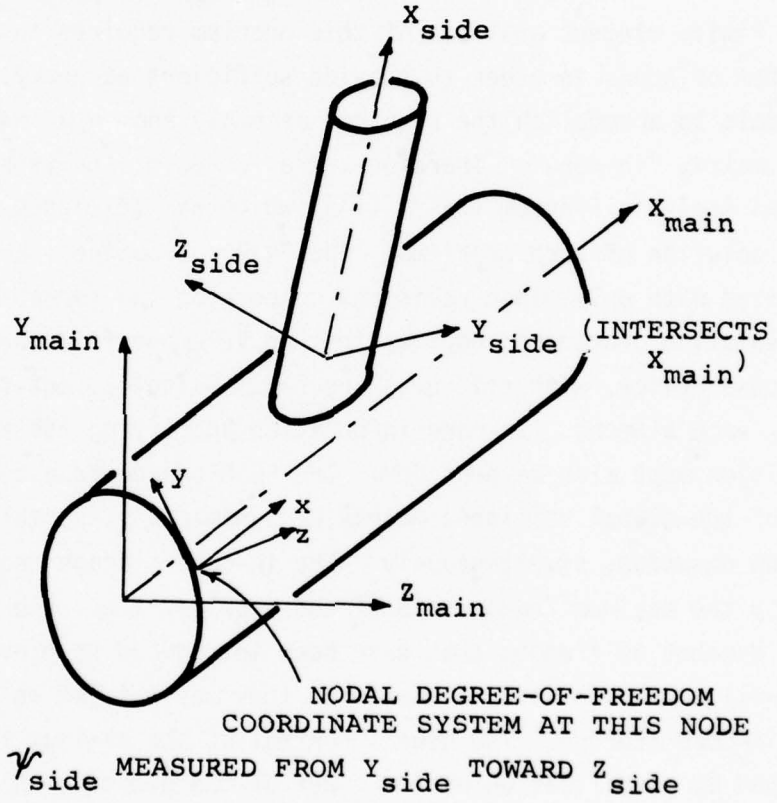


Figure G-2. Side-Tube and Nodal Degree-of-Freedom Coordinate Systems

Each side tube has its own tubular cartesian and polar (cylindrical) systems, TCCS and TPCS, shown in Figure G-2. The origin of each side tube system is the intersection of the tube axis with the surface of the main tube. The x axis runs along the tube axis. The y axis is oriented to lie in the plane of the side and main tube x axes. The polar system angle is measured, as for the main tube, from the y axis toward the z axis.

Nodal locations are specified in the cylindrical (TPCS) systems for the convenience of the user. Of course, only the axial and angular coordinates need be provided, along with the tube number.

Each element has its own local Element Cartesian Coordinate System (ECCS). Each ECCS x axis lies along the line from the first node to the second node of the element. The ECCS y axis then lies normal to the x axis, in the plane of the element, so that the third element node lies in the positive-y half-plane. The ECCS z axis is then normal to the element plane. The element nodes must always be numbered counterclockwise as viewed from outside the tube, so that the ECCS z axis points outward from the tube surface.

At each node, a Nodal Degree-of-Freedom Cartesian Coordinate System (NDCCS) is defined. The NDCCS x axis lies parallel to the TCCS x axis. The NDCCS y axis lies tangent to the tube surface, in the negative Ψ direction. This leaves the NDCCS z axis normal to the tube surface and pointing outward. For nodes located on the intersection of the main tube with a side tube, the NDCCS is defined by the orientation of the main tube, and appears skewed with respect to the orientation of the side tube.

As mentioned earlier, there are some transformations and adjustments which must be performed in order to utilize the planar MLP3K element for modeling curved shells. These measures should provide accurate analysis as long as the angles between adjoining elements in the same tube are small.

First, the element stiffness matrix must be expanded to include definition of the sixth degree of freedom at each node. The MLP3K element provides stiffnesses only for the three deflections and two out-of-plane rotations at each node. The in-plane rotational degree of freedom is defined, and the stiffness matrix expanded to provide zero stiffness for it. This is simply a mathematical convenience in preparation for the next step.

Second, the expanded stiffness matrix must be transformed from the element coordinates (ECCS) into the nodal degree-of-freedom coordinates (NDCCS). This transformation is in general different at each node, since the NDCCS z axis should always be normal to the shell surface at each node.

Third, the transformed stiffness matrix must be adjusted to delete the nodal z rotational degree of freedom. The transformed matrix will show a small but nonzero stiffness for this degree of freedom, which is deleted from the analysis by setting the diagonal stiffness term to unity, setting all off-diagonal terms to zero, and specifying the degree of freedom to be constrained. Elimination of the z rotational degrees of freedom in this manner introduces small modeling errors in the numerical results, but also prevents the assembled stiffness matrix from becoming ill-conditioned.

For intersection nodes, the adjustment procedure is not performed, and all six degrees of freedom are allowed to remain. This is because there is no unique normal to the shell surface at an intersection, so all rotational degrees of freedom remain meaningful.

Because the MLP3K stiffness generation routine requires definition of the nodal locations in a planar coordinate system, the calling program must perform a transformation in addition to that described above. A routine "ELEM" has therefore been prepared which appears to be an element stiffness and stress relation routine for a three or four node planar element. Subroutine ELEM calls MLP3K and MLP3B to perform most of the required computations, performing primarily coordinate transformations itself. It allows specification of nodal locations in the tubular cartesian system (TCCS), and specification of the nodal (NDCCS) systems by provision of each set of nodal unit vectors in TCCS components (equivalent to provision of the TCCS/NDCCS transformation matrix). The ELEM routine prepares the input for the actual element routines in the element (ECCS) system which it computes itself from the nodal locations. It then transforms the results into nodal coordinates using its own ECCS/TCCS transformation, and the provided TCCS/NDCCS transformation.

The provision of nodal (NDCCS) unit vectors in tubular (TCCS) components is straightforward for ordinary nodes. There is some added complication for intersection nodes located on side tube elements, since the NDCCS appears skewed with respect to the side tube at an intersection node. For these cases, the orientation of the side tube with respect to the main tube determines the necessary transformation.

3. TUBE INTERSECTIONS

The intersections of the side tubes with the main tube are analyzed by the program in terms of the tube geometries specified by the user. Points on the intersection can be specified uniquely by providing only the angular position $\bar{\Psi}$ on the side tube. The program computes the axial side tube coordinate $\bar{x}$ and the axial and angular main tube coordinates, x and Ψ, as necessary.

Figure G-3 shows the details of an intersection between a side tube and a main tube. The desired coordinate values are found as follows:

$$b = -\bar{R} \sin(\Psi) \qquad \text{G-1A}$$

$$\Delta\Psi = \sin^{-1}(b/R) \qquad \text{G-1B}$$

$$c = [1 - \cos(\Delta\Psi)]R \qquad \text{G-1C}$$

$$x = a_s + \frac{\bar{R}\cos(\bar{\Psi})}{\sin\Theta} - \frac{c}{\tan\Theta} \qquad \text{G-1D}$$

$$\Psi = \Psi_s + \Delta\Psi \qquad \text{G-1E}$$

$$\bar{a} = \frac{\bar{R}\cos(\bar{\Psi})}{\tan\Theta} - \frac{c}{\sin\Theta} \qquad \text{G-1F}$$

where R is the main tube radius, and $\bar{R}$ the side tube radius. Note that for the limiting case of $\theta = 90°$, the terms with cos θ or tan θ in the denominator are ignored.

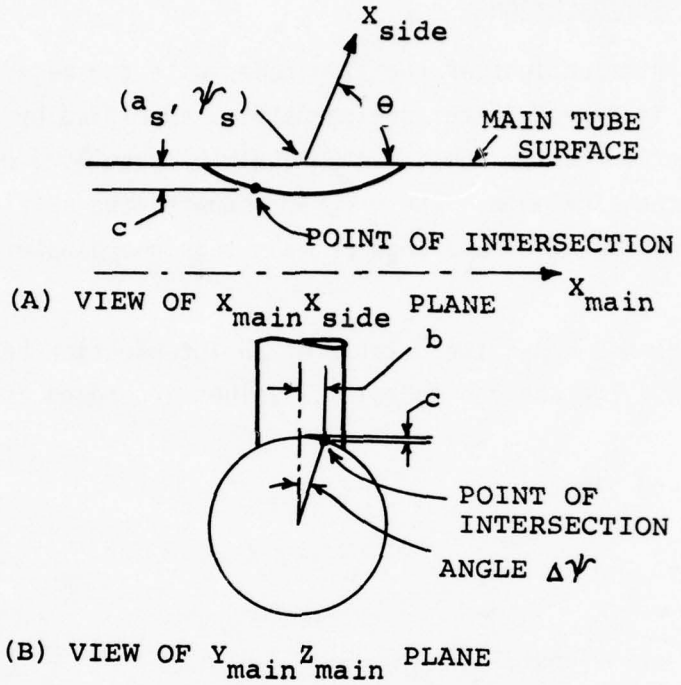


Figure G-3. Details of Tube Intersection Geometry

4. APPLIED FORCES

The user specifies the applied forces in terms of the generalized forces applied to the end of each tube. The program must decompose these generalized forces into nodal forces in accordance with the following procedure. First, the angular distribution of tension and shear in the tube is assumed to be that which would exist in a long uniform tube for the same generalized forces. Second, the distributions of tension and shear are approximated as nodal values of axial and circumferential forces, assuming linear interpolation on the basis of angular position between the nodes. Because the FRAP procedure requires element-level specification of forces, the following relationships are presented for individual elements.

The axial tube load, F_x, consists of a constant angular distribution of tension around the tube:

$$\tilde{F}_x(\Psi) = \frac{F_x}{2\pi} \qquad \text{G-2}$$

For an element with node n_1 at Ψ_1, and n_2 at Ψ_2, the nodal axis force X_1 at node n_1 is:

$$X_1 = \int_{\Psi_1}^{\Psi_2} \left(\frac{\Psi_2 - \Psi}{\Psi_2 - \Psi_1}\right) \frac{F_x}{2\pi} \, d\Psi = 1/2 \, F_x \left(\frac{\Psi_2 - \Psi_1}{2\pi}\right) \qquad \text{G-3}$$

and X_2 is found to be identical.

The tube shear in the TCCS y direction, F_y, consists of shear in the tube wall distributed as:

$$\tilde{F}_y(\Psi) = \frac{-F_y}{\pi r} \sin(\Psi) \qquad \text{G-4}$$

where $\tilde{F}_y(\Psi)$ is TPCS xΨ shear. For one element, the nodal shear force, Y_1, at node n_1 is:

$$Y_1 = \int_{\Psi_1}^{\Psi_2} \left(\frac{\Psi_2 - \Psi}{\Psi_2 - \Psi_1}\right) \left(\frac{-F_y}{\pi r}\right) \sin(\Psi) \, d\Psi \qquad \text{G-5}$$

$$= \frac{F_y}{\pi r} \left[\left(\frac{\sin \Psi_2 - \sin \Psi_1}{\Psi_2 - \Psi_1}\right) - \cos \Psi_1\right]$$

The nodal shear force Y_2 at node n_2 is found in similar fashion. The nodal forces are in the NDCCS negative y direction. The tube shear in the TCCS z direction, F_z, is treated in a manner similar to that for F_y.

The torsional tube load, M_x, is uniformly distributed around the tube. This provides the same relationships as for the axial force F_x, but the radius R enters the computation and the resulting nodal forces are in the NDCCS negative y direction.

The bending moment about the TCCS y axis, M_y, consists of axial forces in the tube walls, distributed as:

$$\tilde{F}_x(\Psi) = \frac{M_y}{\pi R} \sin \Psi \qquad \text{G-6}$$

For an element, the nodal axial force X_1 at node n_1 is then given by:

$$X_1 = \int_{\Psi_1}^{\Psi_2} \frac{(\Psi_2 - \Psi)}{(\Psi_2 - \Psi_1)} \frac{M_y}{\pi R} \sin(\Psi)\, d\Psi \qquad \text{G-7}$$

$$= \frac{M_y}{\pi R(\Psi_2 - \Psi_1)} [(\Psi_2 - \Psi_1)\cos(\Psi_1) - \sin(\Psi_2) + \sin(\Psi_1)]$$

and X_2 is found similarly. The bending moment about the TCCS z axis, M_z, is treated in a manner similar to that for M_y.

Because of the manner in which the program computes the nodal forces, incorrect forces may result if the user modifies the last ring of elements on a tube.

5. USER'S GUIDE

Input cards for the Tee-Joint Analysis Program must be prepared in accordance with the following instructions. Input cards are provided in groups, each starting with a heading card providing:

INWØRD, IN1, IN2, IN3, IN4, IN5, IN6	(A4,6X,6I5)

There are nine forms of heading cards, each with a different four-character INWORD. These are:

TUBE: Define a basic tube geometry, including basic nodes and elements

MATE: Define material properties

MODN: Modify node definitions

MODE: Modify element definitions

PLOT: Plot a tube

RESE: Reset

ELEF: Prepare an element file for the FRAP analysis

ENDT: End tube definition phase

FRAP: Perform FRAP analysis

The usual analysis will be performed in three or more separate runs of the Tee-Joint Analysis Program. First, the user will plot the basic geometry using the sequence:

TUBE (once for each tube)

PLOT (once for each tube)

ENDT

FRAP 0 (not to perform FRAP analysis)

Note that ENDT and FRAP are always required as the last two groups. The user will then prepare the node and element modifications and plot the modified mesh geometry using the sequence:

TUBE (once for each tube)

MODN

```
MODE
PLOT   (once for each tube)
ENDT
FRAP   0
```

The above may be repeated as often as necessary, with corrections to the data cards, until the meshes are formed correctly. Then the actual analysis is performed by the sequence:

```
TUBE   (once for each tube)
MODN
MODE
ELEF
ENDT
FRAP
```

The details for coding each input card group are provided below.

Each "TUBE" input group defines basic tube geometry for one tube. This group consists of a TUBE heading card, plus the geometry and force cards described below. Tube 1, the main tube, must be defined. Tubes 2 and 3, the side tubes, may or may not be defined. Tubes must be defined consecutively starting with tube 1. Each TUBE heading card has integer parameters:

IN1 = tube number

IN2 = print option (0 no, 1 yes) for printing standard nodes generated

IN3 = print option (0 no, 1 yes) for printing standard elements generated, with nodal connections.

IN4 = print option (0 no, 1 yes) for printing geometric data about this tube's intersection with the main tube (not applicable for main tube).

Each TUBE card is followed by a geometry card:

RADIUS, LENGTH, NROUND, NALONG, A, THETA, PSI

(2F10.0,2I10,3F10.0)

RADIUS = radius of tube

LENGTH = length of tube (if not provided,
LENGTH = 2π* RADIUS for side tubes
= 4π* RADIUS for main tube)

NROUND = number of elements around the tube

NALONG = number of elements along the tube
(if not provided, set to make elements as square as possible)

A,THETA,PSI for side tubes only, define orientation with respect to main tube (see Figure G-1 for details):

A = main tube x coordinate of side tube origin

THETA = angle between main and side tube x axes

PSI = angular position of side tube origin on main tube

Following each TUBE and geometry card is the force card:

$F_x, F_y, F_z, M_x, M_y, M_z$

(6F10.0)

F_x = axial load (TCCS x force)

F_y = shear in TCCS y direction

F_z = shear in TCCS z direction

M_x = torsion (moment about TCCS x axis)

M_y = bending moment about TCCS y axis

M_z = bending moment about TCCS z axis

The "MATE" input group defines material properties. There is one material for each tube, plus more as needed up to a maximum of 9. The MATE heading card has integer parameters:

IN1 = number of materials

IN2 = 0 if material properties are handbook quantities
or 1 if tensor quantities (OP parameter of MLP3K element routine)

Each material will then have a NLYR card followed by NLYR property cards:

NLYR	(I5)

NLYR = number of layers

$H,ALPHA,E_{11},E_{22},\nu_{12},\nu_{23},G_{12},G_{23}$	(8D10.6)

H = thickness

ALPHA = angular orientation of layer (with respect to tube x axis)

$E_{11},E_{22},\nu_{12},\nu_{23},G_{12},G_{23}$ = elastic properties

If IN2 = 1, the properties are given instead as:

$E_{LL},E_{TT},\nu_{LT},\nu_{23},G_{LT},G_{23}$

Note that layers are provided in the order from bottom to top (from inside of tube to outside of tube). Also note that materials not used in the analysis may in general be included. However, if an unused material has more layers than the greatest number of layers in the active materials, then program inefficiency will occur.

The "MODN" input group provides modifications of the nodal definitions. The MODN heading card has integer parameter:

IN2 = print option (0 no, 1 yes) to print nodal information as modified

Then a series of nodal modification cards follows:

NOD,NTUBE,X,A	(2I5,2F10.0)

NOD = node number (If NOD was an existing node, the old nodal data is replaced)

NTUBE = tube on which node lies (give side tube number for intersection nodes)

X,A = axial and angular coordinates of node on tube NTUBE

Ordinary nodes (nodes not located on the intersections) are given positive node numbers in conventional fashion. Intersection nodes are given negative node numbers. Intersection nodes are usually numbered starting with -1. The existence of an ordinary node with the same node number magnitude as an intersection node is allowed. For intersection nodes, A must be provided, while the program computes the value of X. To end the series of nodal modification cards, provide a blank card (NOD = 0).

The "MODE" input group provides modifications of the element definitions. The MODE heading card has integer parameter:

IN2 = print option (0 no, 1 yes) to print element information as modified

Then a series of element modification cards follows:

NL,NETYP,NNODS(1),NNODS(2),NNODS(3),NNODS(4)	(6I5)

NL = element number (If NL was an existing element, the old element data is replaced)

NETYP = 0 to delete element NL

or ijk (3 decimal integers) for an existing element, where:

i = IMOD = modification number: must be nonzero if original nodal connections are changed or connected nodes are themselves modified

j = material number (If not specified, material will be as specified by tube number)

k = tube number

NNODS(I) = nodal connections. If NNODS(1) = 0, leave old connections unchanged. If NNODS(1) ≠ 0 and NNODS(4) = 0, this is a triangular element.

To end the series of element modification cards, provide a blank card (NL = 0).

Each "PLOT" input group requests a Calcomp plot of a specified tube, with or without boundaries and/or individual elements shown. A plot may be requested before and/or after the nodes and elements are modified. Each PLOT heading card has integer parameters:

IN1 = tube number

IN2 = 0 not to plot individual elements

≥ 1 plot individual elements

≥ 2 plot element numbers on modified elements

≥ 3 plot element numbers on all elements

IN3 = boundary plotting parameter. For main tube:

IN3 = 0 for no boundary
≥ 1 for boundary
≥ 2 to plot intersection of tube 2
≥ 3 to plot intersection of tube 3

For side tube:

IN3 = 0 for no boundary
1 for boundary

The "RESE" input card deletes all of the information provided by the TUBE, MODN, and MODE input groups. This allows the user to prepare and plot a number of cases within the same computer run. The RESE card may not be used after an ELEF, ENDT, or FRAP group. Therefore, only one finite element analysis may be performed on each run.

The "ELEF" input group defines preparation of the element data file; and the MNUM and LPTR vectors also required for the FRAP analysis. The ELEF heading card has integer parameters:

IN1 = 0 not to prepare
or 1 to prepare, MNUM and LPTR vectors for FRAP analysis

IN2 = 0 not to prepare
or 1 to prepare, an element data file for FRAP analysis

IN3 = ≥1 to print for each element:

LNUM = FRAP element number
IE = internal element number
KNUM = last MNUM position used for the element

≥2 to print for each element:

ELEFOR = forces

IN3 = (continued)

≥3 to print for each element:

EK = stiffness matrix after all transformations and adjustments

≥4 to print for each element:

BMAT = stress-displacement relations

IN4 = element stiffness subroutine print control:

≥1 to print for each element:

XX,YY = nodal locations in ECCS

≥2 to print for each element:

ES = transformation from ECCS to NDCCS

≥3 to print for each element:

EKK = stiffness matrix before transformations or adjustments

≥4 to print for each element:

EK = stiffness matrix after transformations but before adjustments

IN5 = ≥1 to print for each element:

XYZ = nodal locations in TCCS

UXYZ = transformation from TCCS to NDCCS

IN6 = 0 normally (X and Y deflections constrained at first end of main tube)

After the "ELEF" card there will be a series of "specification cards" prescribing the order in which the elements are to be taken for the FRAP analysis. Each specification card is Format (5I10) and consists of KTUBE, KMATL, KMOD, KSTART, KFINIS. Each specification card calls for all elements which match its specification (as described below) and which have

not already been called for by a previous specification card. The series of specification cards is terminated by providing a blank card (KTUBE = 0). Specification is made on the basis of the following parameters for each element:

ITUBE = tube number

IMATL = material number (>0)

JMATL = specified material number ($\geq$0)

(If JMATL >0, IMATL = JMATL
If JMATL = 0, IMATL = ITUBE)

IMOD = modification number (see "MODE" input group)

IE = element number

Each specification card looks for element matches as follows:

KTUBE
<0, any ITUBE OK
>0, KTUBE = ITUBE

KMATL
=0, JMATL = 0
<0, any IMATL or JMATL OK
>0 and <10, KMATL = IMATL
>10, (KMATL - 10) = JMATL

KMOD
<0, any IMOD OK
$\geq$0, KMOD = IMOD

KSTART and KFINIS specify which element numbers to consider, and in which order. In general, element numbers IE = KSTART through IE = KFINIS (can be ascending or descending order) are checked for matches. For convenience, simplified input forms are:

KSTART = KFINIS = 0 means check all elements in ascending order
KSTART >0 and KFINIS = 0 means check element KSTART only

In order to better illustrate the use of the ELEF specification cards, a representative example of a Tee-Joint problem is presented in Figure G-4. In this problem, regions A, D, E, H, and I consist of elements produced by the basic tube mesh generators. Regions B and C, representing the area where extra material strengthens and joins tubes 1 and 2, consist of elements made of materials 4 and 5, respectively. Regions F and G, likewise, represent the area where extra material strengthens and joins tubes 1 and 3, and consist of elements made of materials 6 and 7, respectively. In regions B, C, F, and G, some of the elements are as produced by the basic tube mesh generators with only their material number changed, while others are completely defined by the user.

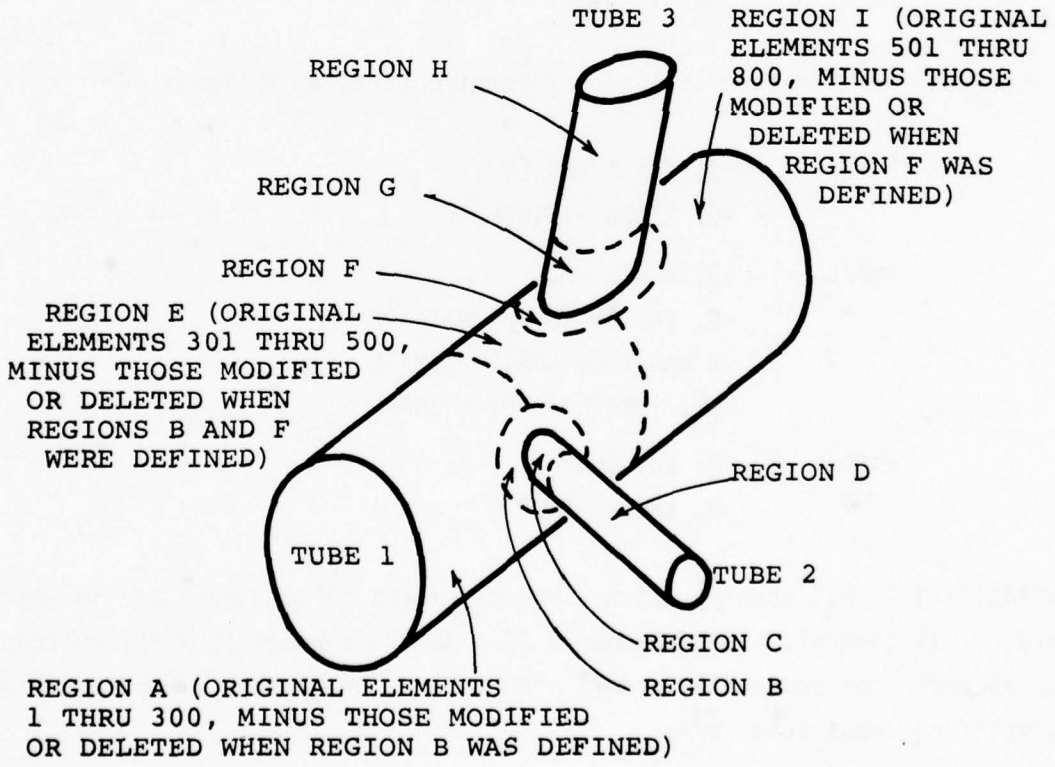


Figure G-4. Example of Tee-Joint Problem

Now, for purposes of program economy, the user desires to have the FRAP procedures treat the elements in alphabetical order of the regions shown, from left to right on the main tube, and from the main tube outward on the side tubes. One way in which the user can accomplish this is by the sequence of specification cards shown here:

KTUBE	KMATL	KMOD	KSTART	KFINIS
1	0	0	1	300
1	4	-1	0	0
2	5	-1	0	0
2	0	0	0	0
1	0	0	301	500
1	6	-1	0	0
3	7	-1	0	0
3	0	0	0	0
1	0	0	0	0
0				

Figure G-5. Example of Specification Card Sequence

In addition to the ordering performed by the above specification cards, the element numbers defined by the user in the MODE input group for Regions B, C, F, and G serve to order the elements within those regions. If the user has not prepared that ordering in the MODE input group, then it may be performed by the specification cards here. This would, of course, require additional specification cards, specifying one or a few elements at a time, replacing the four cards for materials 4 through 7, shown above.

The "ENDT" input card must be the next-to-last input card for each run. It indicates that the tube definition phase is ended.

The "FRAP" input card specifies whether the frontal analysis subroutines ECON and WAFR will be executed. The FRAP heading card has integer parameters:

IN1 = 0 not to run ECON
100 run ECON with minimal printing
101 run ECON with all assembly information printed

IN2 = 0 not to run WAFR
100 run WAFR with minimal printing, do not rewrite element file with results
101 minimal printing, do rewrite file
102 all printing, do not rewrite file
103 all printing, do rewrite file

6. PROGRAM CAPACITY

It is the user's responsibility to prepare the main program and job control language to allow sufficient capacity for each problem. The user must, of course, consider the inefficiencies that will result from preparation for a much larger capacity than will actually be utilized.

First, the user must choose values for:

NN = maximum ordinary node number
NNSPEC = maximum magnitude of intersection node number
NE = maximum internal element number
NEEL = maximum FRAP element number $\leq$NE
MAXFW = maximum front width
MAXL = maximum number of layers in any material
MAXB = number of equations buffered together on equations file (choose to make NWK a reasonable number)
NDOF = maximum number of degrees-of-freedom in FRAP analysis ($\sim$5* NN + 6* NNSPEC)

Then the user must compute:

$$NSIZE_1 = \left(\frac{25*NEEL}{2}\right) + (3*NN) + (5*NE) + (5*NNSPEC) + 2$$

$$NSIZE_2 = \left(\frac{49*NEEL}{2}\right) + 3 + 2*MAXFW + 2*MAXB + MAXFW*MAXB + MAXFW*(MAXFW + 1)/2$$

$$NSIZE = \max(NSIZE_1, NSIZE_2)$$

$$NWEL = 375 * MAXL + 349$$

$$NWEL4 = NWEL * 4$$

$$NWK = MAXB * (MAXFW + 2)$$

$$NWK4 = NWK * 4$$

$$N_{region} = 230 + 4 * \frac{NSIZE}{1000}$$

$$NBK = NDOF/MAXB$$

Then in the main program the user must put:

NSIZE = right hand side of "NSIZE=" statement, and dimension in "COMMON A ( )"

NEEL & NWEL = first two integers in parentheses in "DEFINE FILE 30" statement

NBK & NWK = first two integers in parentheses in "DEFINE FILE 20" statement

NWEL = right hand side of "NWEL=" statement

In the job control language the user must put:

N_{region} = number preceding "K" for REGION parameter on job card

NWEL4 &
NEEL = two integers for SIZE parameter on "G.FT30F001" DD card

NWK4 &
NBK = two integers for SIZE parameter on "G.FT20F001" DD card

A sample of the job control language required for the job is shown below.

For a single run:

```
(job and charge cards)
// EXEC FORG,PROG='USERS.LIBRARY(TEEJOINT)'
//G.FT20F001 DD UNIT=SYSDA,SPACE=(2740,(600)),DISP=(NEW,DELETE)
//G.FT30F001 DD UNIT=SYSDA,SPACE=(4396,(400)),DISP=(NEW,DELETE)
//G.SYSIN DD *
(data)
/*
```

For a series of runs:

```
(job and charge cards)
//RUN1 EXEC FORG,PROG='USERS.LIBRARY(TEEJOINT)'
//G.FT20F001 DD UNIT=SYSDA,SPACE=(2740,(600)),DISP=(NEW,PASS)
//G.FT30F001 DD UNIT=SYSDA,SPACE=(4396,(400)),DISP=(NEW,PASS)
//G.SYSIN DD *
(data for run 1)
//RUN2 EXEC FORG,PROG='USERS.LIBRARY(TEEJOINT)'
//G.FT20F001 DD DSNAME=*.RUN1.G.FT20F001,DISP=(OLD,PASS)
//G.FT30F001 DD DSNAME=*.RUN1.G.FT30F001,DISP=(OLD,PASS)
//G.SYSIN DD*
(data for run 2)
.
.
.
```

APPENDIX H

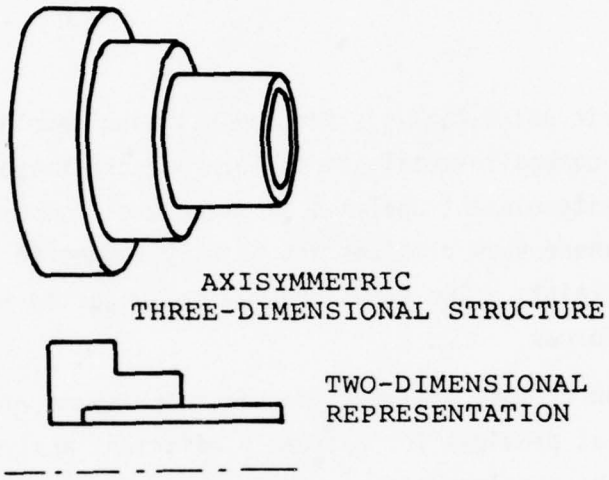
THE AXISYMMETRIC JOINT ANALYSIS PROGRAM (PROGRAM "RADSYM")

1. GENERAL

The Axisymmetric Joint Analysis Program has been developed primarily for analysis of tubular composite-metal joints for spacecraft applications. The program performs finite-element analysis of structures composed of various orthotropic materials, where such problems are axially symmetric in construction, loading, and constraints. The structure may be subjected to thermal loading and/or applied forces.

The restriction of this analysis program to axisymmetric problems limits its usefulness, but provides for extremely efficient analysis. Other analysis programs, such as the Tee-Joint Program described in Appendix G, may be utilized for more general problems. Any problem which is axisymmetric, or which is near enough axisymmetric for the results to be meaningful, may be analyzed by this Axisymmetric Joint Analysis Program at much lower cost. This efficiency results from the fact that an axisymmetric problem may be completely represented by a two-dimensional cross-section of the structure, as shown in Figure H-1. All problem variables are functions of the radial and axial coordinates only. Although the strain-displacement relations are different from those for a planar two-dimensional problem, the computational effort required for solution of the structural problem is almost identical. The principal difference in cost between axisymmetric and full three-dimensional analysis is then caused by the much greater number of degrees of freedom, and much greater bandwidth, of the three-dimensional finite-element mesh. It would not be unusual for the full three-dimensional analysis to raise computation costs two or three orders of magnitude above the costs for an axisymmetric analysis.

A modification of the existing TRIAX3 element [48] has been utilized for this analysis. TRIAX3 is a triangular element, providing convenient modeling of most structural shapes. The element stiffness generation routine assumes that the x coordinate at each node is the radial coordinate for an



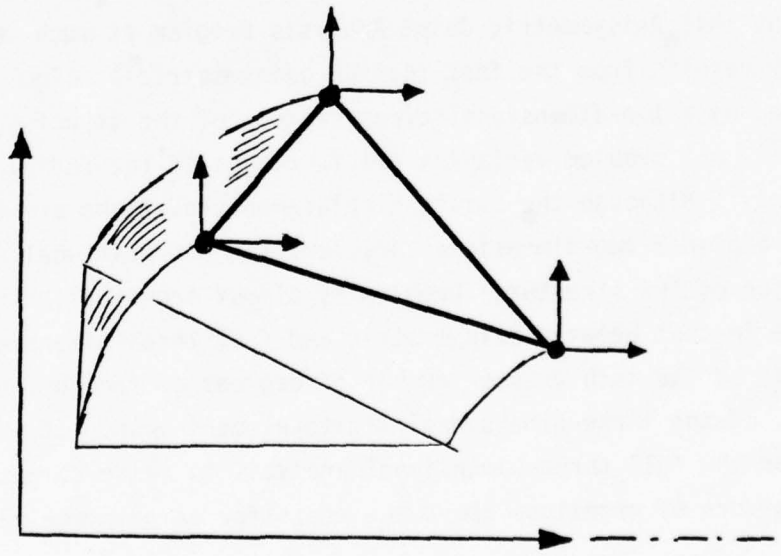


Figure H-1. Two-Dimensional Representation of Three-Dimensional Axisymmetric Structure

axisymmetric problem, and the stiffness matrix is generated accordingly. A set of equivalent element nodal forces is generated for thermal loading.

Two versions of the Axisymmetric Joint Analysis Program have been prepared, for analysis with or without the circumferential deflection degrees of freedom. The version with only radial and axial deflections provides analysis at less than half the cost of the more extensive version.

The TRIAX3 element has been modified and renamed TRAX3M, to provide two capabilities necessary for the analysis of composite tubes. First, the original element allowed only isotropic material properties, and this has been modified to allow specification of orthotropic elasticity and thermal expansion coefficients. Principal axes of the orthotropic materials need not be aligned with the global coordinates (radial, axial, circumferential), but the calling program must perform any necessary coordinate transformations in order to provide the elasticity matrix and thermal expansion coefficient vector in the global coordinates. The original element also considered only radial and axial deflections at the nodes, and this has been modified to consider circumferential deflections as well. This is necessary for analysis of problems with torsion about the axis of symmetry, and for analysis of problems where the circumferential coordinate is not one of the principal axes of an orthotropic material.

Automatic mesh generation has been provided as a convenience to the user of the Axisymmetric Joint Analysis Program. The user need not specify each nodal location and each element connectivity. Rather, the user specifies a set of "basic locations," and rectangular (or general quadrilateral) meshes with such basic locations at their corners. Individual triangular elements may also be specified where quadrilateral meshes are not sufficient. Thermal loading is specified at the basic locations only, with bilinear interpolation in each quadrilateral mesh. Constraints and forces are specified in terms of the individual nodes, but the user can specify a series of nodes forming the boundary of a mesh rather than having to specify the conditions individually at each node.

Because the axisymmetric analysis with a two-dimensional finite-element mesh provides such a small number of degrees-of-freedom and a small bandwidth, compared with a full three-dimensional analysis, it is possible to assemble and solve the global stiffness matrix in-core. The solution procedure uses the Finite Element Analysis Basic Library [48].

2. TRANSFORMATION OF ELASTICITY MATRIX

The Axisymmetric Joint Analysis Program requires the material elasticity matrices [C] in global coordinates, either explicitly or by calculation in the program. The orthotropic material principal axes will in general not be parallel to the global coordinates. For convenience of the user, the elasticity matrix should therefore be describable in terms of its parameters in the principal material axis coordinates, and the orientation of those coordinates in the global coordinates.

The analyses intended to be performed using this program all have the radial direction as one of the principal material axes. The program has been restricted to this case, so the orientation of the material coordinates is given simply as the "ply angle," the angle between the axial coordinate and the first principal material coordinate. The program rotates [C] matrix as necessary to obtain it in global coordinates, as described below.

Finite element analysis of composite materials often requires that a region of the structure, containing non-homogeneous material, be treated as a homogeneous material. For example, one protion of a laminated structure may contain many layers, with the ply angles of the layers alternating $\pm 30°$. A mesh which distinguished each layer would be much too fine. Instead, the portion of the structure may be considered as a homogeneous material with average properties. The user is responsible for the interpretation of results when utilizing this option of the program.

Transformation of the material elasticity matrix is complicated by the fact that it is a matrix representation of a relationship which is really a fourth-order-tensor. The tensor stress σ_{ij} and the tensor strain γ_{ij} are related by the elasticity tensor E_{ijkl} according to:

$$\sigma_{ij} = E_{ijkl}\ \gamma_{kl} \qquad \text{H-1}$$

Given a new coordinate system represented by a tilde (~), the the direction cosines $l_{\tilde{mi}}$ between the new m^{th} and old i^{th} coordinates, the tensor strain transformation is simply:

$$\gamma_{kl} = l_{\tilde{pk}}\ l_{\tilde{rl}}\ \tilde{\gamma}_{pr} \qquad \text{H-2}$$

and hence,

$$\tilde{E}_{mnpr} = l_{\tilde{mi}}\ l_{\tilde{nj}}\ l_{\tilde{pk}}\ l_{\tilde{rl}}\ E_{ijkl} \qquad \text{H-3}$$

Difficulties arise when the stresses and strains are represented as vectors, and the elasticity tensor as a matrix, destroying some of the mathematical simplicity of the relationships. The strain tensor is represented as a vector according to:

$$\{\gamma\} = \{\gamma_{11}, \gamma_{22}, \gamma_{33}, \gamma_{23}, \gamma_{13}, \gamma_{12}\} \qquad \text{H-4}$$

The stress tensor is likewise represented as a vector according to:

$$\{\sigma\} = \{\sigma_{11}, \sigma_{22}, \sigma_{33}, \sigma_{23}, \sigma_{13}, \sigma_{12}\} \qquad \text{H-5}$$

In order to simplify the format of the stress-strain relationship an "engineering strain vector" is then defined as:

$$\{\varepsilon\} = \{\gamma_{11}\ \gamma_{22}\ \gamma_{33}\ 2\gamma_{23}\ 2\gamma_{13}\ 2\gamma_{12}\} \qquad \text{H-6}$$

Now the transformation of strain becomes:

$$\{\varepsilon\} = [R^T]\ \{\tilde{\varepsilon}\} \qquad \text{H-7}$$

where R contains product-pairs of the direction cosines, along with some factors of two.

Giving the stress-strain relationship for the stress vector and the engineering strain vector as:

$$\{\sigma\} = [C]\ \{\varepsilon\} \qquad \text{H-8}$$

the transformation of the elasticity matrix [C] is then seen to be:

$$[\tilde{C}] = [R]\ [C]\ [R^T] \qquad \text{H-9}$$

The thermal expansion coefficients $\{\alpha\}$ must also be transformed into the new (global) coordinate system. Since the thermal strain is proportional to the $\{\alpha\}$ vector, the $\{\alpha\}$ vector will transform in the same manner as strain. Hence,

$$\{\tilde{\alpha}\} = [R^T]^{-1}\ \{\alpha\} \qquad \text{H-10}$$

Note that the rotation matrix [R] is not orthonormal, hence $[R^T] \neq [R]^{-1}$.

3. USER'S GUIDE PART I: MESH GENERATION

The Axisymmetric Joint Analysis Program provides almost completely automatic quadrilateral mesh generation capabilities. This subsection explains these capabilities, and the parameters which the user must specify in order to implement them. The details of input card format are deferred to the following subsection.

The quadrilateral mesh in its simplest form is a rectangle aligned with the radial and axial axes, as shown in Figure H-2. The locations of the four corners are defined by the basic location numbers of the corners, in the order (upper left, upper right, lower left, lower right). In this example the corners are locations (6, 27, 12, 54).

The mesh produced by the program consists of boxes, further subdivided into triangles. The number of rows of boxes (NHIGH) and number of columns of boxes (NWIDE) must be specified. In this case NHIGH = 2 and NWIDE = 3. The boxes are subdivided by diagonals into triangles with all diagonals aligned similarly, with diagonals reaching corners 2 and 3 but not 1 or 4.

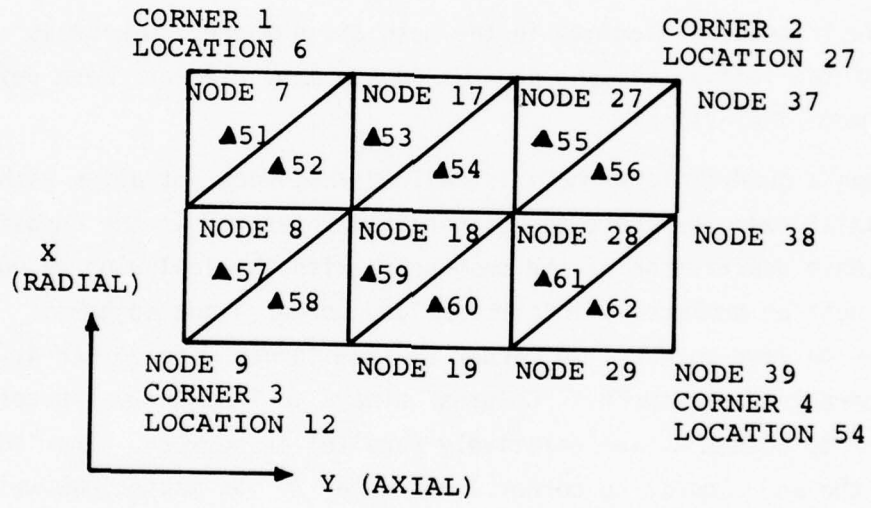


Figure H-2. Example Mesh

The node numbers are specified by providing NSTART, NADD, and sometimes NEXTRA. NSTART is the node number at corner 1; in this case NSTART = 7. The nodes within each column are numbered consecutively. The node numbers at the tops of the columns, except for the first, are calculated as follows. For the general case, each node number at the top of a column is NADD more than that at the top of the previous column. For the case shown, NADD = 10. It is often necessary to have an extra added amount for the top of the second column, which will not be used for later columns, and this may be specified as NEXTRA. That is, the node number at the top of the second column is NSTART + NADD + NEXTRA. There is also a parameter NEXTRI which is intended for a capability not yet implemented, which should always be set to zero.

The triangular elements in the mesh are numbered rowwise as shown. The number of the initial element depends on how many elements were defined by previous mesh definitions.

When a quadrilateral mesh is desired that does not align with the radial and axial axes, or where the diagonals are desired in the opposite sense, the above description of the mesh holds with the following stipulations: The corners must be numbered with corner 1 and corner 4 not adjacent. "Rows" always go from corner 1 to corner 2, from corner 3 to corner 4, and relatively parallel in between. "Columns" always go from corner 1 to corner 3, from corner 2 to corner 4, and relatively parallel in between. The "top" of a column is the end closest to corner 1 or corner 2. No matter how weird the shape and/or organization of the mesh, constraints and forces are always referenced on the global (radial + axial) coordinate system. The temperatures specified at the four locations defining the corners of the mesh are assumed to vary, like the coordinates, bilinearly within the mesh.

Meshes should be designed on the input cards as "type 2," unless they satisfy the requirement which allow them to be designated as "type 3" for more efficiency. A "type 3" mesh must be a parallelogram with top (corner 1 to corner 2) and bottom (corner 3 to corner 4) parallel to the axial axis.

Improved efficiency results from the similarity of all upper or lower triangles in each row.

There are many considerations which the user must keep in mind when preparing meshes. Some are common in finite element structural analysis, such as keeping the boxes in the quadrilateral meshes reasonably near square to assist in maintaining good numerical behavior. Also, mesh fineness must be chosen to provide sufficient accuracy without excessive computational costs.

Other considerations are dictated by the particular numerical solution routines used. In this case, FEABL is used, requiring sequential node numbering starting with 1. No resequencing is performed; the user should prepare the sequencing to provide minimum bandwidth. The program has been designed to make this preparation easy for problems that are longer in the axial direction than in the radial direction, such as tubular joints. Minimum bandwidth can then be obtained by numbering the nodes at each axial location, before proceeding to the next axial location across the structure. The automatic mesh node numbering scheme which was described earlier, primarily based on NSTART and NADD, makes this preparation convenient.

4. USER'S GUIDE PART II: INPUT DATA FORMAT

There are seven types of groups of input cards. These are

MATERIALS:	Definition of materials
LOCATIONS:	Definition of basic locations and temperatures
MESHES:	Definition of quadrilateral meshes of elements, and sometimes single elements
CONSTRAINTS:	Definition of the constrained degrees of freedom
LOADS:	Definition of the applied loads
TEMPERATURES:	Definition of the temperatures at the basic locations, without modification to the basic locations
RUN:	Definition of parameters used in the solution, and computation of the solution

The description of the structural problem to be analyzed is provided to the program using the first 5 groups, in any order. Then a RUN card is used to initiate computation of the result. Variation of the problem may then be made by providing any or all of the first 6 types of groups, followed by another RUN card for a new solution. The input should be prepared carefully, in exact agreement with the specifications contained herein.

Detailed descriptions of each input card group follow. Whenever a field (series of card columns) is to contain a number, the required form of the number is standard Fortran integer (I) format for numbers which are inherently integers, and standard Fortran floating point (F or E) format for other numbers. Alphanumeric information is in standard Fortran A format.

The "MATERIALS" group consists of its title card and several data cards for each material described. There may be a maximum of 20 materials described. The "MATERIALS" title card consists of:

Cols 1-9	"MATERIALS"
Cols 11-15	nmat
Cols 41-80	(title of materials)

The value of nmat prescribes the number of materials described, each of which will have a set of data cards. The first material data card consists of:

Cols 1-5	material number (must be consecutively numbered from 1 to nmat)
Cols 6-10	INCODE, an integer code. If INCODE is zero, the user must provide all 36 entries, row after row, of the 6x6 C (material properties) matrix on the next 5 data cards. If INCODE is not zero, the user must provide the values of Young's modulus, the shear modulus, and Poisson's ratio for the longitudinal and transverse directions on the next card.
Cols 11-20	material weight density (this value is used to calculate the total weight of each material used)
Cols 21-30, 31-40, 41-50	the three thermal expansion coefficients (alpha) for the principal material axes which will be rotated to generate the 6 coefficients in global coordinates (rotation of alphas not presently implemented)

If INCODE is not zero, the second material data card consists of:

Cols 1-10 E_L

Cols 11-20 E_T

Cols 21-30 G_{LT}

Cols 31-40 G_{TT}

Cols 41-50 ν_{TT}

Cols 51-60 ν_{LT}

Cols 61-70 ν_{TL}

Cols 71-80 PLYANG = Ply angle indicator in units of degrees.

a) If PLYANG is between plus and minus 90.0 inclusive, PLYANG is the angle of the plies for the material

b) If PLYANG is between 100 and 190, then the ply angles are plus and minus (PLYANG -100) and the total material properties matrix will be the average of C for +(PLYANG -100) and C for -(PLYANG -100)

c) If PLYANG is 200, then the next 2 data cards will provide the angles and fraction of the material to which that ply angle applies

If INCODE is not zero and PLYANG in Cols 71-80 of the second material card is 200, the third and fourth material data cards consist of:

Cols 1-10 ANG_1
Cols 11-20 ANG_2
Cols 71-80 ANG_8
} where ANG_i is the ply angle indicator for the i^{th} section of plies.

Cols 1-10 $PART_1$
Cols 11-20 $PART_2$
Cols 71-80 $PART_8$
} where $PART_i$ is the fraction of the material whose plies have a ply angle indicator of ANG_i.

If any ANG_i is between plus and minus 90°, the ply angle for section i is ANG_i. If any ANG_i is between 100 and 190, plus and minus (ANG_i-100) are the ply angles for section i and a C matrix which is the average of the C matrix for +(ANG-100)

degrees and the C matrix for -(ANG-100) degrees will be calculated. If a $PART_i$ is zero, it is assumed that there are only i-1 sections in the material. Thus the final C matrix is:

$$C_{final} = \sum_{i=1}^{\#\ of\ sections} PART_i \; C_i \qquad \text{(H-11)} \qquad \text{H-11}$$

where

$$C_i = R_i \; C^{(no\ rot)} \; R_i^T \qquad \text{(H-12)} \qquad \text{H-12}$$

and R_i is the rotation matrix described in Subsection H.2. If INCODE is zero, then all of the above data cards after the first do not appear. The second through sixth material data cards provide the matrix of material properties [C] where:

$$\{\sigma\} = [C]\ \{\varepsilon\}$$

for six stresses and strains in the order:

1) radial extensional
2) axial extensional
3) circumferential extensional
4) axial/circumferential shear
5) radial/circumferential shear
6) radial/axial shear

The C matrix (dimension 6x6) is provided by rows on these next 5 data cards, 8 numbers per card, 10 columns per number.

The "LOCATIONS" group consists of a title card and one data card for each basic location specified. The "LOCATIONS" title card consists of:

Cols 1-9 "LOCATIONS"
Cols 11-15 nbl (number of basic locations)
Cols 16-20 nnt (number of nodes)
Cols 41-80 (title of locations)

The value nbl prescribes the number of locations that will be defined. The value nnt prescribes the total number of nodes that will be used in the analysis. Each locations data card consists of:

Cols 1-5	location number (must be numbered consecutively from 1 to nbl)
Cols 11-20	radial coordinate (X)
Cols 21-30	axial coordinate (Y)
Cols 31-40	temperature

The maximum number of basic locations that may be specified is 60. There is no limit on the number of nodes. If a "LOCATIONS" title card is provided with nbl = 0, then there is no change to the previous specification of locations (by a previous "locations" group of input cards)--but nnt and the "locations" title are modified to the new value and characters provided.

The "MESHES" group consists of its title card, and a data card for each element or mesh specified. The "MESHES" title card consists of:

Cols 1-6	"MESHES"
Cols 11-15	nedt (number of mesh definition cards)
Cols 41-80	(title of meshes)

The format of each mesh data card varies depending on the type of mesh prescribed. It always begins:

Cols 1-5	mesh number (consecutive beginning with 1)
Cols 6-10	mesh type

where type 1 is a single triangle and types 2 and 3 are quadrilateral meshes. The data card for a single triangle is:

Cols 1-5	mesh number
Cols 6-10	"1"
Cols 16-20	material number
Cols 21-25, 26-30, 31-35	basic location numbers at the three corners of the triangle
Cols 36-40, 41-45, 46-50	node numbers at the three corners of the triangle (same order as locations provided)

The data card for a quadrilateral mesh is:

Cols 1-5	mesh number
Cols 6-10	"2" or "3" (see Subsection H.3 for the distinction)
Cols 16-20	material number
Cols 21-25, 26-30, 31-35, 36-40	basic location numbers at the four corners: usually Uleft, Uright, Lleft, Lright
Cols 41-45	nstart
46-50	nadd
51-55	nhigh
56-60	nwide
61-65	nextra
66-70	nextri

The meanings of the parameters on this card were explained in Subsection H.3. The maximum number of meshes that may be specified is 30. There is no limit on the number of triangular elements produced by the meshes.

The "CONSTRAINTS" group consists of its title card and the specified number of constraint data cards. The constraints title card consists of:

Cols 1-7	"CONSTRS"
Cols 11-15	ncdc (number of constraint data cards)
Cols 41-80	(title of constraint)

Each constraint data card specifies one or both constrained degrees of freedom, at one or more nodes. To specify constraints at one node only the form is:

Cols 1-5	node number
Cols 16-20	"1" if X deflection is constrained, "0" if not
Cols 21-25	"1" if Y deflection is constrained, "0" if not
Cols 26-30	"1" if hoop deflection is constrained, "0" if not
Cols 31-35	the value to which the deflection is constrained

To specify constraints at more than one node, the form is:

Cols 1-5	n1 = first node number
Cols 6-10	n2 = last node number

Cols 11-15 nd = delta between node numbers
(=1 if specified as zero)

Cols 16-50 (same as for single node as shown above)

This constrains X,Y and/or Hoop deflection at nodes n1, n1+nd, n1+2nd,...,n2. The program requires that (n2-n1) be a positive integral multiple of nd. The total number of constrained degrees of freedom defined by all constraint input cards may not exceed 200.

The "LOADS" group consists of its title card and the specified number of loads data cards. The "LOADS" tital card consists of:

Cols 1-5 "LOADS"

Cols 11-15 number of loads data cards

Cols 41-80 (title of loads)

Each load specification card consists of:

Cols 1-5 n1

Cols 6-10 n2

Cols 11-15 nd

Cols 16-25 xf

Cols 26-35 xl

Cols 36-45 yf

Cols 46-55 yl

Cols 56-65 hoopf

Cols 66-75 hoopl

Col 80 nhalf

To specify the loads at a particular node, provide n1 as that node number and leave n2 and nd blank. To specify the loads at a sequence of nodes, specify n1, n2 and nd. If nd is specified as zero, a value of 1 is assumed. Thus if n2 is not zero, the loads will be assumed specified at nodes n1, n1+nd, n1+2nd,...,n2. The program requires that (n2-n1) be a positive integral multiple of nd; (n2-n1) may be negative in which case nd must also be negative. The maximum number of nodes at which loads are specified by all loads data cards is 200. The number of load data cards may be zero in which case there are no applied loads. To specify the X, Y and hoop forces at the node(s),

provide xf, yf and hoopf respectively. To specify a linearly varying set of X, Y and hoop forces at a sequence of nodes, specify xf, yf and hoopf as the forces at node 1 and specify xl, yl and hoopl as the forces at node 2. It is not permitted to specify xl, yl or hoopl as zero when using the linearly varying set of forces. Because of program logic,that type of force must be input as non-zero forces for xf, yf, and/or hoopf, zero force for xl, yl and/or hoopl and node numbers decreasing from n1 to n2 with a negative nd. When a sequence of forces at nodes is provided and the forces are to be halved at the first and last nodes only, set nhalf = 1. Then the first forces will be 1/2xf, 1/2yf and 1/2 hoopf and the last force will be 1/2xl, 1/2yl and 1/2 hoopl.

The "TEMPERATURES" group consists of its title card and as many temperature data cards as there are basic locations (as specified by the previous locations group of input cards). The temperature title card consists of:

Cols 1-5 "TEMPS"

Cols 61-80 (title of temperatures)

The (title of temperatures) will replace the second half of the (title of locations) provided by the previous locations group of input cards. Each temperature data card consists of:

Cols 1-5 location number (numbered consecutively from 1 to nbl)

Cols 31-40 temperature

For the usual case, there will be no temperature input group. This is because desired temperatures may be input as part of the locations input group.

Once the other groups of input cards have been provided, the "RUN" card instructs the program to find the solution and also provides some additional information required for the problem. The format of the "RUN" card is:

Cols 1-3 "RUN"

Cols 11-15 usually 0--(unless special test output is desired)

Cols 16-20 usually 0--"1" if output of average stresses in each box rather than in each triangle is desired

Cols 21-30 TREF = reference temperature at which structure was assembled

Cols 41-80 (title of run)

5. PROGRAM CAPACITY

The present version of the program has a capacity for:

a) 20 materials

b) 60 basic locations

c) 30 meshes of elements

d) 200 constrained degrees of freedom

e) 200 nodes at which loads are prescribed

f) 8 ply angles per mixed material

If the user wishes to change these limitations, he must change the appropriate dimensions. To change:

a) the number of materials from 20 to N, he must change the dimensions of DENS, ALPH, C, and WGT by replacing the 20 by N.

b) the number of basic locations from 60 to N, he must change the dimensions of X, Y, and T by replacing 60 by N.

c) the number of meshes from 30 to N, he must change the dimensions of NETYP, NODE, and MAT by replacing 30 by N.

d) the number of constraints from 200 to N, he must change the dimensions of NCDOF and NODEL by replacing 200 by N.

e) the number of nodes at which loads are prescribed from 200 to N, he must change the dimensions of FX, FY, FHP and DISPL by replacing 200 by N.

f) the number of ply angles per material from 8 to N, he must change the dimension of ANGS and PART by replacing 8 by N.

In addition to the above changes, the user may modify the MAIN program dimension of the RE and IN vectors used by the FEABL solution procedure. The value of the dimension of these vectors indirectly determines the program capacity for number of nodes and bandwidth. The program output will note if there are insufficient dimensions present, for each analysis.

The user must also specify the region size required for the program. This size is approximately 90,000 + 4N BYTES, where N is the dimension of RE and IN.

6. EXAMPLE JOINT ANALYSIS

A joint between a 1.5-in. diameter graphite/epoxy tube and an outer steel fitting was analyzed to estimate stress concentration factors and to assess the effects of thermal-shock temperature gradients on fatigue stresses in tubes subjected to accelerated thermal cycle tests. The finite-element mesh is illustrated in Figure H-3. Small variations of bond thickness and number of 90° plies were studied, as indicated by the dimensions in Table H-1. (See Appendices A and C for elastic properties used in the analysis.)

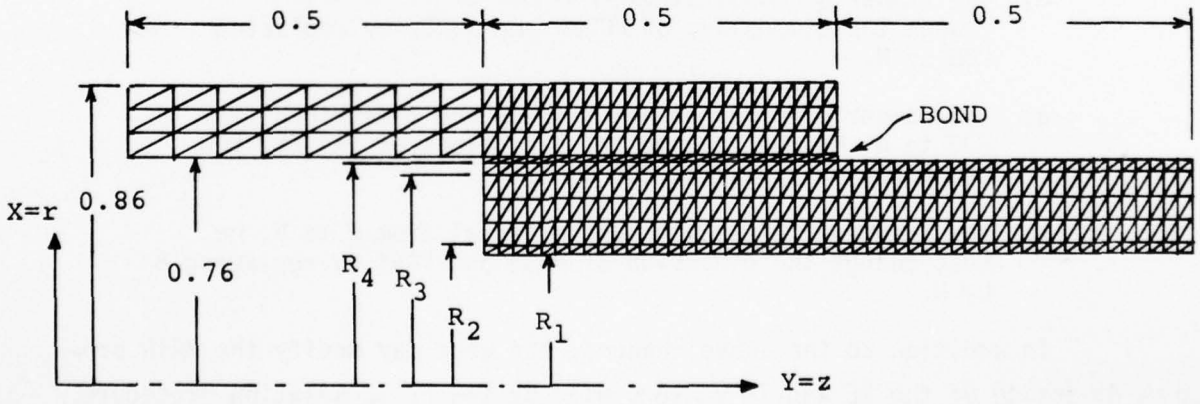


Figure H-3. Finite-Element Mesh

TABLE H-1

CASES STUDIED

Item	C A S E S		
	Nominal	Thin Bond	Extra 90°
Tube Stacking Sequence	$[90^\circ_2/0^\circ_{16}/90^\circ_2]$	$[90^\circ_2/0^\circ_{16}/90^\circ_2]$	$[90^\circ_3/0^\circ_{16}/90^\circ_3]$
Bond Thickness (in)	0.010	0.007	0.010
R_1 (in)	0.620	0.623	0.606
R_2 (in)	0.633	0.636	0.626
R_3 (in)	0.737	0.747	0.730
R_4 (in)	0.750	0.753	0.750

The three models cited above were subjected to three uniform loading conditions. A compressive axial load of 5,520 lb. simulated an extreme launch load equivalent to about twice the first-passage load if the model is scaled up to a feed-truss longeron diameter. A torque of 1,450 lb.in. was chosen arbitrarily to represent a value somewhat larger than the torsional loads expected in either feed-truss design. A temperature change $\Delta T = -217.6°C$ (-392°F) was chosen to represent the cold-soak test equilibrium condition (Appendix C), i.e., transition from room temperature to liquid nitrogen temperature.

Results from these analyses are plotted in Figures H-4 through H-7. Stresses near the outer surface of the graphite/epoxy tube due to axial load are shown in Figure H-4. Stress concentration factors of about 1.5 in the 0° plies and 3.2 in the 90° plies are apparent. Figure H-5 illustrates the corresponding interlaminar stresses in the bond. Here, it is apparent that interlaminar shear is the most significant bond stress.

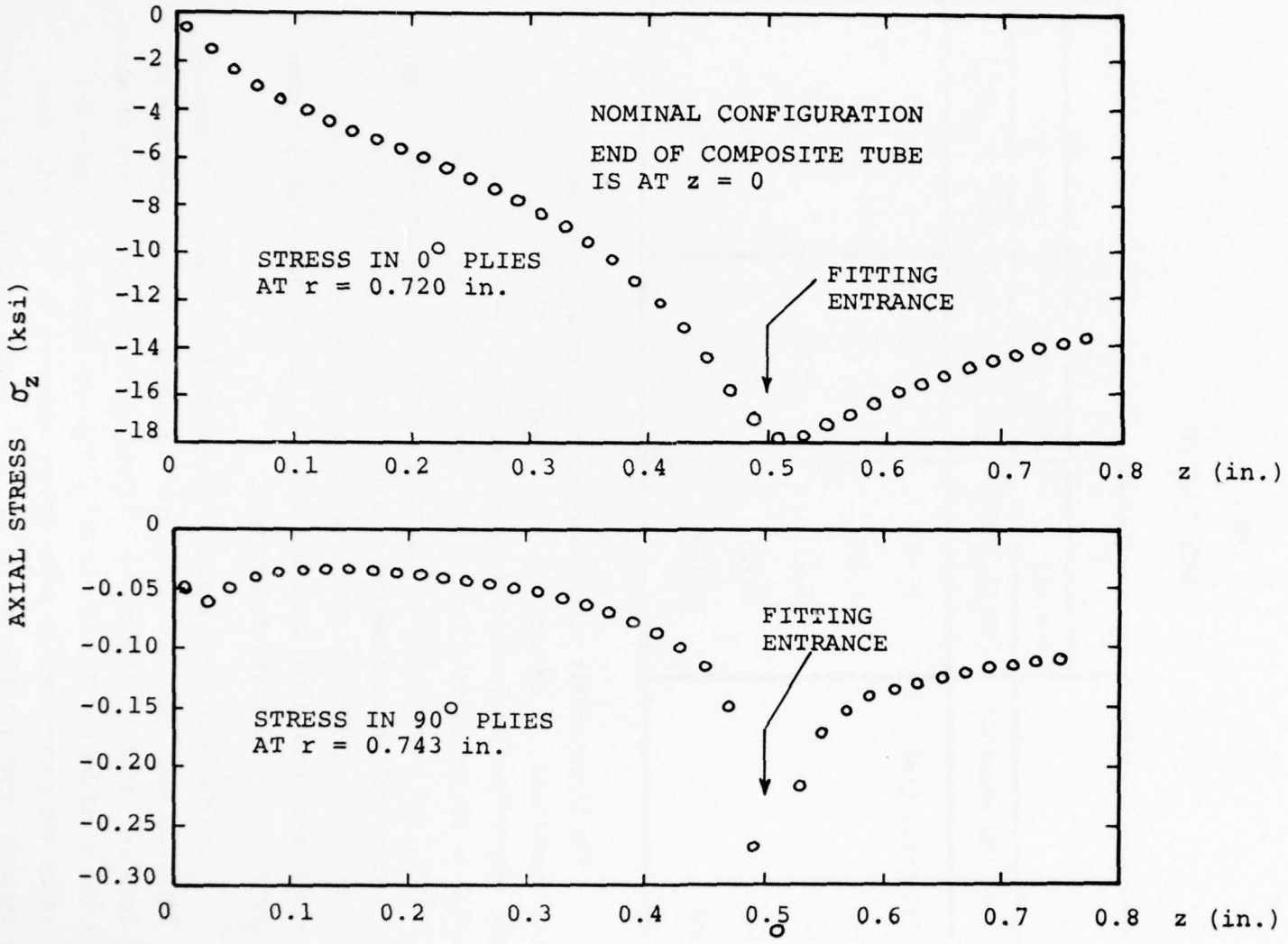


Figure H-4. Tube Axial Stresses Caused by 5,520-lb. Compressive Axial Load

The only significant stress caused by torsion loading is an interlaminar shear in the bond. Figure H-6 illustrates this distribution and shows that the torsional stress is small in comparison with the stresses caused by axial load.

Bondline interlaminar stresses caused by the cold soak are shown in Figure H-7. These stresses are somwhat lārger than the axial-load stresses (compare with Figure H-5). Again, interlaminar shear is more significant than interlaminar normal stress. Also, in all three load cases it is apparent that neither the 30 percent reduction of bond thickness nor the addition of 90° plies has caused any significant change in the stress levels.

Thermal-shock conditions were studied by placing a linear temperature gradient ΔT across the wall of the nominal-tube model, as shown in Figure H-8. A total temperature change $\Delta T = 40°F$ corresponds to the estimated condition for accelerated testing by immersing a bare tube in liquid nitrogen (see Appendix C). Contours of radial, hoop, axial, and shear (τ_{rz}) stresses for this case are plotted in Figures H-9 through H-12. The most significant stress is the hoop component in the 90° plies at the outer surface of the tube (stresses from 1 to 2 ksi). However, the stresses in the bondline appear to be quite low.

An additional check on the bondline was made by calculating the Mises-Hecky equivalent stress:

$$\sigma_{eff} = \sqrt{1/2\,[(\sigma_r - \sigma_\Theta)^2 + (\sigma_\Theta - \sigma_z)^2 + (\sigma_z - \sigma_r)^2] + 3\tau_{rz}^2} \qquad \text{H-13}$$

at the ends and midpoint of the bond. The results, summarized in Table H-2, indicate that the equivalent stresses due to thermal shock are at most only about 10 percent of the cold-soak stresses. Hence, cold-soak equilibrium is expected to be the dominant factor in cyclic thermal fatigue.

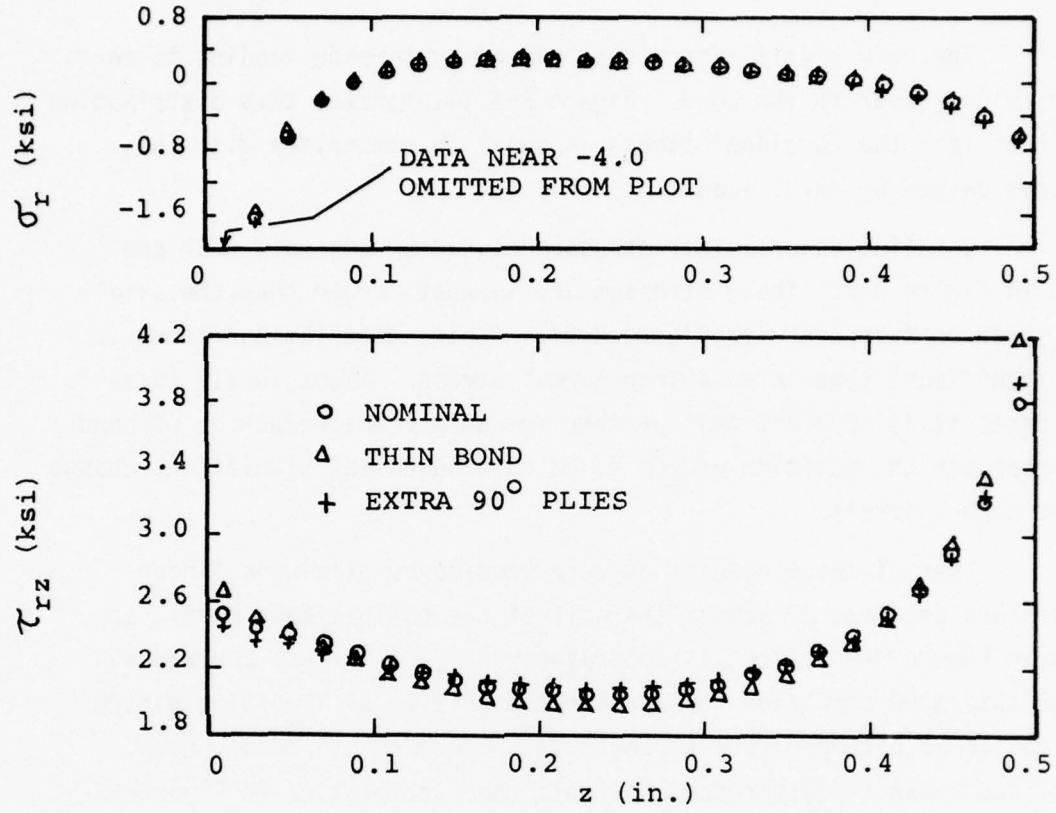


Figure H-5. Bond Stresses Caused by Axial Compression

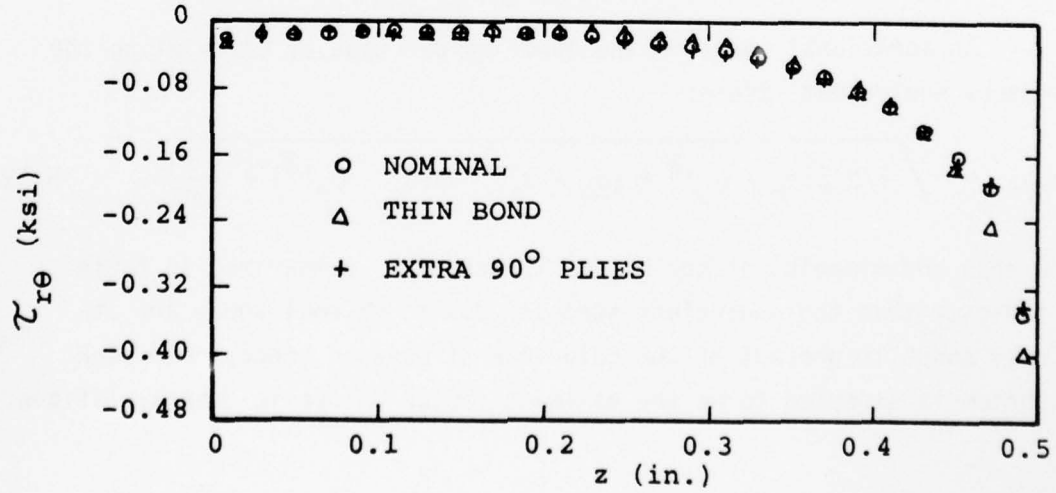


Figure H-6. Bond Stress Caused by 1.45 KIP-IN. Torque

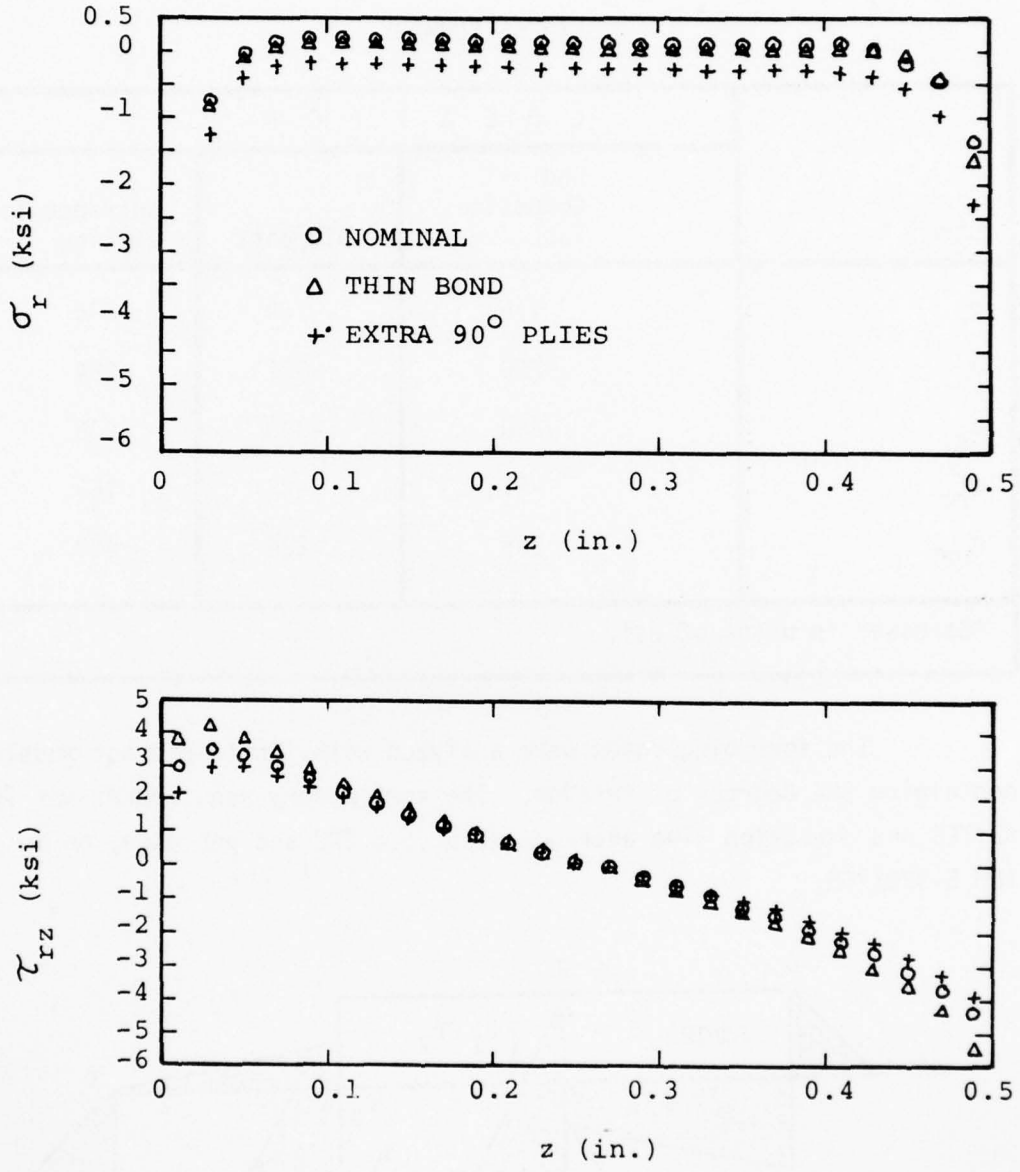


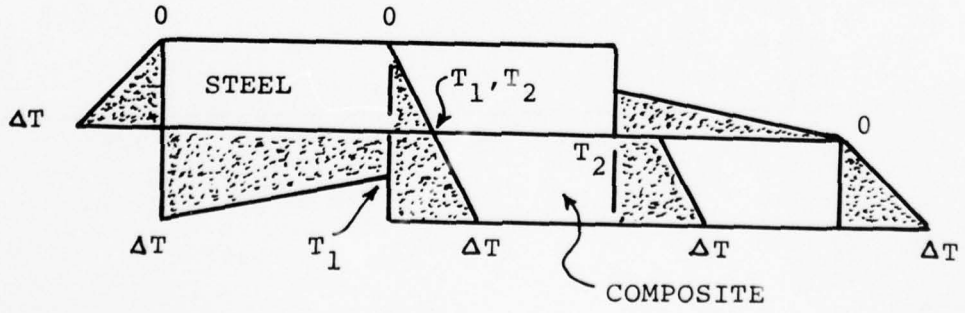
Figure H-7. Bond Stresses Caused by Cold Soak

TABLE H-2

STRESS SUMMARY

Stress*	LOCATION		
	End of Composite Tube	Midpoint	Entrance to Fitting
σ_r	116	-104	45
σ_Θ	-250	-381	-284
σ_z	-230	-390	-306
σ_{rz}	-51	-22	169
σ_{eff}	368	284	450
*Stresses in units of psi.			

The foregoing cases were analyzed with finite-element models containing 884 degrees of freedom. The core memory requirement was 170 KBYTES and execution time averaged about 5.6 CPU sec per case, on an IBM S-370/168.

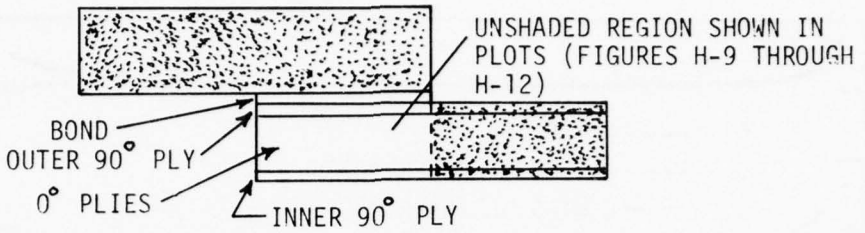


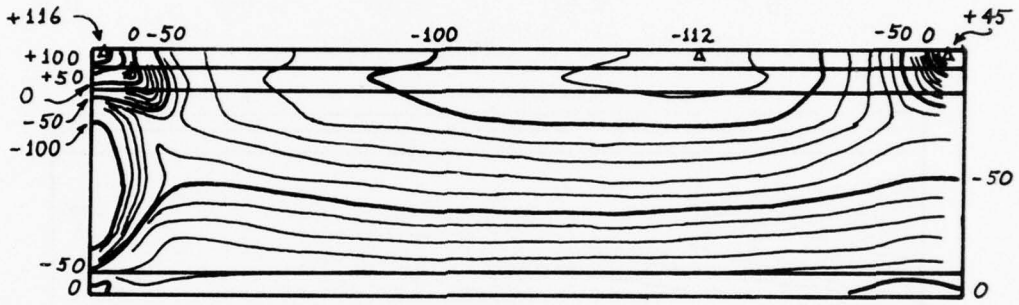
T_1 = TEMPERATURE AT STEEL/BOND INTERFACE

T_2 = TEMPERATURE AT COMPOSITE/BOND INTERFACE

T_1, T_2 OBTAINED FROM ΔT BY LINEAR INTERPOLATION

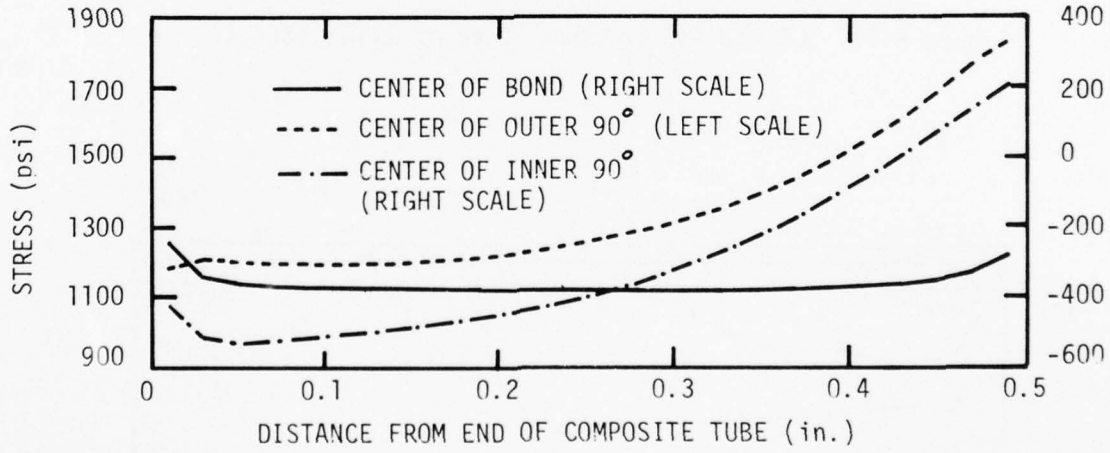
Figure H-8. Assumed Temperature Distribution





CONTOUR INTERVAL = 10 psi

Figure H-9. Contour Plot of Radial Stress



CONTOUR INTERVAL = 100 psi

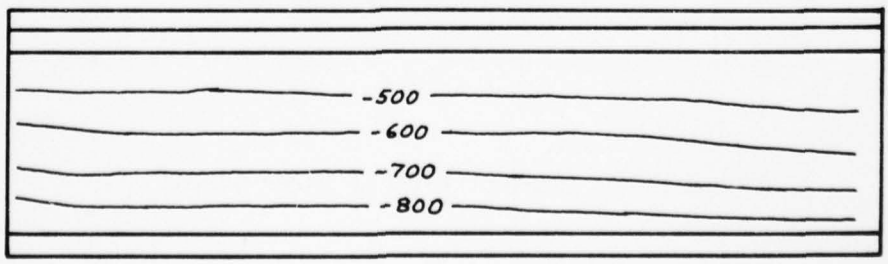


Figure H-10. Linear and Contour Plots of Hoop Stress

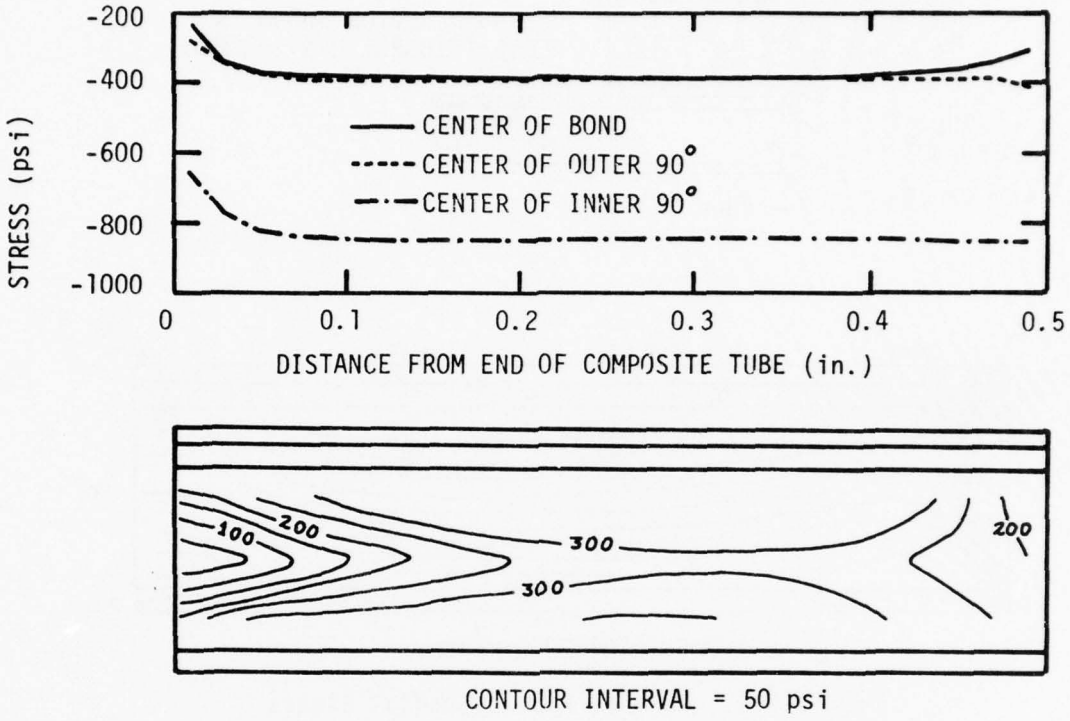


Figure H-11. Linear and Contour Plots of Axial Stress

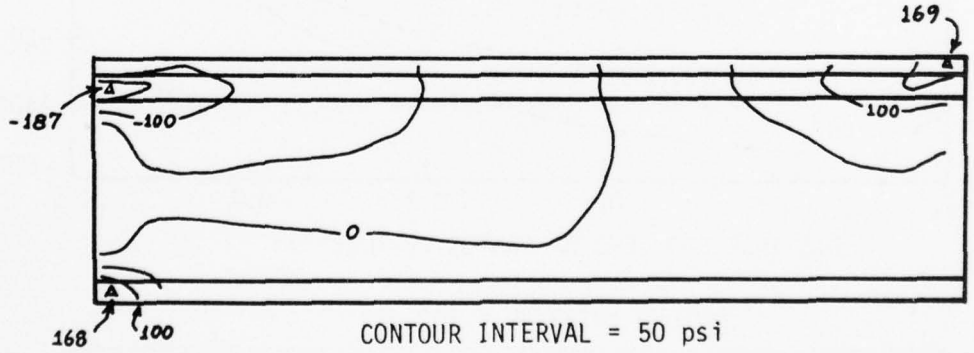


Figure H-12. Contour Plot of Shear Stress

APPENDIX I

EFFECT OF ADHEREND TAPER ON BONDED LAP JOINTS

1. GENERAL

Load transfer in lap joints occurs through a shear stress which tends to peak near the ends of the lap. Material and geometrical parameters in the joint affect the shear stress distribution. A two-dimensional analysis for lap joints has been formulated by Goland and Reissner [62]. Similar one-dimensional analyses of stresses at the fiber/resin interface in composite materials have been formulated by Rosen [63] and Kelly [64]. The class of formulations represented by References 62, 63 and 64 have come to be known as "shear-lag" models. This appendix outlines a one-dimensional shear-lag model for a lap joint which allows for tapering of one adherend representing a metal attachment fitting at the end of a composite tube.

2. FORMULATION

Figure I-1 illustrates the model geometry. A tapered metal fitting (1) and a cylindrical composite tube (2) are joined by a bond of thickness h, and length L. Shear, hoop, and radial stresses are neglected, and the axial stresses are assumed to be uniformly distributed through the walls of both adherends. The flaring couple caused by offset of the adherend stresses is also neglected. The bond material is assumed to be subjected only to a shear stress, which is constant through the bond thickness.

Let s_i, u_i ($i = 1,2$) be the adherend axial stress and displacement fields, respectively, and let s_B represent the shear stress in the bond. Figure I-2 illustrates free-body diagrams of the model, from which the following equilibrium equations are derived:

$$(A_1 s_1)' - 2\pi R s_B = 0 \qquad \text{I-1}$$

$$A_2 s_2' + 2\pi R s_B = 0 \qquad \text{I-2}$$

where $( )' = d( )/dx$. Substituting $A_1(x) = A_{10} - A_{11}x$ in Eq. I-1 then leads to:

$$-A_{11}s_1 + (A_{10} - A_{11}x)s_1' - 2\pi R s_B = 0 \qquad \text{I-3}$$

The stress-strain relations for the adherends and bond can be expressed as:

$$s_1 = E_1 u_1' \qquad s_2 = E_2 u_2' \qquad s_B = \frac{G}{h}(u_1 - u_2) \qquad \text{I-4}$$

Equations I-2 through I-4 can now be combined to eliminate the stresses, leading to the following coupled differential equations for the displacement fields:

$$E_1(A_{10} - A_{11}x)u_1'' - E_1 A_{11} u_1' - \frac{2\pi RG}{h}(u_1 - u_2) = 0 \qquad \text{I-5}$$

$$E_2 A_2 u_2'' + \frac{2\pi RG}{h}(u_1 - u_2) = 0 \qquad \text{I-6}$$

Using Eq. I-6 to eliminate u_1 then yields the following fourth-order differential equation in u_2:

$$\frac{hE_1E_2A_2}{2\pi RG}(A_{10} - A_{11}x)u_2^{(4)} - \frac{hE_1E_2A_{11}A_2}{2\pi RG}u_2''' \qquad \text{I-7}$$

$$-[E_1(A_{10} - A_{11}x) + E_2A_2]u_2'' + E_1A_{11}u_2' = 0$$

The solution of Eq. I-7 can be written as:

$$u_2(x) = \sum_{n=0}^{N} C_n x^n \qquad \text{I-8}$$

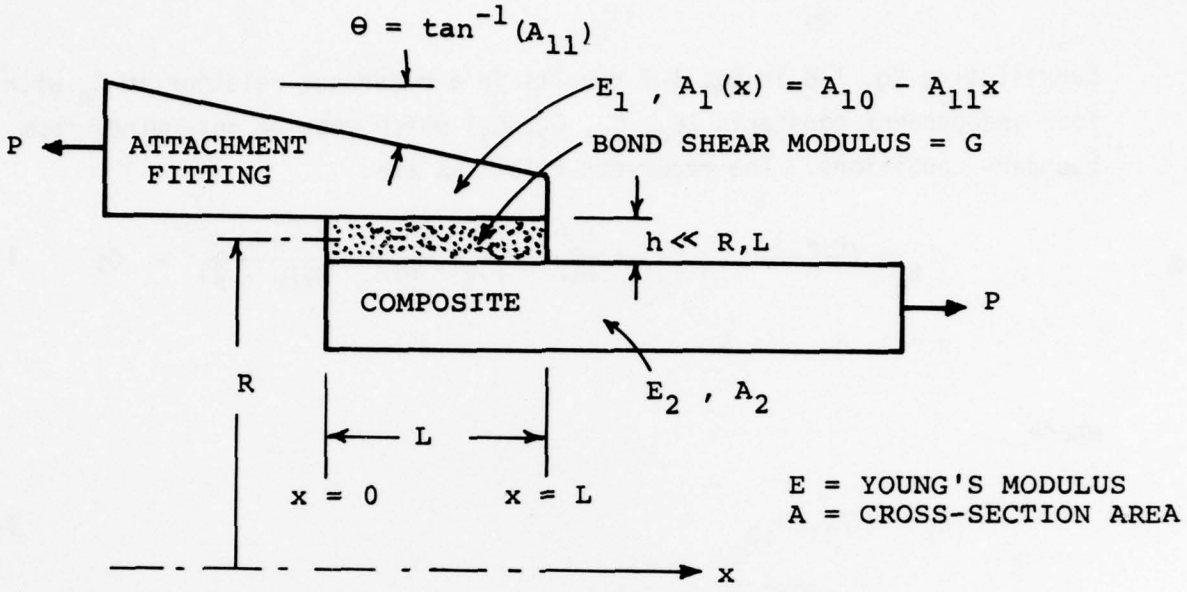


Figure I-1. Lap-Joint Shear-Lag Model

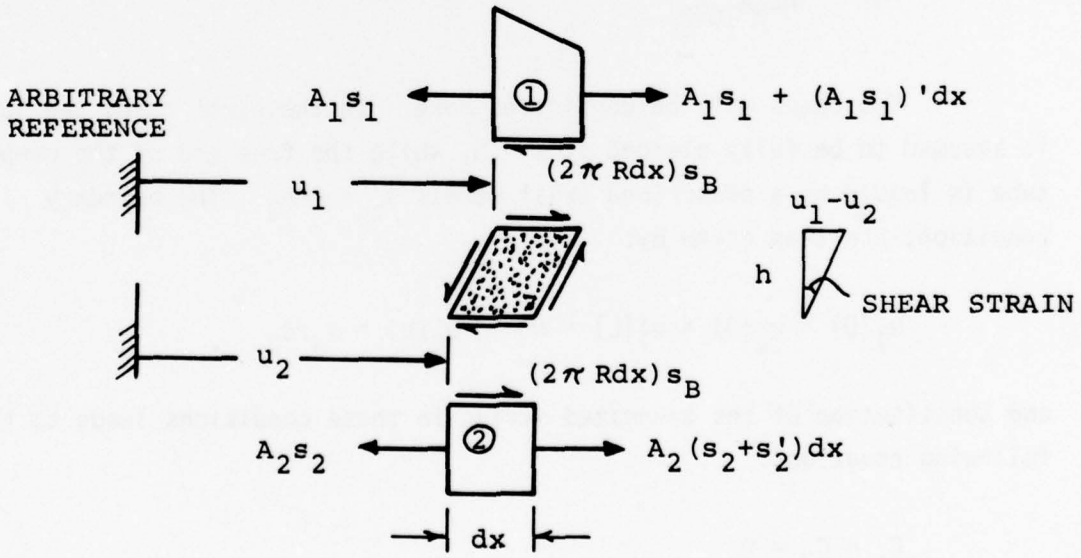


Figure I-2. Free-Body Diagrams

Substituting Eq. I-8 in Eq. I-7 results in a recurrent relation in C_n with four independent constants (C_0, C_1, C_2, C_3) which must be determined from boundary conditions. The recurrent relations are:

$$-C_n + \left(\frac{n-3}{n}\right)\beta_1 C_{n-1} + \frac{\beta_2 C_{n-2}}{n(n-1)} + \frac{(n-3)\beta_3 C_{n-3}}{n(n-1)(n-2)} = 0; \qquad \text{I-9}$$

$$n = 4, 5, \ldots, N$$

where

$$\beta_1 = A_{11}/A_{10} \qquad \text{I-10A}$$

$$\beta_2 = \frac{2\pi RG(E_1A_{10} + E_2A_2)}{hE_1E_2A_{10}A_2} \qquad \text{I-10B}$$

$$\beta_3 = \frac{2\pi RGA_{11}}{hE_2A_{10}A_2} \qquad \text{I-10C}$$

Two cases will be considered here. In the first case, the joint is assumed to be fully clamped at $x = 0$, while the free end of the composite tube is loaded by a prescribed axial stress $s_o = P/A_2$. The boundary conditions are then given by:

$$u_1(0) = u_2(0) = u_1'(L) = 0 \qquad u_2'(L) = s_o/E_2 \qquad \text{I-11}$$

and substitution of the truncated series in these conditions leads to the following equations:

$$C_o = C_2 = 0 \qquad \text{I-12A}$$

$$C_1 + \sum_{n=2}^{N-1} (n+1)\, C_{n+1} L^n \cong s_o/E_2 \qquad \text{I-12B}$$

$$\sum_{n=0}^{N-3} \frac{(n+3)!}{n!} C_{n+3} L^n \cong \frac{2\pi RGs_o}{hA_2(E_2)^2} \qquad \text{I-12C}$$

In the second case, only the tapered fitting is clamped at x = 0, while the composite tube is assumed to be stress-free at that location, and the boundary conditions at x = L are unchanged:

$$u_1(0) = u_2'(0) = u_1'(L) = 0 \qquad u_2'(L) = s_o/E_2 \qquad \text{I-13}$$

Equations I-12A, 12B must then be replaced by the following relations:

$$C_1 = 0 \qquad \text{I-14A}$$

$$C_2 - \frac{\pi RG}{hE_2A_2} C_o = 0 \qquad \text{I-14B}$$

$$\sum_{n=1}^{N-1} (n+1)C_{n+1} L^n \cong s_o/E_2 \qquad \text{I-14C}$$

while Eq. I-12C still applies.

3. SOLUTION PROCEDURE AND RESULTS

Equations I-9, together with four boundary conditions from Eqs. I-12 and I-14, form a set of N + 1 linear equations in the N + 1 unknowns C_0, C_1, C_2,...C_N, with an unsymmetric coefficient matrix. These equations can be solved by a general algorithm which decomposes the coefficient matrix into lower-triangular, diagonal and upper-triangular factors to permit sequential solution [65,66].

A sufficient number of unknowns must be retained to obtain solutions converged to a desired tolerance. This number was found to rise rapidly with increasing taper angle, $\Theta = \tan^{-1}(A_{11})$. In the present case, up to 60 terms were retained to provide four-place accuracy for taper angles up to about 3 degrees.

The attachment-joint DDT article (Appendix C) was adopted as a baseline for the analysis, with some variation in the steel fitting and the bond thickness. The parameters used in the shear-lag analysis are summarized in Table I-1.

TABLE I-1

INPUT DATA FOR TAPERED-JOINT ANALYSIS

Material	Dimensions
1) Steel Fitting	$E_1 = 30 \times 10^6$ psi Wall thickness (at x=0) = 0.046 in. $0.025 \leq$ wall thickness at free end ≤ 0.046 in.
2) Composite Tube	$[90°/0°_{10}/90°]$ $E_2 = 17.7 \times 10^6$ psi Wall thickness = 0.0614 in.
Bond	$G = 0.5 \times 10^6$ psi $0.001 \leq h \leq 0.02$ in. L = 2.0 in.

Results for the fully clamped case are presented in Table I-2. In this case, a shear peak exists only at x = L. Values of this peak, s_B, are reported for various combinations of taper and bond thickness. Also shown are the percent reductions in s_B relative to zero taper and a 0.001-in. bond as a baseline case. The results indicate that very little benefit can be gained by machining a small taper in the fitting. However, tapers in excess of 10° may be worth investigating in the future.

The partially clamped case is of greater interest because it cannot be assumed that a load-transfer path through the end of the composite tube will be available in a realistic design. In this case, shear peaks occur at both ends of the bond. Table I-3 presents the results for both peaks and for the same combinations of taper and bond thickness as in Table I-2. The free-end peak (where the fitting wall thickness is smaller) is uniformly higher than the clamped-end peak. Also, comparison of the results with the shear stresses in Table I-2 shows that removal of the axial load-transfer path from the end of the composite tube has increased the free-end peak by about 10 percent at most. However, the trend of the clamped-end peak suggests that fittings possessing steeper entrance tapers may have a higher shear peak at the clamped end.

The results obtained from the simplified one-dimensional shear-lag model suggest that appreciable reductions in peak bondline shear stresses can be achieved by careful design of the attachment fitting. Specifically, a steep entrance taper ($\Theta \geq 10$ degrees) should be combined with an untapered runout. Also, it should be possible to maintain gross joint stiffness with a very thin bond, but without adverse effects on the peak shears, by incorporating a small amount of bondline taper in the fitting near the ends of the bond. It will be worthwhile in future investigations to perform detailed stress analyses of such joints to determine whether the bondline peak shear reductions are accompanied by comparable reduction of the stress concentrations in the composite tube. A schematic detail of the design concept suggested above is shown in Figure I-3.

TABLE I-2

PEAK SHEAR AT FREE END OF FULLY CLAMPED JOINT

(Axial stress s_o = 1 ksi)

Fitting Wall Thickness at Free End (inches)	Taper (Degrees)	h = 0.001 in.		h = 0.005 in.		h = 0.01 in.		h = 0.02 in.	
		s_B (psi)	% Red	s_B (psi)	% Red	s_B (psi)	% Red	s_B (psi)	% Red
0.046	0	995	-	444	55.4	314	68.5	220	78.0
0.044	0.57	979	1.6	438	56.0	310	68.9	217	78.2
0.039	1.15	961	3.5	432	56.6	306	69.3	215	78.4
0.034	1.72	940	5.5	424	57.4	301	69.8	212	78.7
0.030	2.29	917	7.9	416	58.3	296	70.3	210	79.0
0.025	2.86	-	-	406	59.3	290	70.9	206	79.3

TABLE I-3

PEAK SHEARS IN PARTIALLY CLAMPED JOINT

(Axial stress s_0 = 1 ksi)

Fitting Wall Thickness at Free End (inches)	Taper (Degrees)	h = 0.001 in.		h = 0.005 in.		h = 0.01 in.		h = 0.02 in.	
		s_B (psi)		s_B (psi)		s_B (psi)		s_B (psi)	
		x = L	x = 0	x = L	x = 0	x = L	x = 0	x = L	x = 0
0.046	0	995	668	447	301	322	222	241	176
0.044	0.57	979	671	440	304	318	225	238	178
0.039	1.15	961	675	434	307	314	227	236	180
0.034	1.72	940	678	426	311	309	230	233	182
0.030	2.29	917	683	417	314	303	233	230	184
0.025	2.86	-	-	407	319	297	236	226	186

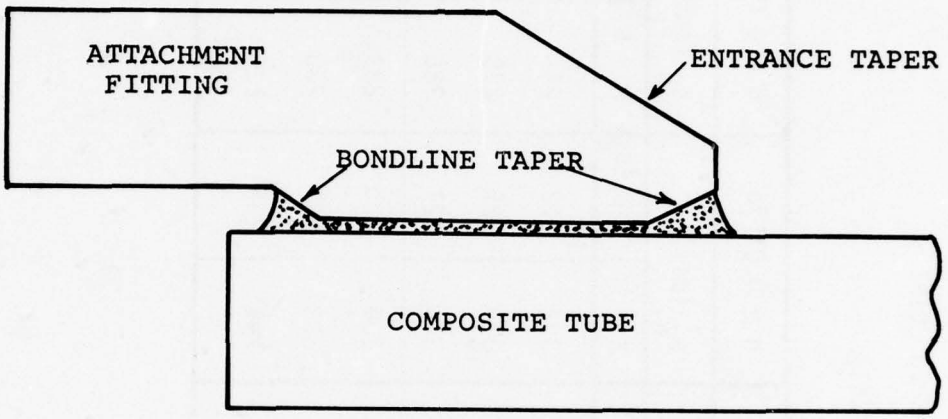


Figure I-3. Hypothetical Improved Attachment Detail

APPENDIX J

DEPLOYMENT DYNAMICS

1. ANTENNA DEPLOYMENT SCENARIO

The parabolic reflector antenna is deployed by igniting squibs to realease the antenna ribs from the housing doubhnut. The pre-deployment configuration is shown schematically in Figure J-1. The antenna ribs are kept in a state of initial strain by a tight wrap around the core of the housing. The reflector mesh is attached to the ribs, and hangs in folds between them.

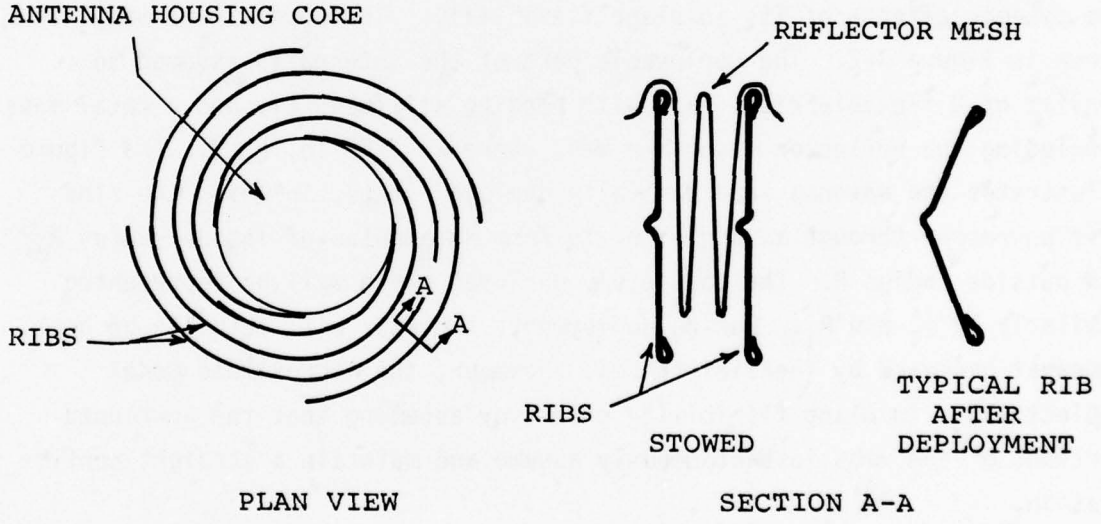


Figure J-1. Antenna Storage Scheme

Upon release, the ribs spring back toward an unstrained state, applying a transient torque to the feed truss through the housing. The maximum torque for a 50-foot diameter antenna is estimated to be 4,000 lb. ft.; this load was applied statically to the ATS/3-Ring and Tripod-B designs in the first phase of the study to estimate the stress levels associated

deployment [1]. A survey of the computations disclosed maximum static stresses of 7.25 ksi in ATS/3-Ring and 77.3 ksi in Tripod-B.

However, a better assessment of deployment stress peaks can be made by modeling the truss/antenna as a one-degree-of-freedom dynamic system, taking into account the transient nature of the torque. It is shown subsequently that the torque applied to the feed truss must be treated as a step function with an initial ramp.

2. ANTENNA MODEL

While it is being deployed, the reflector antenna acts as a non-linear dynamic system because of its large change in radius. However, an approximate equation of motion for the antenna can be derived by ignoring the dynamic effects of its in-plane flexibility. The approximate model is shown in Figure J-2. The deployable part of the antenna is assumed to consist of N flexible ribs, each with bending stiffness EI, and a total mass (including the reflector mesh) M = W/g, where W $\simeq$ 250 lb. [1]. The figure illustrates the antenna in a partially deployed state, in which the ribs have unwrapped through an angle, ϕ, to form an annulus of inside radius R_o and outside radius R. The completely deployed state will be represented similarly by ϕ_1 and R_1. During deployment, the ribs will actually be bent somewhat backward by inertial forces. However, the approximate model neglects this in-plane flexibility effect by assuming that the unwrapped portions of the ribs instantaneously assume and maintain a straight configuration.

Under the foregoing assumptions, an equation for the instantaneous deployment velocity, $\dot{\phi}$, can be derived from an energy balance. At any deployment angle, ϕ, the strain energy

$$U = N\left(\frac{EI}{R_o^2}\right)\ell = N\frac{EI}{R_o}\phi \qquad \text{J-1}$$

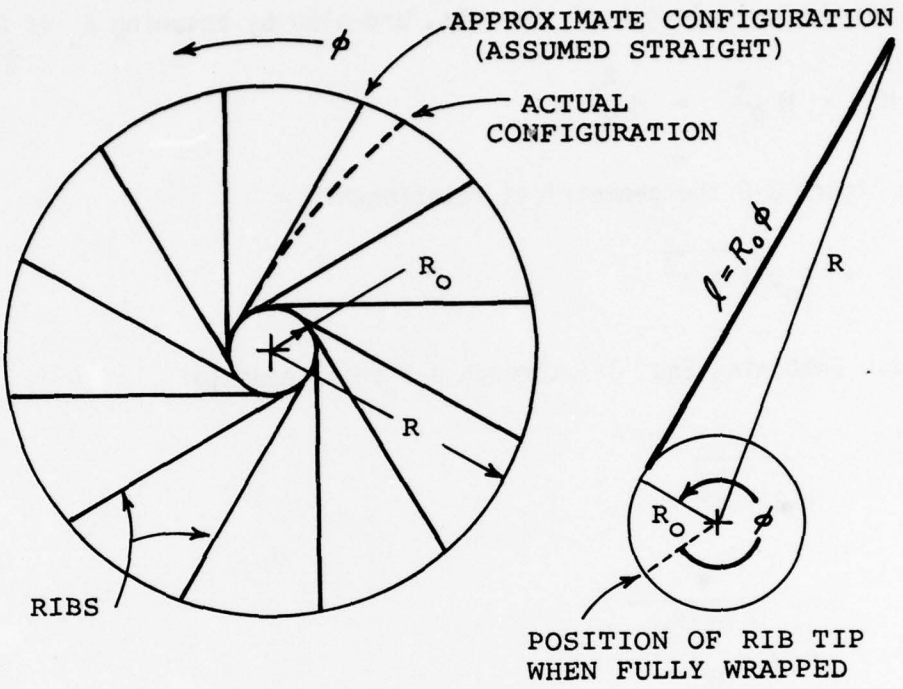


Figure J-2. Antenna Deployment Model

has been released by elastic unbending of the ribs. This energy must appear as kinetic energy of angular motion of that part of the antenna which has been deployed:

$$U = 1/2\ I_p \dot{\phi}^2 \qquad \text{J-2}$$

where I_p is the current mass polar moment of inertia. The moment of inertia can be estimated by assuming a uniform distribution of mass, M', over the annulus:

$$I_p = M'(R_o^2 + R^2)/2 \qquad \text{J-3}$$

The deployed mass, M', can be estimated by assuming its value to be proportional to the deployed length of the ribs, and also by assuming $R_o << R_1$:

$$M' \cong M \frac{\ell}{R_1} = M \frac{R_o}{R_1} \phi \qquad \text{J-4}$$

Also, from Figure J-2 the geometrical relationship:

$$R = R_o \sqrt{1 + \phi^2} \qquad \text{J-5}$$

is apparent. Combining Eqs. J-1 through J-5 then leads to:

$$\dot{\phi} = \frac{\lambda}{\sqrt{2 + \phi^2}} \qquad \text{J-6}$$

where

$$\lambda = 2 \sqrt{\frac{NEIR_1}{MR_o^4}} \qquad \text{J-7}$$

Differentiation of Eq. J-6 also yields, after substitution for $\dot{\phi}$, the following expression for angular acceleration:

$$\ddot{\phi} = - \frac{\lambda^2 \phi}{(2 + \phi^2)^2} \qquad \text{J-8}$$

The model can be calibrated by writing the equation of motion relating reaction torque, T, to angular acceleration:

$$T = I_p \ddot{\phi} = - \frac{\beta \phi^2}{2 + \phi^2} \qquad \text{J-9}$$

where

$$\beta = 1/2 \, M \frac{R_o^3}{R_1} \lambda^2 \qquad \text{J-10}$$

From Eq. J-9, it is apparent that the torque, which will also act upon the feed truss, is a rapidly, then slowly, increasing function of ϕ. The magnitude $|T/\beta|$, is illustrated in Figure J-3.

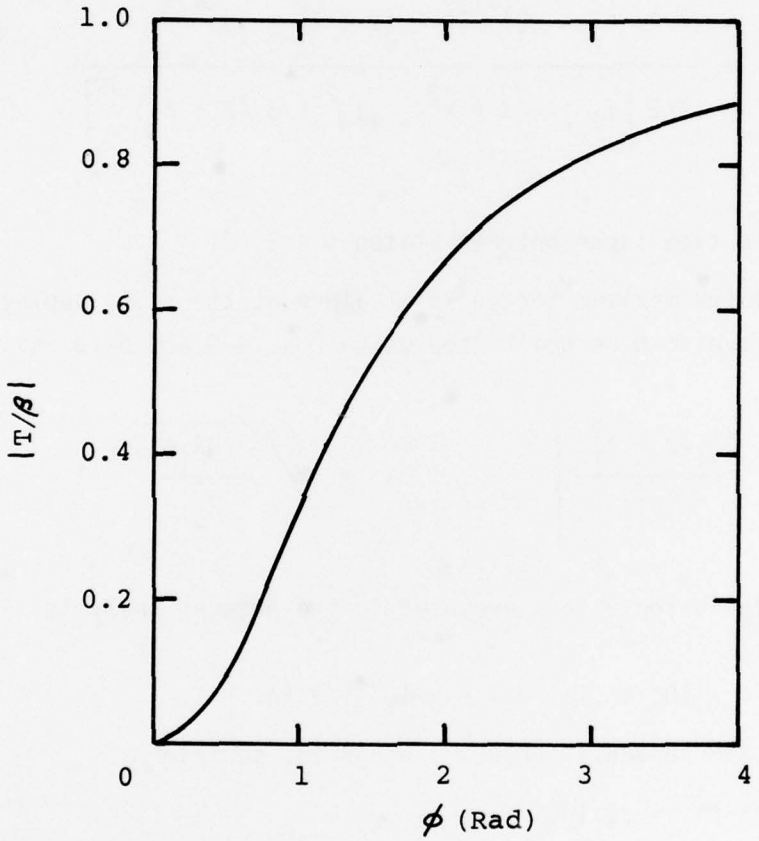


Figure J-3. Torque as a Function of Deployment Angle

3. SOLUTION AND CALIBRATION OF ANTENNA MODEL

An approximate solution of the antenna deployment can be obtained by computing $\dot{\phi}$ and $\ddot{\phi}$ from Eqs. J-6 and J-8 for closely spaced values of ϕ. It is then assumed, within each interval, that $\Delta\dot{\phi} \tilde{=} \ddot{\phi}\Delta t$ in order to calculate

the time lapse between computed states. The calculations are actually carried out in accordance with:

$$\lambda \Delta t_i = \frac{(2 + \phi_i^2)^{-1/2} - (2 + \phi_i^2 - 1)^{-1/2}}{1/2 \left[\phi_{i-1} (2 + \phi_i^2 - 1)^{-2} + \phi_i (2 + \phi_i^2)^{-2} \right]} \qquad \text{J-11}$$

where Δt_i is the time lapse between states i - 1, i.

Since the maximum torque is attained at the fully deployed state $\phi_1 = R_1 \Theta$, the model can be calibrated using Eqs. J-9 and J-10 as:

$$\beta = \left| \frac{T_1 (2 + \phi_1^2)}{\phi_1^2} \right| \qquad \lambda = \sqrt{\frac{2MR_1\beta}{R_o^3}} \qquad \text{J-12}$$

The following values are used in the present analysis:

$T_1 = 4 \times 10^3$ lb.ft. $= 4.8 \times 10^4$ lb. in.

$M = 250$ lb/386.4 in/sec^2 $= 0.646$ lb. sec^2/in.

$R_o \cong 3$ ft. $= 36$ in.

$R_1 \cong 25$ ft. $= 300$ in.

$\phi_1 = \sqrt{(R_1/R_o)^2 - 1} \cong 8.3$ rad.

The above parameters give $\beta \cong 4.94 \times 10^4$ lb. in. and $\lambda \cong 31.4$ sec^{-1}.

Since the reaction torque will be applied to a feed truss whose mass polar moment is decreasing as the moment in the deployed antenna increases, some attention must be given to the potential change in the response frequency of the truss. Also, the analysis should account for

deployment of the solar panels, which are positioned before the antenna is released. The weight budget for the deployment scenario is shown schematically in Figure J-4.

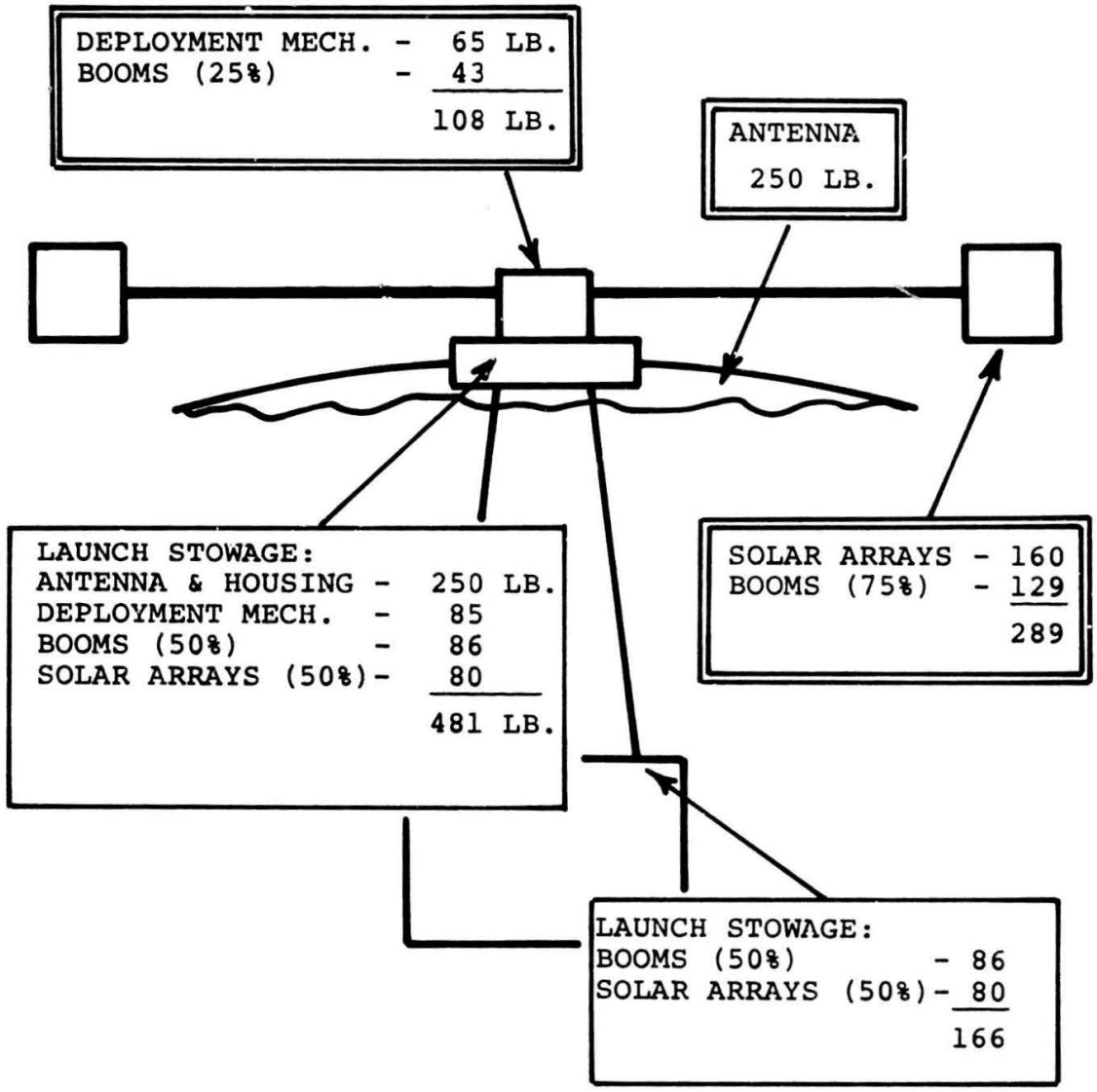


Figure J-4. Deployment Weight Budget

The first-torsion frequencies of the ATS/3-Ring and Tripod-B trusses were computed to be 9.93 and 2.67 Hz, respectively (see Appendix D). These computations assumed the 481 lb. hardware budget shown in Figure J-4 to be stowed at the antenna housing for launch. Let J_p represent the mass polar moment corresponding to the stowed configuration. Since the solar-array booms are quite flexible, it is reasonable to assume that only about 25% of the mass of the booms will be effective in providing inertial reaction to the antenna deployment. This mass, together with the mass of the boom deployment mechanism, makes a total of 108 lb. which remains at the housing. The 250 lb. antenna weight is also concentrated at the antenna housing initially. Now, let J_p' represent the mass polar moment of the truss at the start of antenna deployment, and assume that the effective radius of gyration remains constant. Then:

$$f_n'/f_n = \sqrt{J_p/J_p'} \simeq \sqrt{\frac{481}{108 + 250}} = 1.16 \qquad \text{J-13}$$

where f_n is the first-torsion frequency during launch and f_n' is the effective first-torsion frequency at the start of antenna deployment. During deployment, as mass is transferred from the housing to the antenna, the frequency ratio is given by:

$$f_n'(\phi)/f_n \simeq \sqrt{\frac{481}{358 - 250\ (\phi/\phi_1)}} \qquad \text{J-14}$$

Non-dimensional plots of the reaction torque and truss first-torsion frequency as functions of time are shown in Figure J-5. Antenna deployment is quite rapid, consuming about 1.17 sec. from start to attainment of maximum torque, T_1. The torque-time history can be treated approximately as a linear ramp:

$$T(t) = T_1 t/0.2;\ 0 \leq t \leq 0.2 \text{ sec} \qquad \text{J-15}$$

followed by $T = T_1$ for $t > 0.2$ sec. The frequency plot indicates that an average scaling factor, $f_n'/f_n \cong 1.25$ over the first 0.2 sec., can be used to represent the feed truss as a linear system.

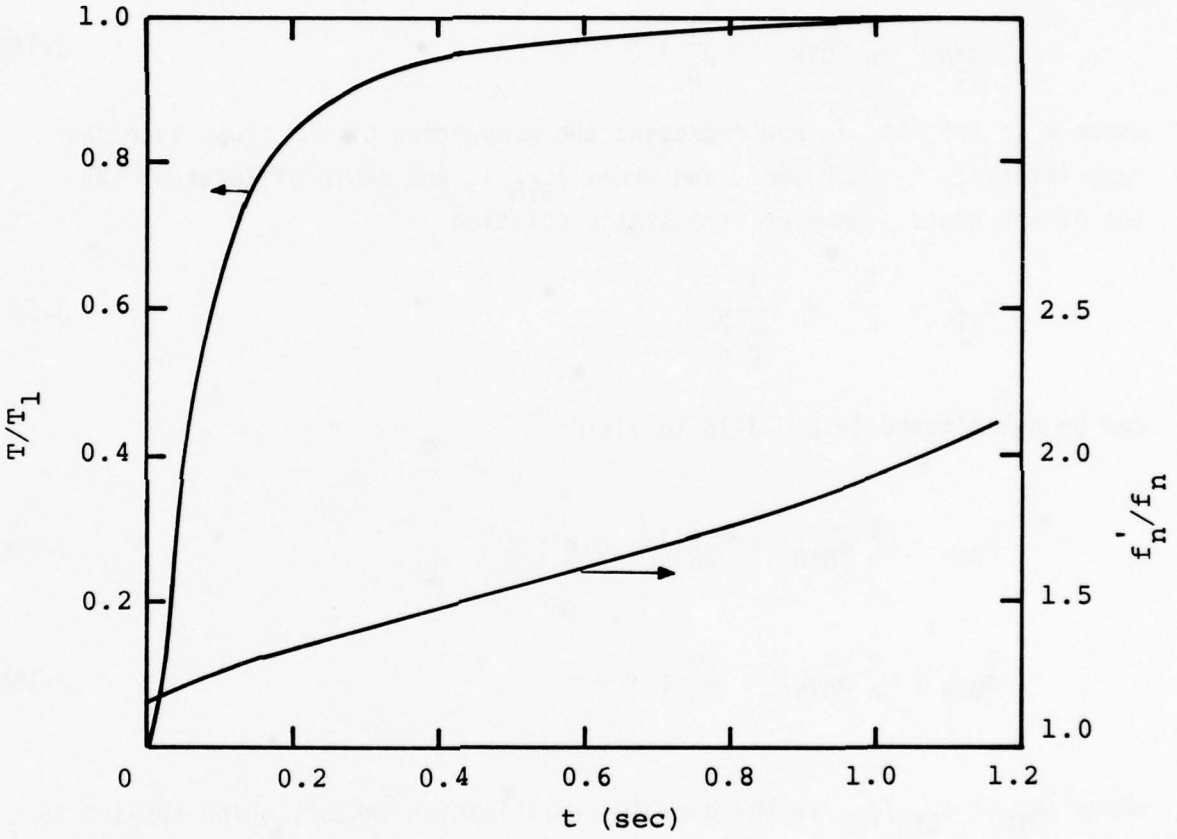


Figure J-5. Torque and Frequency Time-Histories

4. DYNAMIC LOAD FACTORS

Static stress levels of 7.25 ksi in ATS/3-Ring and 77.3 ksi in Tripod-B were obtained by static analyses with the maximum torque, T_1, applied [1]. Since the damping factor assumed for the first torsion mode is quite low ($\zeta = 0.02$), dynamic load factors can be estimated by analyzing

the response of an undamped linear system:

$$\ddot{\phi}_{DYN} + \omega_n^2 \phi_{DYN} = \frac{T_1}{J_p} (t/\tau);\ 0 \leq t \leq \tau \qquad \text{J-16A}$$

$$\ddot{\phi}_{DYN} + \omega_n^2 \phi_{DYN} = \frac{T_1}{J_p};\ t > \tau \qquad \text{J-16B}$$

where $\omega_n = 2\pi f_n$ and J_p now represent the properties of the truss over the ramp interval, $\tau = 0.2$ sec., and where ϕ_{DYN} is the angle of twist at the top of the truss. However, the static solution

$$\phi_{ST} = \frac{T_1}{K} = \frac{T_1}{J_p \omega_n^2} \qquad \text{J-17}$$

can be substituted in Eq. J-16 to yield:

$$\ddot{\bar{\phi}}_{DYN} + \omega_n^2 \bar{\phi}_{DYN} = \omega_n^2 \frac{t}{\tau};\ 0 \leq t \leq \tau \qquad \text{J-18A}$$

$$\ddot{\bar{\phi}}_{DYN} + \omega_n^2 \bar{\phi}_{DYN} = \omega_n^2;\ t > \tau \qquad \text{J-18B}$$

where $\bar{\phi}_{DYN} = \phi_{DYN}/\phi_{ST}$ is the dynamic amplification factor, which applies to loads and stresses as well as the twist angle, since a linear system is assumed.

The solutions of Eqs. J-18, assuming $\dot{\bar{\phi}}_{DYN} = \bar{\phi}_{DYN} = 0$ at $t = 0$, are given by:

$$\bar{\phi}_{DYN}(t) = \frac{t}{\tau} - \frac{\sin(\omega_n t)}{\omega_n \tau};\ 0 \leq t \leq \tau \qquad \text{J-19A}$$

$$\bar{\phi}_{DYN}(t) = 1 + \frac{\sin[\omega_n(t - \tau)] - \sin(\omega_n t)}{\omega_n \tau} ; \; t > \tau \qquad \text{J-19B}$$

The maximum value of the dynamic load factor occurs in the range $t > \tau$, and is given by:

$$\phi_{DYN}^{max} = 1 + \frac{2}{\omega_n \tau} \qquad \text{J-20}$$

Results for the two candidate designs are summarized in Table J-1.

TABLE J-1

SUMMARY OF RESULTS

ITEM	D E S I G N	
	ATS/3-Ring	Tripod-B
f_n during launch (Hz)	9.93	2.67
f_n for deployment (Hz)	12.4	3.34
ω_n for deployment (sec^{-1})	77.9	21.0
$\omega_n \tau$	15.6	4.2
$\bar{\phi}_{DYN}^{max}$	1.13	1.48
Peak dynamic stress (ksi)	8.16	114

5. DISCUSSION AND CONCLUSIONS

The deployment dynamic analysis indicates that no significant stresses will be developed in ATS/3-Ring during antenna release. However, the dynamic load factor, when applied to Tripod-B, gives a peak nominal stress of 114 ksi. Hence, static strength might be exceeded at the longeron end-attachment joints, where stress concentration factors in the range of 1.5 to 2.0 are expected.

It is possible that a more refined analysis of the nonlinear deployment mechanics might reduce the dynamic load factor for Tripod-B. Such analysis may be worthwhile for other similar applications in situations where the joint design is severely constrained. However, in the present case doublers can be incorporated at the Tripod-B end-attachments to reduce the stress concentration.

The deployment analysis also highlights another aspect of the communications satellite design problem. Although the solar-array booms have little effect on the feed truss during antenna deployment, the combination of boom flexibility and the high mass polar moment contributed by the arrays suggest that dynamic models of the type described above be used to analyze transient stresses in the booms.

APPENDIX K

FABRICATION OF TUBULAR GRAPHITE/EPOXY COMPONENTS

1. BACKGROUND

Some deficiencies in the tube fabrication procedures used in the present program were noted briefly in Appendix C. Since composite tubes are likely to continue to be considered for space applications, including larger diameter tubes for large space structures, it is appropriate to review the experiences of other investigators who have fabricated composite tubes. This background, together with a review of tube quality in the present program, will provide a basis for suggestion of future avenues of research.

The choice of mandrel material and configuration is an important factor in tube quality. The use of an inner steel mandrel (Fig. K-1) has been criticized in the literature on the grounds that wrinkling occurs in the outer plies as hoop compression is placed upon the layup by applying pressure in the cure cycle. Such wrinkling, particularly in 0° plies, can lead to serious degradation of axial strength and stability properties.

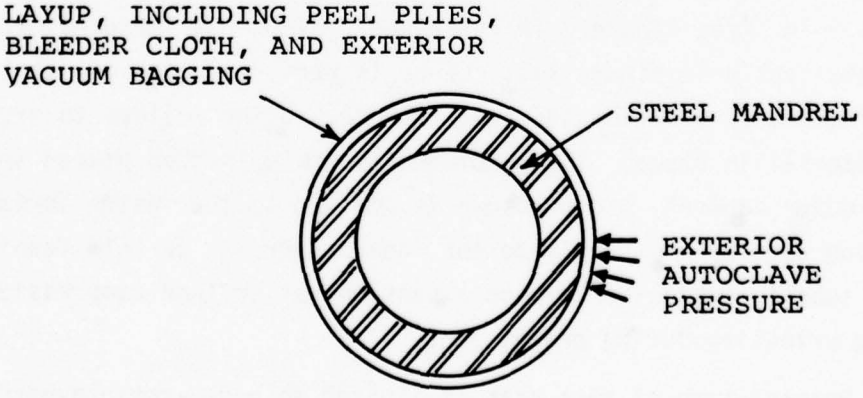


Figure K-1. Tube Layup on Inner Mandrel

Several investigators have proposed alternate layup procedures for the primary purpose of obtaining high-quality tubes to be used as materials test specimens. However, the work of these investigators also has an important bearing on production of tubes for use as structural components.

A solid Teflon inner mandrel was proposed by Davis [19] for the fabrication of $[0°_4]$ S-glass/epoxy and boron/epoxy tubes with approximately 0.5-in. diameter. After prepreg material was wrapped on the mandrel, the layup was covered with a heat-shrinkable Teflon sleeve, which shrinks tightly around the layup and squeezes air out the ends of the assembly as a heat gun is applied. The assembly is placed inside a steel tube during autoclaving to prevent the mandrel from sagging. Typical dimensional variations reported for boron/epoxy tubes fabricated by this procedure were $\pm$0.005 in. O.D. and $\pm$ 0.002 in. wall thickness. Strength tests conducted by potting the ends of the tubes in steel fixtures to prevent brooming succeeded in developing apparent compressive strengths for both materials about 20 percent higher than data previously reported. Thus, use of a Teflon inner mandrel system apparently eliminates the wrinkling problem for tubes fabricated from a few axial plies.

Whitney et al. fabricated 0° and 0°/$\pm$45°/90° tubes containing up to 8 plies from glass/epoxy, boron/epoxy and graphite/epoxy using a four-piece outer mandrel system [20]. Tube diameter is not reported, but appears to be about 3 to 5 in. (see Figure 7 in reference). The outer mandrel technique is shown schematically in Figure K-2. Layup is performed over an elastomeric bladder attached to a perforated inner mandrel, using rollers to press the prepreg material in place. The completed assembly is then placed in a close-tolerance outer mandrel, and pressure is applied to the inside surface of the layup during cure by air supply to the inner mandrel. In this fashion, the composite tube is subjected to hoop expansion rather than compression, thus preventing wrinkling during processing.

Presentation of test data is limited to hydrostatic pressure tests of short rings cut from 0° boron/epoxy tubes. The authors [20] recommend the ring test as a quality-control procedure for acceptance/rejection of the tubes as compression strength test specimens. The data reported in the paper indicate

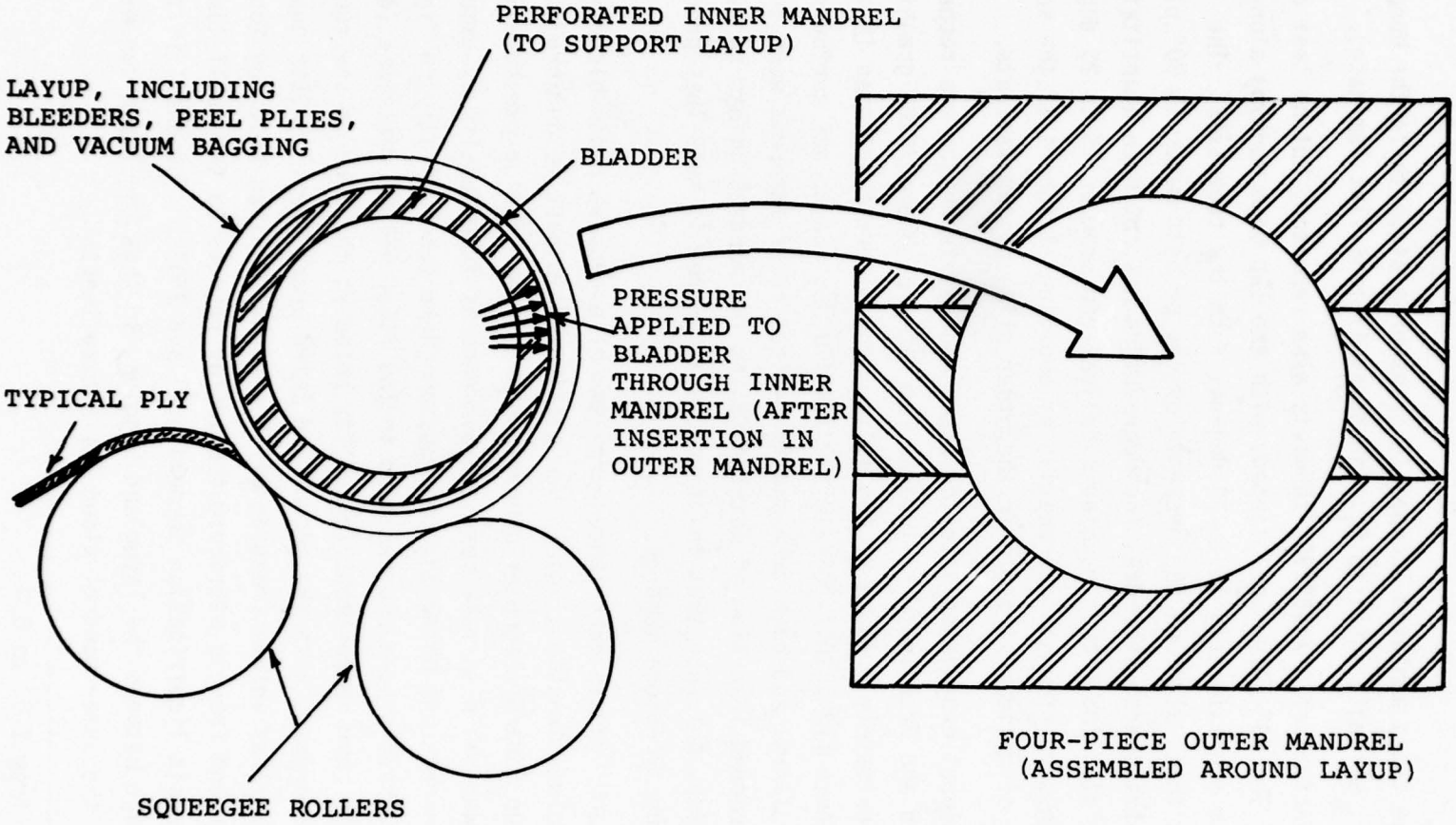


Figure K-2. Layup on Inner Mandrel with Curing on Outer Mandrel

that most of the tubes achieved acceptable transverse strength in the hoop direction (i.e., strength equal to F_{T2} in the equivalent flat laminate).

Manufacture of 0°/±45°/90° tubes is also reported, but no test data are presented. The 90° plies were lapped, with the lap seam running along a helix with angle approximately 15 to 20 degrees from the tube axis. The authors comment that, although the presence of lap or butt seams in 90° plies should degrade transverse strength, the degradation has not been quantitatively assessed. They also imply that running a helical lap seam at 15 to 20 degrees might avoid excessive strength degradation by avoiding alignment of the seam with directions of minimum strength in the other plies of the laminate.

Additional experience with the outer mandrel technique was reported recently by Weed and Francis [67]. Tubular laminates of Modmor/5208 graphite/epoxy with approximately 3 in. O.D. and 65 in. length were fabricated in an unbalanced sequence $[70°_2/30°/-70°/-20°/30°/20°/70°]$*. Layup was performed with squeegee rollers, and both two- and four-piece outer mandrels were tried. The authors recommend insertion of metal shims at the mandrel joints to avoid pinching the layup, but note that the four-piece mandrel is much less prone to pinching than the two-piece mandrel.

Weed and Francis experienced problems of excessive resin bleeding and low fiber volume fraction, which they attributed in part to outward expansion of the layup toward the outer mandrel when interior curing pressure is applied. They were able to make some improvements of tube quality by experimenting with cure cycles, using the progression shown schematically in Figure K-3. The first three procedures resulted in low fiber volume fractions (45 to 50 percent), with some improvement in quality noted at the ends of the tubes fabricated in accordance with the second and third procedures. Better quality generally, and a fiber volume fraction of 58 percent resulted from the fourth procedure. Weed and Francis attribute the latter results to the dwell times between 200°F (resin liquification temperature) and 250°F. The dwell is thought to permit slippage between the layup and bagging, so that the layup can expand enough to reach the outer mandrel along its entire length.

*Sequence given from I.D. to O.D.

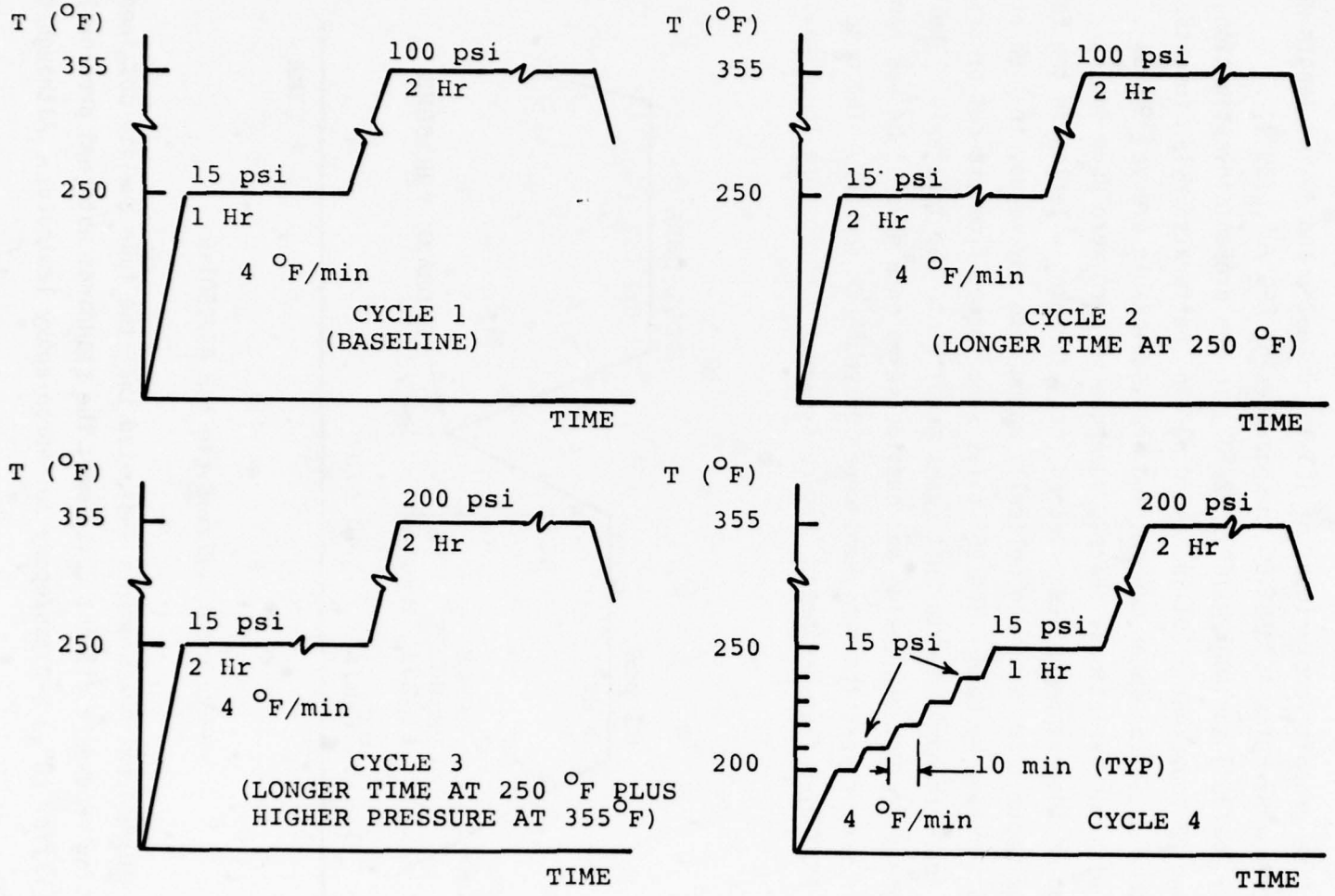


Figure K-3. Cure Cycles (After Weed and Francis)

2. EXPERIENCE IN PRESENT PROGRAM

Nine graphite/epoxy tubes of 1.3-in. diameter and 36-in. length were fabricated from Hercules AS/3501-6 in sequences of $[90°/0°_{10}/90°]$, $[90°/M1/0°_{10}/M1/90°]$ and $[90°/M2/0°_{10}/M2/90°]$ in the present investigation, where M1 and M2 represent 0.001-in. and 0.002-in. perforated Mylar inserts. Davis' method of Teflon inner mandrel and heat-shrinkable sleeve [19] was employed, with two variations. First, squeegee rollers were used during application of the prepreg plies. Second, heat-shrinkable Teflon in the form of a ribbon about 1 in. wide was helically wound onto the layup, in lieu of installing a sleeve by hand. The 90° plies were formed from pre-cut prepreg material, and were applied with butt seams parallel to the tube axis. The angular separation between inside and outside seams on a given tube was random, although in some cases, the two seams were located back to back. The baseline cycle for AS/3501-6 flat laminates (Figure K-4) was used to cure the tubes.

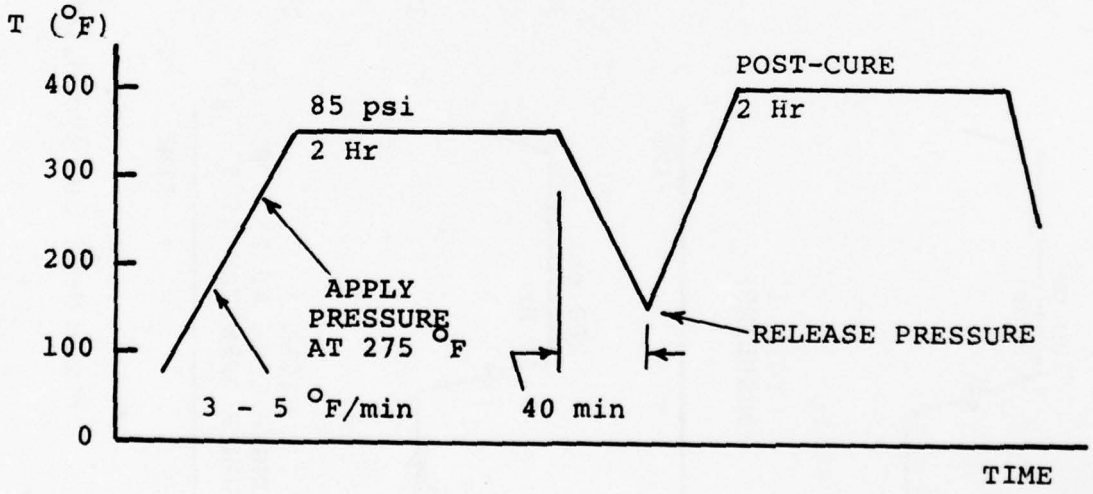


Figure K-4. Cure Cycle for AS/3501-6

Dimensional measurements indicated that the tube quality obtained by the foregoing procedure did not quite meet the standards obtained previously by Davis [19] for $[0°_4]$ S-glass/epoxy and boron/epoxy laminates. Although the

I.D. measurements were comparable (all observations within ±0.002-in. tolerance), variations in O.D. of ±0.010 to ±0.015 in. were noted, and one tube was observed to have O.D. variations to ±0.020 in. The larger variation in O.D. is tentatively attributed to the increased wall thickness of the present tubes (12 plies, versus 4 in the laminates fabricated by Davis). The presence of inner and outer 90° plies and the use of heat-shrinkable ribbon may also have contributed to the O.D. variation.

Other deficiencies of a potentially more serious nature were also observed. Some of the tubes with Mylar inserts possessed visibly elliptical cross sections. A typical example is shown in Figure K-5. The ellipticity suggests deformation response to residual stresses accumulated when the laminate cools from cure temperature to room temperature. This hypothesis was reinforced by examination of the tubes with M2 inserts. Debonded areas in these tubes could be identified by crackling of the Mylar when applying fingertip pressure to the outer surface. These deficiencies provide arguments against the use of Mylar inserts, in addition to the data presented previously for interlaminar strength trends (Appendix B).

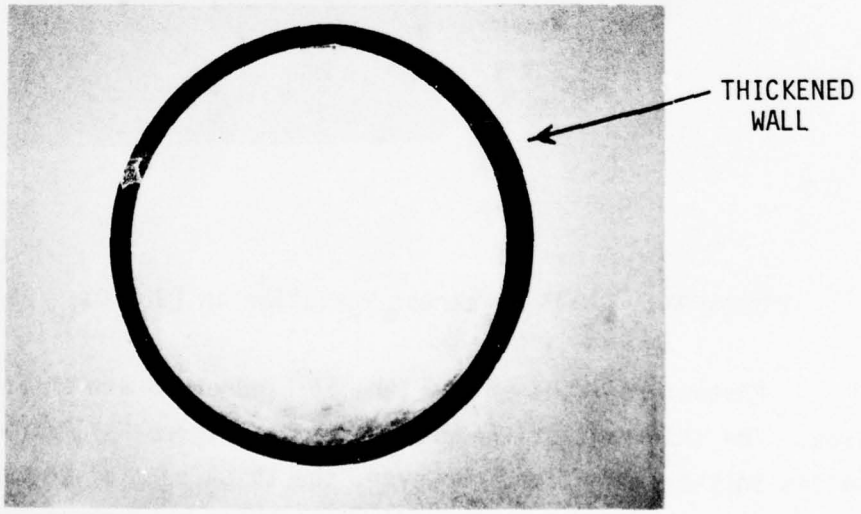


Figure K-5. [90°/M1/0°$_{10}$/M1/90°] Tube with Elliptical Cross Section

Close examination of Figure K-5 also reveals a circumferential variation of wall thickness. The wall-thickness variation was found to occur even in the $[90°/0°_{10}/90°]$ tubes. A composite photograph of a cross section and axial section of a typical $[90°/0°_{10}/90°]$ tube (Figure K-6) indicates that the angular location of the thickened part of the wall is independent of axial location. Hence, effects of squeegee-roller pressure transients and/or gravity during cure are suggested as possible causes.

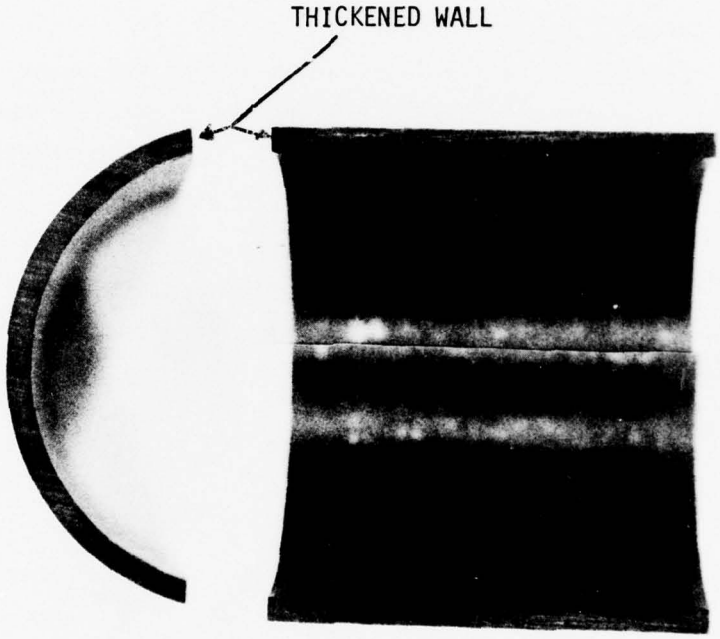


Figure K-6. Wall Thickness Variation in $[90°/0°_{10}/90°]$ Tube

Photomicrographs of the tube in Figure K-6 are shown in the following figures. The thin part of the cross section (Figure K-7) shows no evidence of anomalies in the lamination. However, the thick part of the cross section (Figure K-8) shows evidence of voids distributed through the wall, and indicates that the use of a heat-shrinkable outer cover in lieu of vacuum bagging may have contributed to the thickness variation.

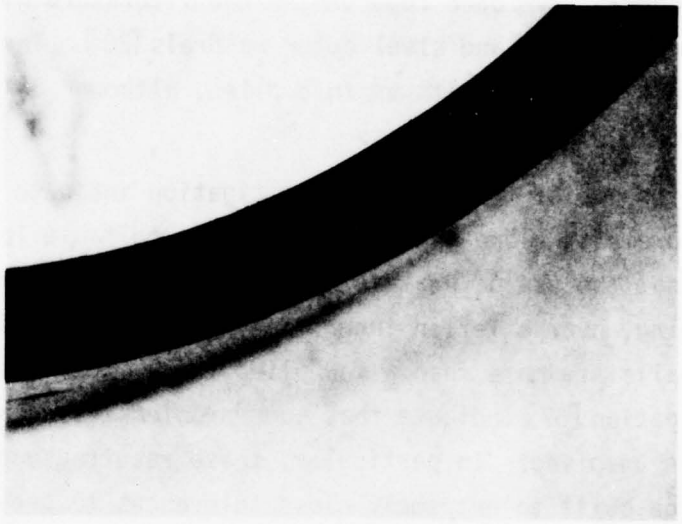


Figure K-7. Nominal Wall Region



Figure K-8. Thickened Wall Region

3. DISCUSSION AND CONCLUSIONS

Improvements in tube quality over that obtained by vacuum-bagging on steel inner mandrels have been reported in the literature by the use of both Teflon inner mandrels [19] and steel outer mandrels [20]. The reported test data covered only 0° tubing with up to 8 plies, although 0°/±45°/90° tubes were fabricated in one case [20].

The results of the present investigation indicate that I.D. and wall-thickness measurements alone are not necessarily reliable indicators of tube quality, and that the use of heat-shrinkable Teflon outer sleeving, in place of vacuum bagging, over a Teflon inner mandrel may not yield good quality tubing when the walls are more than a few plies thick. The results of another recent investigation [67] indicate that some problems associated with steel outer mandrels remain unsolved. In particular, these results suggest that such mandrels must be built to extremely close tolerances to prevent over-expansion of the laminate when it is pressed to the mandrel surface.

The results obtained with both inner and outer mandrels suggest that achievement of good tube quality depends upon avoidance of excessive mechanical expansion or compression of the laminate when the resin liquifies early in the cure cycle. The inner mandrel technique is more appealing because of its relative simplicity, but some thought is required to design such a mandrel properly. The advantage of Teflon over steel in this respect can be demonstrated by a simple calculation of the radial expansion or hoop strain tendency in each case. For a solid mandrel of radius R, the hoop-strain tendencies are given by:

$$\varepsilon_\theta^{(\Delta T)} = \alpha \text{ per degree} \qquad \text{K-1}$$

for heating, and

$$\varepsilon_\theta^{(p)} = -\frac{1-\nu}{E} \text{ per psi} \qquad \text{K-2}$$

for external pressure. The dynamic ranges of temperature and pressure available to control expansion are limited by the requirements of the cure cycle. Typically, ΔT is about 300°F and p is about 100 psi. The resulting dynamic ranges in hoop strain are compared for Teflon, steel and aluminum in Table K-1.

TABLE K-1

COMPARISON OF MANDREL MATERIALS

Item	M A T E R I A L		
	Teflon[1]	Steel	Aluminum
E(psi)	~5 x 10^4	~ x 10^7	10^7
ν	~0.5	0.3	0.3
$\alpha(°F^{-1})$	~3 x 10^{-5}	6.3 x 10^{-6}	12 x 10^{-6}
$\varepsilon_\Theta^{(\Delta T)}$ (ΔT = 300°F)	9 x 10^{-3}	1.89 x 10^{-3}	3.6 x 10^{-3}
$\varepsilon_\Theta^{(p)}$ (p = 100 psi)	10^{-3}	2.33 x 10^{-6}	7 x 10^{-6}

[1]Teflon properties from Ref. 68.

The thermal expansion coefficients of cured epoxy resins are known to be in the range 1.7 x 10^{-5} to 5.4 x 10^{-5} per °F, i.e., comparable to Teflon [68]. Although no data are available for epoxies in the B-stage, comparison of the cured expansion coefficient with the data in Table K-1 suggests that the Teflon mandrel has been successful because of its thermal and pressure dynamic ranges. Teflon probably possesses a slight tendency to over-expand a graphite/epoxy laminate containing a high percentage of axial plies, but this tendency is corrected by the pressure term. The fact that the thermal and pressure dynamic ranges for Teflon differ by only one order of magnitude suggests that even better process control might be obtained by experimenting with pressure increments during the cure cycle, in the manner suggested by Weed and Francis [67] for temperature control when using an outer mandrel. Ideally, one should be able to deduce from resin expansion measurements an optimum pressure-temperature-time history. There appears to be no reason why this approach should not be applied to the combination of a Teflon inner mandrel with vacuum bagging instead of a heat-shrinkable sleeve.

With regard to detail design, the results in Appendix C verify the prediction of Whitney, et al.[20] that the presence of straight butt seams in 90° plies introduces a local failure mode in the tube at loads much lower than the theoretical crippling strength. However, whether any significant improvement is possible by running butt seams on a bias, and/or by replacing butt seams with lap seams remains to be investigated. The present authors conjecture that such improvements will be limited by the effect of concentration in applied stresses on the interlaminar strength of the composite. The hydrostatic short-ring proof test suggested by Whitney, et al. as a quality-control procedure could be adapted to such a study.

Even without the problem of inserts, there appear to be a number of unresolved questions about proper procedures for fabricating structural tubing with composite materials. Use of preimpregnated materials appears to be necessary, at least for axial plies, when slender tubes with high stiffness and low thermal expansion coefficients are required. Additional investigation of processing methods should focus on tubes of larger diameter.

APPENDIX L

COMPONENT PROOF TESTING

1. APPLICABILITY

Proof testing of structural components is advisable when requirements for high reliability cannot be met by nondestructive inspection (NDI). The Tripod-B truss illustrates both situations. The antenna-support legs are critical in buckling, based on elastic stability considerations for ideally straight columns. Hence, NDI is the proper approach for the support legs because the axial modulus can be predicted with high confidence and because accurate measurements of initial imperfection (bowing) can be made. The NDI in this case is, in essence, a nondestructive proof test.

On the other hand, the Tripod-B longerons are critical in compressive bursting (assuming fabrication with butt seams). In this case, one can expect variations in the burst load caused by variations in the manufacturing tolerances of the tubes. Such parameters as the gap between fiber ends in the butt seam, resin bleed during cure, etc., are subject to small variations that cannot be quantified easily, and that influence bursting strength in an unknown manner. Therefore, since there exists no rational method for defining a lower bound to the bursting strength of any individual tube, proof testing will be required to censor the population for the purpose of achieving a high launch survival reliability.

Choice of a proof-load level now becomes a crucial question. A proof load set too low may qualify components which should have been rejected, but too high a load may damage components which were acceptable before the test. This appendix first considers a probabilistic definition for the proof load, based on an expected cost criterion. It will be shown that proof loads below the damage constraint can be defined in this manner if testing and design are treated interactively. To simplify the analysis, the proof-load formulation will be derived by assuming that the tube is to be given an axial compression test. Subsequently, a simple model will be presented to relate the axial proof load to a hydrostatic pressure test.

2. PROBABILISTIC DEFINITION OF PROOF LOAD

Structural design optimization is a well developed mathematical art in which various search methods are applied to maximize an objective merit function or minimize an objective penalty function [69,70,71,72]. Such optimization methods have also been applied to structures assumed to consist of components possessing random strengths [73] and using expected cost as a penalty function [74]:

$$E_c = C_o + F\,C_F \qquad \text{L-1}$$

where E_c is the expected system cost, C_o is the initial cost (represented as a function of structural weight), F is the probability of failure, and C_F is the cost of failure. Optimization may consist of either unconstrained minimization of E_c, minimization of E_c subject to constraints (e.g., buckling), or weight minimization using E_c as a constraint. Expected cost criteria have also been used to optimize periodic proof-test loads for composite structure in aircraft [75]:

A simplified expected cost model applicable to pre-launch proof testing of structural components will be presented here. The model considers only the effects of launch reliability and proof-test rejection rate:

$$E_c = C_L\,(1 + F_L) + N_c\,C_c\,F_c \qquad \text{L-2}$$

where C_L is the cost of a launch, F_L is the probability of structural failure during launch, N_c is the total number of nominally identical components in the structure, C_c is the component cost (including test cost), and F_c is the probability of component failure during test. A lower bound for launch reliability can be derived from Eq. L-2 by making the conservative assumption that the censored population (all components that pass the proof test) has a deterministic strength equal to the proof load. Structural failure during launch is then determined by first-passage statistics for the most highly loaded component in the assembled structure.

Let P be the design characteristic load for the component (e.g., design axial compression load for the Tripod-B longerons), and let αP represent the proof-test load. Assume that manufacturing quality is represented by a standard deviation σ_c in the strengths of a population of components designed to mean strength P. Assume that the effect of the launch environment on the critical component can be represented by stationary Gaussian statistics with standard deviation σ_L (in the units of P) and zero-crossing rate $\bar{\nu}_o$ (in units of total occurrences per launch). There will then be associated with the censored lower-bound strength an expected exceedance rate 1/N during launch ($N >> 1$), which can be taken as an estimator of launch failure probability:

$$F_L = 1/N = \frac{1}{2} \bar{\nu}_o \, e^{-\alpha^2 P^2 / 2\sigma_L^2} \qquad \text{L-3}$$

Finally, if it is assumed that $\sigma_c << P$, the hypothetical pre-test population of components can be modeled by a Gaussian strength distribution. Hence, the probability for failure of a component in the proof test can be expressed in terms of the cumulative Gaussian function:

$$F_c = \Phi(z); \quad z = (\alpha P - P)/\sigma_c \qquad \text{L-4}$$

where z is the standard normal variate ($\mu_z = 0$, $\sigma_z = 1$).

Now consider a constrained optimization of Eq. L-2, allowing only the choice of proof-load level, α, to vary:

$$dE_c/d\alpha = C_L(dF_L/d\alpha) + N_c \, C_c(dF_c/d\alpha) = 0 \qquad \text{L-5}$$

The derivatives in Eq. L-5 can be calculated from Eqs. L-3 and L-4 as follows:

$$dF_L/d\alpha = -\frac{1}{2} \bar{\nu}_o \left(\frac{\alpha P^2}{\sigma_L^2}\right) e^{-\alpha^2 P^2 / 2\sigma_L^2} \qquad \text{L-6}$$

$$dF_c/d\alpha = (d\Phi/dz)(dz/d\alpha) = \frac{P}{\sigma_c} (d\Phi/dz) \qquad \text{L-7}$$

By definition,

$$d\Phi/dz = \phi(z) = \frac{1}{\sqrt{2\pi}} e^{-z^2/2} \qquad \text{L-8}$$

and substitution of these results in Eq. L-5 yields, after some manipulation:

$$\alpha \exp\left[\frac{(\alpha-1)^2}{2} \left(\frac{P}{\sigma_c}\right)^2 - \frac{\alpha^2}{2} \left(\frac{P}{\sigma_L}\right)^2\right] = \frac{2}{\sqrt{2\pi}} \left[\frac{1}{\bar{\nu}_o}\right] \left[\frac{P/\sigma_c}{(P/\sigma_L)^2}\right] \left[\frac{N_c\, C_c}{C_L}\right] = \beta \qquad \text{L-9}$$

The effects of the terms in brackets on the right side of Eq. L-9 can be readily identified. Small values of β tend to force the optimum proof load to large values. Increased exposure to the environment ($\bar{\nu}_o$ large), poor manufacturing quality (P/σ_c small), and a low test/launch cost ratio ($N_c\, C_c/C_L$) lead to large αP. The apparently similar trend of conservative design (large P/σ_L) is actually reversed by the P/σ_L - term in the exponent on the left side. The most significant driver of high proof-test loads is the cost ratio.

Equation L-9 can be solved iteratively to optimize the proof test while maintaining high launch reliability. A value of P/σ_L is assumed first by engineering judgement, or by choosing the design load to meet a given initial reliability estimate defined by:

$$R' = 1 - 1/N' = 1 - \frac{1}{2} \bar{\nu}_o\, e^{-P^2/2\sigma_L^2} \qquad \text{L-10}$$

After α has been determined, the actual lower-bound reliability can be calculated from:

$$R = 1 - 1/N = 1 - \frac{1}{2} \bar{\nu}_o\, e^{-\alpha^2 P^2/2\sigma_L^2} \qquad \text{L-11}$$

Optimization of a proof load for the Tripod-B longerons was carried out in accordance with the above procedure, assuming the parameter values given in Table L-1. The results, also summarized in the table, show that a reasonable proof load and acceptable launch reliability are achieved. Strictly

speaking, the optimization should be carried out by minimizing E_c with respect to α and P/σ_L simultaneously. However, this unconstrained approach leads to the unrealistic solution $\alpha = 0$, $P/\sigma_L = \infty$ unless an additional penalty term (e.g. the cost of extra weight required by increased P/σ_L) is included in E_c. The constrained approach was adopted instead because the most significant penalty may involve the effect of P/σ_L on truss distortion of the microwave path between the broadcasting dipoles and the reflector antenna, an effect which has not yet been quantified.

TABLE L-1

SUMMARY OF EXAMPLE ANALYSIS

Parameter	Value	Remarks
$\bar{\nu}_o/2$	1.64×10^4	Per launch (from Appendix D)
P/σ_c	10	10 percent manufacturing coefficient of variation
P/σ_L	8.82	Design load twice first-passage load (see Appendix D)
N_c	3	
C_c	$\$ 4 \times 10^3$	Estimated cost per longeron [1]
C_L	$\$ 5 \times 10^7$	Typical cost of satellite plus Titan-IIIC launch
R'	$0.9_{12}794$	
R	$0.9_5 87$	
α	0.774	Proof-load damage expected for $\alpha > 0.8$

3. RELATING PROOF LOAD TO HYDROSTATIC TEST

The axial load that will cause bursting of a longeron tube with a straight butt seam in the 90° plies was defined in Appendix C as:

$$P = 4\pi R t_1 \, s_\theta \, f\,(\nu_{LT}, \nu_{TL}, t_1/t_2) \qquad \text{L-12}$$

where R is the tube's mean radius, t_1 and t_2 are respectively the thicknesses of M and N plies in a $[90°_M/0°_{2N}/90°_M]$ tube, ν_{LT} and ν_{TL} are the ply Poisson ratios, and s_θ is an unknown resin strength parameter in terms of hoop stress in the 90° plies. If the model in Appendix C is assumed to be subjected to uniform internal pressure, p, instead of axial load, it is easy to show that the failure pressure is given by:

$$p = \frac{2t_1}{R}\left(1 + \frac{\nu_{TL}}{\nu_{LT}}\frac{t_2}{t_1}\right) s_\theta \, . \qquad \text{L-13}$$

for either plain strain or plane stress conditions. Combining Eqs. L-12 and L-13 to eliminate s_θ and solve for the burst pressure then yields:

$$p = \left(\frac{P}{2\pi R^2}\right)\left[\frac{1 + \dfrac{\nu_{TL}}{\nu_{LT}}\dfrac{t_2}{t_1}}{f(\nu_{LT}, \nu_{TL}, t_1/t_2}\right] \qquad \text{L-14}$$

Thus, an equivalent pressure for a hydrostatic proof test can be defined in terms of the axial proof-load level. Substitution of the Tripod-B longeron dimensions and estimated axial burst load (based on scaling of the test data in Appendix C) gives an order-of-magnitude estimate $p \approx 50$ psi. Hence, it appears reasonable to use a hydrostatic proof test. However, the actual correlation between axial load and pressure should be established by laboratory tests, in view of the approximate nature of the failure model.

REFERENCES

1) McCarthy, J.F. and Orringer, O., "Preliminary Design of a Composite Structure for an Air Force Space Application," Center for Space Research, MIT, Cambridge, MA, AFFDL-TR-76-53, May 1976.

2) Rosen, P., MacLellan, D.C., Reiffen, B. and Niessen, C.W., "Space Communications," Lincoln Laboratory, MIT, Lexington, MA, Quarterly technical summary reports to AFSC, 1975/1976/1977.

3) Burns, J.N. and Toland, R.H., "Design and Analysis of the ATS Graphite Epoxy Satellite Truss," Proc. Conference on Fibrous Composites in Flight Vehicle Design, Dayton, OH, AFFDL-TR-72-130, September 1972.

4) Neff, R.M. et al. (ed.), "Advanced Composites Design Guide," Air Force Flight Dynamics Laboratory (AFFDL/FB), Wright-Patterson Air Force Base, OH, 3rd edition (3rd revision), January 1977.

5) Specifications, "Functional Requirements for MJS 1977, Environmental Design Requirements," Jet Propulsion Laboratory, Pasadena, CA, MJS77-3-240, 14 March 1975.

6) Crandall, S.H. and Mark, W.D., Random Vibration in Mechanical Systems, Academic Press, New York, 1973.

7) Burris, P.M. and Bender, M.A., "Aircraft Load Alleviation and Mode Stabilization (LAMS)," The Boeing Company and Honeywell, Inc., AFFDL-TR-68-158, April 1969.

8) Lackman, L.M. and Pagano, N.J., "On the Prevention of Delamination in Composite Laminates," AIAA Paper No. 74-355, AIAA/ASME/SAE 15th Structures, Structural Dynamics and Materials Conference, Las Vegas, NV, 17-19 April 1974.

9) Anon., "Standard Methods of Test for Interlaminar Shear Strength of Structural Reinforced Plastics at Elevated Temperatures," American Society for Testing and Materials, ASTM Standard D-2733, December 1970.

10) Anon., "Apparent Horizontal Shear Strength of Reinforced Plastics by Short Beam Method," American Society for Testing and Materials, ASTM Standard D-2344, March 1976.

11) Pagano, N.J. and Pipes, R.B., "Some Observations on the Interlaminar Strength of Composite Materials," IntJMechSci, Vol. 15 (1973), 679-688.

12) Dong, S.B., Wolf, J.A. and Peterson, F.E., "On a Direct-Iterative Eigensolution Technique," IntJNumMethEng, Vol. 4 (1972), 155-161.

13) Bathe, K.J., "Solution Methods for Large Generalized Eigenvalue Problems in Structural Engineering," Structural Engineering Laboratory, University of California, Berkeley, CA, UC SESM 71-20, November 1971.

14) Whiteside, D.W. and Hungate, J.W., "Titan-IIIC Payload User's Guide," Denver Division, Martin-Marietta Corporation, Denver, CO, MCR 68-62, October 1968.

15) Bendat, J.S., Principles and Applications of Random Noise Theory, Wiley, New York, 1958.

16) Spilker, R.L., Chou, S.C. and Orringer, O., "Alternate Hybrid-Stress Elements for Analysis of Multilayer Composite Plates," JComposite Materials, Vol. 11 (January 1977), 51-70.

17) Ryder, J.T., "Effect of Compression on Fatigue of Graphite/Epoxy Composites," Mechanics of Composites Review, Air Force Materials Laboratory, Symposium at Bergamo Center, Dayton, OH, 28-29 January 1976.

18) Ryder, J.T., "Effect of Compressive Loading on the Fatigue Lifetime of Graphite/Epoxy Composites," Mechanics of Composites Review, USAF Materials Laboratory/Office of Scientific Research/Flight Dynamics Laboratory, Symposium at Bergamo Center, Dayton, OH, 25-27 October 1977.

19) Davis, J.G., "Fabrication of Uniaxial Filament-Reinforced Epoxy Tubes for Structural Applications," Proc. Symposium on Advanced Techniques for Material Investigation and Fabrication, SAMPE, Cocoa Beach, FL, 5-7 November 1968, Section II-2A-1.

20) Whitney, J.M., Pagano, N.J. and Pipes, R.B., "Design and Fabrication of Tubular Specimens for Composite Characterization," Composite Materials: Testing and Design (Second Conference), American Society for Testing and Materials, ASTM STP 497, 1971, 52-67.

21) Henneke, E.G., Reifsnider, K.L. and Stinchcomb, W.W., "Defect-Property Relationships in Composite Materials," Mechanics of Composites Review, Air Force Materials Laboratory, Symposium at Bergamo Center, Dayton, OH, 28-29 January 1976.

22) Crossman, F.W. (Lockheed Missiles and Space Company, Palo Alto, CA) and Reiter, G.S. (Hughes Aircraft Company, El Segundo, CA), private communications to authors, March 1978.

23) Kerridge, J.F., "Micrometeorite Environment at the Earth's Orbit," Nature, Vol. 228 (14 November 1970), 616-619.

24) Millman, P.M., "The Meteoritic Hazard of Interplanetary Travel," American Scientist, Vol. 59 No. 6 (1975), 700-705.

25) Cour-Palais, B.G., "The Current Micrometeoroid Flux at the Moon for Masses $\leq 10^{-7}$g from the Apollo Window and Surveyor 3 TV Camera Results," Proc. 5th Lunar Conference (Supplement 5, Geochimica et Cosmochimica Acta), Vol. 3 (1974), 2451-2462.

26) Kalaghan, P.M., Arnold, D.A., Colombo, G., Grossi, M.D., Kirchner, L. and Orringer, O., "Study of the Dynamics of a Tethered Satellite System (Skyhook)," Smithsonian Astrophysical Observatory, Cambridge, MA, Final Report, Contract NAS8-32199 (NASA/MSFC), March 1978.

27) Morrow, W.E. (Lincoln Laboratory, Lexington, MA), private communication to authors, 1975.

28) Bell, L.E. et al., "Solar Power Satellite Concept Evaluation," NASA/JSC, Houston, TX, July 1977.

29) Anon., "Solar Power from Satellites," Hearings before the Subcommittee on Aerospace Technology and National Needs of the Committee on Aeronautical and Space Sciences, United States Senate, 94th Congress, 2nd Session, 19-21 January 1976.

30) Scala, S. (Re-Entry and Environment Systems Division, General Electric Company, Philadelphia, PA), private communication to authors, 1977.

31) Grossi, M.D. (Smithsonian Astrophysical Observatory, Cambridge, MA), private communication to authors, 1977.

32) Smylie, R.E., "Long Duration Exposure Facility (LDEF) Guide for Experiment Accommodations," Headquarters, National Aeronautics and Space Administration (NASA/RS), Washington, DC, 2 December 1975.

33) McCarthy, J.F., Tiffany, C.F. and Orringer, O., "The Application of Fracture Mechanics to Decisions on Structural Modifications of Existing Aircraft Fleets," Case Studies in Fracture Mechanics (T.P. Rich and D.J. Cartwright, ed.), U.S. Army Materials and Mechanics Research Center, Watertown, MA, AMMRC MS 77-5, June 1977.

34) Puppo, A.H. and Evensen, H.A., "Interlaminar Shear in Laminated Composites Under Generalized Plane Stress," JComposite Materials, Vol. 4 (April 1970), 204-223.

35) Pipes, R.B. and Pagano, N.J., "Interlaminar Stresses in Composite Laminates Under Uniform Axial Extension," JComposite Materials, Vol. 4 (October 1970), 538-548.

36) Grossman, D.T., "Fatigue Behavior of Angle-Ply Fibrous Composite Laminates," SM Thesis, Department of Aeronautics and Astronautics, MIT, Cambridge, MA, May 1971.

37) Chiao, C.C., Moore, R.L. and Chiao, T.T., "Measurement of Shear Properties of Fiber Composites - I: Evaluation of Test Methods," Composites, July 1977, 161.

38) Sandhu, R.S. (Air Force Flight Dynamics Laboratory, AFFDL/FBC, Wright-Patterson Air Force Base, OH), private communication, 1977.

39) Pipes, R.B., "Solution of Certain Problems in the Theory of Elasticity for Laminated Anisotropic Systems," PhD Thesis, University of Texas, Arlington, TX, March 1972.

40) Pagano, N.J., "On the Calculation of Interlaminar Normal Stress in Composite Laminate," JComposite Materials, Vol. 8 (January 1974), 65-82.

41) Frankenfeld, R.L. (Quality Assurance Dept., Hercules, Inc., Magna, UT), private communication giving material properties for specific lot, 18 August 1977.

42) Anon., "Graphite Materials," Hercules, Inc., Magna, UT, April 1976.

43) Pagano, N.J. and Pipes, R.B., "The Influence of Stacking Sequence on Laminate Strength," JComposite Materials, Vol. 5 (January 1971), 50-57.

44) Rybicki, E.F., "Approximate Three-Dimensional Solutions for Symmetric Laminates Under Inplane Loading," JComposite Materials, Vol. 5 (July 1971), 354-360.

45) Wang, A.S.D. and Crossman, F.W., "Some New Results on Edge Effect in Symmetric Composite Laminates," JComposite Materials, Vol. 11 (January 1977), 92-106.

46) Rybicki, E.F., Schmueser, D.W. and Fox, J., "An Energy Release Rate Approach for Stable Crack Growth in the Free-Edge Delamination Problem," JComposite Materials, Vol. 11 (October 1977), 470-487.

47) Hoffman, O., "The Brittle Strength of Orthotropic Materials," JComposite Materials, Vol. 1 (April 1967), 200-206.

48) Bendat, J.S. and Piersol, A.G., Random Data: Analysis and Measurement Procedures, Wiley, New York, 1971.

49) Haji-Sheikh, A. and Sparrow, E.M., "The Solution of Heat Conduction Problems by Probability Methods," Trans. ASME, JHeat Transfer, May 1967, 121-131.

50) Bathe, K.J., "ADINAT - A Finite Element Program for Automatic Dynamic Incremental Nonlinear Analysis of Temperatures," Mechanical Engineering Department, MIT, Cambridge, MA, AVL 82448-5, May 1977.

51) Berenson, P.J., "Film-Boiling Heat Transfer from a Horizontal Surface," Trans. ASME, JHeat Transfer, August 1961, 351-358.

52) Anon., "High Peel Epoxy Composition A-1333-B," B.F. Goodrich Company, Akron, OH, Circular No. 1770, undated.

53) Meirovitch, L., Analytical Methods in Vibrations, MacMillan Company, New York, 1967.

54) Wilkinson, J.H., The Algebraic Eigenvalue Problem, Clarendon Press, Oxford, 1965.

55) Dahlquist, G. and Björk, Å., Numerical Methods, Prentice-Hall, Englewood Cliffs, NJ, 1974.

56) Ralston, A. and Wilf, H.S. (ed.), Mathematical Methods for Digital Computers, Wiley, New York, 1962.

57) Mau, S.T. and Pian, T.H.H., "Linear Dynamic Analyses of Laminated Plates and Shells by the Finite Element Method," Aeroelastic and Structures Research Laboratory, MIT, Cambridge, MA, AMMRC CTR 73-40, October 1973.

58) Orringer, O. and French, S.E., "FEABL-2/4/5 (Finite Element Analysis Basic Library) and EGL (Element Generator Library) User's Guide," Aeroelastic and Structures Research Laboratory, MIT, Cambridge, MA, ASRL TR 1024, January 1978.

59) Palmgren, A., "Die Lebensdauer von Kugellager," ZVDI, Vol. 68 (1924), 339-341.

60) Miner, M.A., "Cumulative Damage in Fatigue," JApplMech, Vol. 12 (1945), A159-A164.

61) Orringer, O., "FRAP (Front Analysis Program) User's Guide," Aeroelastic and Structures Research Laboratory, MIT, Cambridge, MA, ASRL TR 1023, March 1974.

62) Goland, M. and Reissner, E., "The Stresses in Cemented Joints," JApplMech, March 1944, A17-A27.

63) Rosen, B.W., "Tensile Strength of Fibrous Composites," AIAAJ, Vol. 2 (1964).

64) Kelly, A., Strong Solids, Oxford, 1966.

65) Gantmacher, F.R., The Theory of Matrices, Vol. 1, Chelsea Publishing Co., New York, 1960.

66) Orringer, O., "Subroutine EQSVR," Aeroelastic and Structures Research Laboratory, MIT, Cambridge, MA, internal technical memorandum G.1.012, November 1976.

67) Weed, D.N. and Francis, P.H., "Process Development for the Fabrication of High-Quality Composite Tubes," JFibreSciTech, Vol. 10 (1977), 89-100.

68) McClintock, F.A. and Argon, A.S., Mechanical Behavior of Materials, Addison-Wesley, Reading, MA, 1966.

69) Schmit, L.A., Kicher, T.P. and Morrow, W.M., "Structural Synthesis Capability for Integrally Stiffened Waffle Plates," AIAAJ, Vol. 1 (December 1963), 2820-2836.

70) Felton, L.P., Nelson, R.B. and Bronowicki, A.J., "Thin-Walled Elements in Truss Synthesis," AIAAJ, Vol. 11 (December 1973), 1780-1782.

71) Khot, N.S., Venkayya, V.B. and Berke, L., "Optimum Structural Design with Stability Constraints," IntJNumMethEng, Vol. 10 (1976), 1097-1114.

72) Schmit, L.A. and Ramanathan, R.K., "Multilevel Approach to Minimum Weight Design Including Buckling Constraints," AIAAJ, Vol. 16 (February 1978), 97-104.

73) Moses, F. and Kinser, D.E., "Optimum Structural Design with Failure Probability Constraints," AIAAJ, Vol. 5 (June 1967).

74) Mau, S.T., "Optimum Design of Structures with a Minimum Expected Cost Criterion," Department of Structural Engineering, Cornell University, Ithaca, NY, TR 340, 1971.

75) Yang, J.N., "Reliability Prediction and Cost Optimization for Composites Including Periodic Proof Tests in Service," Department of Engineering Science and Mechanics, Virginia Polytechnic Institute and State University, Blacksburg, VA, AFML-TR-76-224, November 1976.

☆U.S.Government Printing Office: 1979 — 657-002/570